# Momentum and Heat Transfer Characteristics of Axisymmetric Particles in Non-Newtonian Fluids: Sphere and Spherical Segments

*A Thesis Submitted*

*in Partial Fulfilment of the Requirements for the*

*Degree of*

## DOCTOR OF PHILOSOPHY

*by*


**Preeti**

**(2019CHZ0005)**




**DEPARTMENT OF CHEMICAL ENGINEERING INDIAN INSTITUTE OF TECHNOLOGY ROPAR**


**June, 2024**

Preeti: *Momentum and Heat Transfer Characteristics of Axisymmetric Particles in Non-Newtonian fluids: Sphere and Spherical Segments.*

*Dedicated to my family*

# Declaration of Originality

I hereby declare that the work which is being presented in the thesis entitled **Momentum and Heat Transfer Characteristics of Axisymmetric Particles in Non-Newtonian Fluids: Sphere and Spherical Segments** has been solely authored by me. It presents the result of my own independent investigation/research conducted during the time period from December 2019 to May 2024 under the supervision of Dr. Swati A. Patel, Former Assistant Professor and Dr. Tarak Mondal, Assistant Professor. To the best of my knowledge, it is an original work, both in terms of research content and narrative, and has not been submitted or accepted elsewhere, in part or in full, for the award of any degree, diploma, fellowship, associateship, or similar title of any university or institution. Further, due credit has been attributed to the relevant state-of-the-art and collaborations (if any) with appropriate citations and acknowledgments, in line with established ethical norms and practices. I also declare that any idea/data/fact/source stated in my thesis has not been fabricated/ falsified/ misrepresented. All the principles of academic honesty and integrity have been followed. I fully understand that if the thesis is found to be unoriginal, fabricated, or plagiarized, the Institute reserves the right to withdraw the thesis from its archive and revoke the associated Degree conferred. Additionally, the Institute also reserves the right to appraise all concerned sections of society of the matter for their information and necessary action (if any). If accepted, I hereby consent for my thesis to be available online in the Institute's Open Access repository, inter-library loan, and the title & abstract to be made available to outside organizations.

Signature

Name: Preeti (Preeti Suri)
Entry Number: 2019CHZ0005
Program: PhD
Department: Chemical Engineering
Indian Institute of Technology Ropar
Rupnagar, Punjab 140001
Date: June 2024

# Acknowledgement

*I would like to express my deepest gratitude and appreciation to all those who have supported and guided me throughout my journey in completing this Ph.D. thesis. Without their assistance and encouragement, this achievement would not have been possible.*

*First, I am very grateful to my former advisor, Dr. Swati A Patel, for her guidance throughout my journey. Her guidance has been invaluable, not only for my professional but also in personal life will inspire me to carry on this demanding journey. Her constant support and enthusiasm guided me over the years of development. She always provides me with moral support while covering many rough patches of life. This work would not have been complete without her meticulous scrutiny and unwavering support throughout my PhD. I am truly fortunate to work under her supervision. I am quite fortunate to work with the two supervisors. My current supervisor, Dr. Tarak Mondal, I have not spent much of my time with him. But he is always there in need of time. He is so cooperative and understanding that I never felt a sense of change. He provides me with all the freedom to carry out my work effortlessly.*

*I would also like to extend my thanks to Prof. Raj Chhabra for providing me with the much-needed guidance throughout my degree. The way of explaining and elaborating the concept always makes it easy to understand the complexity of the transport phenomena and the rheological studies. It has been an honor to work under his supervision. I would also like to extend my heartfelt thanks to the members of my thesis committee for their valuable insights, constructive feedback, and rigorous examination of my work. Their expertise and critical input have significantly enhanced the quality of this thesis.*

*I am also thankful to the staff, faculty and the HOD of the Department of Chemical Engineering for providing me with all the necessary facilities to conduct my research smoothly. I would like to express my sincere appreciation to the Institute for providing the funding and scholarships that have supported my research financially.*

*I extend my thanks to my lab mates Anshuman Verma, Khyati, Richa, Niharika, and friends Anisha and Amrish Choudhary, who have provided a positive and cheerful environment. Lastly, I am grateful to my family, without their constant support, positive criticism, and belief, I would never be able to go on this journey.*

*Above all, I am eternally grateful to God who always enlighten my path.*

*Preeti Suri*

# Certificate

This is to certify that the thesis entitled **Momentum and Heat Transfer Characteristics of Axisymmetric Particles in Non-Newtonian Fluids: Sphere and Spherical Segments**, submitted by **Preeti (2019CHZ0005)** for the award of the degree of **Doctor of Philosophy** of Indian Institute of Technology Ropar, is a record of bonafide research work carried out under my guidance and supervision. To the best of my knowledge and belief, the work presented in this thesis is original and has not been submitted, either in part or full, for the award of any other degree, diploma, fellowship, associateship or similar title of any university or institution.

In my opinion, the thesis has reached the standard fulfilling the requirements of the regulations relating to the Degree.

28/6/24

Signature of the Supervisor(s)

Dr. Tarak Mondal

Chemical Engineering

Indian Institute of Technology Ropar

Rupnagar, Punjab 140001

Date: June 2024

# Lay Summary

Fluid-particle interactions are a common occurrence in various industrial processes. These processes include slurry transportation, pharmaceutical product manufacturing, food processing, paper production, catalytic processes, mineral extraction, cooling/heating of mineral slurries, drying of powders, and pneumatic conveying. Many transport, dispersion and dissolution processes in nature involve interaction between fluid and particles inherently, e.g., the flowing of seeds in wind, sand or soil in a flowing water stream. Unit operations such as fluidization, sedimentation, filtration, etc., well recognize processes involving fluid-particle interactions in various engineering applications. Evidently, a few of the assumptions in designing these processes consider a particle to be a perfect sphere in shape. Though this assumption facilitates design calculations, the drag values for non-spherical particles can deviate significantly from that of a sphere. For instance, in the estimation of the rates of heat and mass transfer in packed and fluidized beds, the use of the results of a single sphere is well-known in literature. Indeed, the drag experienced by the particle is a strong function of its size, shape, and orientation in the surrounding fluid medium. On one hand, the assumption of spherical particles may facilitate ease of solving non-spherical particulate systems, it makes the process designing less reliable by compromising the accuracy up to a certain level. Generally, the non-spherical shapes of the particle can be categorized in various ways. The first distinction can be made based on their regularity (sphere, cylinder, cube, polyhedron, disc, spheroid, cones, etc.) and irregularity (ash, sand, gravels, additives for polymeric or food products, pharmaceutical powders, etc.) in their shapes. The non-spherical shape of regular particles is, typically, characterized by sphericity (ratio of the surface area of the equal-volume sphere to the actual surface area of the particle), $\psi$ as a shape descriptor e.g., settling/sedimentation and transport of particles. For given dimensions of the regular non-spherical particle, one can easily calculate the surface area and hence the sphericity of the particle in a straightforward manner. The major drawback of this approach is that particles of different shapes may have the same values of sphericity. In spite of this limitation, sphericity is used widely in literature. Hence, the shape of the particle, being a crucial entity in studying hydrodynamic and thermal attributes of various applications, remains of great interest to researchers. Spherical caps or segments which are seen in the coagulation or breakdown phenomena of spherical particles which may not follow the regularity of their parent particles. Such shapes have received very little attention in the literature. This study examines the role of spherical segments in various flow regimes, including steady creeping, forced, and natural convection. The study also investigates the effects of confinement and fluids with non-linear rheology, such as power-law and Bingham plastic fluids on momentum and heat transfer characteristics. Additionally, as the Reynolds number approaches zero, non-Newtonian fluids tend to behave more like Newtonian fluids. To measure zero-shear rate and shear stress-shear rate data for power-law shear-thinning fluids, the Falling Ball Method (FBM) has been extended to non-Newtonian systems including virgin and filled polymer melts, composites, polymer-solutions, etc.

# Abstract

This thesis contributes towards understanding the flow and heat transfer characteristics of generalized fluids past a particle of the shapes: sphere and spherical segments. In processes like fluidization, the interaction between the fluid and solid components plays a crucial role in enhancing heat and mass transfer, as well as promoting fluid mixing. The pneumatic transport of the particulate matter also involves the hydrodynamic interactions of the particle and the conveying medium. Various scenarios, such as solid-fluid interaction in sewage sludge, suspensions, drilling muds in oil recovery, sedimentation, thickening of slurries, and waste treatment in mineral industries, involve non-Newtonian fluids frequently interacting with non-spherical particle shapes. Furthermore, in biological applications of fluid-particle systems, instances like the motion of red blood cells in capillary flow and drug delivery systems showcase the relevance of understanding these interactions. Thus, the current interest in studying the momentum and heat transfer from spherical segments and a sphere as a limiting case of spherical segment in different types of fluids and/or under different conditions stems from both fundamental and pragmatic considerations. Generalized Newtonian fluids are encountered in a wide range of applications: toothpaste, butter, jam, cosmetic creams, mortars, foams, polymeric solutions melt, etc. A great many industrial processes involve Generalized Newtonian fluids, power-law, and Bigham plastic, ranging from the creation of chocolate to concrete used for the construction of buildings and the paper pulp suspensions, dairy products, polymers and polymeric solutions, etc. To achieve the underlying objective of this thesis, a finite element based numerical approach has been employed to study the crossflow of Bingham plastic or power-law fluids and Newtonian fluids as a limiting case past a spherical segment in creeping, forced-, and natural-convective regimes. The numerical experiments were conducted using the finite element-based simulation software COMSOL Multiphysics. The Bingham plastic fluid behavior was modeled using a regularized continuous constitutive relation *Papanastasiou model*. The evaluation of yielded and unyielded sub-domains in the flow field due to *the Papanastasiou model* has been further substantiated by reproducing similar results using the other regularization approaches available in the literature, *i.e.*, *the bi-viscous model* and *Bercovier and Engelman model*. The range of nondimensional parameters considered in this study is such that the flow and temperature fields remain steady. Using the numerical technique outlined above, two noteworthy contributions were made toward understanding the flow and heat transfer characteristics of Bingham plastic or power-law fluid flow past spherical segments. First, the *influence of the shape* of the particle, *i.e.*, sphericity of the spherical segment ($\psi$) on the flow and thermal characteristics has been examined for the unconfined/confined flow of Newtonian, Bingham plastic or power-law fluid in forced/free convection regime. In each case, extensive results for the topology of the yielded/unyielded regions, recirculation zones, isotherms, drag and heat transfer coefficients as a function of the pertinent parameters have been presented and analyzed in detail to elucidate the effect of the shape of the particle and of the confinement on momentum and heat

transport. The second contribution was the numerical results for the creeping flow of power-law fluids past a sphere, which have been used to develop a scheme to construct the shear stress–shear rate curves using the Falling Ball Method. The work was concluded by presenting extensive comparisons with experimental results for Newtonian fluids and shear-thinning polymer solutions in the low-shear region including the zero-shear viscosity and the shear-thinning region.

# List of Publications

**Journal**

1. **Suri, P.**, Patel, S. A., Chhabra, R. P. Falling ball method for determining zero shear and shear-dependent viscosity of polymeric systems: Solutions, melts, and composites. *Journal of Vinyl and Additive Technology*, **2022**, 29(4), 670-684.
2. **Suri, P.**, Verma, A., Patel, S. A., Chhabra, R. P. Free convection from a single and a pair of spheres in power-law fluids at very small Grashof numbers. *Journal of Non-Newtonian Fluid Mechanics*, **2023**, 320, 105109.
3. **Suri, P.**, Patel, S. A. Effect of shapes of particle on flow and heat transfer in confined flow. *Sādhanā*, **2023**, 48(4), 242.
4. **Suri, P.**, Patel, S. A. Particle shape matters: Flow and heat transfer characteristics of non-spherical particles. *Powder Technology*, **2024**, 431, 119102.
5. **Suri P.**, Mondal T., Patel S.A., Settling of spherical segment in yield-stress fluid. *Chemical Engineering Science.* **(Submitted)**
6. **Suri P.,** Patel S.A., Effect of shape of spherical segments on flow and thermal characteristics in yield stress fluid. **(In preparation)**
7. **Suri P.,** Patel S.A., Thermal characteristics of spherical segments in yield stress fluid under free convection regime. **(In preparation)**

**Conference Proceeding**

1. Verma A., **Suri P**., Patel S. A. On Creeping flow of yield stress fluid past a square cylinder. *Proceeding of 8th international and 47th national conference on fluid mechanics and fluid power*. IIT Guwahati, Assam, December 9-11, 2020.
2. Nalluri S., **Suri P.**, Patel S. A. Natural convection from a confined sphere in yield stress fluids. *Proceedings of the 26thNational and 4th International ISHMT-ASTFE Heat and Mass Transfer Conference*, IIT Madras, Chennai, December 17-20, 2021.
3. **Suri P**., Tosawara N. K., Patel S. A. (2023) Flow and heat transfer from a heated cylinder moving adjacent to wall in yield stress fluids. *8th Thermal and Fluids Engineering Conference*, ASTFE digital library. University of Maryland, College Park, MD, USA, March 26-29, 2023
4. Raja A.H., **Suri P**., Patel S. A., Chhabra R.P. Laminar forced convection from a 2-D heated transverse plate in power-law fluids. *Proceeding of the 27$^{th}$ National and 5$^{th}$ International ISHMT-ASTFE heat and mass transfer conference*. IIT Patna, Bihar, December 14-17, 2023.
5. Kumar S., **Suri P**., Dutt N., Patel S. A. Thermal analysis of the effect of non-Newtonian fluid on the optimally spaced elliptical cylinder. *Proceeding of the 9$^{th}$ International conference on Experimental and Numerical Flow and Heat Transfer*. Imperial College of London, United Kingdom, April 11-13, 2024.
6. Kumar K. A., Dutt N., **Suri P**., Patel S. A. Optimization Study of Power-Law Fluids Staggered Circular Cylinders in Laminar Forced Convection. *Proceeding of the 9$^{th}$ International conference on Experimental and Numerical Flow and Heat Transfer*. Imperial College of London, United Kingdom, April 11-13, 2024.

# CONTENT

# List of Tables

# List of Figures

# Nomenclature

$a,b,c,d$ coefficient of equations, *dimensionless*

$A_p$ projected area of particle, $m^2$

$Bn$ Bingham number $\left[=\tau_o l_c/\mu_B V_c\right]$ , *dimensionless*

$Br$ Brinkmann number $\left[=\mu_B V_c^2/k\left(T_h-T_c\right)\right]$, *dimensionless*

$C$ heat capacity of fluid, *J/kg K*

$C_D$ drag coefficient, *dimensionless*

$C_{DF}$ frictional drag coefficient, *dimensionless*

$C_{DP}$ pressure drag coefficient, *dimensionless*

$C_P$ pressure coefficient, *dimensionless*

$C_s$ Stokes drag coefficient, *dimensionless*

$d$ diameter of sphere or spherical particle, *m*

$d_c$ chord length at the base of the spherical segment, *m*

$d_{eq}$ equivalent diameter of sphere, *m*

$D_\infty$ diameter of the computational domain, *m*

$F_D$ drag force, *N*

$F_{DF}$ frictional component of drag force, *N*

$F_{DP}$ pressure component of drag force, *N*

$g$ acceleration due to gravity, $m\ s^{-1}$

$Gr_B$ Grashof number for Bingham plastic fluid $\left[=\rho_\infty^2 g\beta\Delta T l_c^3/\mu_B^2\right]$ , *dimensionless*

$Gr_{PL}$ Grashof number for power-law fluid $\left[=\rho_\infty^2\left(g\beta\Delta T\right)^2 l_c^{n+2}/m^2\right]$ , *dimensionless*

$h$ local heat transfer coefficient, $W/m^2\ K$

$h_c$ height of the spherical segment, $W/m^2\ K$

$H$ width of the domain in the creeping regime, *m*

$\bar{h}$ average heat transfer coefficient, $W/m^2\ K$

$k$ thermal conductivity of fluid, *W/m K*

$l$ gap between the twin sphere, *m*

$l_c$ characteristic length, *m*

$L$ length of the domain, *m*

$m$ flow consistency index, $Pa\ s^n$

$M$ growth rate parameter, *dimensionless*

$n$ flow behvaiour index, *dimensionless*

$\boldsymbol{n_s}$ unit vector normal to the surface of cylinder, *dimensionless*

$N_C$ total no. of element at the curved surface of the spherical segment, *dimensionless*

$N_f$ total no. of element at the flat surface of the spherical segment, *dimensionless*

$N_T$ total no. of element at the surface of the particle, *dimensionless*

$N_T$ total no. of element in the grid, *dimensionless*

$Nu_l$ local Nusselt number, *dimensionless*

$Nu_{avg}$ average Nusselt number, *dimensionless*

$p$ pressure, *dimensionless*

$Pe$ Peclet number $\left[=Re\times Pr\right]$, *dimensionless*

$Pr_B$ Prandtl number for Bingham plastic fluid $\left[=C\mu_B/k\right]$, *dimensionless*

$Pr_{PL}$ Prandtl number for power-law fluid $\left[=Cm\left(V_c/l_c\right)^{n-1}/k\right]$, *dimensionless*

$Ra$ Rayleigh number $\left[=Gr\times Pr\right]$, *dimensionless*

$Re$ Reynolds number $\left[=\rho_\infty V_c l_c/\mu\right]$, *dimensionless*

$Re_B$ Reynolds number $\left[=\rho_\infty V_c l_c/\mu_B\right]$, *dimensionless*

$Re_{PL}$ Reynolds number $\left[=\rho_\infty V_c^{2-n} l_c^n/m\right]$, *dimensionless*

$Re_c$ critical Reynolds number, *dimensionless*

$S$ heat transfer area of particle, $m^2$

$T$ temperature of fluid, $K$

$T_c$ inlet temperature of the fluid, $K$

$T_h$ constant wall temperature at the surface of the particle, $K$

$\boldsymbol{V}$ velocity vector, *dimensionless*

$V_c$ characteristic velocity, *m/s*

$U$ free stream velocity, *m/s*

$V_p$ Volume of the particle, $m^3$

$X_{BP,f}$ drag correction factor for bingham plastic fluid, *dimensionless*

$X_{BP,s}$ drag correction factor for spherical segment, *dimensionless*

$Y(n)$ drag correction factor for sphere in power-law fluid, *dimensionless*

*Greek symbols*

| | |
|---|---|
| $\alpha_f$ | thermal diffusivity ($k/\rho_\infty C$), $m^2/s$ |
| $\alpha$ | Shape factor of spherical segments, *degree* |
| $\beta$ | coefficient of volumetric expansion, $1/K$ |
| $\delta$ | growth rate parameter in Bercovier and Engelman model, $s^{-1}$ |
| $\dot{\gamma}_{ij}$ | components of the rate of strain tensor, *dimensionless* |
| $\eta$ | effective viscosity, *dimensionless* |
| $\mu$ | Newtonian fluid viscosity, *Pa s* |
| $\mu_B$ | plastic viscosity, *Pa s* |
| $\lambda$ | confinement ratio, *dimensionless* |
| $\nu$ | momentum diffusivity, $m^2/s$ |
| $\theta$ | position on the surface of particle, *degree* |
| $\rho$ | fluid density, $kg/m^3$ |
| $\xi$ | temperature of fluid, *dimensionless* |
| $\omega$ | surface vorticity, *dimensionless* |
| $\boldsymbol{\tau}$ | stress tensor, *dimensionless* |
| $\tau_{ij}$ | components of the extra stress tensor, *dimensionless* |
| $\tau_o$ | yield stress, *Pa* |
| $\varphi$ | apex angle of the cone, *dimensionless* |
| $\psi$ | sphericity, *dimensionless* |
| $\Omega$ | modified Nusselt number in power-law fluid, *dimensionless* |

*Subscripts*

| | |
|---|---|
| *r, z* | cylindrical coordinates |
| $\infty$ | refers to free stream condition |
| *f* | refers to fluid |
| *B* | Bingham plastic fluids |
| *N* | Newtonian fluid |
| *PL* | power-law fluids |
| *S* | Shape of spherical segment |

# Chapter 1
# Introduction

## 1.1 Focus of the present study and motivation

Fluid-particle interactions are encountered in numerous industrial settings such as slurry transport, food processing, pharmaceutical product manufacturing, catalytic processes, paper production, coating of materials, cooling/heating of mineral slurries, drying of powder, pneumatic conveying, food processing, mineral extraction, to name a few. Many transport, dispersion and dissolution processes that occur in nature involve interaction between fluid and particles inherently, e.g., the flowing of seeds in wind, sand or soil in a flowing water stream. The processes involving fluid-particle interactions in various engineering applications are well recognized by unit operations such as fluidization, sedimentation, filtration, etc. Evidently, a few of the assumptions in designing these processes consider a particle to be a perfect sphere in shape. Though this assumption facilitates design calculations, the drag values for non-spherical particles can deviate significantly from that of a sphere. For instance, in the estimation of the rates of heat and mass transfer in packed and fluidized beds, the use of the results of a single sphere is well-known (Comiti *et al*., 2000; Mauret and Renaud, 1997; Peev *et al*., 2002). Indeed, the drag experienced by the particle is a strong function of its size, shape, and orientation of the particle in the surrounding fluid medium (Chhabra, 1995; Wang *et al*., 2009; Dulhani *et al*., 2014). On one hand, the assumption of spherical particles may facilitate ease of solving non-spherical particulate systems, it makes the process designing less reliable by compromising the accuracy up to a certain level. Generally, the non-spherical shapes of the particle can be categorized in various ways. The first distinction can be made based on their regularity (sphere, cylinder, cube, polyhedron, disc, spheroid, cones, etc.) and irregularity (ash, sand, gravels, additives for polymeric or food products, pharmaceutical powders, etc.) in their shapes. The non-spherical shape of regular particles is, typically, characterized by sphericity (ratio of the surface area of the equal-volume sphere to the actual surface area of the particle), $\psi$ as a shape descriptor e.g., settling/sedimentation and transport of particles.

$$\text{Sphericity, } \psi = \frac{S_s}{S_p} = \frac{\textit{Surface area of the volume-equivalnet sphere}}{\textit{Surface area of the actual particle}} \tag{1.1}$$

For given dimensions of the regular non-spherical particle, one can easily calculate the surface area and hence the sphericity of the particle in a straightforward manner. There are several other shape factors found in the literature for non-spherical regular shaped particles based on the circularity, perimeter and projected area of the particle. For instance, Krumbein (1942) used circularity as the characteristics parameter to define the shape of the particle.

$$X_p = \frac{P_s}{P_p} = \frac{Perimeter\ of\ equivalent\ projected\ area\ sphere}{Projected\ perimeter\ of\ the\ actual\ particle} \tag{1.2}$$

The combination of both sphericity and the perimeter is also considered by several researchers in the literature (Dellino et al., 2005; Dioguardi and Mele, 2015) as

$$Y = \frac{\psi}{X_p} = \frac{Sphericity\ of\ the\ particle}{Circularity\ of\ the\ particle} \tag{1.3}$$

Last but not least, in order to study the effect of the particle elongation Corey (1950) have proposed a new shape factor based on the three principal axes of the particle which is defined as follows:

$$\beta = \frac{c}{\sqrt{ab}} \tag{1.4}$$

Many researchers have used sphericity as a shape descriptor to characterize non-spherical particles. However, one major drawback of this method is that particles of different shapes can have the same sphericity value. Despite this limitation, sphericity is still widely used in literature to describe particle shapes. As the shape of a particle is a crucial factor in studying the hydrodynamic and thermal attributes of various applications, it remains of great interest to researchers. In numerous industrial and natural settings (drilling of petroleum, food processing, cosmetic and pharmaceutical manufacturing, fluidization, avalanche flow, etc.), these non-spherical particles often encounter non-Newtonian fluids. The rheological properties of non-Newtonian fluids are very distinct and obscured from Newtonian fluids. Multiphase fluids and many high molecular polymer melts show different fluid properties with respect to the applied shear rate or shear stress. Their apparent viscosity either increases or decreases based on the nature of the fluid like power-law fluids or they can possess the dual nature like yield stress fluid. Different non-Newtonian fluids that are often encountered in industrial applications are summarized by Pang *et al.* (2020). **Figure 1.1** shows the shear stress and shear rate plot for the meat extract and carbopol solution and their resultant nature of yield stress fluid. The initial stress that is required by these fluids are known as critical stress below which they behave like a solid. The dual nature of the fluid has an enormous effect on the hydrodynamics behavior as well as on their heat transfer rates.

In the fluidization process, the fluid-solid interaction plays a vital role in enhancing the heat and mass transfer and mixing of the fluid. The solid-fluid interaction in the case of sewage sludge, suspensions, drilling muds in oil recovery, sedimentation, thickening of slurries, and disposal of waste treatment from mineral industries are a few examples where non-Newtonian fluids are often encountered with non-spherical particle shapes. Other biological applications of fluid-particle systems also include the motion of the red blood cell in capillary flow and drug delivery systems.

Studying single particles in non-Newtonian fluid builds a solid foundation for knowledge of muti-particle systems, and indeed, fluid mechanics has witnessed remarkable progress in this area, especially with the

advent of numerical techniques and the enormous improvement in computational abilities. Many non-spherical shapes like circular cylinders (Zisis and Mitsoulis, 2002; Roquet and Saramito, 2003; Deglo de Besses *et al.*, 2003; Bharti and Chhabra, 2006; Bharti *et al.*, 2007;Tokpavi *et al.*, 2008; Mossaz *et al.*, 2010, 2012; Nirmalkar and Chhabra, 2014), elliptical cylinders (Sivakumar *et al.*, 2007; Bharti *et al.*,

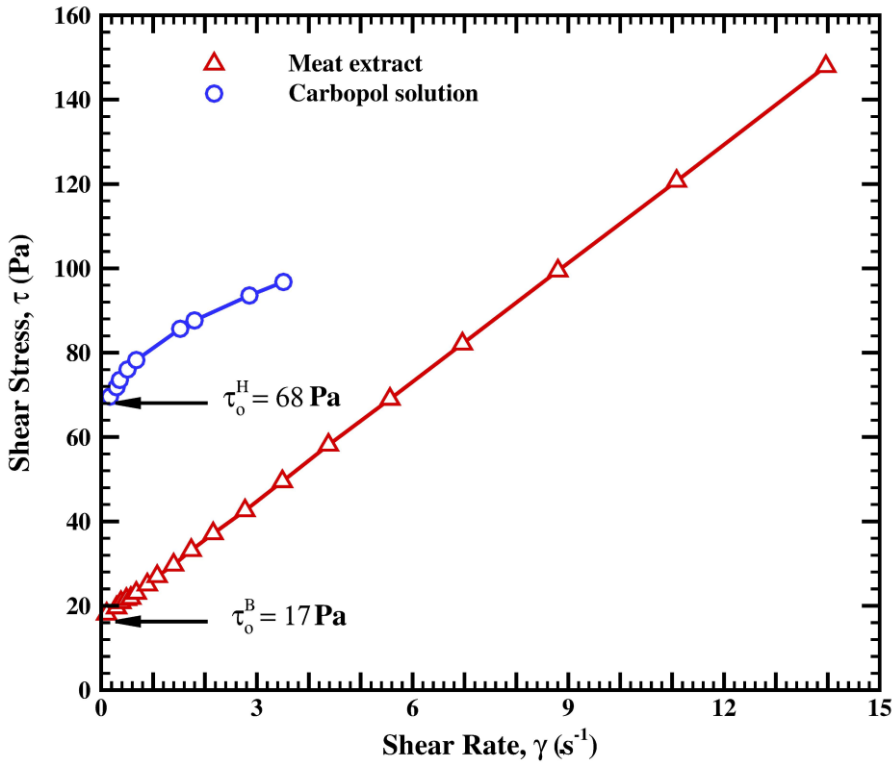


**Figure 1.1** Rheogram for yield stress fluids with their plastic viscosity (Chhabra and Patel 2023).

2008; Patel and Chhabra, 2013, 2014, 2016), spheroid (Tripathi *et al.*, 1994; Gupta *et al.*, 2014; Gupta and Chhabra, 2014, 2016), disks (Nitin and Chhabra, 2005, 2006; Gupta *et al.*, 2017), and cones (Sharma and Chhabra, 1991; Ahonguio *et al.*, 2015) have been widely studied by researchers in Newtonian and non-Newtonian fluids. However, the shapes like segments from the sphere which can be formed due to breakdown or coagulation of the spherical particle during process or naturally formed shapes in pharmaceutical or catalyst forming processes have received little attention in literature so far. So far, the hemisphere is the only spherical segment that have received the attention under various fluid regimes numerically (Sasmal *et al.*, 2013; Sasmal and Chhabra, 2014; Nalluri *et al.*, 2015; Prakash *et al.*, 2017).

The motivation of the present work derives from our interest in the flow of non-Newtonian and Newtonian fluid past axisymmetric particles, i.e., spherical segments including sphere as a limiting case due to their numerous applications like mine tailing, clay suspensions, mineral slurries, microplastic, semiconductor and food industry particularly for the spherical segment. The aim of the present study is focused on the sphere and spherical segments under appropriate conditions via. forced and free convection. The momentum and heat transfer characteristics from a range of spherical segments varying in shape dissected

from a sphere have been explored in this work over a range of governing parameters corresponding to free or forced convection phenomena in steady state flow regime. The results were also extrapolated in each case for the sphere as a limiting shape. Furthermore, the proximity of the external walls to the heated spherical segment also modifies the flow and heat transfer characteristics. The effort has been made to explore the effect of confinement on the forced convection heat transfer from spherical caps in Newtonian fluids. The free convection in very weak buoyancy flow field (a very low Grashof number) has been investigated considering sphere and a pair of spheres as a hot bluff body (or bodies) in the non-Newtonian power-law fluids in steady-state flow regime. A universal correlation for the average Nusselt number has been proposed to bridge the gap between the conductive heat transfer having a limiting Nusselt number, i.e., 2 and high buoyancy convective regime for an isothermal sphere in Newtonian and power-law fluids. Additionally, interaction between a pair of spheres in the weak buoyancy flow has been examined by varying the distance in the vertical direction. The effect of the spacing between the two spheres modifies the condition limit Nusselt number and eventually overall heat transfer characteristics. Finally, the applicability of the falling ball method (FBM) which is proven very effective in measuring the viscosity of Newtonian fluids under ambient as well as high temperature and pressure condition has been extended to evaluate the zero-shear viscosity of non-Newtonian polymer melts, composites solutions (shear-thinning power-law fluids). The theoretical results for the flow of power-law fluids past a sphere have been used to extract the values of the zero-shear viscosity and shear-dependent viscosity in the low-shear rate limit (creeping flow). The theoretical scheme outlined in this study has been validated by presenting comparisons with experimental results for scores of polymer solutions for which both falling sphere and rheological data are available in the literature.

## 1.2 Objective of the study

In particular, this dissertation is concerned with the following specific inter-related problems:

1. To advance the understanding of the settling and stability criterion of spherical segments in yield stress fluids in the creeping flow regime.
2. To determine the effect of fluid rheological and kinematic parameters on the momentum and heat transfer characteristics of Newtonian and non-Newtonian fluids in forced and natural convection regimes.
3. To quantify the impact of axisymmetric shapes of the particle on the flow and thermal characteristics in Newtonian and non-Newtonian fluid media.
4. To identify the role of the confinement in the case of forced convection from non-spherical particles in Newtonian fluids.
5. To establish the correlations between the pertinent parameters and the macroscopic flow and heat transfer characteristics thereby enabling their a priori estimation in a new application.

6. To develop a scheme to construct the shear rate-shear stress curves for polymeric system (power-law fluids) based on Falling Ball Method (FBM) by employing numerical results for the creeping flow of power-law fluids past a sphere.

## 1.3 Outline of the thesis

The overall purpose of the present work is to explore the fluid mechanical and heat transfer aspects of the free-falling motion of asymmetric rigid particles in non-Newtonian fluids, specifically spheres and segments dissected from a sphere. The numerically conducted research spans a broad range of flow regimes, including creeping to Newtonian flow. The thermal characteristics of Newtonian and non-Newtonian fluids (Bingham plastic and power-law) flowing past non-spherical particles of various shapes have been extended to study the forced as well as natural convection phenomena. *Chapter 1*, the introductory Chapter, gives a detailed overview of the motivation, objectives, and contributions of this thesis work in detail. It introduces the characteristics of the rigid particles and the pervasive nature of the non-Newtonian fluids encountered in day-to-day life as well as in a wide range of engineering applications.

*Chapter 2* illustrates the specific problems statements defined in this work, followed by demonstrating the relevant governing equations of fluid dynamics and heat transfer – the continuity, momentum, and energy equations– together with the constitutive laws for the Bingham plastic and power-law fluids. The discussion has been subsequently followed by the simplifying assumptions employed for each problem. The chapter includes the governing dimensionless parameters for momentum and heat transfer phenomena that evolve during the scaling of the aforementioned equations. The specific issues associated with the numerical implementation of the ideal Bingham plastic model have also been discussed, and alternatives to overcome the inherently discontinuous nature of the Bingham constitutive model have been introduced here. Finally, the details of the numerical methodology employed for this work have been outlined.

*Chapter 3* deals with the free motion of spherical segments dissected from a sphere settling in Bingham plastic fluids under the influence of gravity. The momentum transfer from the settling particle to yield stress fluids in the creeping flow regime has been explored numerically. The effect of the shapes of the particle has been analyzed in terms of yield surfaces, stability criteria, and drag coefficients over the range of Bingham plastic fluids.

*Chapters 4* and *5* represent the extensive results on forced and free convection phenomena, including relevant literature, assessment of the methodology, result analysis, and discussion on momentum and thermal characteristics.

*Chapter 4* extends the role of the particle shape in unbounded and bounded Newtonian fluids media, illustrating the functional dependence of drag coefficients and average Nusselt numbers on the pertinent governing parameters in the forced convection regime. For unconfined flow, the flow and temperature

fields are analyzed by plotting the streamlines, isotherms, local Nusselt number. The results of streamline profiles show that the shape or lateral surfaces of the particles strongly influence the size of the wake and the location of the separation point from the particle surface. Notably, at low Reynolds numbers, particles with identical base area and height exhibit the drag in the order of cone < spherical segment < short cylinder. The drag coefficient as well as average Nusselt number plots for the three shapes with curvature, slanted and flat surfaces suggest that the correlation of drag and average heat transfer coefficients over the range of shape factors necessitate additional shape descriptors to enhance the level of fitting.

The confined Newtonian fluid flow past spherical segments has been studied over the range of geometrical parameters, i.e., shapes of spherical segments and confinements examined in terms of streamlines, isotherms, drag coefficients and average Nusselt numbers. The impact of the shape on the momentum and heat transfer has been quantified by comparing the results of spherical segments with the circular disc and sphere. The work has been summarized by proposing a correlation, for drag and average Nusselt number with a reasonable accuracy.

The effect of yield stress on the flow and heat transfer is illustrated in this chapter spanning the range of particle shape in the unconfined flow conditions. The flow kinematics has been studied by mapping the flow field in the form of streamlines and yielded/unyielded regions while thermal field has been examined by plotting the isotherms and local Nusselt number over the range of the geometrical, kinematic and rheological parameters. Correlations to predict drag coefficients and average Nusselt numbers have been proposed over the pertinent range of parameters.

*Chapter 5* focuses on obtaining reliable results of total drag and average Nusselt number for a heated isolated sphere and for vertically aligned two spheres under a very low Grashof number free convection regime in power-law fluids. For the vertically aligned twin sphere case, center-to-center spacing between two spheres, defined as gap ratio, has been varied to explore the hydrodynamic interference between the two spheres. The results of the hydrodynamic drag, drag correction factors, local and average Nusselt numbers are examined in detail. The gap ratio plays a vital role in determining the severity of interference between the velocity and temperature boundary layers and, hence, the drag and heat transfer coefficients for the twin spheres.

The chapter further includes the free convection from spherical segments exploring the thermal characteristics in Bingham plastic fluids. The results are presented in the form of streamlines, yielded/unyielded regions, isotherm contours and average Nusselt numbers as a function of geometrical, kinematic and rheological parameters. The specific characteristics of the yield stress fluids showing fluid-like and solid-like regions under the prevailing shear stress field allow identifying the conduction limit for the particular shape of the particles. The conduction limit refers to the transfer of heat solely governed by the conduction mechanism that has been determined as a function of the particle shape in this work.

In *Chapter 6*, the numerical results for the creeping flow of power-law fluids past a sphere have been used to develop a scheme to construct the shear stress–shear rate curves using the falling ball method. For a sphere falling in Newtonian fluids, one needs to apply corrections to both the surface averaged shear stress and shear rate. For power-law fluids, both these correction factors are functions of the power-law index only in the creeping flow regime. The simple expressions have been developed for these correction factors in this chapter. The power-law index is given by the slope of the double log plot of the nominal average shear stress and shear rate on the surface of the sphere. This work is concluded by presenting extensive comparisons with experimental results for Newtonian fluids and shear-thinning polymer solutions in the low-shear region, including the zero-shear viscosity and the shear-thinning region, with reasonably good agreement.

Finally, *Chapter 7* presents a summary of major findings of this work followed by an identification of the areas meriting further investigation.

# Chapter 2

# Governing equations and numerical scheme

Fluids can exhibit both continuum and statistical behaviors at different length scales and time periods. However, for most practical purposes, at macroscopic scale the fluid behaves as a continuum. This hypothesis allows us to assume definite values of fluid properties such as density, temperature, and velocity at every point as a continuous function of time and of the position in the fluid. In this particular work, the flow and heat transfer are governed by - conservation of mass, conservation of momentum (Newton's second law of motion), and conservation of energy (First law of thermodynamics) - according to the continuum hypothesis to model momentum and energy transfer. These conservation equations, known as Continuity, Cauchy momentum, and energy equations, are tailored to the specific flow regime.

## 2.1 Governing equations

The governing equations presented here are based on the mass, momentum and energy balances with the assumptions of the steady, incompressible and laminar flow of fluid over the range of parameters employed in this work. These equations in their non-dimensional forms are written as:

Continuity equation: $\nabla \cdot \boldsymbol{V} = 0$ (2.1)

Momentum equation: $\left(\boldsymbol{V}.\nabla \boldsymbol{V}\right) = -\nabla \boldsymbol{p} + \left[\boldsymbol{N}_1\right]\nabla.\tau + \left[\boldsymbol{N}_2\right]\beta\xi\delta_{iy}$ (2.2)

Energy equation: $\left(\boldsymbol{V}.\nabla\right)\xi = \left[\boldsymbol{N}_3\right]\nabla^2\xi + \left[\boldsymbol{N}_4\right]\tau : \nabla \boldsymbol{V}$ (2.3)

Beside the non-dimensional primitive variables, namely, pressure ($p$), velocity ($V$) and temperature ($\xi$) in above equations, they further involve fluid properties, namely, density, $\rho_\infty$ ; shear stress, $\tau$; thermal conductivity, $k$; specific heat, $C$ and thermal expansion coefficient $\beta$.

The two phenomena of forced and free or natural convection have been analyzed in this work by investigating momentum and heat transfer characteristics in Newtonian and non-Newtonian fluids. Beginning with the forced convection, in the forced convection regime where flow is externally imposed and the variation of the fluid properties with temperature is insignificant over the narrow range of temperature interval (thereby justifying their evaluation at the mean film temperature) which makes it possible to solve for the flow field independent of the temperature field. In contrast, in natural convection regime, the fluid motion arises due to the density difference caused by the temperature difference, as a result, the flow and heat transfer equations are coupled. Due to prevailing body force field, the density difference gives rise to the buoyancy forces. This body force appears in the momentum equation when the Boussinesq approximation plugs into it to represent the linear relationship between the density and temperature. The linear relation between density-temperature is approximated by the standard Boussinesq

relationship as:

$$\rho = \rho_\infty \left[1 - \beta\left(T - T_c\right)\right] \tag{2.4}$$

The variation of density $\rho$ everywhere in the equations can be replaced by the constant density $\rho_\infty$, except the body force term in the momentum equation. Also, the temperature $T_c$ far away from the geometry is taken as the reference temperature in the buoyancy term. This part of approximation is tantamount to the assumption of the incompressible flow.

**Table 2.1** Dimensionless groups in **Eqs. (2.1) - (2.3)**

| Cases | Forced convection | Free convection |
|---|---|---|
| $V_c$ | $U$ | $\sqrt{g\beta\left(T_h - T_c\right)l_c}$ |
| $[N_1]$ | $1/Re_f$ | $\sqrt{Pr_f/(Gr_f \times Pr_f)}$ |
| $[N_2]$ | 0 | 1 |
| $[N_3]$ | $1/\left(Re_f Pr_f\right)$ | $1/\left(\sqrt{Ra_f Pr_f}\right)$ |
| $[N_4]$ | $Br_f/\left(Re_f Pr_f\right)$ | $Br_f/\left(\sqrt{Ra_f Pr_f}\right)$ |

$f = B$ for Bingham plastic fluids; $f = PL$ for power-law fluids; without subscript = Newtonian fluids

The viability of the results obtained by solving the governing equations expands by introducing the non-dimensional variables. The non-dimensional forms of the governing **Eqs. (2.1**) to **(2.3)** have been derived by scaling the variables length, shear stress, pressure and temperature using the $l_c$, as characteristics length; $\mu_f V_c / l_c$, $\rho_\infty V_c^2$ and $(T\text{-}T_c)/(T_h\text{-}T_c)$, respectively. The choice of characteristics velocity, $V_c$ depends upon the flow regime. Hence, the coefficients in the parenthesis are summarized in **Table 2.1** along with the choice of characteristics velocity.

The stress tensor $\tau$ in **Eq. (2.2)** is related to the nature of the fluid via shear stress-shear rate constitutive relationship. Similarly, the definition of the dimensionless parameters in governing equations, i.e., $Re_f$, $Pr_f$, $Gr_f$ and $Ra_f$ also varies with the choice of the constitutive relations for type of fluid. Time-independent class of fluid or generalized Newtonian fluids are considered in this work and depending upon the functional relationship between shear rate and shear stress, they are categorized into two types:

### (i) Shear-thinning and shear thickening fluids

Shear thinning or pseudo plasticity is the most commonly encountered non-Newtonian behavior in the fluids. A few common examples are polymer solutions, colloidal suspensions, blood, milk etc. The apparent viscosity of such fluids decreases with increasing shear rates and fluids becomes thinner as the shear rate increases. Shear thickening or dilatant fluids, on the contrary, show opposite behavior. Their apparent viscosity increases with the increase in shear rates. The most widely used constitutive equation

to mathematically model shear thinning, or shear thickening fluid behavior is two parameter power-law models.

$$\tau = m\dot{\gamma}^n \tag{2.5}$$

where *m* and *n* are empirical parameters known as flow consistency index and flow behavior index,

**Table 2.2** Values of power-law index for fluids at room temperature (Chhabra, 2006)

| Non-Newtonian fluids | *m* (Pa.s$^n$) | *n* |
|---|---|---|
| Chocolate | 0.7 | 0.5 |
| Mayonnaise | 5-100 | 0.6 |
| Toothpaste | 120 | 0.28 |
| Nail polish | 750 | 0.86 |
| Yoghurt | 25 | 0.5-0.6 |

respectively. The value $n < 1$ is for shear thinning fluids, $n > 1$ is for shear thickening fluids, and $n = 1$ for Newtonian fluids. **Table 2.2** has summarized a few examples of power-law fluids frequently encountered in various applications.

The extra stress tensor for power-law fluids in **Eq. (2.2)** is given as:

$$\tau_{ij} = m\left(\frac{\prod_{\dot{\gamma}}}{2}\right)^{n-1/2}\dot{\gamma}_{ij} \tag{2.5a}$$

Where, $\prod_{\dot{\gamma}} \equiv \sqrt{\sum_{i,j}\frac{1}{2}\dot{\gamma}_{ij}^2}$

### (ii) Yield stress fluids

These are the fluids which behave as plastic solids if the applied stress is less than a critical shear stress value, $\tau_0$ , known as a yield stress. Once applied stress exceeds the critical shear stress value, $\tau_0$ , the fluids subsequently exhibit linear or non-linear relationship between applied shear stress and the resultant shear rate. A fluid with the linear flow curve for $\tau > \tau_0$, is known as Bingham plastic fluid. The model representing the behavior of such fluids is called Bingham plastic fluid given in dimensional form as,

$$\tau' = \tau_o + \mu_B\dot{\gamma}' \qquad for \quad |\tau'| > \tau_o \tag{2.6a}$$

$$\dot{\gamma}' = 0 \qquad for \quad |\tau'| \le \tau_o \tag{2.6b}$$

The non-dimensional form of the Bingham plastic fluid model is expressed in the following form:

$$\tau = 1 + Bn\frac{\dot{\gamma}}{|\dot{\gamma}|} \qquad for \quad |\tau| \ge Bn \tag{2.7a}$$

$$\dot{\gamma} = 0 \qquad for \quad |\tau| < Bn \tag{2.7b}$$

The extra stress tensor for Bingham plastic fluids is given as:

$$\tau_{ij} = \left(1 + \frac{Bn}{\sqrt{\prod_{\dot{\gamma}}}}\right)\dot{\gamma}_{ij} \qquad \text{for} \quad \prod_{\tau} > Bn^2 \tag{2.7c}$$

$$\dot{\gamma}_{ij} = 0 \qquad \text{for} \quad \prod_{\tau} > Bn^2 \tag{2.7d}$$

Where, $\prod_{\sigma} \equiv \sqrt{\sum_{i,j} \frac{1}{2}\tau_{ij}^2}$ and $\prod_{\dot{\gamma}} \equiv \sqrt{\sum_{i,j} \frac{1}{2}\dot{\gamma}_{ij}^2}$

*Viscosity regularization methods for Bingham plastic fluids:*

Owing to the inherent discontinuous nature of the Bingham plastic model, **Eqs. (2.6)** and **(2.7)**, cannot be employed directly in computing such flows. The constitutive equation of an ideal Bingham plastic fluid, **Eqs. (2.6a)** and **(2.6b)**, shows that it applies in two distinct regions in the fluid which are not known a priori, namely yielded and unyielded regions. Consequently, the apparent viscosity in **Eq. (2.6b)** becomes unbounded or infinite as the shear rate vanishes in the unyielded regions.

This problem can be circumvented by using regularization methods proposed in the literature that enable the transition from the unyielded to yielded regions smooth during solving numerically, avoiding the inherent discontinuity of the ideal Bingham plastic model. (Papanastasiou, 1987; Glowinski and Wachs, 2011). Papanastasiou (1987) approximated the Bingham plastic viscosity by introducing an exponential regularization parameter as:

$$\eta_p = 1 + Bn\left(\frac{1 - e^{-M|\dot{\gamma}|}}{|\dot{\gamma}|}\right) \tag{2.8}$$

where $M$, the regularization parameter scaled using $l_c/V_c$ as the characteristic time scale to be dimensionless. According to the previous studies (Papanastasiou, 1987; Burgos *et al.*, 1999; Mitsoulis and Zisis, 2001; Glowinski and Wachs, 2011) stronger the yield stress effects, larger is the value of the regularization parameter $M$ needed to obtain accurate predictions of yielded/unyielded regions. While $M \rightarrow \infty$ reproduces the true Bingham plastic fluid behaviour, $M = 0$ corresponds to the Newtonian fluid behavior in **Eq. (2.8)**. Most of the results reported in this thesis have been obtained using Papanastasiou approximation, limited results were cross-checked by employing the two other regularization approaches available in the literature, namely, the so-called bi-viscosity model (O'Donovan and Tanner, 1984; Poole and Chhabra, 2007) and the one due to Bercovier and Engleman (Bercovier and Engleman, 1980), both of which are written as:

Bi-viscosity model: $\eta_{Bv} = \dfrac{\mu_y}{\mu_B} \quad if \quad |\tau| < Bn$ (2.9)

$$\eta_{Bv} = 1 + Bn\left[1 - \left(\frac{1}{\mu_y/\mu_B}\right)\right]\frac{1}{|\dot{\gamma}|} \quad if \quad |\tau| \geq Bn \tag{2.10}$$

Bercovier and Engleman model: $\eta_{BE} = 1 + Bn\left(\dfrac{1}{|\dot{\gamma}| + \delta}\right)$ (2.11)

Basically, the bi-viscous model, **Eqs. (2.9)** and **(2.10)**, overcomes the unbounded nature of fluid viscosity for the stress levels below the fluid yield stress by treating it as a highly viscous fluid of viscosity $\mu_y$ (yielding viscosity) which is typically several orders of magnitude larger than the Bingham plastic viscosity $\mu_B$. Similarly, **Eq. (2.11)** circumvents the discontinuity in the fluid behavior by replacing the zero-shear rate in the unyielded part by a very small value, denoted here by $\delta$. In summary, the three previous approximations replace the true Bingham fluid with a fluid that has vastly different viscous characteristics above and below the yield stress. Furthermore, all three approaches rely on selecting a suitable regularization parameter, $M$ or $\mu_y$ or $\delta$.

## 2.2 Dimensionless governing parameters

Dimensionless analysis reveals that the momentum and heat transfer characteristics of forced and free convection are governed by the following dimensionless parameters:

**(i) Power-law fluids:**

*Reynolds number:* This denotes the ratio of the inertial forces and viscous forces as:

$$Re_{PL} = \frac{Inertial\ forces}{Viscous\ forces} = \frac{\rho V_c^{2-n} l_c^{\,n}}{m} \tag{2.12}$$

*Prandtl number:* It is the ratio of the momentum diffusivity to thermal diffusivity.

$$Pr_{PL} = \frac{Momentum\,diffusivity}{Thermal\,diffusivity} = \frac{C_p m\left(V_c / l_c\right)^{(n-1)}}{k} \tag{2.13}$$

*Grashof number:* In natural convection, Grashof number defined as the ratio of buoyancy forces to the viscous forces.

$$Gr_{PL} = \frac{Buoyancy\ forces}{Viscous\ forces} = \frac{\rho_\infty^2 \left(g\beta\Delta T\right)^2 l_c^{n+2}}{m^2} \tag{2.14}$$

where, $Ra_{PL}$ Rayleigh number, i.e., $Ra_{PL} = Gr_{PL} \times Pr_{PL}$ is defined as the product of the Grashof number and Prandtl number.

**(ii) Bingham plastic fluids:**

*Reynolds number:* This denotes the ratio of the inertial forces and viscous forces as:

$$Re_B = \frac{Inertial\ forces}{Viscous\ forces} = \frac{\rho_\infty V_c^2 l_c^2}{\mu_B V_c l_c} = \frac{\rho_\infty V_c l_c}{\mu_B} \tag{2.15}$$

*Bingham number:* This represents the ratio of yield stress to viscous (shear) stress.

$$Bn = \frac{Yield\ stress}{Viscous\ stress} = \frac{\tau_o}{\mu_B \left(V_c / l_c\right)} = \frac{\tau_o l_c}{\mu_B V_c} \tag{2.16}$$

In the limit of $Bn = 0$, it represents the Newtonian fluid behavior. In the other limit, $Bn \to \infty$ corresponds to the fully plastic flow condition.

*Prandtl number:* It is the ratio of the momentum diffusivity ($\nu$) to thermal diffusivity ($\alpha$).

$$Pr_B = \frac{Momentum\,diffusivity}{Thermal\,diffusivity} = \frac{\nu}{\alpha} = \frac{C\mu_B}{k} \tag{2.17}$$

*Grashof number:* In natural convection, Grashof number defined as the ratio of buoyancy forces to the viscous forces.

$$Gr_B = \frac{Buoyancy\ forces}{Viscous\ forces} = \frac{\rho_\infty^2 g \beta \Delta T\, l_c^3}{\mu_B^2} \tag{2.18}$$

where, $Ra_B$ Rayleigh number, i.e., $Ra_B = Gr_B \times Pr_B = \frac{\rho_\infty^2 g \beta \Delta T\, l_c^3 C}{\mu_B k}$ is defined as the product of the Grashof number and Prandtl number.

**(iii) Sphericity:** This denotes the ratio of the surface area of the sphere with the same volume as the particle to the actual surface area of the particle.

$$\psi = \frac{\pi^{1/3}\left(6V_p\right)^{2/3}}{A_p} \tag{2.19}$$

where $V_p$ volume of the non-spherical particle and $A_p$ is the area of the non-spherical particle.

The characteristics length $l_c$, vary for the sphere and spherical segment. In case of sphere the diameter of the sphere is taken as the characteristic length, while in case of the spherical segment the diameter equivalent of sphere, $d_{eq} = \sqrt[3]{6V_p/\pi}$ is considered as their characteristic length in this work.

## 2.3 Numerical solution strategies

The finite-element based COMSOL Multiphysics® (version 5.3a and 5.6) is used to solve the non-dimensional governing **Eqs. (2.1) - (2.3)** along with the appropriate boundary conditions. The triangular

elements have been selected for meshing the computational domain to resolve the steep velocity, pressure and temperature gradients in the thin momentum and thermal boundary layers near the particle. A smooth transition from fine to coarse mesh regions has been achieved by using an appropriate stretching function in the far away domain having quadrilateral mesh elements. In most cases, the steady, two-dimensional, laminar module with the linear direct solver PARDISO (Parallel Sparse Linear Direct Solver) is used to solve the system of equations. The equations discretized by the Finite Element method (FEM) result in a sparse linear system. PARDISO can handle a wide variety of sparse matrix types - whether they are real or complex, symmetric, structurally symmetric, or nonsymmetric. It can solve these systems of equations of the form AX = B on a shared or distributed memory architecture. A simulation was deemed to have converged when the field variables satisfied the relative convergence criterion of $10^{-6}$ for the continuity, momentum and thermal energy equations everywhere in the flow domain. A user defined function is introduced for the regularization of the Bingham plastic model through the Papanastasiou approach (or bi-viscosity model or Bercovier and Engleman model) to estimate the absolute viscosity ($\eta$) to be used as an input.

The numerical solution of **Eqs. (2.1) - (2.3)** in conjunction with the suitable boundary conditions maps the flow domain in terms of the velocity ($V$), pressure ($p$) and temperature ($\xi$) fields, which are post-processed to determine the local as well as the global momentum and heat transfer characteristics as functions of the pertinent governing parameters (*Re*, *Pr*, *Bn*, *Gr*, α). In the ensuing section, we briefly introduce the definitions of these parameters.

***Drag coefficient:*** This is a measure of the net hydrodynamic force exerted by the fluid on the immersed spherical segment in the flow direction. The total drag coefficient ($C_D$) is made up of two components, called as, friction drag ($C_{DF}$) due to the shearing forces and pressure, or form drag ($C_{DP}$) due to the normal forces exerted on the cylinder. These are defined as follows:

Total drag coefficient: $C_D = C_{DF} + C_{DP}$ (2.20)

Friction drag coefficient: $C_{DF} = \dfrac{F_{DF}}{\frac{1}{2}\rho_\infty V_c^2 A_p}$ (2.21)

Pressure drag coefficient: $C_{DP} = \dfrac{F_{DP}}{\frac{1}{2}\rho_\infty V_c^2 A_p}$ (2.22)

where, $A_p$ is the projected area of the particle as seen from the oncoming fluid stream.

***Pressure coefficient:*** The ratio of difference between the local pressure and the free stream pressure to the normalized dynamic pressure is defined as local pressure coefficient, $C_p$ which can be given mathematically as follows:

$$C_p = \frac{p - p_\infty}{\frac{1}{2}\rho_\infty V_c^2} \tag{2.23}$$

Where $p$ is the local pressure at a specific point on the particle and $p_\infty$ is the free stream pressure.

***Nusselt number:*** The Nusselt number is the dimensionless heat transfer coefficient characterizing the rate of convective heat transfer between the particle and the surrounding fluid. The local Nusselt number, *Nu*, at a point on the surface of particle is evaluated using the temperature field as follows for the isothermal boundary condition:

$$Nu = \frac{hl_c}{k} = -\frac{\partial \xi}{\partial \boldsymbol{n}_s}\bigg|_{surface} \tag{2.24}$$

where $h$ is the convective heat transfer coefficient and $n_s$ is a unit normal vector on the surface of the particle.

The average Nusselt number is obtained by integrating the local Nusselt number over the surface of the particle as follows:

$$Nu = \frac{\bar{h}d_c}{k} = \frac{1}{S}\int_S Nu \; dS \tag{2.25}$$

Where $\bar{h}$ is the average heat transfer coefficient over the surface of the particle and $d_c$ diameter in case of sphere and largest chord length in case of spherical segment. Hence, for spherical segments having $\alpha \leq 90°$ it will be the base diameter while for $\alpha \geq 90°$ it will be the diameter of the frontal area. In the cases of cone and short cylinders, dc will be the base diameter.

In *Chapters* 3 to 6, the momentum and thermal characteristics of spherical and non-spherical particles in Newtonian and non-Newtonian fluids are explored in both forced and free convection regimes.

# Chapter 3

# Sedimentation of non-spherical particles

This chapter focuses on the sedimentation of non-spherical particles in the yield stress fluids. The effect of the shapes of the spherical segments in two-parameters yield stress fluid, i.e., Bingham plastic fluid has been examined on drag coefficient while settling in Bingham plastic fluids. The results of drag experienced by spherical segments compared with that of the sphere in the same media in the form of correction factor while another correction factor was defined to examine the deviation in drag of spherical segments in Bingham plastic fluids from that in the Newtonian fluid. The yield stress at stability limit and stokes drag have been investigated over the range of Bigham number for each shape.

## 3.1 Previous work

The very first attempt to introduce sphericity as an expression to represent the shape of the non-spherical particle was made by Wadell (1934) for sedimenting rock particles in Newtonian fluids. Subsequent efforts have been reported in literature to further explore the shape in terms of circularity, flatness, projected area normal to the flow field to characterize non-spherical particle shapes (Clift *et al*., 1978; Michaelides, 2006). Pettyjohn and Christiansen (1948) have correlated the effect of shape on the drag experienced by the particle experimentally. They evaluated the drag values for various isometric shapes having sphericity in range of 0.67 - 1 and proposed a direct correlation for drag and sphericity of particles at high Reynolds numbers. Xie and Zhang (2001) have compared their experimental results of non-spherical agriculture particles ($\psi$ = 0.2 - 1) with Pettyjohn and Christiansen (1948) and affirmed that the particle sphericity could be related to the stokes shape factor ($K_V$) in laminar regime as follow:

$$K_V = \psi^{0.83} \tag{3.1}$$

In 1991, Thompson and Clark (1991) introduced a single shape parameter, scruple or Newton's shape factor ($K_N$), to make the results more accessible, similar to the moody diagram for pipe friction factor and merged the drag coefficient and Reynolds number data on a single graph for non-spherical particles for different values of Newton's shape factor. Due to the advancement of instrumental and computational techniques, vast and reliable data for sedimenting particles for different type of fluids becomes available in the literature over the range of shapes and flow regimes. The interest in merging these data into a universal correlation persists many researchers to continue investigation in this subject. Haider and Levenspiel (1989) have attempted to provide a generalized correlation using a single characteristic (sphericity) of particle shape resulted with a good, however cumbersome correlation based on experimental data, which also have some inherent errors.

$$C_D = 24/Re\ (1+ARe^B)+C/(1+D/Re) \tag{3.2}$$

Later on Ganser (1993) has improvised the correlation with one more shape factor in addition to sphericity, i.e., the projected area in the direction of motion for non-spherical shapes spanning over the sphericity range of $\psi$ = 0.1 - 1. Furthermore, Chhabra *et al.* (1999) have performed a detailed study to analyze the available correlations to predict the drag coefficient of non-spherical particles and found that the Ganser's approach was a good fit with the known sphericity of particles. Similarly, Yow *et al.* (2005) also proposed a three-parameter correlation for regular non-spherical particles based on the Kaskas (1964) equation with 97% accuracy with the experimental data.

Apart from Newtonian fluids, a range of non-Newtonian fluids encountered in various industrial and day-to day settlings contain presence of particles in the form of dilute suspension or dispersion, such as polymer suspensions, colloidal solutions, cosmetics, process foods, pharmaceutical, petroleum products, biological products, etc. Sedimentation or settling of particles over the wide range of non-Newtonian fluids, especially in the presence of yield stress fluids significantly modifies the settling behavior of the particle. A simplest type of yield stress fluids is the Bingham plastic fluids that are characterized by two parameters, i.e., yield stress ($\tau_o$) and plastic viscosity ($\mu_B$). The Bingham plastic fluids are able to resists deformation up to the critical value of yield stress ($\tau_o$) above which their flow resembles to the Newtonian fluids with constant plastic viscosity ($\mu_B$). Interestingly, to start settling in the yield stress fluid, the net gravitational force exerted on the particle has to be overcome by the force acting on the particle in the upward direction due to yield stress. This is known as a stability criterion for the sedimenting particle in yield stress fluids. While studying the particles in yield stress fluids, researchers were consciously interested in finding the stability criterion, flow visualization and drag experienced by the particles.

Volarovich and Gutkin (1953) first comprehended this dual behavior around a sphere, and Rae (1962) detected that a small solid rigid zone adheres to the sphere's surface. A critical study of the free boundary problem to precisely comprehend the shape of the yield surface around the sphere is given by Beris *et al.* (1985). Furthermore, numerous studies including both experimental (Valentik and Whitmore, 1965; Ansley and Smith, 1967; Atapattu *et al.*, 1995) and numerical (Beaulne and Mitsoulis, 1997; Blackery and Mitsoulis, 1997) work has confirmed the presence of the fluid envelope surrounding the bluff body. As the yield stress of fluid increases, the particle may or may not be able to settle under its own weight in quiescent Bingham fluid, known as yield gravity parameter $Y_g$. The value of $Y_g$ ranges from 0.080-0.2 above which the sphere will not fall or get suspended in liquid is calculated employing experimental (Broadman and Whitmore, 1961; Brookes and Whitmore, 1968) and numerical approaches (Beris *et al.*, 1985; Beaulne and Mitsoulis, 1997; Blackery and Mitsoulis, 1997).

Hence, considering the pertinent literature, it is impressive to notice that the spherical segments, which are often happening in industrial applications, have received scant engagement. In this work, the settling of the different spherical segments ($30° \leq \alpha \leq 180°$) is studied in the creeping flow of yield stress fluid.

The effect of the broad range of rheological parameters ($0.001 < Bn \leq 10^6$) is also studied in terms of yielded/unyielded surfaces and drag correction factors.

## 3.2 Physical model and problem formulation

The problem describes the settling of a spherical segment base diameter, $d_c$ and height $h_c$ sectioned from a sphere of diameter $D_s$ in a creeping flow regime of yield stress fluids as shown in **Fig. 3.1**. Different spherical segments (α = 30°, 60°, 90°, 120°, and 150°) are considered in this work which are dissected from a sphere by a chord that is formed by subtending an angle α from the vertical axis. The flow occurs due to the settling of the particle with the flat surface facing downward and is assumed to be axisymmetric with respect to the direction of gravity. The equivalent problem is framed here by considering the spherical segment appears to be at rest while the surrounding fluid is flowing at a uniform velocity $U$. The unbounded flow condition for the problem has been approximated by enclosing the spherical segment in an artificial vertical tubular domain of length $L$ and diameter $2H$ (**Fig. 3.2**). In the absence of inertia, the steady flow of incompressible flow of Bingham plastic fluid is governed by equations of conservation of mass and momentum stated in non-dimensional forms **Eq. (2.1)** and **(2.2)**.

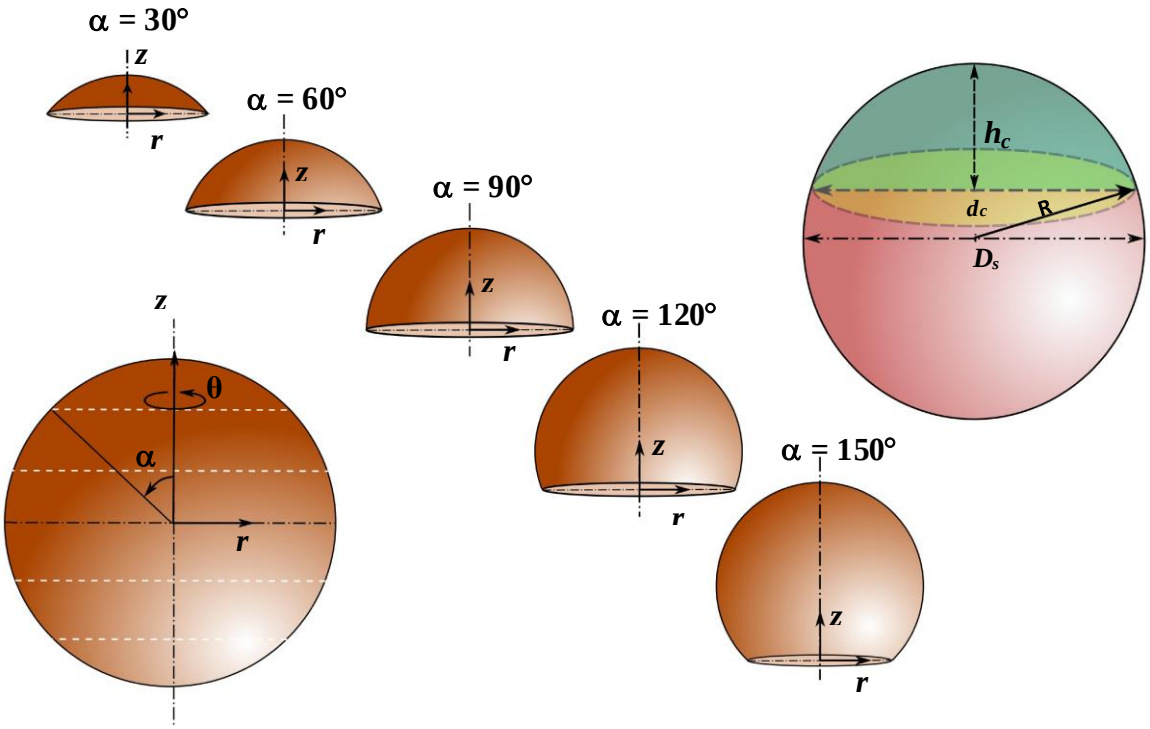


**Figure. 3.1** Schematics of spherical cap or segment.

The problem statement considering axisymmetric flow, has been completed by identifying the physical realistic boundary conditions with that includes:

At the inlet and outlet, $V_z = 1, V_r = 0$ (uniform velocity at upstream and downstream far away from the particle)

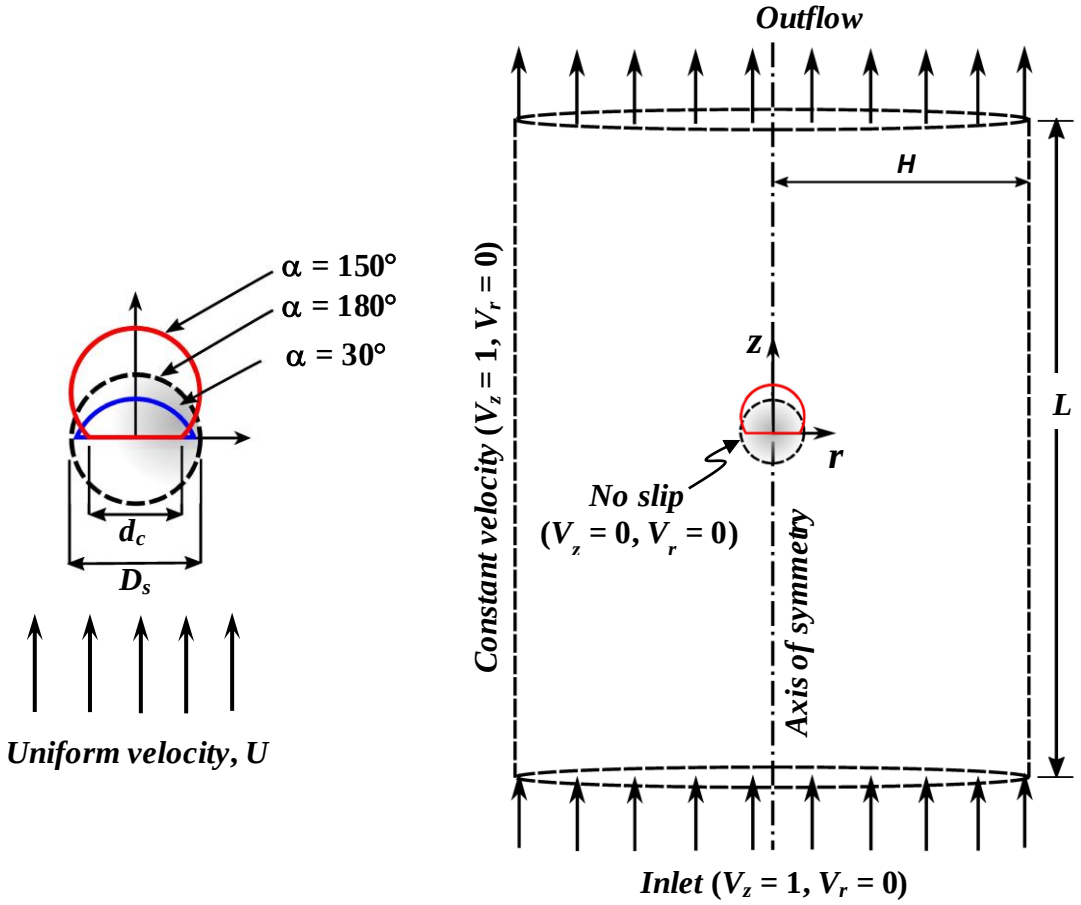


**Figure 3.2** Schematics of flow and computational domain.

On the surface of the particle, $V_r = V_z = 0$ (no-slip condition)

On the far away wall of cylindrical envelope, $V_z = 1, V_r = 0$

At the center line, $r = 0$, $\frac{\partial V_z}{\partial r} = 0, V_r = 0$

In the preceding equations **Equations (2.1)-(2.2)**, the scaling of variables has been rendered by using the characteristic length, i.e., volume equivalent sphere diameter $\left(d_{eq} = \sqrt[3]{6V_p/\pi}\right)$ as a length scale, $U$ for velocities and viscous stress, $\mu_B U/d_{eq}$, for pressure and shear stress.

The yield stress fluid flow around the spherical segment has been governed by dimensionless parameters, Bingham number ($Bn$), ratio of the strength of the yield stress to the viscous stress or the dimensionless yield stress ($\tau_y$), ratio of the yield force to the drag force defined as:

$$Bn = \frac{\tau_o d_{eq}}{\mu_B U} \tag{3.3}$$

$$Y_g = \frac{\tau_o A_p}{F_B} \tag{3.4}$$

where $A_p$ is the frontal area of the spherical segment, and $F_B$ is the drag force acting on the particle. Furthermore, the dimensionless form of the drag force, $C_s$ scaled by viscous stresses is defined as:

$$C_s = \frac{4F_B}{\pi\mu_B U d_{eq}} \tag{3.5}$$

which can be further related to Bingham number ($Bn$) and dimensionless yield stress ($\tau_y$) by

$$\tau_y = \frac{Bn}{C_s} \tag{3.6}$$

In the limit of $Bn \to 0$, $\tau_y \to 0$, the fluid represents Newtonian behavior. At the other extreme limit of $Bn \to \infty$, $\tau_y$ attains a constant value, beyond which the particle cannot sediment in the infinite medium under its own weight. For a sphere (Beris *et al*., 1985; Blackery and Mitsoulis, 1997) settling in infinite media, the value of $\tau_y$ = 0.143.

The drag experienced by non-spherical particles in Bingham plastic fluids will be further examined in terms of normalized drags with respect to fluid media, i.e., Newtonian fluid ($Bn$ = 0) and shape of the particle, i.e., spherical particle ($d_c$ = $D_s$) in the otherwise identical conditions. The normalized drag coefficient ($X_{BP,f}$) is defined as the ratio of the drag coefficient of the spherical segment in Bingham plastic fluid to the drag experienced by the identical spherical segment in Newtonian fluid.

$$X_{BP,f} = \frac{C_{DB}}{C_{DN}} = \frac{F_B}{F_N} \tag{3.7}$$

where $F_N$ and $C_{DN}$ are the drag force and drag coefficient of the spherical segment in the Newtonian fluids, respectively.

Similarly, the normalized drag coefficient with respect to spherical particle, $X_{BP,s}$ can be expressed as:

$$X_{BP,s} = \frac{C_{DB}}{C_{DS}} = \frac{F_B}{F_S} \tag{3.8}$$

where $F_S$ and $C_{DS}$ are the drag force and drag coefficient of the spherical particle in the Bingham plastic fluid, respectively.

In this problem, all the non-dimensional **Eqs. (2.1) - (2.2)** governing conditions are solved using the finite element scheme based COMSOL Multiphysics (Version 5.3a) platform. The linear direct solver, PARSIDO disintegrates the PDEs into linear algebraic equations, which is further solved by the software using LU matrix factorization. The numerical method never provides the exact solution to the problem. However, it approximates the solution of the boundary value problem using the error minimization technique up to some fixed criterion, hence this optimization of the criterion and the numerical parameters is a fundamental requisite to obtain a prudent solution for the problem.

## 3.3. Choice of numerical parameters

The most distinctive property of creeping flow is its inherent upstream and downstream symmetry while flowing past a regular-shaped geometries such as sphere. Nevertheless, in this case, we have irregular or

non-spherical shapes which are lacking the anticipated symmetry with respect to the flow direction. Owing to non-symmetry of the shape in the direction of flow, the problem has been solved in the domain considering axisymmetry in particle shape. The solution of the numerical technique firmly adheres to the choice of numerical parameters. The present study has explored various shapes of particles. Computational time and CPU memory usage during computation are influenced by factors such as the size of the domain, the number of grids and type of grid elements. In consideration of these aspects and

**Table 3.1** Domain Independence test at $Bn = 0.001$ and $Bn = 10^6$.

| Domain | $\alpha = 30°$ | | | $\alpha = 90°$ | | | $\alpha = 180°$ | | |
|---|---|---|---|---|---|---|---|---|---|
| | $L/D_s$ | $H/D_s$ | $C_D$ | $L/D_s$ | $H/D_s$ | $C_D$ | $L/D_s$ | $H/D_s$ | $C_D$ |
| | | | | | $Bn = 0.001$ | | | | |
| D1 | 20 | 10 | 8.43 | 100 | 50 | 18.15 | 100 | 50 | 9.91 |
| D2 | 50 | 25 | 8.17 | 200 | 100 | 17.85 | 200 | 100 | 9.74 |
| D3 | 100 | 50 | 8.17 | 400 | 200 | 17.72 | 400 | 200 | 9.65 |
| | | | | | $Bn = 10^6$ | | | | |
| D1 | 20 | 10 | $2.05 \times 10^7$ | 100 | 50 | $2.65 \times 10^7$ | 100 | 50 | $1.12 \times 10^7$ |
| D2 | 50 | 25 | $2.05 \times 10^7$ | 200 | 100 | $2.65 \times 10^7$ | 200 | 100 | $1.12 \times 10^7$ |
| D3 | 100 | 50 | $2.05 \times 10^7$ | 400 | 200 | $2.65 \times 10^7$ | 400 | 200 | $1.12 \times 10^7$ |

with the aim of obtained optimized results, two distinct computational domains have been employed. One is designated for spherical caps with $\alpha < 90°$, and the other for those with $\alpha \geq 90°$, strategically chosen to enhance computational efficiency. **Table 3.1** represents the domain independence test for three geometrical shapes with $\alpha = 30°$, 90° and 180°. The effect of the size of the domain on the drag coefficient

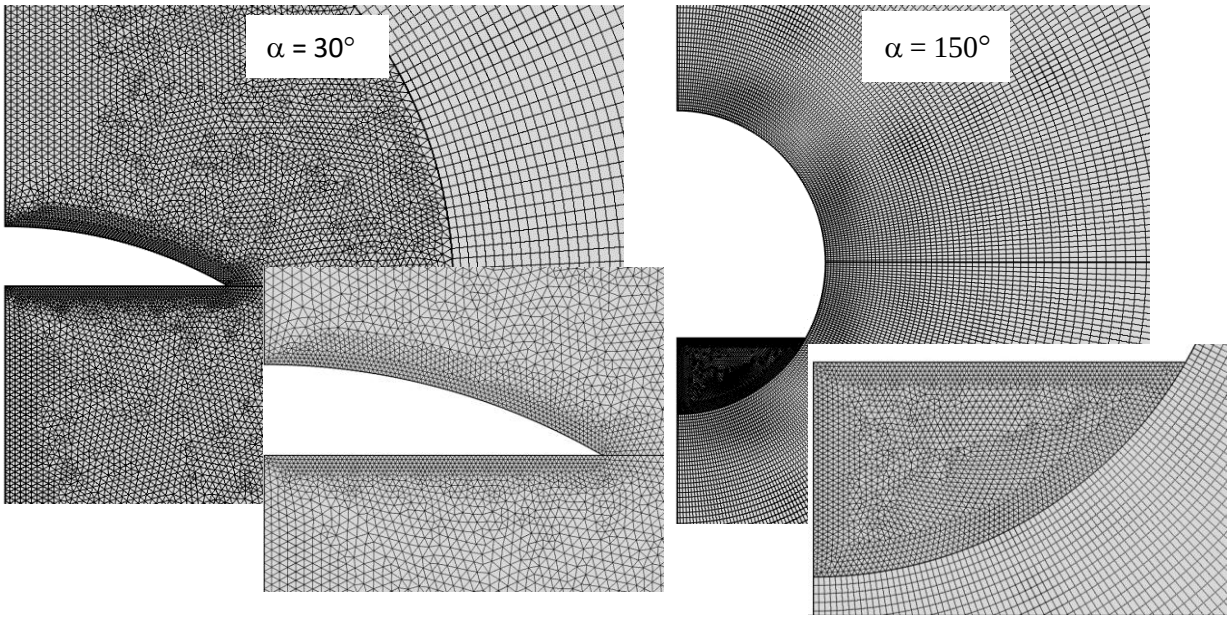


**Figure. 3.3** Grid structure in the vicinity of the geometry.

has been examined at the extreme values of Bingham number $Bn$ = 0.001 and $10^6$ for the present work. As Bingham number increases the momentum boundary layer thickness decreases. Hence, from **Table 3.1** it can be concluded that the domain size D2 is adequate over the range of Bingham number and the shape geometries considered in this work. Beyond D2 the further increase in the size of domain has not shown any significant difference (< 1%) for the drag coefficient values.

Similarly, **Fig. 3.3** illustrates two different grid types of triangular and quadrilateral grids used to discretize the domain. The geometries considered in this problem featured sharp corners which often lead to singularities at corners in numerical simulations. Furthermore, steep velocity gradients exist in the proximity of the geometry surface due to the no-slip boundary condition. Both of these facts mandate an exceptional grid distribution in the vicinity of the geometry. Consequently, a free triangular grid is employed to precisely capture the thinnest momentum boundary layer adjacent to the geometry. While in the far away region, a relatively coarse and mapped/quadrilateral mesh is utilized. The effect of the grid is examined on the extreme values of the Bingham number, $Bn$ = 0.001 and $10^6$ by analyzing the total and pressure drag coefficients. As shown in **Table 3.2**, the G3 grid produces comparable results with less than a 1% deviation from grid G2, confirming that G2 is an adequate choice for this work.

In addition to solid boundaries, fluid characteristics also play a crucial role in influencing hydrodynamic drag force that need special attention while solving the equations. This work focuses on the sedimentation of particles in Bingham plastic fluid which exhibit dual behavior of fluid-like (sheared) and solid-like (unsheared) around a specific point of shear stress in the flow domain, known as the critical yield stress.

**Table 3.2** Grid Independence test at $Bn$ = 0 and $Bn$ = $10^6$.

| α | Grids | $N_T$ | $N_P$ | $Bn$ = 0 | | $Bn$ = $10^6$ | |
|---|---|---|---|---|---|---|---|
| | | | | $C_D$ | $C_{DP}$ | $C_D$ | $C_{DP}$ |
| | G1 | 39723 | 100 | 7.871 | 7.046 | $2.05\times10^7$ | $1.90\times10^7$ |
| **30** | G2 | 44849 | 160 | 7.753 | 6.998 | $2.05\times10^7$ | $1.91\times10^7$ |
| | G3 | 51033 | 200 | 7.875 | 7.118 | $2.04\times10^7$ | $1.92\times10^7$ |
| | G1 | 54736 | 100 | 17.346 | 9.638 | $2.65\times10^7$ | $2.27\times10^7$ |
| **90** | G2 | 69114 | 160 | 17.396 | 9.753 | $2.65\times10^7$ | $2.28\times10^7$ |
| | G3 | 76406 | 200 | 17.430 | 9.827 | $2.65\times10^7$ | $2.29\times10^7$ |
| | G1 | 33700 | 100 | 19.147 | 6.359 | $2.23\times10^7$ | $1.70\times10^7$ |
| **180** | G2 | 56200 | 200 | 19.152 | 6.370 | $2.23\times10^7$ | $1.71\times10^7$ |
| | G3 | 69700 | 260 | 19.160 | 6.386 | $2.23\times10^7$ | $1.71\times10^7$ |

Numerically, this discontinuity of Bingham fluid is effectively addressed by employing regularization models available in the literature, i.e., Papanastasiou (1987), Bercovier (1980), and Biviscous (2000) models that play an indispensable role in studying the momentum behaviour of the particle in yield-stress

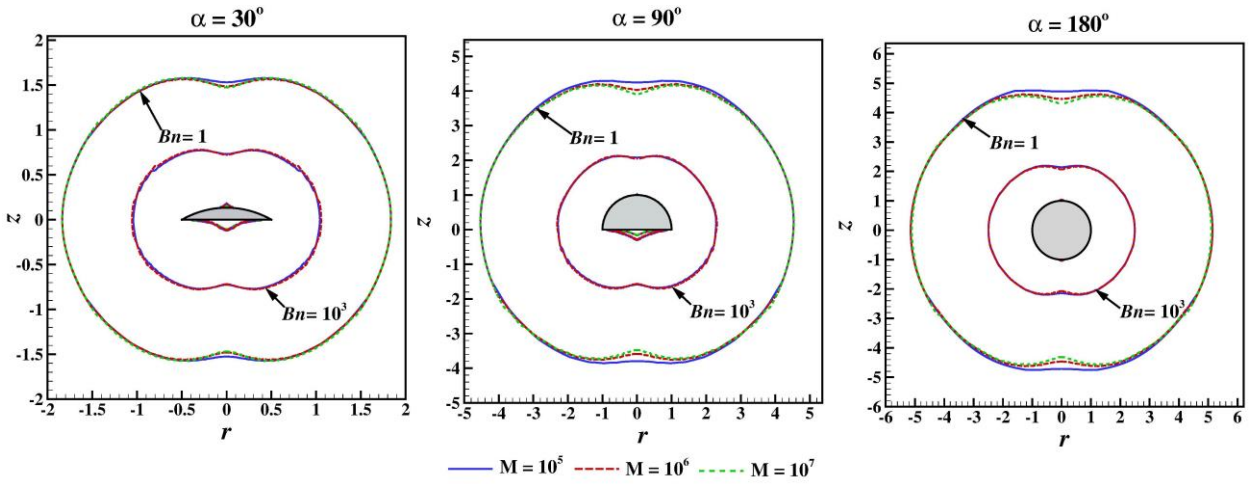


**Figure 3.4** Regularization parameter test for Papanastasiou model.

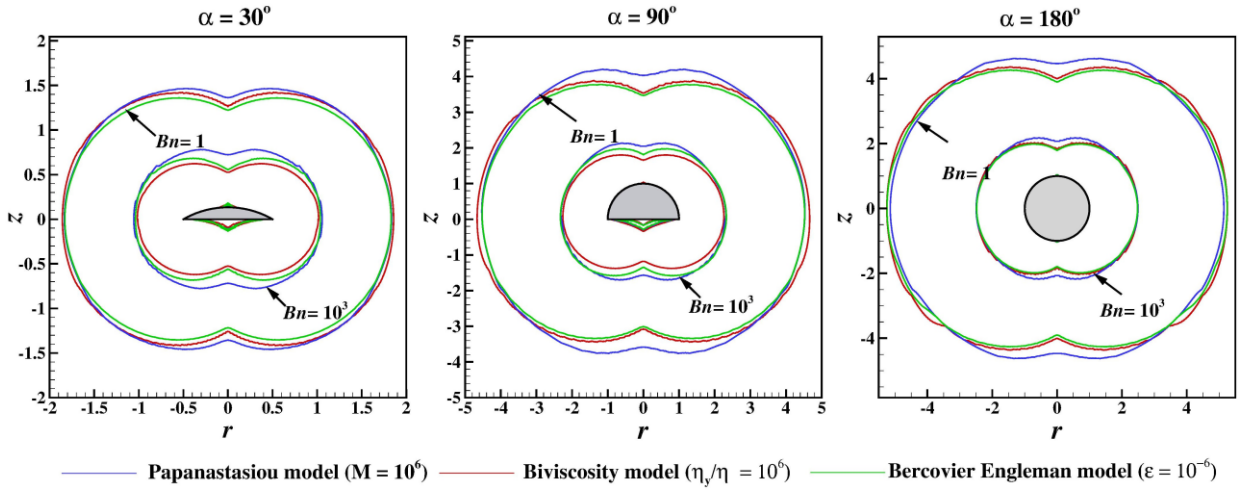


**Figure 3.5** Comparison of regularization models.

fluids. The regularization parameter test for the Papanastasiou model, illustrated in **Fig. 3.4**, confirms the selection of $M = 10^6$ for this study. This choice is based on assessing the effect of $M$ on yielded (fluid-like) and unyielded (solid-like) regions. Furthermore, the effectiveness of the selected model and model parameter is compared with the other models in **Fig. 3.5** to substantiate the selection of the chosen model. In **Fig. 3.5,** the prediction of yielded surfaces by Bi-viscosity and Bercovier Engleman models along with the Papanastasiou model are included and the close correspondence between the three results instills confidence in the chosen model in this study. The von Mises Yield criterion is implemented with a minimum tolerance value of $10^{-6}$ for estimating of yield surfaces which distinguish yielded and unyielded regions defined by isovalues, $|\tau| = \tau_o$ . The convergence criteria for mass and momentum equations are fixed at $10^{-6}$ throughout the domain.

## 3.4. Results and Discussion

The sedimentation of non-spherical particles is numerically studied over the wide range of Bingham numbers (0.001 to $10^6$) in a very low Reynolds number flow, i.e., creeping flow regime. This section

broadly deciphered the impact of particle shape on the overall drag coefficient, yield values and yielded/unyielded zone. The study analyzes various shapes individually and in comparison, to spherical particles. A general correlation of the drag coefficient concerning the range of shapes is also proposed over the range of Bingham fluids in this work. However, before presenting the new results, it is customary to validate the numerical methodology adopted in this study. For that in the subsequent section, we have presented the benchmark validation comparing the present findings with the limiting cases results from the available literature.

### 3.4.1 Assessment of numerical procedure

Researchers conducted an extensive study on the sedimentation of a sphere in both Newtonian and Bingham plastic fluids, focusing on low Reynolds number flow regimes. In **Table 3.3**, numerical values of the present drag coefficient, $C_{s,N}$ of a sphere in Newtonian fluids ($Bn$ = 0) are compared with the numerical values of Blackery Mitsoulis (1997) and estimated by Bohlin

**Table 3.3** Comparison with the drag coefficient of results of sphere in Newtonian fluid

| $D_c/D$ | $C_{s,N}$ (Blackery and Mitsouli, 1997) | $C_{s,N}$ (Bohlin's Equation)* | $C_{s,N}$ (Present) |
|---|---|---|---|
| 2:1 | 5.9389 | 5.9229 | 5.8990 |
| 4:1 | 1.9779 | 1.9789 | 1.9668 |
| 8:1 | 1.3529 | 1.3495 | 1.3418 |
| 10:1 | 1.2619 | 1.2632 | 1.2559 |
| 50:1 | 1.0471 | 1.0439 | 1.0377 |

$$*C_{s,N}=\left[1-2.1044\left(\frac{R}{R_c}\right)+2.0887\left(\frac{R}{R_c}\right)^3-0.9481\left(\frac{R}{R_c}\right)^5-1.372\left(\frac{R}{R_c}\right)^6+3.87\left(\frac{R}{R_c}\right)^8-4.19\left(\frac{R}{R_c}\right)^{10}\right]^{-1}$$

approximation (1997) The difference between the present and literature values remains less than 0.5% over the range of confinement ratio $D_c/D$. Furthermore, the comparison of the yielded/unyielded fluid regions in creeping flow of Bingham plastic fluid past a sphere for $D_c/D$ ratio = 50:1 for present study with Blackery and Mitsoulis (1997) in **Fig. 3.6**. The yielded surfaces appear to be almost identical in size. However, yield surfaces in the present study are sharper and clearer as compared to the published results due to the employment of denser grids. Similarly, the Stoke's drag coefficient, $C_s$, spanning over the range of Bingham number ($10^{-3} \leq Bn \leq 10^3$) is also compared for different confinement ratios in **Fig. 3.7**. The close agreement between the two sets of results confirms the credibility of the chosen numerical technique.

The results of Stokes drag coefficient, $C_s$, from the benchmark study of unconfined flow of Bingham plastic fluid past a sphere by Beris *et al*. (1985) are compared in **Fig. 3.8** with the present results having difference less than 1% over the range of yield stress parameter $Y_g$. Additionally, **Fig. 3.9** depicts a close and accurate resemblance in the comparison of strain rate contours from present work and that by Beris

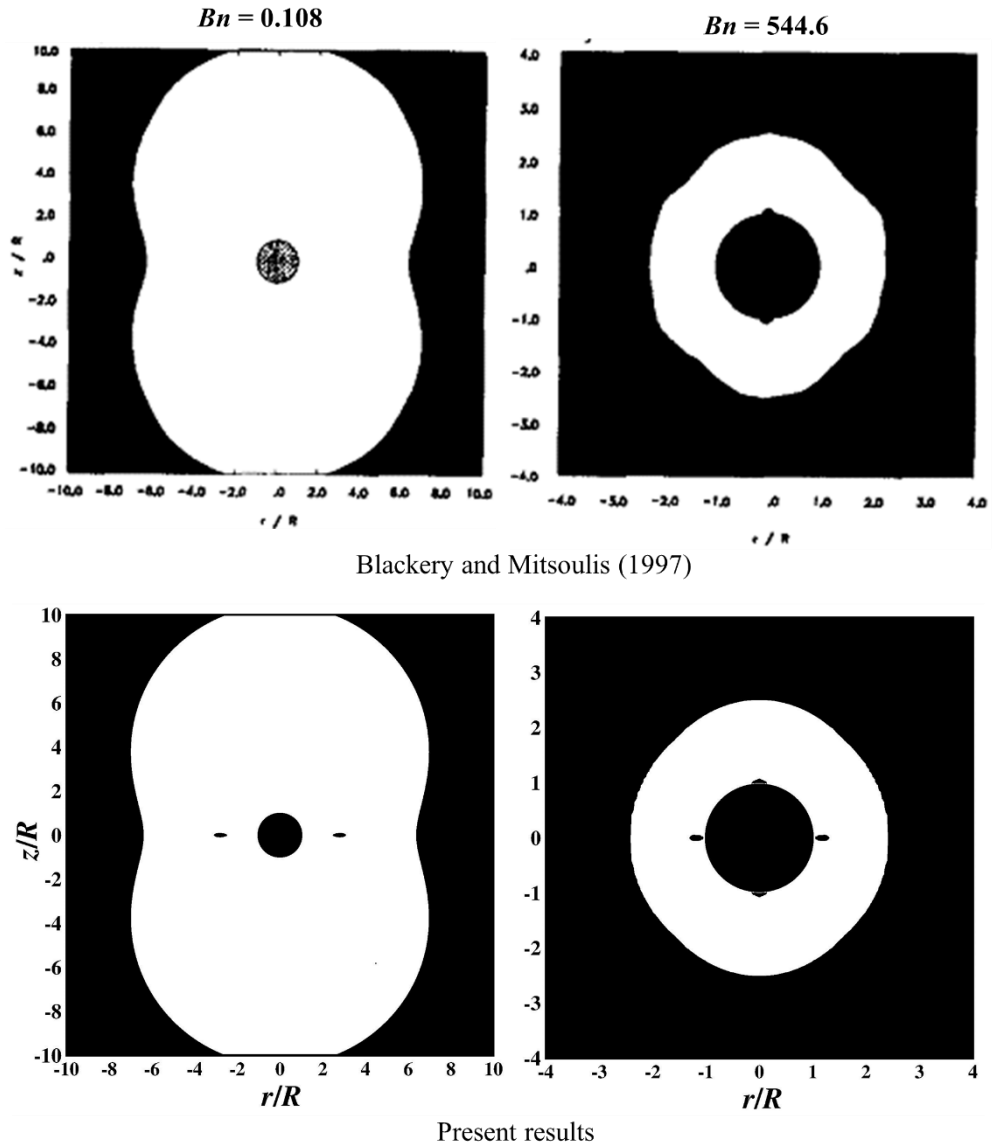


**Figure 3.6** Comparison of the extent and shape of the yielded/unyielded regions for $D_c/D$ = 50:1 for Bingham plastic fluid flowing past a sphere.

*et al.* (1985). The aforementioned comparison of the present predictions with the relevant results available in the literature substantiates the reliability and adequacy of the numerical methodology and parameters employed in the present study.

### 3.4.2 Morphology of yielded/unyielded region and velocity profiles

The settling of particles in yield stress fluids demonstrates a unique characteristic of the formation of yielded/unyielded regions under prevailing shear stress field. The shape of yield surfaces separating fluid like and solid like regions depends on the particle shape and Bingham number. The structure of yield surfaces in Bingham plastic fluids in the vicinity of the settling particle is presented in **Fig. 3.10** over the range of Bingham number, $0.01 < Bn \leq 10^6$, encompassing various shapes of spherical caps including sphere as well. These yield surfaces serve as delineations between yielded and unyielded fluid regions

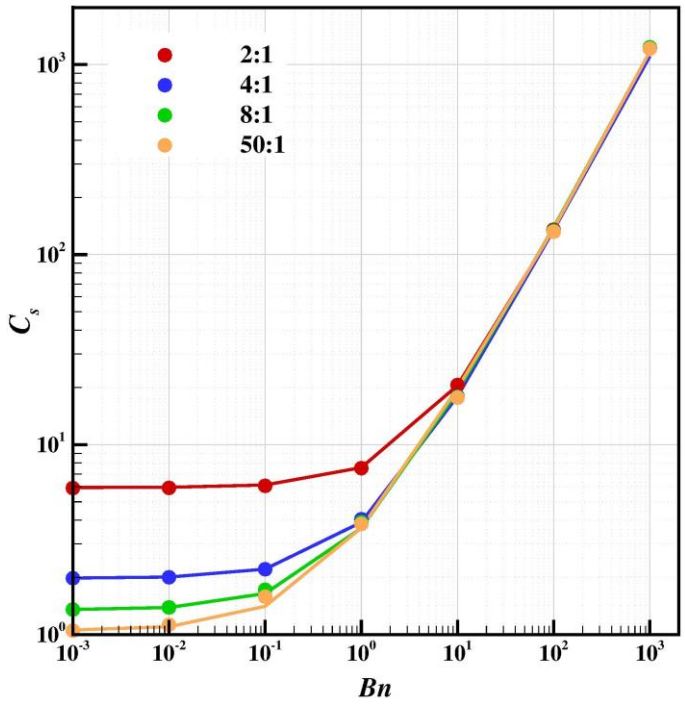


**Figure 3.7** Comparison of the drag coefficient for a creeping flow of a Bingham plastic fluid past a sphere in a tube for different diameter ratios (symbol: present results, line: Blackery and Mitsoulis (1997)).

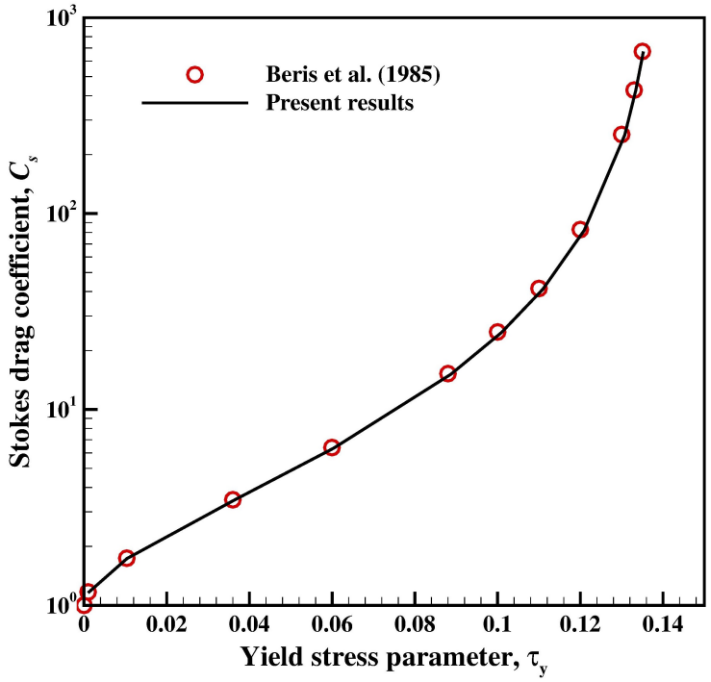


**Figure 3.8** Comparison of the Stokes drag coefficient for unconfined creeping flow of Bingham plastic fluid past sphere.

near the particle, where the fluid undergoes shearing owing to the no-slip conditions on the particle surfaces. As expected, the unyielded fluid remains attached forming triangular caps to the front and rear

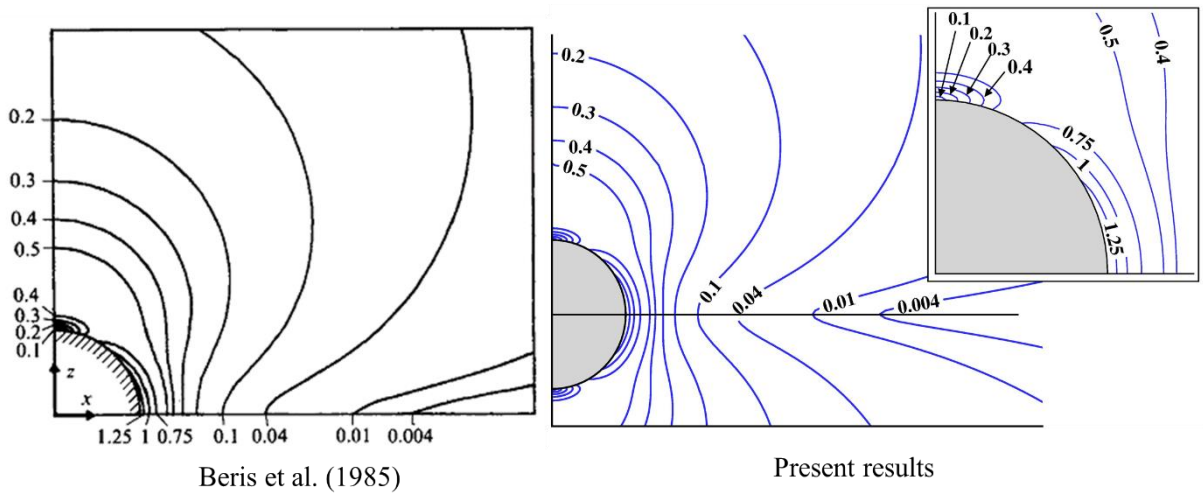


**Figure 3.9** Comparison of the strain rate contours for Stoke's law.

stagnation points at the particle surface. Furthermore, unyielded fluid envelope encompasses fluid zones far away from the particle. All zones are found to be symmetric around the *z*-axis, i.e., representing the flow direction. A cursory inspection of **Fig. 3.10** reveals that the location and shape of the yield surfaces are more and less similar for particles varying in shape. As expected, all the static unyielded zones grow while fluid like zone shrinks with increase in yield stress. **Figure 3.10** shows that $Bn > 10$ the change in the location of yield surfaces at the front stagnation point and far away from the particle surface remains insignificant irrespective of the shape of the particles. However, there is a notable observation pertaining to the formation of static triangular cap (polar cap) at the rear stagnation point of the particle as observed by Blackery and Mitsoulis (1997) for spherical particles in creeping flow regimes. Unlike the unyielded envelope away from the particle, the triangular polar cap attached to the particle surface exhibits a significant impact of the shape of the particle. Appeared for $\alpha < 90°$ and $\alpha > 120°$, the rear static unyielded triangular cap disappears for $\alpha = 90°$ and $120°$ as shown in **Fig. 3.10**. However, it is critical to comment on the exact shape of the yielded/unyielded regions, especially for tiny shapes. Since the continuous nature of the regularization model used in this work predicts the discontinuity in the fluid behavior in unyielded zones by an extremely small value deformation instead of zero shear rate value for chosen regularization parameters. Hence it is essential to examine the velocity in such disputed regions to assure their existence and modulation in shape as a function of particle shape and Bingham number. **Figures 3.11** and **3.12** plot the non-dimensional *z*-component of velocity in the radial- and axial- directions from the base and rear stagnation point, respectively. As shown in **Fig. 3.11** the velocity variation in the radial direction for $Bn = 0.1$ and $10^6$ over the range of particle shapes segmented as I-II and II-III indicating fluid-like and solid-like regions. As Bingham number increases, the rigid envelope (II-III) enclosing the fluid-like region (I-II) decreases in size irrespective of the shape of the particle. As a result, one case observes the acceleration of velocity in I-II region at $Bn = 10^6$. Also, the rigid envelop (II-III) is dynamic

in nature and moves with the free stream velocity, *U* like a solid plug. The disparity of reverse trend in **Fig. 3.11** from α = 120° to 180° is exclusive because of the chosen location to plot the dimensionless

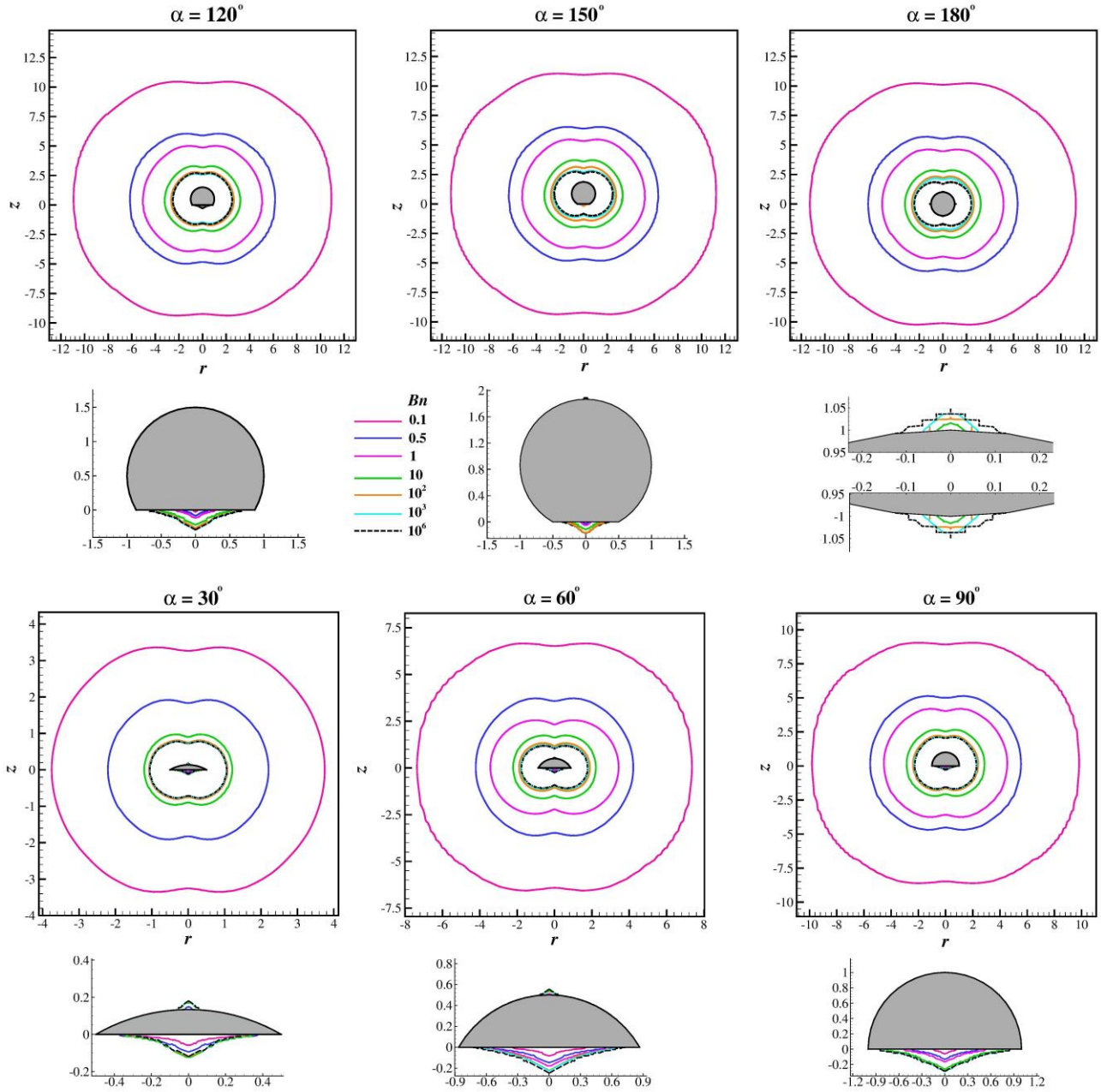


**Figure 3.10** Progressive variation of yield surfaces with Bingham number.

velocity as shearing of the fluid is affected by the longest chord length, i.e., the diameter of the geometry. On the other hand, in the *z*-direction, two triangular static unyielded zones adhere to the front and the rear ends of the particle. The front static zones formed at the base of the particle are larger in size as compared to the rear triangular polar cap. However, with the increase in α, the shape of the particle consists of a larger portion of the spherical lateral surface. Thus, at α = 180° due to perfect spherical shapes, these static zones become symmetrical in shape and size. Unlike the fluid zones, these static triangular rigid

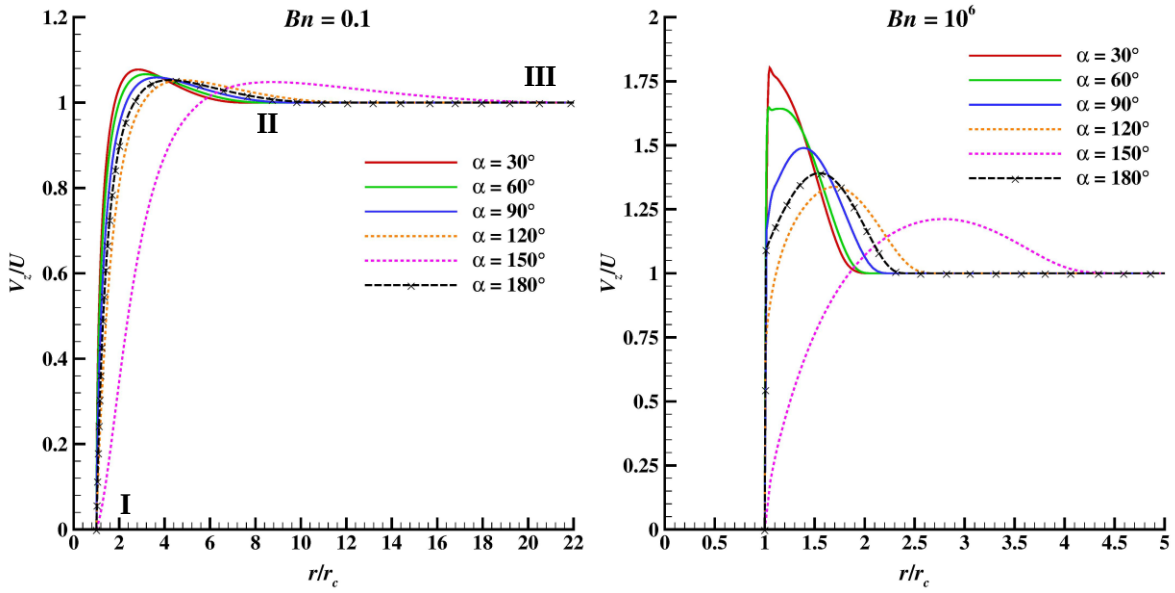


**Figure 3.11** Variation of dimensionless velocity component $V_z/U$ at $z = 0$ as a function of $r/r_c$.

zones grow in size with the increase in Bingham number. The front-end static zone exists over the range of Bingham numbers, however, the rear-end static zone remains absent at low yield stress and is only formed at high Bingham numbers over the range of the particle shape. The presence of these zones is ascertained by plotting the dimensionless velocity component $V_z$ at the rear end of the geometry at $Bn = 10^6$. As shown in **Fig. 3.12** segment I-II indicates the static unyielded triangular cap while the segment

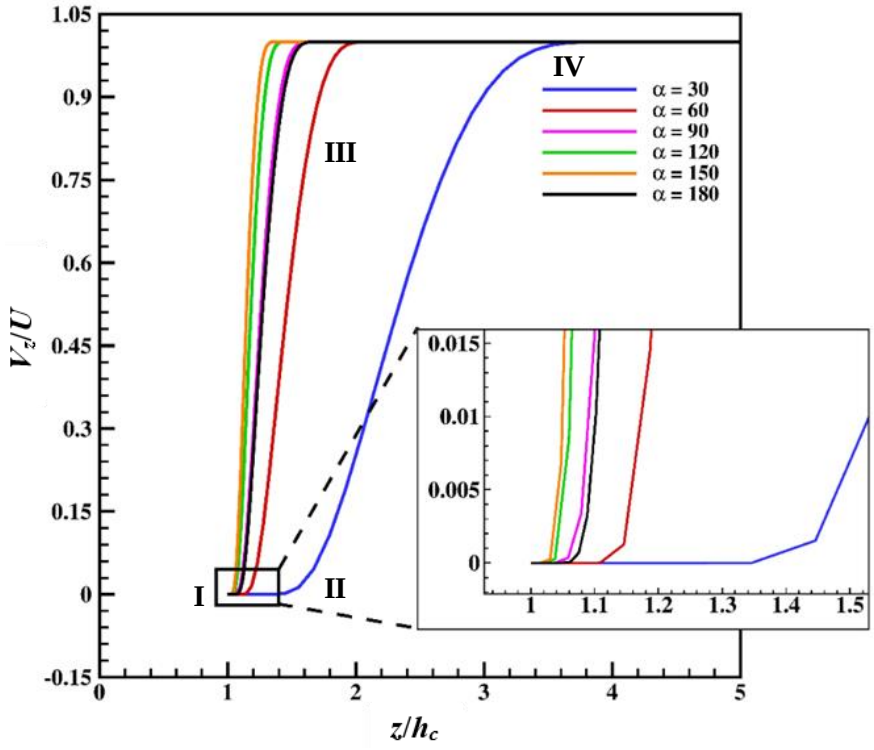


**Figure 3.12** Variation of dimensionless velocity component $V_z/U$ as a function of $z/h_c$ at $Bn = 10^6$.

(III-IV) with the constant velocity $V_z = 1$ corresponds to the outer unyielded envelope flows with a constant plug velocity. The segment II-III represents the fluid-like region at the symmetrical axis over the range of the particle shape. Here, also the profiles follow a similar trend for α discussed for the velocity profiles in the radial direction in the same section.

### 3.4.3 Yield Values and Drag Coefficient

In Bingham plastic fluid, the yield stress balances the gravity force acting on the sedimenting particle. Above a certain yield stress value spherical segments are not able to settle down under their own weight. Hence, their drag values cease to infinity or much larger values so that the particle remains suspended in a fluid which is often required in various applications (Brummer, 2006). **Fig. 3.13a** illustrates the dependence of Stokes drag coefficient on the nondimensional yield stress values over the range of the shape of the particle shapes. **Figure 3.13a** shows that the Stokes drag coefficient increases asymptotically as $Y_g \rightarrow \infty$. Also, the smallest spherical segment becomes motionless at a lower yield stress value of ~ 0.077 to get stabilized in the fluid. With the increase in α values, the yield stress value required for

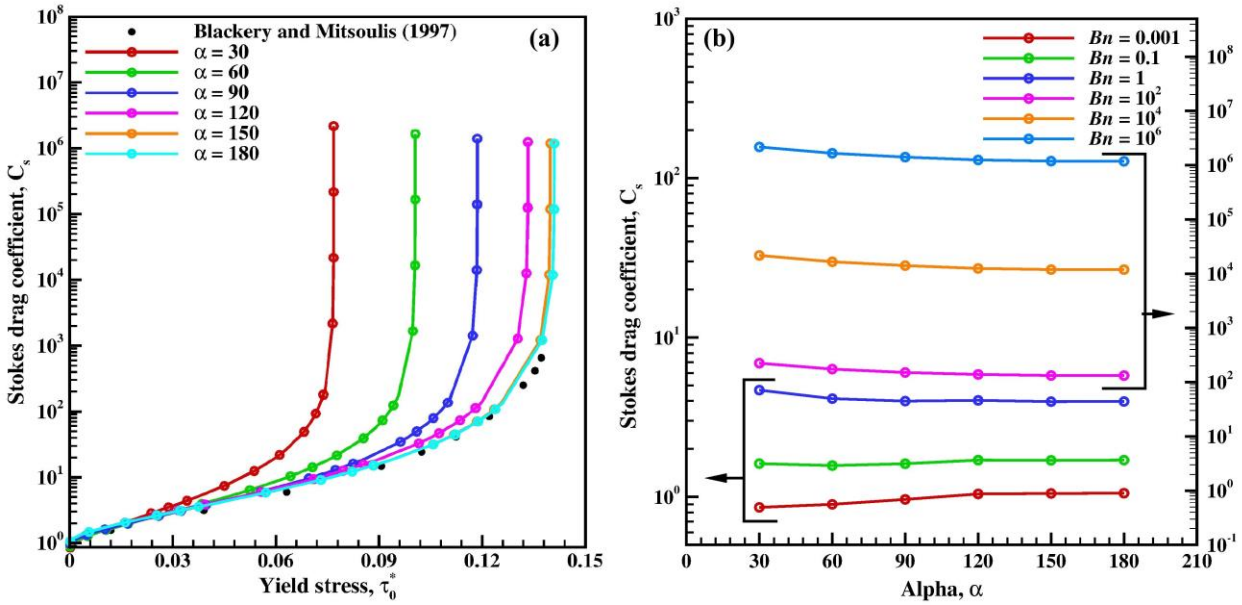


**Figure 3.13** Variation of Strokes drag coefficient $C_s$ with (a) yield stress (b) shape factor.

stabilization will also increase in the case of the sphere by ~ 0.141. The yield stress value of the sphere is also compared with the available literature values (Blackery and Mitsoulis, 1997) for settling sphere in Bingham plastic fluids which show a close correspondence between two sets of data.

On the other hand, the drag force, i.e., resistance force, experienced by freely falling particles also has much importance from a designing and process calculation point of view. The Stoke drag coefficient eventually increases with the increase in Bigham number or yield stress which can also be seen clearly in **Fig. 3.13b**. However, under a constant Bingham value, the drag experienced by segments exponentially

decreased with the increase in α value from 30° to 150° and almost become constant after 150°. The values of stroke drag coefficient for individual shapes can be correlated in a simplified form as a function of Bingham number as:

$$C_s = I + aBn^b \tag{3.9}$$

**Table 3.4** Coefficient value for **Eq. (3.9)**

| | **α = 30°** | **α = 60°** | **α = 90°** | **α = 120°** | **α = 150°** | **α = 180°** |
|---|---|---|---|---|---|---|
| | | | **$0.001 \leq Bn \leq 10$** | | | |
| $I$ | 0.952 | 0.977 | 1.037 | 1.113 | 1.117 | 1.122 |
| $a$ | 3.837 | 3.257 | 3.046 | 3.011 | 2.933 | 2.934 |
| $b$ | 0.822 | 0.798 | 0.778 | 0.763 | 0.758 | 0.757 |
| $\delta_{avg}$ | 4.00 | 3.47 | 3.09 | 2.84 | 2.76 | 2.75 |
| | | | **$10 < Bn \leq 10^6$** | | | |
| $I$ | 6.635 | 7.948 | 9.513 | 13.618 | 12.727 | 13.852 |
| $a$ | 2.170 | 1.658 | 1.406 | 1.252 | 1.193 | 1.184 |
| $b$ | 1 | 1 | 1 | 1 | 1 | 1 |
| $\delta_{avg}$ | 0.84 | 1.84 | 2.92 | 6.04 | 5.32 | 6.47 |

The coefficients $I$, $a$ and $b$ of **Eq. (3.9)** are tabulated in **Table 3.4**. The dependence of Stokes drag coefficient on Bingham number is observed to be ambiguous for each shape till $Bn \leq 10$. However, for high Bingham numbers, the coefficient $b$ becomes constant and does not vary with the α values. Thus, **Eq. (3.9)** is split into two ranges of Bingham number i.e., $0.001 \leq Bn \leq 10$, $10 < Bn \leq 10^6$ and corresponding coefficients are tabulated in **Table 3.4** along with the maximum and average errors. Furthermore, an attempt has been made to collate the Stokes drag coefficient over the range of particle shape (α) and Bingham number ($Bn$). Thus, for all considered spherical segments Stokes drag coefficient is correlated as a function of Bingham number ($Bn$) and shape factor (α) in a single correlation as follows:

$$C_S = a\cos(\alpha)(1+Bn)^b + \frac{c}{(1+Bn)^d} + e \tag{3.10}$$

From **Eq. (3.9)** it is obvious that the Stroke drag coefficient is very sensitive at low Bingham numbers than high values of $Bn$. Consequently, here also, the range of $Bn$ is divided into two ranges in a similar manner as **Eq. (3.9)** and the coefficients of **Eq. (3.10)** have been tabulated in **Table 3.5** along with the average and maximum deviations.

**Table 3.5** Coefficient value for **Eq. (3.10)**

| | ***a*** | ***b*** | ***c*** | ***d*** | ***e*** | **% $\delta_{avg}$** | **% $\delta_{max}$** |
|---|---|---|---|---|---|---|---|
| **$0.001 \leq Bn \leq 10$** | 0.083 | 1.620 | 4.535 | -0.694 | -3.5 | 12.53 | 29.16 |
| **$10 < Bn \leq 10^6$** | 0.479 | 0.999 | 1.559 | -1 | 9.774 | 8.86 | 39.25 |

### 3.4.4 Drag Correction Factor

For ideal cases of spherical particles in creeping flow regime, a vast literature is available over a range of fluids. Nevertheless, we often encountered non-spherical shapes and/or different fluids in real cases rather than perfect spherical particle in Newtonian or non-Newtonian fluids. Hence, to predict the drag force experienced by non-spherical particles in Newtonian or non-Newtonian fluids, engineers often use correction factors or normalized factors to incorporate the diversity of shape and/or fluid characteristics compared to the classical spherical shape and/or Newtonian fluid cases. In this work, two types of drag correction factors $X_{BP,f}$ and $X_{BP,s}$ have been discussed in this section to show the influence of the fluid characteristics for a given shape of the particle and of the shape for a given Bingham plastic fluid, respectively.

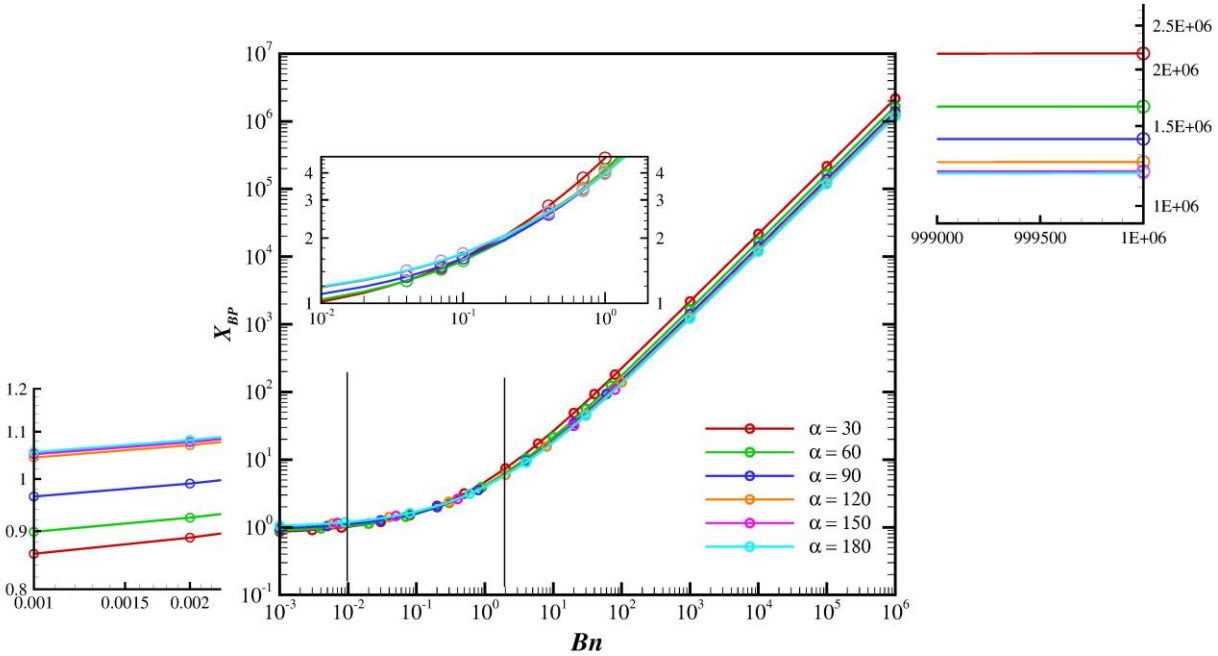


**Figure 3.14** Effect of Bingham number on correction factor $X_{BP,f}$ .

The ratio of the drag experienced by the spherical caps in Bingham fluid to that in a Newtonian fluid, $X_{BP,f}$ has been plotted in **Fig. 3.14.** It appears that over a low Bingham number range, $Bn$ <~ 0.2, $X_{BP,f}$ remains close to unity. However, the zoom in section in **Fig. 3.14** shows that for $\alpha \leq 90°$, the drag force experienced by a spherical segment is higher in Newtonian fluids compared to Bingham plastic fluids, for a given shape of the particle ($X_{BP,f}$ increases with the increase in $\alpha$). However, for $\alpha > 90°$, the drag force will be dominant in Bingham plastic fluids as compared to Newtonian fluids, while the effect of the particle shape becomes insignificant. With the increase in Bingham number for $Bn > 0.2$ the correction factor is clearly accentuated in the Bingham plastic fluids for all shapes. It is noticeable that the variation of drag correction factor with respect to shape factor $\alpha$ has been flipped over above $Bn = 0.2$ showing inverse dependency on $\alpha$.

Finally, **Fig. 3.15** illustrates the variation of the shape correction factor in Bingham plastic fluids, $X_{BP,s}$ over the range of the shapes and Bingham number. Broadly, with the increase in the Bingham number, the shape correction factor $X_{BP,s}$ grows rapidly with the increase in Bingham number for $\alpha$ = 60° and 90°. The peculiar trend in the variation of $X_{BP,s}$ is observed for $\alpha$ = 30° for $Bn$ <~ 0.2 and the possible reason can be drawn from the variation of drag coefficient over the range of shapes and Bingham number plotted in **Fig. 3.13b**. It shows that the drag experienced by $\alpha$ = 30°in the limit of Newtonian behaviour ($Bn$ = 0.001) remains lower than the sphere due to obvious reason of the difference in the

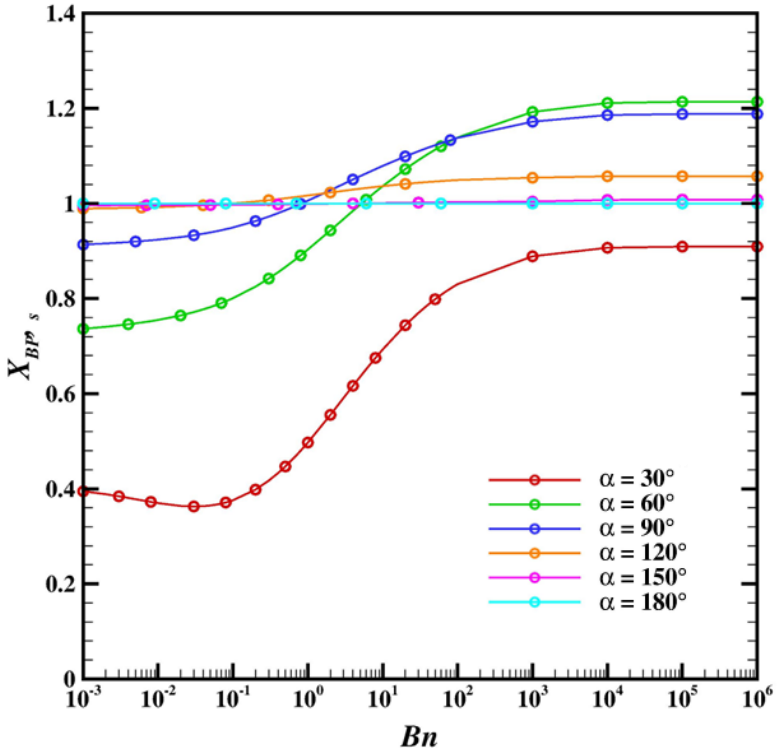


**Figure 3.15** Effect of Bingham number on correction factor $X_{BP,s}$.

frontal area of the two shapes, i.e., frontal area of spherical segment $\alpha$ = 30° is less than that of the parent sphere from which it was dissected. For $\alpha$ > 90°, $X_{BP,s}$ remains almost constant, ~ 1 , over the low values of Bingham number, $Bn$ <~ 0.2. The increase in $X_{BP,s}$ for all shapes followed plateau as Bingham number increases above $Bn$ ~ 100. It needs to be realized here that the increase in both the projected and lateral surface areas has accentuated the drag experienced by the non-spherical particles compared to the spherical shape. Eventually, at $Bn$ = $10^6$, the factor $X_{BP,s}$ is observed to be highest for $\alpha$ = 60°, possibly because of the shape of the particle. of the particle.

# Chapter 4
# Forced convection

This Chapter aims to explore the forced convection phenomenon from heated spherical segments immersed in a uniform stream of a Newtonian or Bingham plastic fluids in steady laminar flow regime. The effect of (i) the axisymmetric shapes of the particles in Newtonian and Bingham plastic fluids and (ii) channel confinement to the particle in Newtonian fluid have been examined. Results of drag, heat transfer coefficient, and flow kinematics are compared with the other similar shapes in order to identify the effect of the particle shape. The range of the shapes considered in this study is defined by a shape factor, $\psi$, and the particle longest chord length or base diameter to height ratio.

## 4.1 Flow past axisymmetric shapes in Newtonian fluids

### 4.1.1 Previous work

The study of the motion of particles in fluid has received much attention from researchers to understand the momentum and heat transfer phenomena. The research explores a wide spectrum of aspects including the effect of kinematic parameters, fluid rheology, flow confinement, shape and/or orientation of particles, flow regimes, etc. This section limits the review of literature that mainly focuses on the impact of particle shape on flow and heat transfer characteristics for fluid-particle interactions. Particularly for axisymmetric shapes of the particles, due to the wide occurrence and highest degree of symmetry, the spherical shape is the most studied shape by researchers. Considering the sphere as an abundantly studied shape, a plethora of research for this shape has been available in the literature based on experimental, analytical, and numerical techniques (Dennis and Walker, 1971; Clift *et al.*, 1978; Coulson and Richardson, 1990; Chhabra and Patel, 2023). As a result, reasonable forms of correlations are now available for spheres for the drag values prediction spanning the entire range from Stokes to Newton regimes. These can be found in the literature comprising the reviews and research studies by Clift *et al.* (1978), Chhabra and Patel (2023), Khan and Richardson (1987), Morrison (2013), Goossens (2019), Kalman and Matana (2022). On the other hand, convective heat transfer from a heated sphere has been reported in the literature over a broad range of fluids, namely, liquid metals ($Pr \sim 0.01$), air ($Pr = 0.7$), water ($Pr = 7$) that further extended to the other Newtonian fluids ($Pr > 7$) found in Witaker (1972), Clift *et al.* (1978), Krieth (2000), Polyanin *et al.* (2001), Dhole *et al.* (2006), Rodriguez and Compo (2023) covering a range of Reynolds number.

Unlike spheres, the non-spherical particles describe by more than one length scale. Even though such non-spherical particles vary in shape, they might have identical equivalent diameter or characteristic length. Additionally, the hydrodynamic and thermal behavior of such particles depends on their orientation with respect to the flow direction. Amidst the lack of clarity about the measure of shape, scale,

and orientation of non-spherical particles, regular shapes like spheroid, disc, short cylinder, cones, hemisphere, and irregular shapes have been examined over the period of time and made available in literature by Bagheri and Bonadonna (2016), Govindan *et al*. (2020), Chhabra and Patel (2023), Francalanci *et al*. (2021), Michaelides and Feng (2023). The predictive correlations/expressions for the drag of non-spherical regular shapes are available either considering an individual particle shape and orientation or for a range of shapes and orientations altogether. Obviously, the first type of correlation has limited applicability with reasonably good accuracy. On the contrary, the second type allows one to predict the drag coefficient with a single correlation with less accuracy over the broad spectrum of the shape/orientation of particles. It is recommended to provide the correlation applicable universally from the engineering application point of view, however, it cannot be extrapolated for the missing shapes of particles. Based on the accuracy of the correlations, the most reliable models for estimating the drag coefficient include that proposed by Haider and Levenspiel (1989) and Ganser (1993) which cover a wide range of particle shapes. Haider and Levenspiel (1989) have established the explicit form of the drag correlation as $C_D = f(Re, \psi)$ considering range of shapes of isometric particles ($\psi \geq 0.67$, $Re < 2.5 \times 10^4$) and disks ($\psi < 0.67$, $Re < 500$). For all together shapes, the correlation fits isometric particle data reasonably good as compared to poor prediction for disks. The expression for drag coefficient proposed by Ganser (1993), $C_D = f(Re, K_S, K_N)$, consists of $K_S$ and $K_N$ as Stokes' and Newton's shape factors, respectively. This correlation based on similarity and scaling analysis was found to be promising for low Reynolds numbers and isometric shapes with known orientations. Recently, Bagheri and Bonadonna (2016) have established a correlation for the drag coefficient with increased accuracy considering 300 regular and irregular shapes covering Stokes' flow regimes ($Re < 0.1$) to Newton's regime ($Re < 3 \times 10^5$) in their experimental work. Hence, much work has been reported in the literature on drag and heat transfer in Newtonian fluids from non-spherical particles.

A thorough review of the literature, particularly for axisymmetric shapes, suggests that spheroid (Masliyah and Epstein, 1970; Kishore and Gu, 2011), disc (Nitin and Chhabra, 2005), short cylinder (Vakil and Green, 2009), cones (Sharma and Chhabra, 1991; Mishra *et al.*, 2019), hemisphere (Goharzadeh *et al.*, 2012; Kim and Choi, 2003), spherical segments (Hochmuth and Sutera, 1970; Wang *et al.*, 2009) have received attention to some extent. These shapes have been studied numerically and experimentally to explore hydrodynamics and/or convective heat transfer characteristics along with the correlations for drag and average Nusselt number. However, spherical caps or segments which are seen in the coagulation or breakdown phenomena of spherical particles may not follow the regularity of their parent particles. Such shapes have received very little attention in the literature. Thus, for instance, very scant data is available in the literature for spherical caps and segments, even in Newtonian fluids. Hochmuth and Sutera, (1970) conducted experiments for the spherical segments by varying the segment diameter to thickness ratio from 0.17 to 0.5 in a very low Reynolds number Poiseuille flow. Their experimental study clearly suggests a strong influence of segment diameter on velocity and pressure drop.

No more studies are available for spherical segments in literature to the best of our knowledge. However, the hemisphere, which corresponds to a limiting case of the spherical segment has received some attention. For instance, Kim and Choi, (2003) studied numerically the flow past a hemisphere over the wide Reynolds number range (up to $Re \sim 300$) and have determined the critical Reynolds number above which the flow becomes unsteady and periodic in nature for $Re \sim 190$–$200$. The PIV (Particle Image Velocimetry) measurements around the hemisphere are reported up to $Re = 800$ in a rectangular channel (Goharzadeh *et al.*, 2012). Similarly, scant experimental results for the dependence of drag coefficient on Reynolds number and orientation are also available in the literature (Wang *et al.*, 2009). Their results show that when the flat base is oriented upstream, the drag experienced by the hemispherical particle is higher than that for the flat base oriented downstream. However, the generalized correlations developed by Haider and Levenspiel (1989), Ganser (1993), Bagheri and Bonadonna (2016) mentioned above do not include spherical caps or segments.

Thus, it is fair to summarize here that the hydrodynamic and thermal characteristics of spherical segments have received very little attention in the literature. Hence, this study explores the momentum and heat transfer from a spherical cap or segment in the steady laminar flow regime. Furthermore, the present work also ascertains the adequacy of the use of sphericity as a shape factor with or without additional geometric characteristics. Finally, the present results for spherical segments and caps are compared with the closest shapes like short cylinders, cones, etc. with the same projected areas of the spherical segments.

### 4.1.2 Problem formulation

The schematic representation of the two-dimensional flow of fluid past a spherical segment has been shown in **Fig. 4.1a**. The uniform flow of air ($Pr = 0.72$) at velocity, $U$ and temperature $T_c$ is considered parallel to the axis of symmetry of a particle that is maintained at temperature $T_h$ ($T_h > T_c$) as shown in **Fig. 4.1b**. The spherical segments considered in this work are formed by dissecting a sphere of diameter $D_s$ ($= 2R$) at an angle $\alpha$ from its positive $y$-direction as shown in **Fig. 4.2**. A total of five segments from a sphere ($\alpha = 180°$), i.e., $\alpha = 30^o$, $60^o$, $90^o$, $120^o$, and $150^o$ are considered for this work as shown in **Fig. 4.2**. Each segmental particle can be characterized by its base diameter, $d_c$, and height $h_c = 0.5\left[D_s - \sqrt{\left(D_s^2 - d_c^2\right)}\right]$. Bearing in mind the dimensions of spherical segments i.e., $d_c$ and $h_c$, these shapes are compared with their possibly closest axisymmetric shapes such as cone, short cylinder, and sphere (having identical dimensions of $d_c$ and $h_c$) as shown in **Fig. 4.1a**. The flow past a particle is assumed to be two-dimensional, incompressible, and axisymmetric with thermo-physical quantities (thermal conductivity, $k$, specific heat constant, $C$, density, $\rho$, and viscosity, $\mu$) to be constant.

The scaling parameters are employed to render the aforementioned **Eqs. (2.1) – (2.3)** in non-dimensional forms are $U$, $\rho U^2$, and $(T - T_c)/(T_h - T_c)$ for velocity, pressure, and temperature respectively. To circumvent

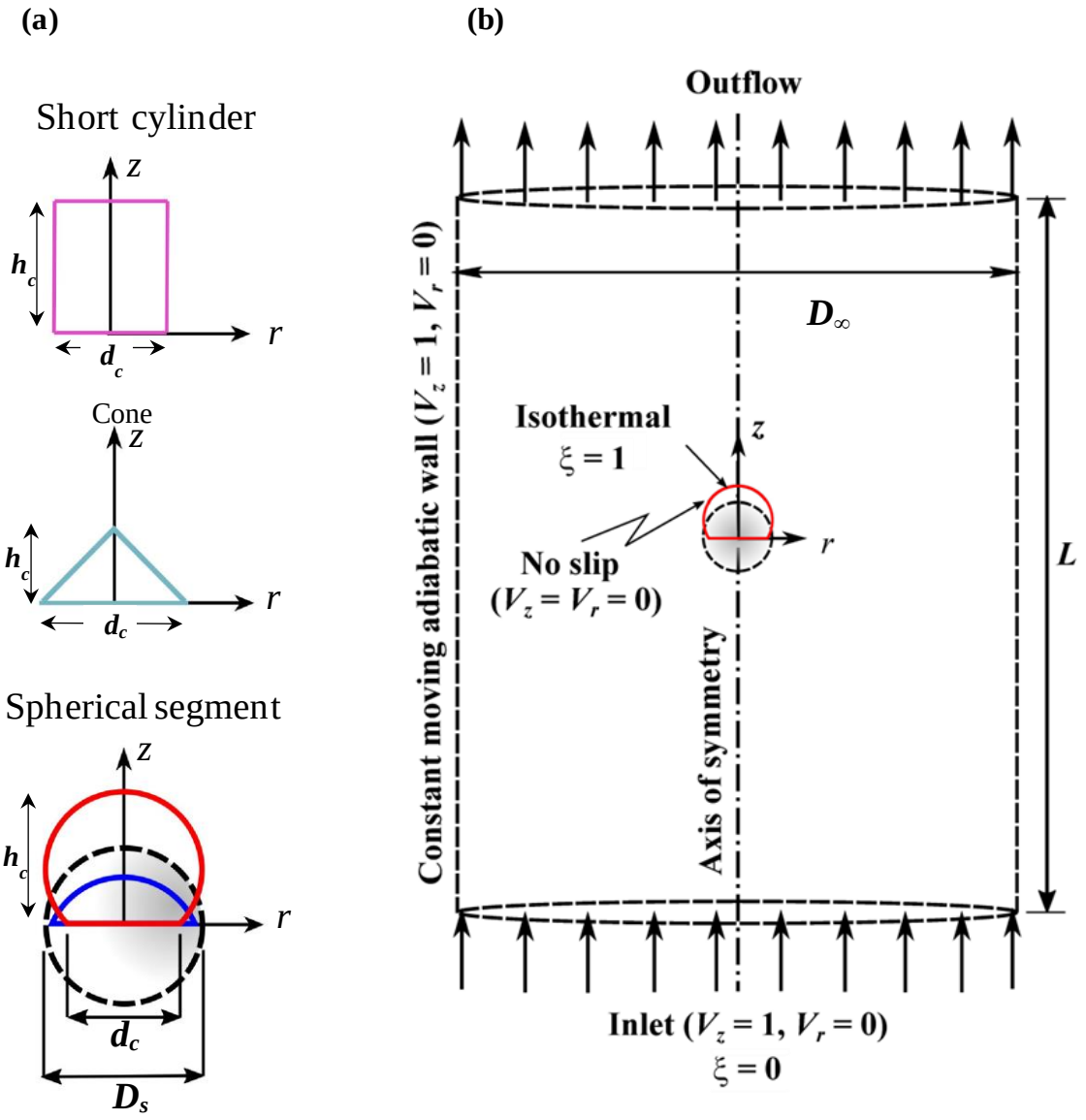


**Figure 4.1** Schematics of (a) geometries of various shapes (b) computational domain of problem statement.

the complexity of shapes in practical application, the dimensions of the non-spherical particles are presented in terms of equivalent spherical diameter $d_{eq}$ $\left(=\sqrt[3]{6V_p/\pi}\right)$ which are used as length scale here. This choice leads to Reynolds number being defined as, $Re=\frac{\rho U d_{eq}}{\mu}$. The Prandtl number, $Pr=\frac{\mu C}{k}$ evolves as an intrinsic property of fluids in this study for air, $Pr = 0.7$ has been used. In addition to these, sphericity ($\psi$) is employed as a geometric parameter to quantify the effect of shape of the particle on drag over the range of conditions.

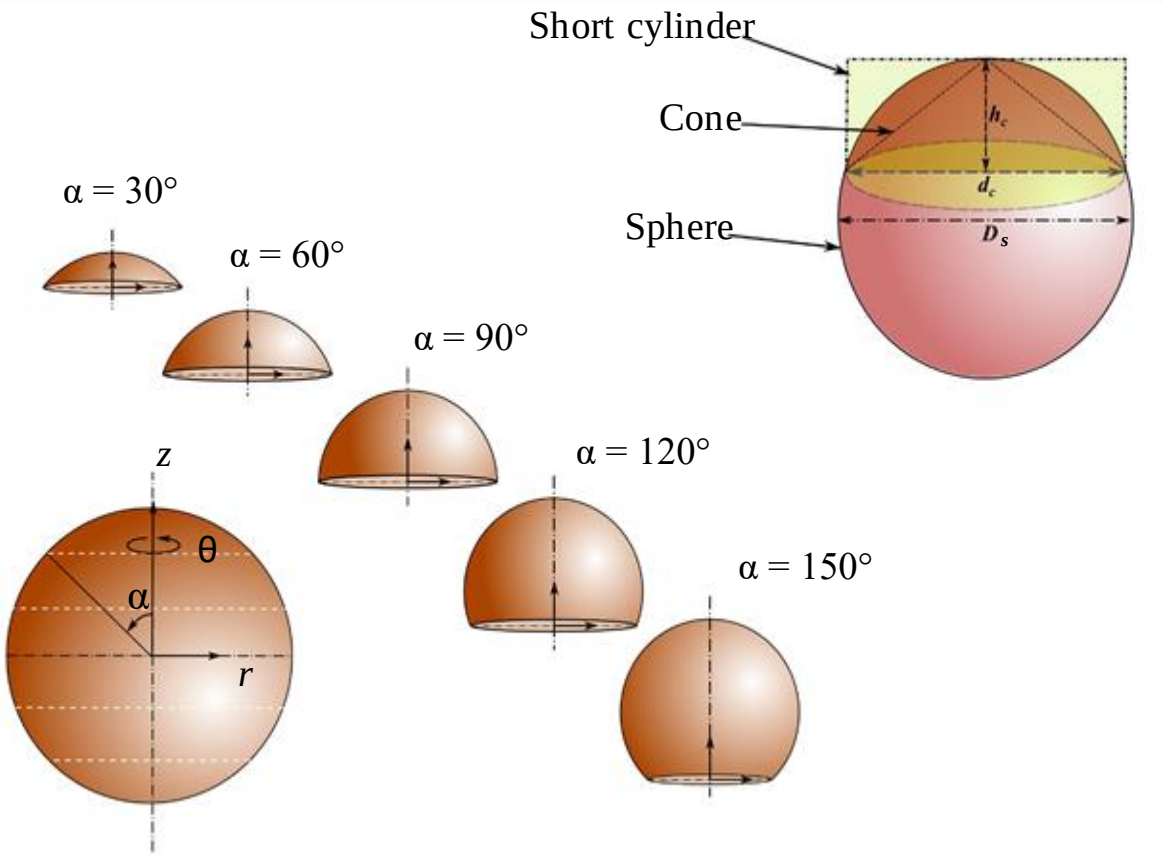


**Figure 4.2** Representation of geometries of spherical segments.

$$\psi = \frac{Surface\,area\,of\ equal\,volume\,sphere}{Actual\,surface\,area\,of\ \ particle} = \frac{6V_p}{d_{eq}A_{surface}} \tag{4.1}$$

Where $V_p$ and $A_{surfaœ}$ are the volume and surface area of the particle, respectively. The sphericity for a spherical segment of the base diameter $d_c$ and $h_c$, segmented from a sphere of diameter $D_s$ is given by:

$$\psi = \frac{d_{eq}^2}{\frac{1}{2}d_c^2 + h_c^2} \tag{4.2}$$

Considering two-dimensional axisymmetric unconfined flow, the above-mentioned partial differential equations are solved considering the following boundary conditions:

At the surface of the particle: $V_z = V_r = 0$ and $\xi = 1$

At the inlet boundary: $V_z = 1$ $V_r = 0$ and $\xi = 0$

At the hypothetical cylindrical domain wall: $V_z = 1$ $V_r = 0$ and $\partial\xi/\partial r = 0$

At the outlet (Neumann boundary condition): $\frac{\partial \zeta}{\partial z} = 0$ where $\zeta = V_z$, $V_r$, and $\xi$; $p = 0$

At the axisymmetric axis: $V_r = 0$, $\partial V_z / \partial r = 0$, $\partial \xi / \partial r = 0$

The solution of **Equations (2.1) – (2.3)** yields the pressure ($p$), velocity ($V_r$, $V_z$), and temperature ($\xi$) fields which are further post-processed to analyze in terms of streamlines, pressure coefficient ($C_{DP}$), frictional drag ($C_{DF}$), total drag coefficient ($C_D$), and local ($Nu_l$) and average Nusselt numbers ($Nu$).

### 4.1.3 Choice of numerical parameter and assessment of numerical methodology

The continuity, momentum, and energy equations (**Eqs. 2.1-2.3**) subjected to boundary conditions described in the previous section are solved by using finite element-based commercial software COMSOL 5.3. The numerical results over the range of shapes should be unimpeded by the domain size, number and type of grid elements, and convergence criterion. Hence, the optimum domain size over the range of the shape of particles has been identified by systematically varying the domain from D1 to D3 at the Reynolds number, $Re = 1$ (to capture the broadest thickness of boundary layer) for two extreme shapes, $\alpha = 30°$ and 150° as shown in **Table 4.1**. The average values of $C_D$, $C_{DP}$, and $Nu$ in **Table 4.1** reveal that the increase in domain size from D2 to D3 has a marginal effect (< 1%) on the gross results.

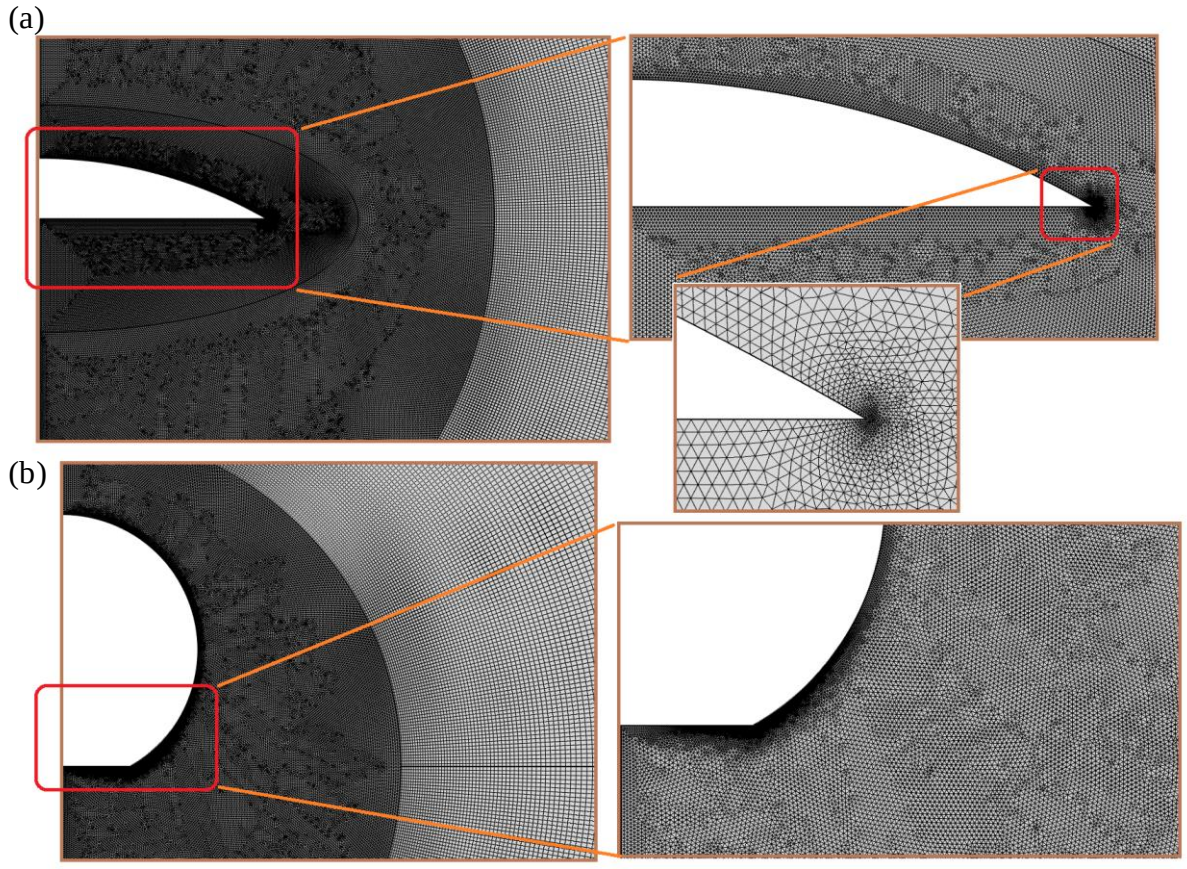


**Figure 4.3** Grid structure in the vicinity of the spherical segments (a) $\alpha = 30°$ and (b) $\alpha = 150°$.

**Table 4.1** Domain independence test at $Re$ = 1.

| | $L/D_s$ | $D_\infty/D_s$ | $C_D$ | $C_{DP}$ | $Nu$ |
|---|---|---|---|---|---|
| **α = 30°** | | | | | |
| D2 | 400 | 400 | 11.735 | 11.109 | 2.9971 |
| D3 | 600 | 600 | 11.684 | 11.029 | 2.9974 |
| **α = 150°** | | | | | |
| D2 | 400 | 400 | 27.069 | 9.2812 | 2.2564 |
| D3 | 600 | 600 | 27.055 | 9.2757 | 2.2564 |

Hence, the domain D2 ($L = D_\infty = 200$) has been chosen to approximate the unconfined flow condition having boundaries sufficiently far away from the particle. Furthermore, the selection of the grid is a crucial step for the geometry with sharp corner in addition to capturing the steep changes of momentum

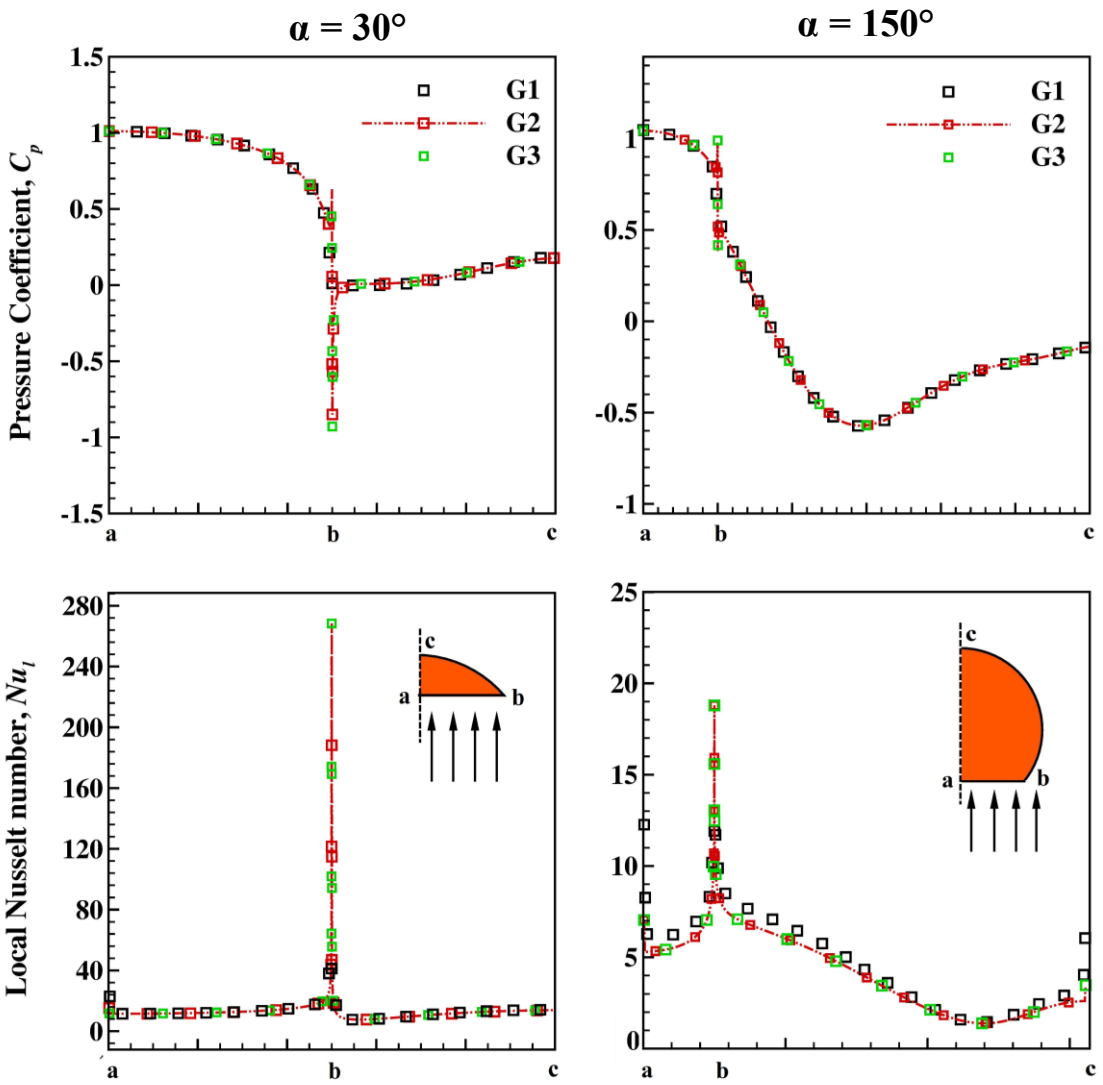


**Figure 4.4** Effect of grids on pressure coefficient and local Nusselt number distribution at $Re$ = 150 for two extreme shapes of spherical segments.

and thermal boundary layers at the extreme value of the Peclet number, $Pe$ (=$Re \times Pr$). Thus, the effect of grids has been examined in terms of local and average numerical results at $Re$ = 150 for two spherical segment shapes, α = 30° and 150°. **Figure 4.3** shows the grid structure in the vicinity of the particle with triangular elements while the remaining domain is discretized in quadrilateral elements. The sharp corner of the geometry has been refined with finer mesh to resolve the local singularity at the corner (infinite gradients of stress or heat flux). The grid independence test is performed at a high value of Reynolds number as the boundary layer is expected to be thinnest at $Re$ = 150 for three grids G1, G2, and G3 at α = 30° and 150°. The grid effects have been examined on the local distribution of pressure coefficient and Nusselt number along the surface of the spherical segments as shown in **Fig. 4.4**. The obtained results for G2 and G3 in **Fig. 4.4** are seen to be indistinguishable from each other. The number of elements required for each spherical segment geometry to capture momentum and thermal characteristics reduces gradually with the increase in their surface curvature with the increase in α. Therefore, chosen grid G2 has ~350000 and ~159000 elements for the numerical study of α = 30° and 150°, respectively.

**Table 4.2** Comparison of experimental results with present results of drag coefficient for sphere in air.

| ***Re*** | **Drag coefficient, $C_D$** | | **Nusselt number, $Nu$ ($Pr$ = 0.72)** | |
|---|---|---|---|---|
| | **Clift *et al.* (1978)** | **Present** | **Ranz and Marshall (1952)** | **Present** |
| 1 | 27.16 | 27.20 | 2.54 | 2.25 |
| 2 | 14.76 | 14.85 | 2.76 | 2.44 |
| 3 | 10.52 | 10.61 | 2.93 | 2.59 |
| 5 | 7.03 | 7.10 | 3.20 | 2.85 |
| 7 | 5.48 | 5.53 | 3.42 | 3.06 |
| 10 | 4.26 | 4.28 | 3.70 | 3.34 |
| 20 | 2.74 | 2.70 | 4.41 | 4.05 |
| 30 | 2.12 | 2.11 | 4.92 | 4.59 |
| 50 | 1.57 | 1.57 | 5.81 | 5.44 |
| 70 | 1.31 | 1.30 | 6.50 | 6.12 |
| 100 | 1.09 | 1.08 | 7.38 | 6.97 |

To gain confidence in the adequacy and reliability of the chosen numerical model, methodology, and parameters, a few benchmark validations have been performed for the numerical and experimental results available in the literature. In particular, spherical segments have been found to be the least studied shape in the literature. Considering sphere and hemisphere as liming shapes with α =180º and 90º the available results for these two shapes in Newtonian fluids have been validated for this study. **Table 4.2** shows the

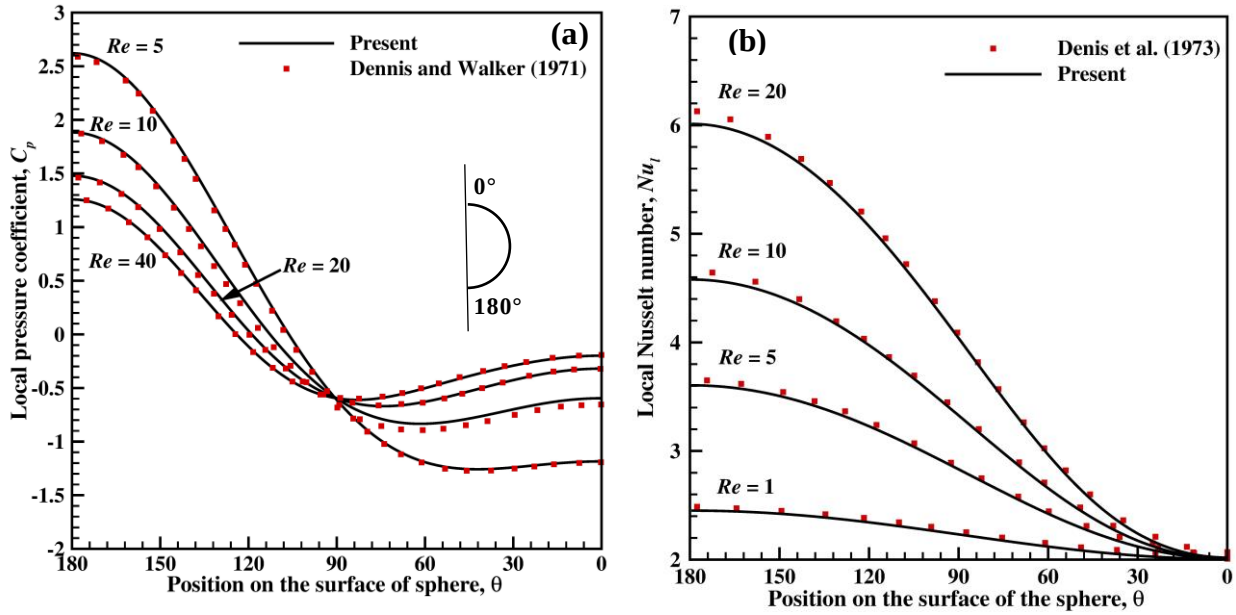


**Figure 4.5** Comparison of the (a) pressure coefficient and (b) local Nusselt number on the surface of sphere over a range of Reynolds number for $Pr$ = 0.72.

comparison of the present results of the drag coefficient and average Nusselt number for the sphere with that of the experimental results by Ranz and Marshall (1952) and Clift *et al.* (1978). The results have shown good agreement with each other. To gain more confidence, the present prediction of the local values of pressure coefficient ($C_p$) and Nusselt number on the surface of the sphere are compared with the available numerical results (Dennis *et al.*, 1973; Clift *et al.*, 1978) over the range of Reynolds number as shown in **Fig. 4.5**. They shows very good correspondence with each other with less than 3% error. Furthermore, the experimental results of drag coefficient value by Wang *et al.* (2009) of the upright configuration of the hemisphere is compared with the present value in **Fig. 4.6** that shows a close correspondence between the experimental and numerically predicted values. Aside from this, validation has been conducted for other shapes, e.g., cone (Mishra *et al.*, 2019) with apex angle, φ = 20º in Newtonian fluid tabulated in **Table 4.3** to acquire further confidence for the results of other shapes, cone, and short cylinder considered in this study. The results seem to be reasonably close to each other.

**Table 4.3** Validation of conical geometry of apex angle φ = 20° in air.

| ***Re*** | **Drag coefficient, $C_D$** | |
|---|---|---|
| | **Mishra *et al.* (2019)** | **Present value** |
| 1 | 34.116 | 33.211 |
| 20 | 3.2193 | 3.1776 |
| 50 | 1.8156 | 1.8084 |
| 100 | 1.2468 | 1.2531 |

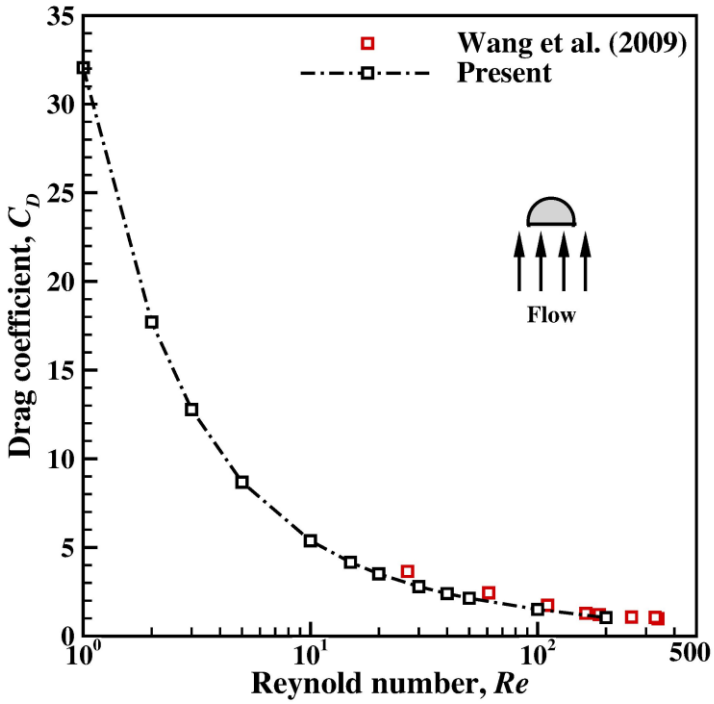


**Figure 4.6** Comparison of experimental results of drag coefficient of the hemisphere with the present study for $Pr = 0.72$.

### 4.1.4 Results and discussion

The present work explores the effect of particle shape on momentum and heat transfer characteristics by considering five different geometries for spherical segments characterized by α ($30° \leq \alpha \leq 150°$). The range of Reynolds numbers covers $1 \leq Re \leq 150$ for air ($Pr = 0.72$) as a working fluid. Bearing in mind the asymmetricity of the spherical segments, the closest other possible shapes, cone and short cylinders, with identical height and base area have been incorporated in this work to quantify the shape effect on momentum and heat transfer phenomena. As shown in **Table 4.4**, spherical segments for $\alpha \leq 90°$ have been compared with both shapes of cone and short cylinder. While for $\alpha > 90°$, recognizing the shapes of the spherical segment, $\alpha = 120°$ is compared with a short cylinder only having the same base area and

**Table 4.4** Sphericity of the axisymmetric shape in present work.

| Cone | | Spherical segment | | | Short cylinder | |
|---|---|---|---|---|---|---|
| $C^{\alpha}$ | ψ | α | $r_c/R$ | ψ | $SC^{\alpha}$ | ψ |
| $C^{30}$ | 0.324 | 30° | 0.5 | 0.424 | $SC^{30}$ | 0.541 |
| $C^{60}$ | 0.511 | 60° | 0.866 | 0.663 | $SC^{60}$ | 0.726 |
| $C^{90}$ | 0.658 | 90° | 1 | 0.840 | $SC^{90}$ | 0.825 |
| - | - | 120° | 0.866 | 0.952 | $SC^{120}$ | 0.872 |
| - | - | 150° | 0.5 | 0.996 | - | - |

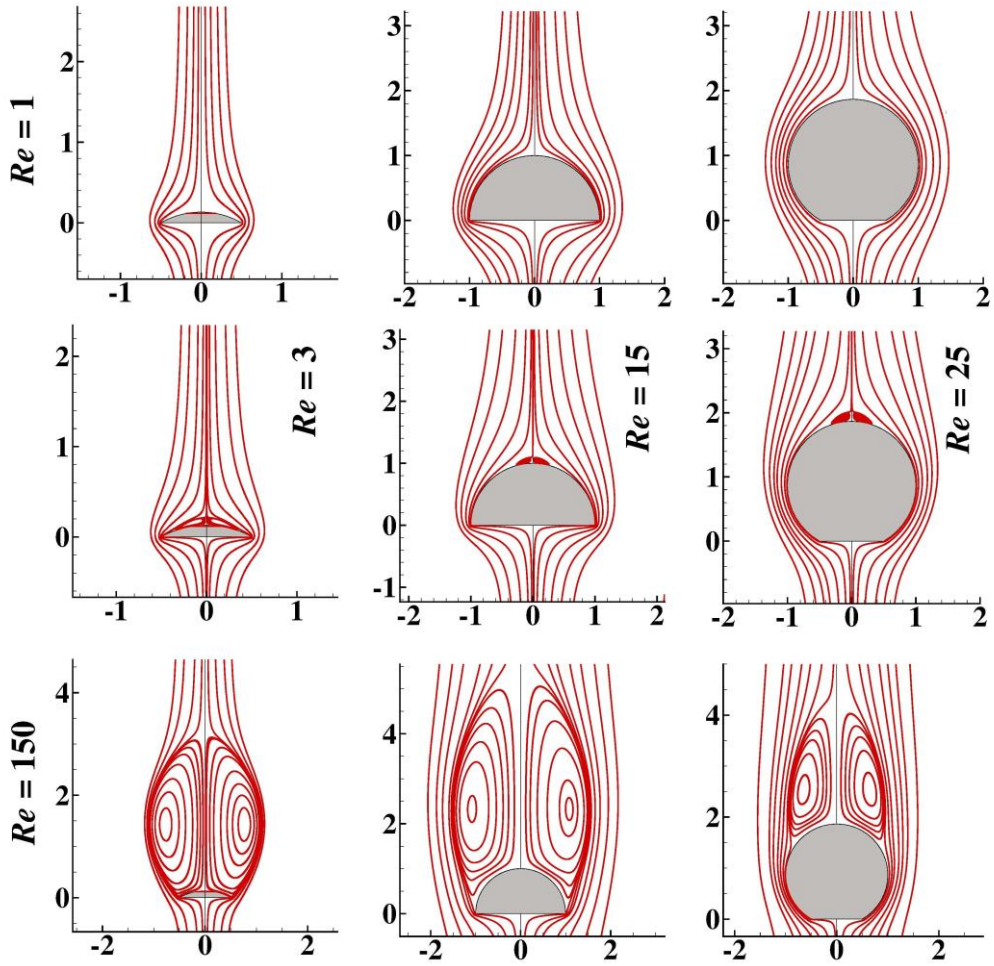


**Figure 4.7** Wakes at the rear end of the spherical segment over the range of Reynolds number.

height. The results of the effect of Reynolds number and shape factor on wake characteristics, total drag coefficient, isotherms, local Nusselt number, and average Nusselt number have been discussed in the next section.

*4.1.4.1 Flow separation and wake characteristics*

Visualization of flow structure in the vicinity of non-spherical particles is an interesting phenomenon in general with a significant impact on practical applications. The spatial variation of velocity around the particle has been visualized in terms of streamlines to understand the characteristics of fluid flow past a particle. **Figure 4.7** elucidates the effect of the Reynolds number on the flow past the spherical segment by plotting the streamlines for $\alpha = 30^{o}$, $\alpha = 90^{o}$, and $\alpha = 150^{o}$. Intuitively, the location of the flow separation depends primarily on the geometry of the particle. The flow separation from the particle surface occurs due to the adverse pressure gradient associated with the sudden change in the body contour of the particle geometry. At a low Reynolds number, $Re = 1$, fluid follows the body contour under the low inertial force without losing kinetic energy and remains attached to the particle surface irrespective of the shapes. The critical Reynolds number, $Re_c$ defined as the value above which flow has been detached from the particle surface. For $\alpha = 30^{o}$, the flow separation occurs early at the critical Reynolds number, $Re_c \sim 3$, due to the

sharp corner and low curvature to the lateral area. On the other hand, for the spherical segment with α = 150º, the flow separation occurs at $Re_c$ ~ 22. The values of the critical Reynolds number in **Table 4.5** are ascertained with the accuracy of ±1 *Re*.

**Table 4.5** Critical Reynolds number for axisymmetric shape in the present work.

| Spherical Segment | | | Cone | | | Short cylinder | | |
|---|---|---|---|---|---|---|---|---|
| **α** | **No wake** | **Wake** | **$C^{\alpha}$** | **No wake** | **Wake** | **$SC^{\alpha}$** | **No wake** | **Wake** |
| | ***Re*** | ***$Re_c$*** | | ***Re*** | ***$Re_c$*** | | ***Re*** | ***$Re_c$*** |
| 30° | 2 | 3 | $C^{30}$ | 1 | 2 | $SC^{30}$ | - | 1 |
| 60° | 6 | 7 | $C^{60}$ | 5 | 6 | $SC^{60}$ | 1 | 2 |
| 90° | 13 | 14 | $C^{90}$ | 13 | 14 | $SC^{90}$ | 2 | 3 |
| 120° | 19 | 20 | - | - | - | $SC^{120}$ | 3 | 4 |
| 150° | 21 | 22 | - | - | - | | - | - |
| For sphere, α = 180°, $Re_c$ ~ 22 | | | | | | | | |

Intuitively, it would be expected that the distinct shape of the particle with identical frontal areas tends to modify the wake structure formed at the rear of the particles. **Figure 4.8** compares the wake characteristics for all three shapes over the range of α for the value of Reynolds number just above the critical values, $Re_c$ (**Table 4.5**). For α = 30º, streamlines travel along the base of the particles until they detached from the surface due to the abrupt change of the lateral surface and formed separation bubbles for all three shapes. **Figure 4.8** shows that the lateral surfaces of the spherical segment (curvature) and cone (slanted) while the flat surface of the short cylinder have been fully enveloped by the twin symmetric vortices. For α = 30º, it is noticeable that as compared to the curvature, the slant surface of the particle has placed the outer boundary of the wake further down forming the broader separation bubbles. Similarly, the wake boundary will be pushed further away due to the completely flat rear end of the short cylinder which offers a flat surface followed by the vertical surface to the flow as shown in **Fig. 4.8**.

As α increases, at α = 60°, the geometry of the spherical segment gains shape in a further smooth curvature surface while the cone acquires a less slanted surface compared to α = 30º. While the short cylinder shows the corresponding change in the height of the geometry only. In the case of a spherical segment, the separation bubbles are shifted towards the rear end due to the smooth curvature from the base of the particle. On the other hand, the cone with a less slanted surface formed separation bubbles that engulfed the complete lateral surface whereas the short cylinder separation bubble remains attached to the flat surface. The wake characteristics follow a similar trend with the further increase in α (see results for α = 90º). For α = 90º, the shape of the spherical segment has no significant effect on $Re_c$ as seen in **Table 4.5** and the value appears to be similar or close to that of the sphere. The obvious reason that even with the

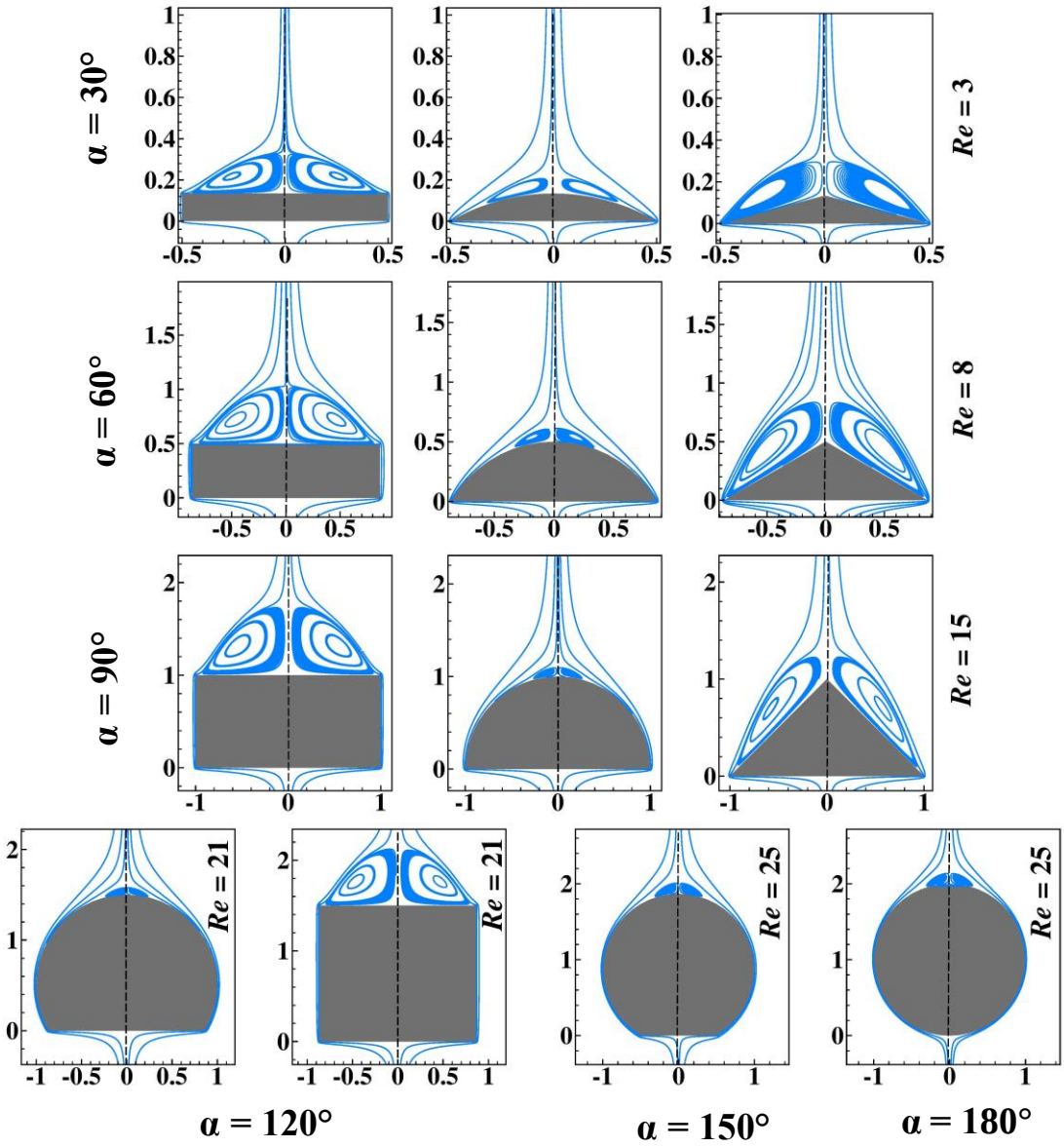


**Figure 4.8** Comparison of the wake formation of spherical segments with their closest non-spherical geometries and sphere.

flat frontal area, a major part of the shape of these particles, i.e., the lateral area resembles the spherical shape.

The wakes or separation bubbles are generally characterized by the wake or separation length, i.e., a measure of the distance between the rear stagnation point and the confluence point (termination of wake separation point) of the flow on the streamwise rear axis of the particle. The confluence point can be determined from the velocity profile plotted along the rear axis downstream of the rear stagnation point. **Figure 4.9** illustrates the velocity profiles for $Re = 150$ over the range of α values for spherical segments over the normalized rear axis to estimate the effect of shapes on the separation length. At the confluence point, the magnitude of the velocity is zero showing the transition from negative to positive values. **Figure**

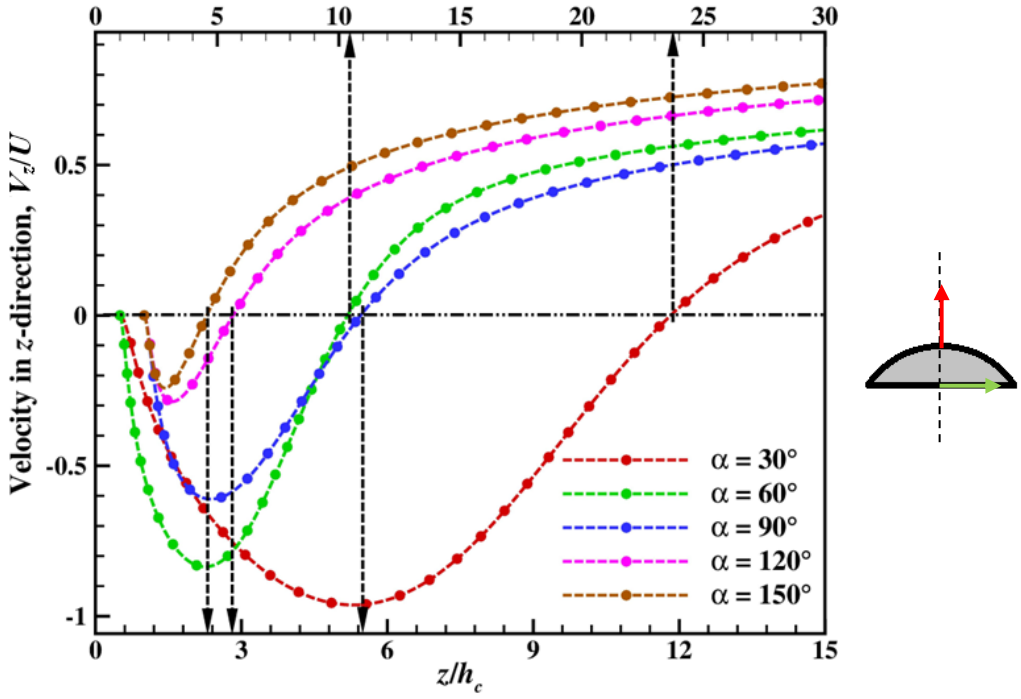


**Figure 4.9** Non-dimensional velocity profile at the rear of the spherical segments at $z = 0$.

**4.9** clearly shows that at a given Reynolds number, the largest separation length is observed for α = 30º and that gradually decreases with the transition of the shape towards more spherical with the increase in α. Before leaving this section, the role of shape on the separation length for the spherical segment, cone,

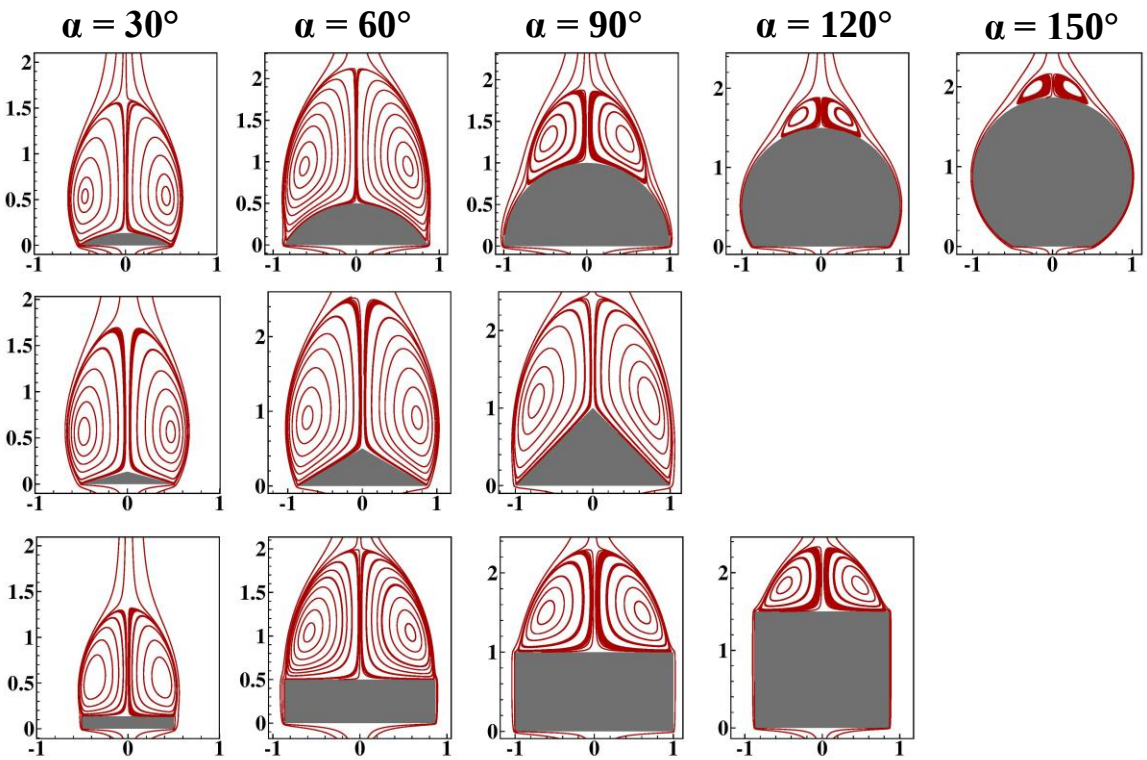


**Figure 4.10** Representative streamline profiles for spherical segments at *Re* = 30.

and short cylinder has been visualized by plotting the streamlines over the range of α as shown in **Fig. 4.10** at *Re* = 30 to gain further insight into the prevailing flow structure in the surrounding of the particle. It shows that the shape of the particle has a significant influence on the wake structure under otherwise identical conditions.

*4.1.4.2 Drag coefficients*

Process designing associated with multiphase and/or particulate systems essentially requires the knowledge of the drag characteristics of the particles along with the physics of fluids. The pressure and frictional forces experienced by a particle collectively contribute to the resultant drag force. By knowing the most stable orientation of the particle in the fluid, in the absence of (or negligible) wall effect, the non-dimensional drag force on the non-spherical particle will be expressed as $C_D = f(Re, \psi)$. For acquiring a clear understanding of the effect of particle shape on the drag coefficient, the dependence of $C_D$ on *Re*, and ψ has been plotted in **Fig. 4.11-4.13**. The dependence of drag on the shapes of the spherical segment has been shown in **Fig. 4.11(a)** and **4.11(b)** depict that the shape descriptor (α or ψ) has a significant effect on $C_D$ at low values of Reynolds number (*Re* = 1 and 10) that becomes almost independent of Reynolds number as *Re* increases. A sharp increase in the drag coefficient has been observed for $Re \leq 10$ for $\alpha \leq 120°$ ($\psi \leq 0.952$) in **Fig. 4.11(a)** beyond these values, the drag tends to be constant. As discussed in the previous section, at *Re* = 1, the flow remains attached to the spherical segment over the range of the shape dominated by the frictional or viscous drag. As the viscous drag pertains to the surface area of the particle subjected to the flow, the drag coefficient increases with α or ψ as the lateral surface area increases shown in **Fig. 4.11(a)**. A similar trend has been observed for *Re* = 10 as well in **Fig. 4.11(a)**.

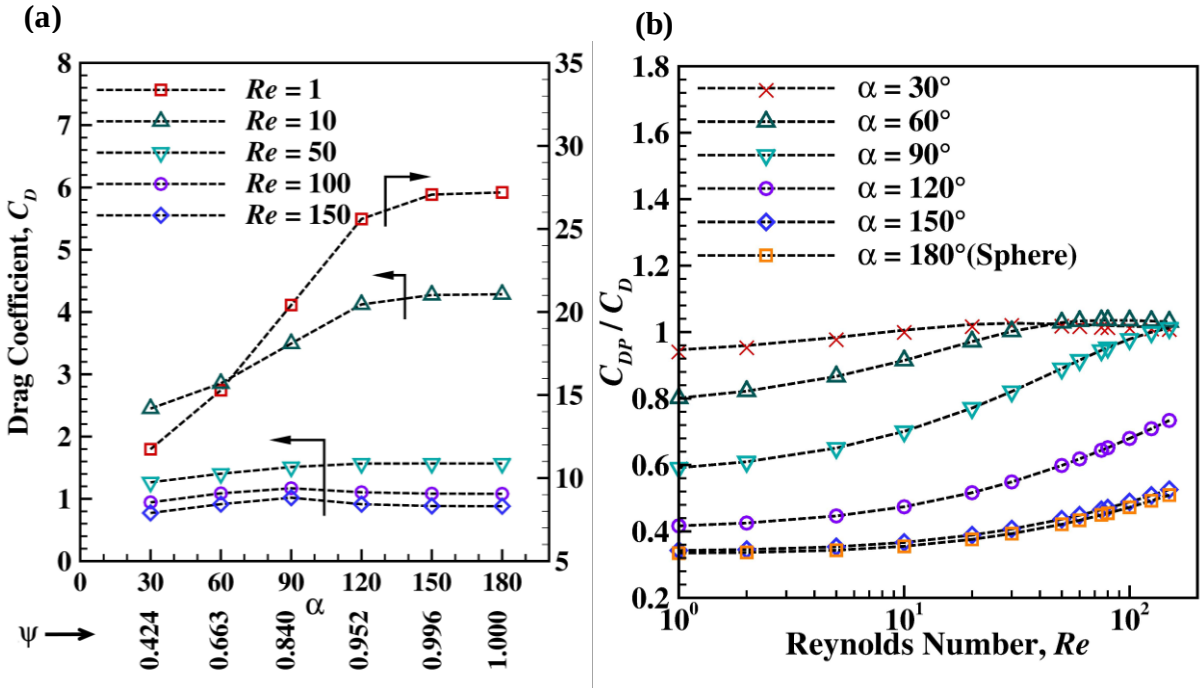


**Figure 4.11** Variation of (a) drag coefficient (b) the ratio of pressure drag coefficient to the total drag coefficient for a range of spherical segments and Reynolds numbers.

As the Reynolds number increases further beyond *Re* = 10, the drag coefficient decreases over the range of α. With the increase in Reynolds number, the total drag dominates by pressure drag with less contribution of viscous drag. Hence, as the Reynolds number increases the frontal area of the particle has more significance as compared to the surface area. Moreover, in such prevailing conditions, the drag coefficient shows weak dependence on shape as well as the Reynolds number. It is noticeable that for *Re* > 50 the drag coefficient increases to the maximum at α = 90° having the largest base area as a frontal area over the range of α. Even though having an identical frontal area for α = 90°, 150° and 120° shapes, α = 150° and 120° show a decline in drag coefficient as compared to α = 90°. It is noticeable that the drag coefficient values for α = 60° and 30° seemed to be close to the drag experienced by spherical segments having identical base areas, i.e., α = 120° and 150°, respectively. Hence, it shows that beyond *Re* = 50, the drag of the particle is a strong function of the base or frontal area irrespective of the shape of the particle.

**Figure 4.11(b)** shows the relative contributions of the viscous and pressure drag corresponding to the shape of the spherical segment over the range of Reynolds number spanned here. **Figure 4.11(b)** reveals that for α ≤ 90°, the pressure drag contributes more to the total drag with a little contribution from the

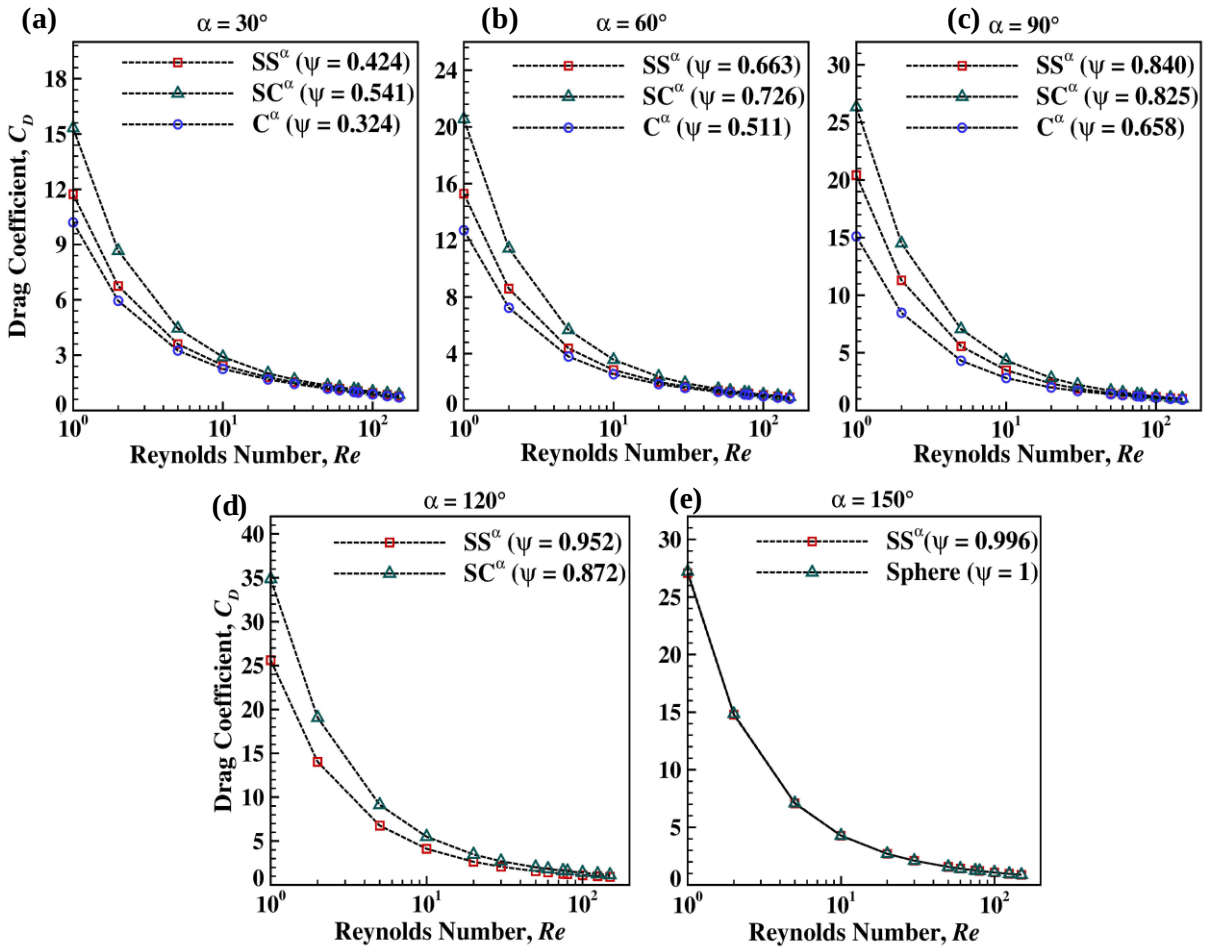


**Figure 4.12** Drag coefficients of the spherical segment (SS), cone (C), and short cylinder (SC) of identical base diameter and height as a function of Reynolds number.

viscous drag, specifically for $Re \geq 50$. As the shape of the particle tends to be more spherical in shape with the increase in α or ψ, for the given value of the Reynolds number, due to the increase in lateral surface area the ratio $C_{DP}/C_D$ decreases. In summary, the drag force acting on the spherical segment displays proportionality to the surface area at the lower values of $Re$ (<~50). Beyond this value of the Reynolds number, the drag coefficient is proportional to the projected area.

To represent the effect of the Reynolds number on the shape of the particles more precisely, **Fig. 4.12** has been plotted for shapes with identical height and frontal area while varying in lateral surface area as, spherical segment, cone, and short cylinder. The lateral area has been considered as the surface area of the particle projected on the vertical plane. In **Fig. 4.12(a) - (e)** it has been evident that for $Re$ < ~50 the drag coefficient values dominated by viscous drag differ reasonably for three shapes because of the difference in lateral areas. While the drag coefficient drawing little contribution from the viscous drag is governed by the frontal area irrespective of the shape of the particle beyond $Re$ ~ 50. It is worth commenting here on the shape of the particles (differs in the lateral surfaces or body contours) and how it modulates the drag force at the low Reynolds numbers. Particles with slander (cone), vertical (short cylinder), and curvature (spherical segment) surfaces experience the drag in the order of cone < spherical segment < short cylinder for the identical base area and height (**Fig. 4.12**).

Finally, **Fig. 4.13** shows the dependence of drag coefficients for all three shapes on the shape factor ψ. It is noticeable that the drag curves for cone and spherical segments show smooth variation with the increase

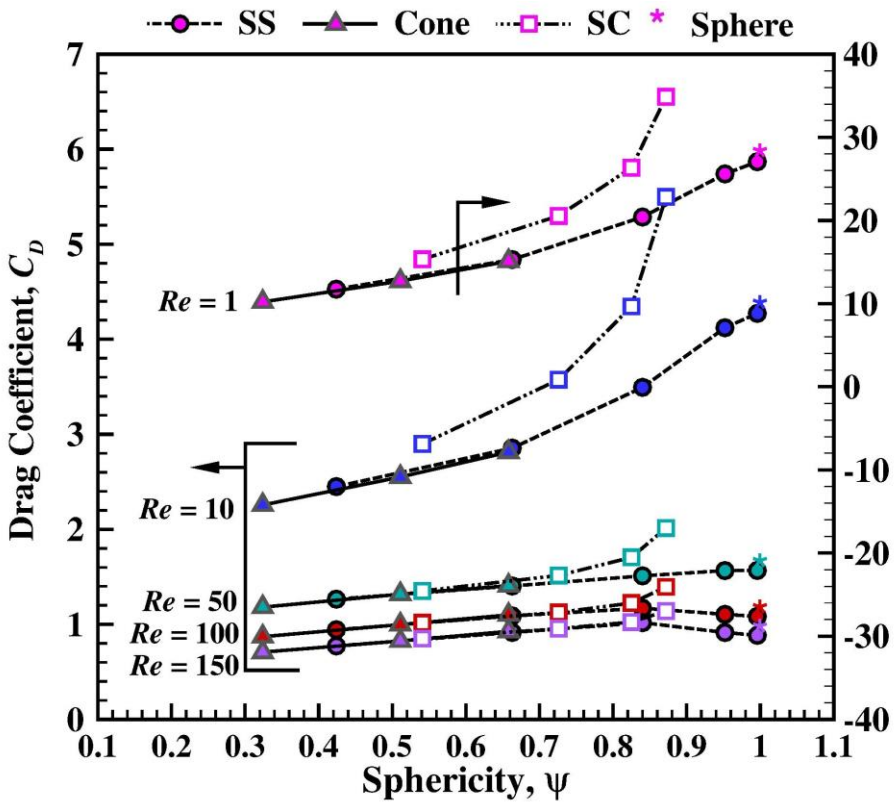


**Figure 4.13** Drag coefficient as a function of sphericity and Reynolds number.

in ψ irrespective of the shapes. Contrary to the drag variation of cone and spherical segments, the drag curve for short cylinders has been seen to be veering away from the cone and spherical segments over the range of Reynolds number. Moreover, this deviation seems to be significant at a low Reynolds number that becomes trivial with the increase in Reynolds number, particularly for $\psi < 0.8$ as seen in **Fig. 4.13**.

It is clear from the above discussion that the shape factor ψ will be not sufficient to describe the drag coefficient variation over the range of Reynolds number for particles varying in shape. Hence, a correlation for drag coefficient has been proposed as a function of Reynolds number and two shape descriptors ψ and ($d_c/h_c$) as

$$C_D = 0.828 + \frac{28.546}{Re^{0.881}}\psi^{0.721}\left(\frac{d_c}{h_c}\right)^{-0.186} \tag{4.4}$$

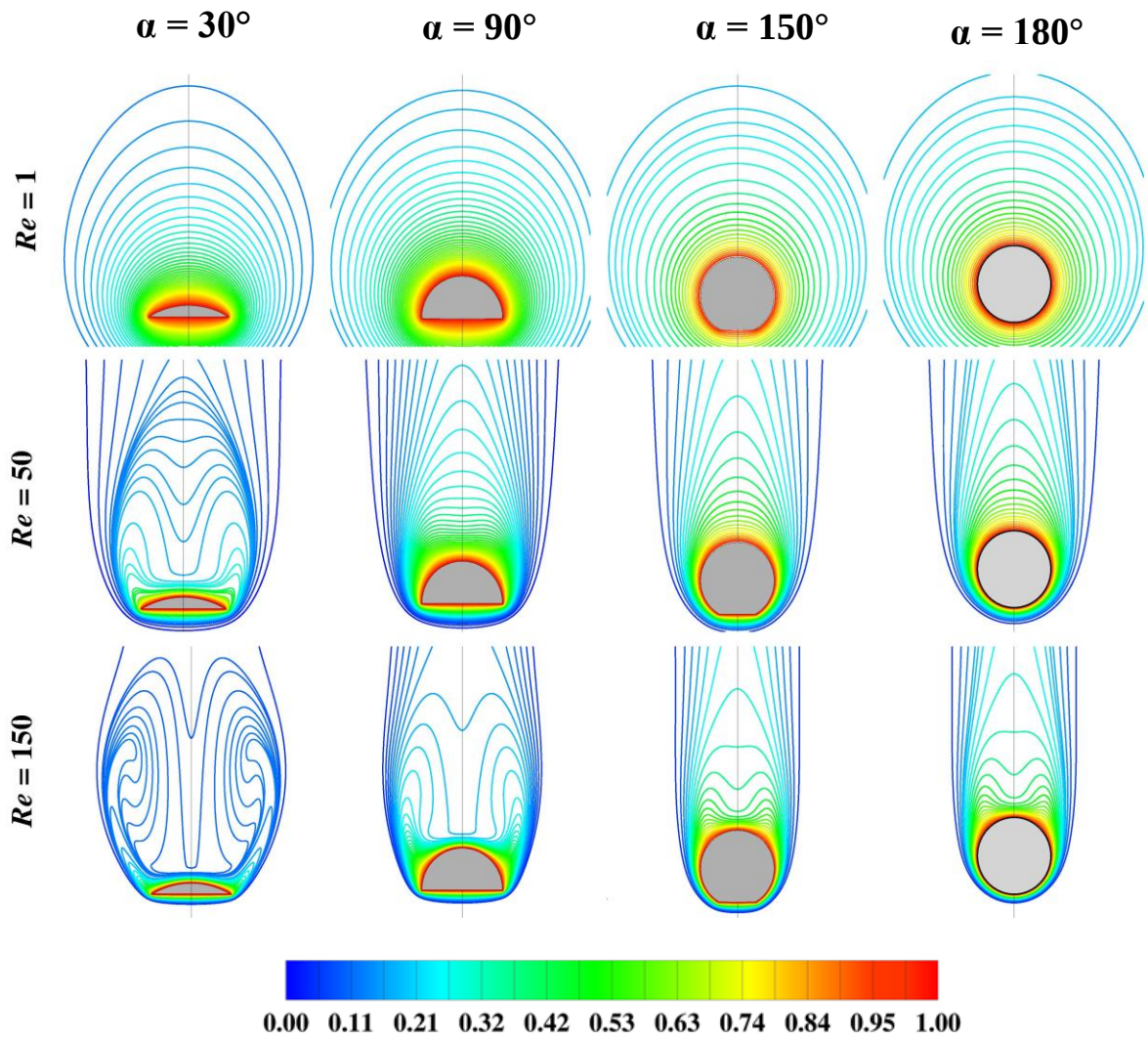


**Figure 4.14** Representative isothermal contours for spherical segments at Reynolds number at *Pr* = 0.72.

The addition of another shape descriptor ($d_c/h_c$) to **Eq. (4.4)** successfully correlates the total of 169 data over the range of the shape factor, $0.324 \leq \psi \leq 1$, and Reynolds number range, $1 \leq Re \leq 150$ with the average and maximum error of 10% and 33%, respectively.

In addition to devising **Eq. (4.4)** here using the present numerical results for spherical segment, it is also worthwhile to revisit some of the existing drag correlations in the literature. Thus, for instance, the form of the correlation Haider and Levenspiel (1989) can be modified as follows for the present results:

$$C_D = \left(\frac{24}{Re}\right)\left(1 - \frac{2.70exp\left(-1.878\psi\right)}{Re^{0.281+2.227\psi}}\right) + \frac{0.241Re\ exp\left(1.860\psi\right)}{Re - 1.023\ exp\left(-0.134\psi\right)} \tag{4.5}$$

**Eq. (4.5)** correlates our 169 data points with the average and maximum deviation of 17% and 95%, respectively. The above expression yields poor results for $\psi \geq 0.952$, particularly, for $Re \geq 60$. Similarly, the other model proposed by Haider and Levenspiel (1989) has been adopted here which is the modified form of the Clift-Gauvin Equation (1971) for spherical particles by introducing the constants as function of the sphericity.

$$C_D = \left(\frac{24}{Re}\right)\left(1 - \left(\frac{1.090}{\psi^{0.037}}\right)Re^{0.037}\right) - \frac{36.75}{1 - \frac{\left(2.174/\psi^{0.567}\right)}{Re^{-0.567}}} \tag{4.6}$$

**Eq. (4.6)** shows a reasonably good fit with the resulting average and maximum % errors of 13.5% and 35%, respectively. However, **Eq. (4.6)** contains many more fitting parameters than **Eq. (4.4)**.

It is worthwhile to note here that the original form of the functional relationship of drag coefficient by Haider and Levenspiel (1989) successfully reproduces the results for $\psi \geq 0.511$ within the reported range of overall average and maximum errors of 16% and 275% respectively. However, its performance deteriorated as the value of the sphericity dropped below 0.511. In summary, **Eq. (4.4)** seems to reproduce the present results for spherical segment than **Eqs. (4.5)** and **(4.6)**.

*4.1.4.3 Heat transfer characteristics*

The visualization of the temperature field in the vicinity of the hot particle in the flow domain helps map the regions of relatively low (cold spot) and high (hot spot) temperatures. **Figure 4.14** shows the isotherm contours for spherical shape particles over the range of Reynolds number. At low *Re*, the heat transfer is primarily governed by conduction mode showing the symmetric contours surrounding the hot particles. With the increase in Reynolds number, due to advection the isotherms distorted in the downstream of the particle reflecting the structure of vortices. In **Fig. 4.15**, the local heat transfer coefficient is plotted over the surface of the spherical segment of $\alpha = 30°$, 90°, 150°, and 180°. Advection phenomena of air mainly promote heat transfer from the hot particles. The maximum value of the local Nusselt number has been observed at the front stagnation point over the range of Reynolds number irrespective of the shape of particle. Almost constant values of the local Nusselt number observed along the base of the particle fall

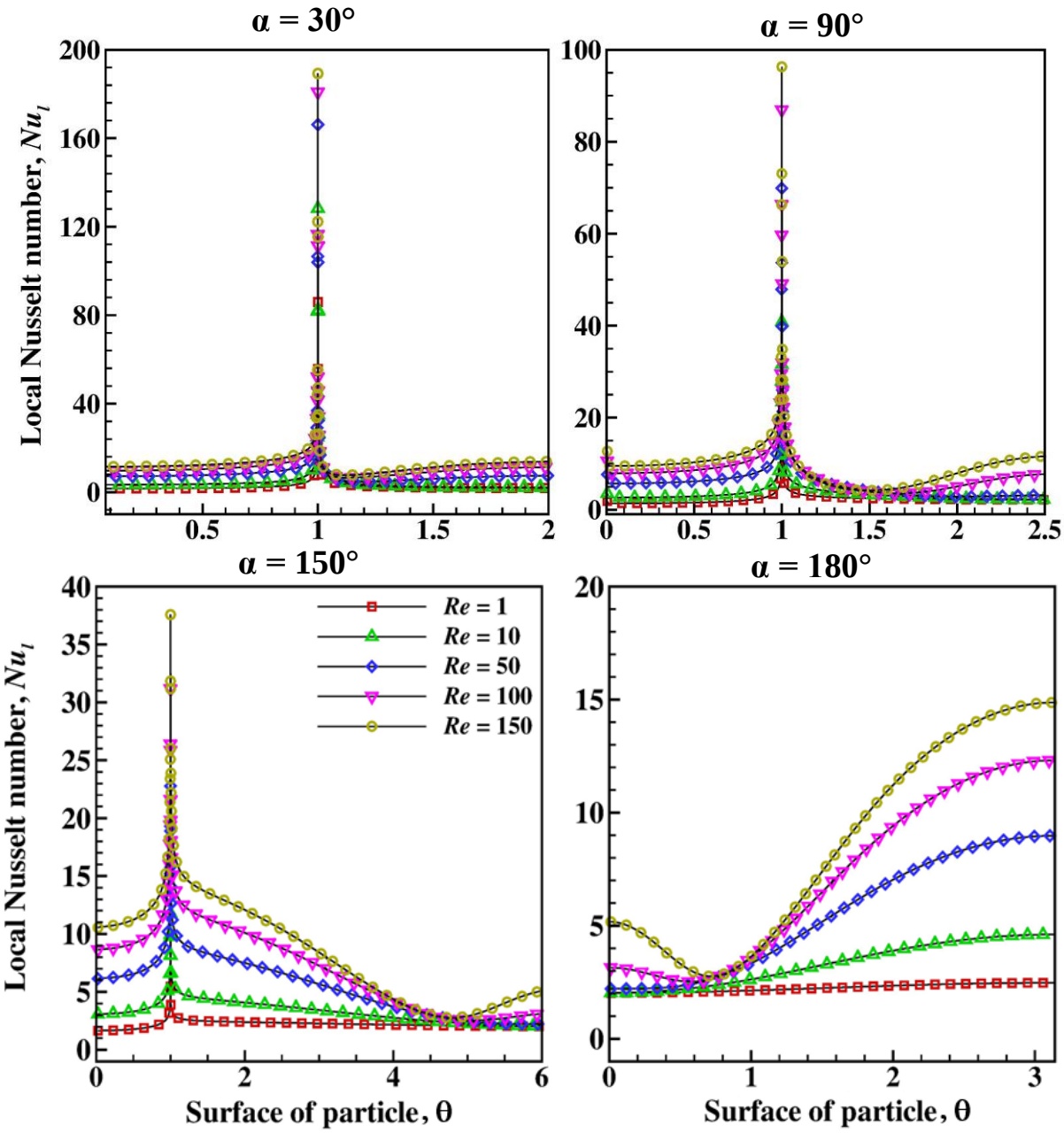


**Figure 4.15** Local Nusselt number variation for spherical segments over the range of Reynolds number.

to a minimum once they cross the sharp corner of the geometry that precisely indicates the flow separation points in **Fig. 4.15**. It is also evident that the location of flow separation is a strong function of the particle shape. Hence, the minima in the local Nusselt number for the spherical segments shift away from the corner of the shape with the increase in α. Finally, the peaks observed in the local Nusselt number are of no particular significance from a practical standpoint as the corresponding heat transfer area at this location of the geometry is zero.

The average Nusselt number plays a vital role in the process calculations as well as the sizing of equipment where heat transfer in various fluid-particle interactions is an inherent phenomenon. In general, the average Nusselt number shows a positive dependence on the Reynolds number shown in **Fig. 4.16a**

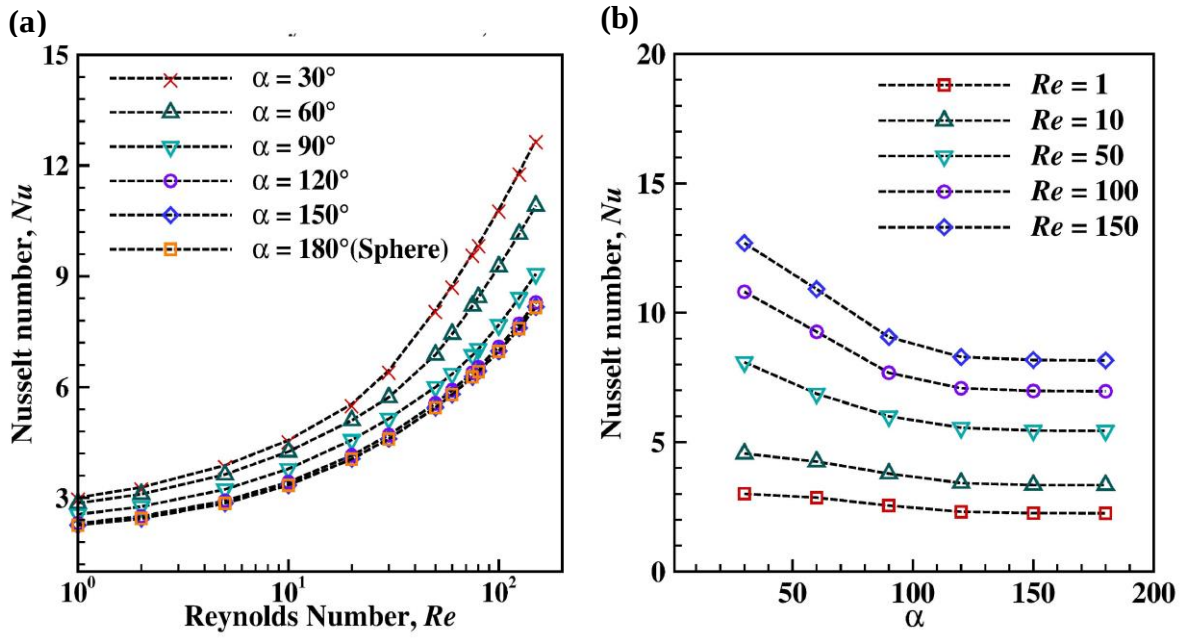


**Figure 4.16** Average Nusselt number as a function of (a) Reynolds number (b) range of the shape of spherical segment α.

over the range of spherical segments. On the other hand, as shown in **Fig. 4.16b**, with the increase in α the average Nusselt number decreases, and beyond α = 120º, the rate of heat transfer becomes independent

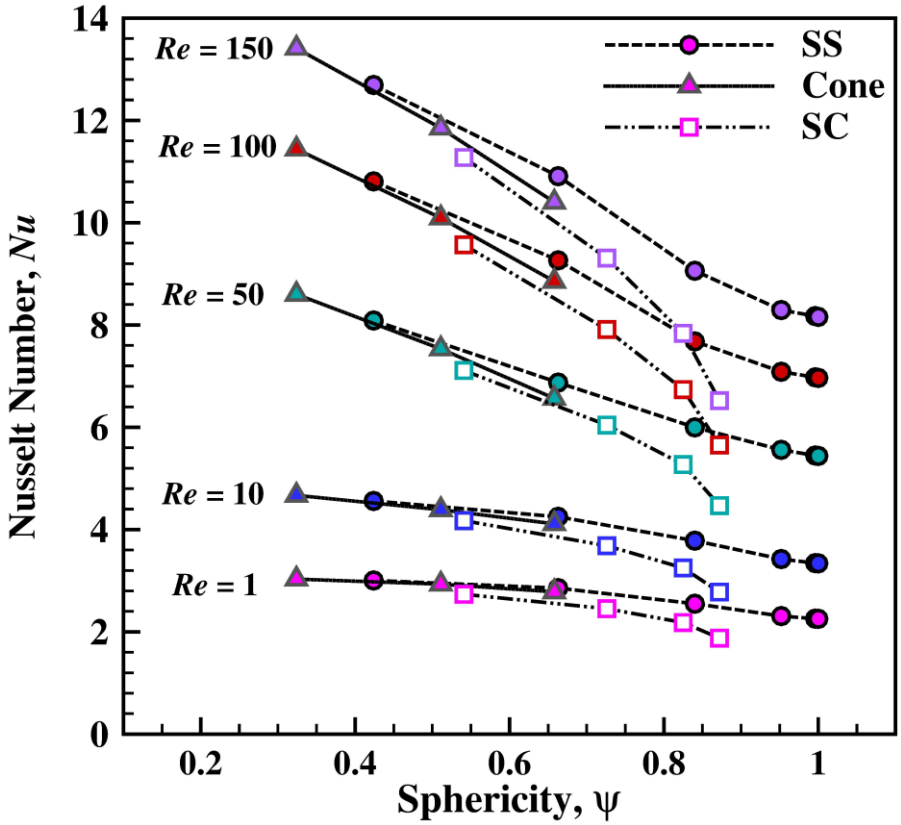


**Figure 4.17** Variation of Nusselt number as a function of sphericity and Reynolds number.

of the shape of the particle. It is observed that at $Re = 150$, the value of the average Nusselt number for $\alpha = 30^0$ is ~ 3 times higher than the particles with $\alpha > 120^0$. The average Nusselt number for different shapes has been shown in **Fig. 4.17** as a function of the shape factor, $\psi$. It again reveals that similar to drag coefficient curves, the cone, and spherical segments show the continuity of the variation of $Nu$ over the range of $\psi$ irrespective of the shape of the particles. However, the average Nusselt number of short cylinders deviates reasonably from cone and spherical segments over the range of $\psi$. In summary, for the average Nusselt numbers of the particles varying in shape, it is essential to introduce additional shape descriptor that will aid to establish a more accurate correlation.

Over the range of the shape factor ($0.324 \leq \psi \leq 1$) and Reynolds number ($1 \leq Re \leq 150$) the average Nusselt number has been correlated by employing two shape descriptors $\psi$ and ($d_c/h_c$) as follows:

$$Nu = A + BRe^{0.516} Pr^{1/3} \psi^{-0.460} \left( \frac{d_c}{h_c} \right)^{0.104} \tag{4.7}$$

Where, $A$ = 1.870 and B = 0.499 (**Fig. 4.18**). **Equation (4.7)** correlates a total of 169 data points with the average and maximum deviations of 6.5% and 27%, respectively. **Figure 4.18** includes the present numerical results compared with the results available in the literature for the intermediate values of $\psi$ =

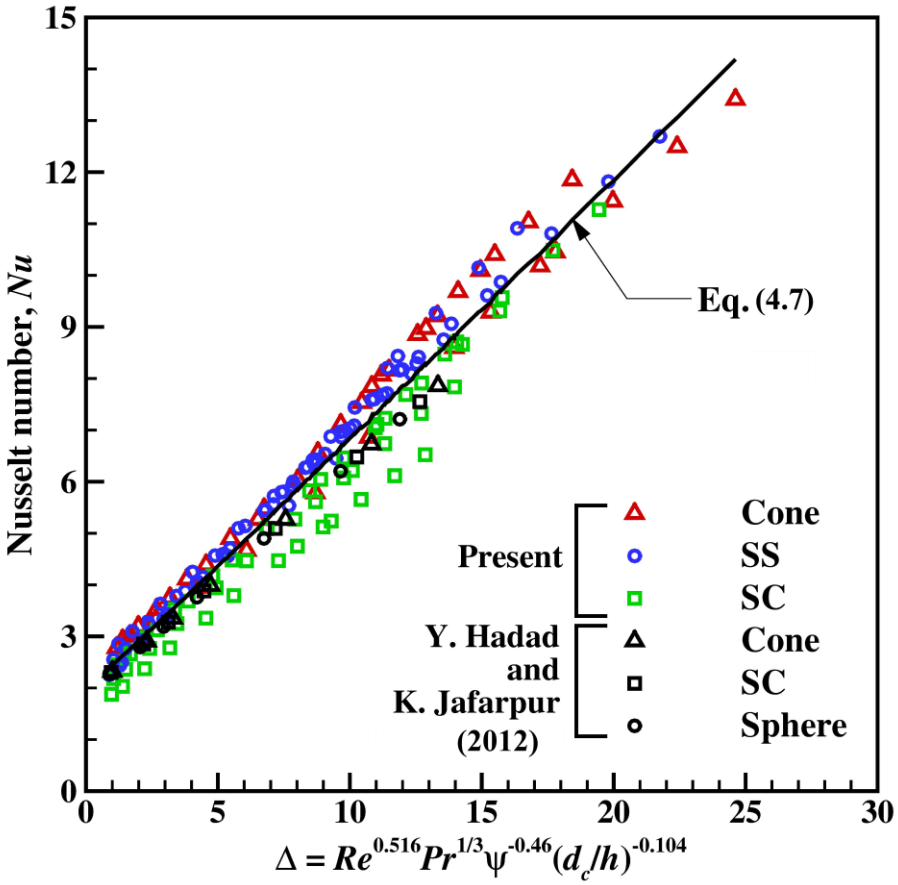


**Figure 4.18** Comparison of the present results of the average Nusselt number with the published results.

0.779 and 0.874 for the cone and short cylinder, respectively, along with the sphere. The good overlapping of the data sets inspires confidence in the newly proposed correlation. Moreover, for a sphere ($\psi = 1$, $d_c/h_c = 1$) above equation reduces to the form, i.e., $Nu = 1.87 + 0.499 Re^{0.516} Pr^{1/3}$ that is consistent with the proposed correlation for air by Ranz and Marshall (1952) and Thorpe and Mason (1971) from experimental results. It is worth mentioning here that the widely accepted correlation for a sphere over the range of Reynolds and Prandtl numbers consists of $A = 2$ which denotes the Nusselt number for pure conduction Whitaker (1972) in the limit of $Re \to 0$. The present numerical results of the average Nusselt number for a spherical particle are found to be well with a maximum deviation of 8% from Whitaker (1972) while with Feng and Michaelides (2000) it raised to a maximum of 15%.

Before leaving this section, it is worth noting here that the flow remains steady for all particle shapes over the range of Reynolds number considered in this study. The only shape $SC^{30}$ ($\psi = 0.541$) shows transition of flow from steady axisymmetric to steady asymmetric at $Re' \sim 135$ and that becomes periodic for $Re' \sim \geq 155$ as observed by Shenoy and Kleinstreuer (2008). Hence, the results for $SC^{30}$ ($\psi = 0.541$) using a steady solver are probably less reliable for Reynolds number range $135 \leq Re \leq 150$. This work assumes a fixed orientation of the particles in the applications involving free-falling particles, where the orientation may change and/or the particle may undergo mixed motion involving rotation and translation. Clearly, in this case, three-dimensional time-dependent simulations are required which tend to be computationally intensive. It is, therefore, believed that the results presented here can serve at least a first-order approximation to estimate the values of drag and Nusselt number in a new application.

## 4.2 Flow past a non-spherical particle in confined Newtonian media

### 4.2.1 Previous work

A comprehensive review of the literature on regular shaped particles such as spheres, cylinders (circular, square, semi-circular, etc.), and non-spherical with axisymmetry in an unconfined Newtonian fluid is presented in **section 4.1**. The momentum and thermal boundary layers in a steady flow of fluid past such geometries are greatly influenced by the shape of the particles, confinement, presence or absence of buoyancy force, orientation, etc. Non-spherical particles are frequently encountered in various processes, such as the processing of food particles, mining, paper, coal, pharmaceuticals, cosmetics, and fine chemicals, to name a few. In literature, the knowledge about non-spherical particles in various applications is still not as well established, even in the unconfined domain, let alone confined flow. Due to the frequent occurrence of non-spherical shapes in various applications, non-spherical particles remain an intriguing subject for researchers to study and interpret the effect of shape on drag and heat transfer coefficients in more efficient ways. There are numerous descriptors reported in the literature to characterize the deviation in shape of the non-spherical particles from a sphere, e.g., sphericity, volume equivalent or surface area equivalent to sphere. In literature Pettyjohn and Christiansen, 1948 and Haider and Levenspiel, 1989 have attempted correlations for the drag coefficient for non-spherical particles in

an unconfined domain having negligible wall effect, using sphericity as a standard shape descriptor. Although, in many practical applications, like pneumatic conveying, drying fluidization, etc. the concept of an infinite wall is unrealistic. These applications always follow some finite boundaries that confines the flow and that causes extra retardation on particles that instigate more drag. Uhlherr and Chhabra (1995) studied the effect of the wall factor on the Reynolds number. In their experimental study, they have reported that the effect of wall factor on Reynolds number has been significant for $0.5 \sim> Re <\sim 1000$. Beyond this range, the Reynolds number shows dependence on the sphere-to-tube diameter ratio. Further, Wham *et al*. (1996) proposed two correlations for the falling sphere in the cylindrical domain as a function of confinement ratio, i.e., ratio of diameter of sphere to that of the tube ($0.08 \leq \lambda \leq 0.70$). The study suggested that increasing confinement suppresses the wake formation and decreases the wake length.

On the other hand, Shahcheraghi and Dwyer (1998) studied hydrodynamics and heat transfer characteristics for a sphere in laminar Newtonian flow for eccentric position of sphere in the tube. The three-dimensional flow has been studied numerically to explore the effect of Reynolds number ($Re$ = 25, 125) and confinement values ($\lambda$ = 0.2, 0.4) drag, lift and heat transfer coefficients. Furthermore, Maheshwari *et al*. (2006) studied the momentum and heat transfer characteristics around single and three-sphere systems in the Reynolds number range $1 \leq Re \leq 100$ for water and air as a fluid media. Results showed that confinement strongly influences momentum transfer over the heat transfer. Krishnan and Kannan (2010) also found a similar finding for the momentum and heat transfer studied for a heated sphere in a pipe with a fully developed parabolic velocity profile at the inlet. They also suggested that the effect of confinement was more dominating in the case of low to moderate Reynolds numbers. As the confinement ratio increases, the flow becomes more and more stable and requires a high Reynolds number for boundary layer separation.

As discussed previously, various applications in engineering settings like ore drilling, sea mining, fluidization, etc., may not always encounter a perfect spherical shape, in contrast, they may involve other non-spherical shapes, such as disc, spheroid, spherical cap, cone, needle-like, and so on. Chhabra (1995) investigated the effect of confinement on the terminal velocity of the non-spherical particle experimentally and correlated the wall factor with confinement ratio, Reynolds number and shape factor. In literature, some shapes like short cylinder (Unnikrishnan and Chhabra, 1991), needle, cube (Chhabra, 1995), disc (Nitin and Chhabra, 2005), spheroid (Kishore and Gu, 2010) and hollow cylinder (Mohammad and Munshi, 2023) are studied under the wall effect. On the other hand, no prior studies have been reported for the non-spherical shape, i.e., spherical cap. Hence, the present work aims to study the range of the shapes of the spherical cap ($\alpha = 30^\circ, 60^\circ, 90^\circ$) in two different confinement ratios, $\lambda = 0.2$, and 0.5. Furthermore, the results of smallest spherical segment ($\alpha = 30^\circ$) are compared with circular disc and sphere for a fixed confinement ratio (defined as diameter of particle to diameter of the tube) of $\lambda = 0.5$ over a range of Reynolds number, $1 \leq Re \leq 100$ in air to compare and to gain insight into the effect of the shape with axisymmetry in confinement.

### 4.2.2 Problem formulation

In this study, a heated spherical cap (or a circular disc) at temperature, $T_h$ of the base diameter or largest chord length, $d_c$ is located in the cylindrical confinement of diameter $D$ facing the flat side in the downward direction, as shown in **Fig. 4.19**. Being a segment of a spherical shaped particle of diameter $D_s$, a shape of spherical caps considered in this work has a base diameter $d_c$ and corresponding height of the segment, $h_c = 0.5\left[D_s - \sqrt{\left(D_s^2 - d_c^2\right)}\right]$. A total of three segments from a sphere, i.e., $\alpha = 30^o$, $60^o$ and $90^o$ are considered for this work for two confinement ratios, $\lambda = d_c/D = 0.2$, and 0.5 and the results are compared with the case of unconfined flow from **section 4.1**. In the case of circular disc located in the fixed value of confinement $\lambda = d_c/D = 0.5$, the diameter and height are chosen to be identical to $d_c$ and $h$ of the spherical cap of $\alpha = 30°$. The flow of air ($Pr = 0.72$) is moving upward in the $z$-direction with a constant velocity of $U$ and temperature, $T_c$ ($T_c < T_h$). Intuitively, the wall confinement imparts stability to the flow, it defers the flow separation to the higher Reynolds number. Hence, the assumption of flow to be steady over the range of the Reynolds number, $1 \leq Re \leq 100$ is rational for this this study (Sagar *et al.*, 2017). The thermo-physical properties of the air (density, $\rho$; specific heat, $C$; viscosity, $\mu$ and thermal conductivity, $k$) are assumed to be constant. The effect of viscous dissipation is assumed to be negligible over the range of parameters. The scaling parameters employed to render the aforementioned **Eqs. (2.1) – (2.3)** in non-dimensional forms are $U, \rho U^2$, and $(T - T_c)/(T_h - T_c)$ for velocity, pressure, and temperature,

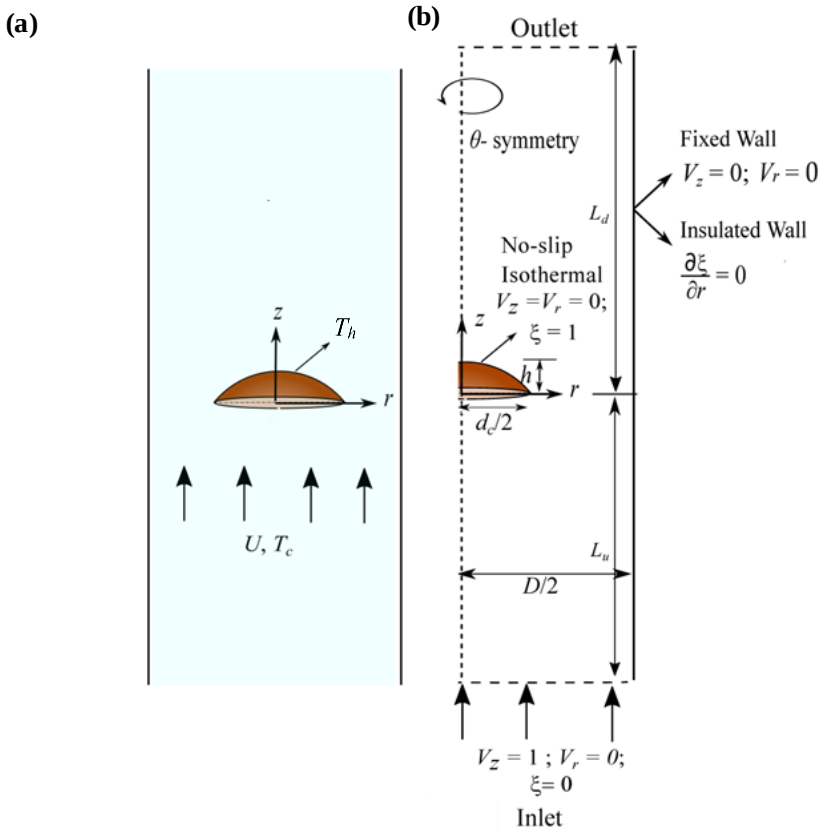


**Figure 4.19** Schematics of the problem statement (a) Physical domain (b) Computational domain.

respectively. To circumvent the complexity of shapes in practical application, the dimensions of the non-spherical particles are presented in terms of equivalent spherical diameter $d_{eq}$ $\left(=\sqrt[3]{6V_p/\pi}\right)$ which are used as a length scale here. This choice leads to Reynolds number being defined as, $Re=\frac{\rho U d_{eq}}{\mu}$. The Prandtl number, $Pr=\frac{\mu C}{k}$ evolves as an intrinsic property of fluids in this study for air, $Pr = 0.7$ has been used. In addition to these, sphericity ($\psi$) is employed as a geometric parameter to quantify the effect of shape of the particle on drag over the range of conditions as **Eqs. (4.1)** and (**4.2)**.

For axisymmetric flow assumed over the range of conditioned spanned in this problem, the physical realistic boundary conditions in the nondimensional form are given as:

At the surface of the particle: $V_z = V_r = 0$ and $\xi = 1$

At the inlet boundary: $V_z = 1$ $V_r = 0$ and $\xi = 0$

At the pipe wall: $V_z = V_r = 0$ and $\partial\xi/\partial r = 0$

At the outlet (Neumann boundary condition): $\frac{\partial \zeta}{\partial z} = 0$ where $\zeta = V_z$, $V_r$, and $\xi$; $p = 0$

At the axisymmetric axis: $V_r = 0$, $\partial V_z/\partial r = 0$, $\partial\xi/\partial r = 0$

The solution of **Eqs. (2.1) - (2.3)** yields the pressure ($p$), velocity ($V_r$, $V_z$), and temperature ($\xi$) fields which are further post-processed to analyze in terms of streamlines, pressure coefficient, total drag coefficient, and local and average Nusselt numbers as discussed in **section 2.3**.

### 4.2.3 Choice of numerical parameter and validation

Flow around a spherical cap (or a circular disc) is solved using the finite element-based commercial software COMSOL Multiphysics (Version 5.3a). The PARDISO scheme is used in order to solve the set of continuity, momentum, and energy equations for air. The accuracy and reliability of the chosen numerical scheme purely depend on the choice of numerical parameters, domain size, and grid. The domain independent test has been conducted by varying the domain length in the upstream and downstream directions at $Re = 1$ and $Pr = 0.72$. The results of the pressure and total drag coefficients and average Nusselt number ensure that the length of $20d_c$ and $40d_c$ in the upstream and downstream, respectively are not changing the results significantly (<0.5%) on further increase in the domain size. Furthermore, the chosen domain size is found to be in lined with that of considered by Nitin and Chhabra (2005) for their numerical study of circular disc in confinement to study hydrodynamics and thermal behavior for forced convection phenomena. In a similar manner, the grid independence test is carried

**Table 4.6** Grid Independence test at $Re$ = 100 and $Pr$ = 0.72 for spherical cap.

| Grid | $N_P$ | $N_T$ | $C_D$ | $C_{DP}$ | $Nu$ |
|---|---|---|---|---|---|
| G1 | 170 | 38039 | 5.18 | 5.22 | 6.50 |
| G2 | 475 | 99256 | 5.20 | 5.27 | 6.47 |
| G3 | 630 | 180293 | 5.23 | 5.30 | 6.48 |

$N_p$ = Number of elements on the particle surface in the computational domain

$N_T$ = Number of elements in the computational domain

**Table 4.7** Validation of Drag coefficient for a sphere with moving wall at $\lambda$ = 0.5.

| $Re$ | Present | Song *et al.* (2009) | Thumati (2016) |
|---|---|---|---|
| 1 | 142.77 | 139.577 | 139.112 |
| 5 | 28.694 | 28.136 | 28.009 |
| 10 | 14.55 | 14.217 | 14.222 |
| 50 | 3.621 | 3.583 | 3.548 |
| 100 | 2.323 | 2.263 | 2.278 |

out at the highest value of $Re$ = 100. The steep and sharp corner of the geometry elevates the difficulty in solving momentum and energy equations due to the singularities at the corners. To capture these steep velocity gradients around the corner and to neutralize the effect of sharp corners, a very fine free triangular grid is constructed in the vicinity of the geometry walls while far away from the geometry mapped grid is generated. Three different grids G1, G2 and G3 are formed for spherical cap (circular disc), and their effect is observed on the average drag coefficient and Nusselt number (**Table 4.6**) and local profiles of Nusselt number and pressure coefficient shown in **Fig. 4.20**. As we move from G1 to G2 and G2 to G3 there is no significant difference observed in the average value in **Table 4.6**. However, the local profiles

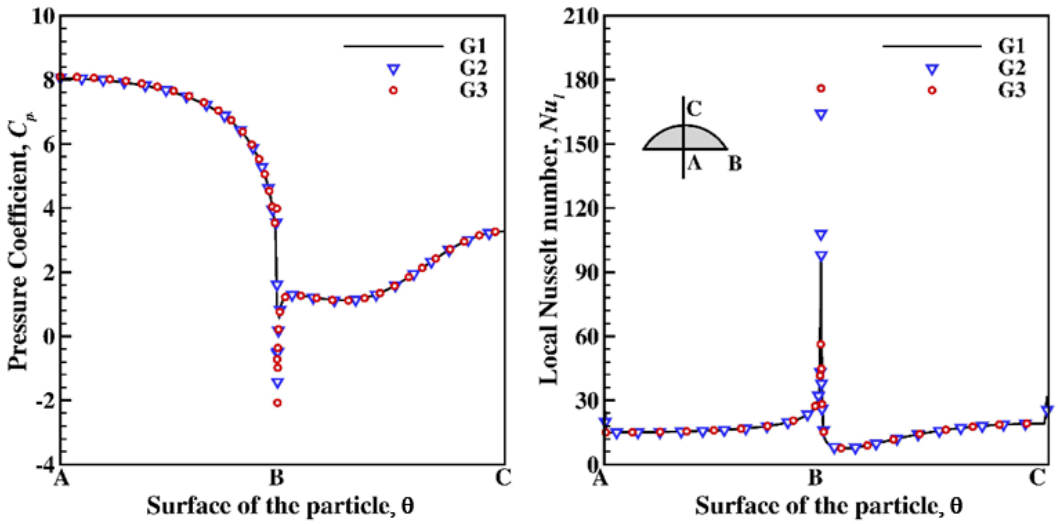


**Figure 4.20** Grid independence test at $Re$ = 100 and $Pr$ = 0.72.

of the pressure coefficient and Nusselt number over the particle surface show that G1 is not sufficient to capture the local variation while G2 and G3 trends are close enough as shown in **Fig. 4.20**. This justifies our chosen grid G2 having 475 elements on the surface and a total of 99256 elements in the computational domain are sufficient to capture the steepest gradient in the case of spherical cap as well as circular disc. The convergence criterion of $10^{-5}$ was set for both momentum and energy equations.

The reliability of the chosen numerical technique and level of accuracy of new results is ascertained by comparing the present results with the available results for the limiting cases. As mentioned previously, sphere is the most extensively studied geometry in the past and the cap is considered as a small dissecting portion of the sphere. Hence, the drag values for a sphere at $\lambda = 0.5$ have been compared with Song *et al.* (2009) and Thumati (2016) in **Table 4.7**. Furthermore, **Table 4.8** exhibits the comparison between the average Nusselt number of a sphere in Poiseuille flow in the confinement of $\lambda = 0.5$ with Song *et al.* (2012) at $Re$ = 10 and 100 over a range of $Pr$ values. The comparison establishes a good correspondence. In literature, extensive data is available for the circular disc with and without wall effect. Therefore, considering the disc as the closest shape to the spherical cap, benchmark validation for the circular disc has been performed to get more hold on the numerical scheme used in the present study. In

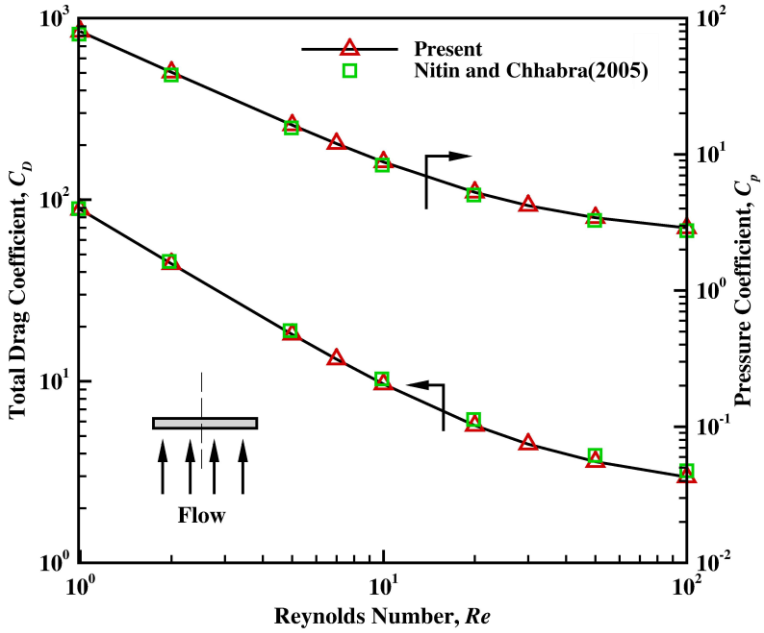


**Figure 4.21** Validation of total drag and pressure drag coefficient with Nitin and Chhabra (2005) or circular disc (moving wall boundary condition).

**Fig. 4.21**, the total drag, and pressure drag coefficient is compared with the circular disc in confinement of $\lambda = 0.5$ with Nitin and Chhabra (2005) providing an excellent match between both results. Furthermore, qualitatively, **Fig. 4.22** compares the azimuthal vorticity and the streamline for the circular disc with Shenoy (2008). That seems to be in good agreement with each other. A good correspondence between the foregoing comparisons establishes confidence in the chosen numerical scheme for the reliability of the new data reported here.

**Table 4.8** Validation of average Nusselt number for sphere in Poiseuille flow at $\lambda = 0.5$.

| *Re* | *Pr* | Song *et al.* (2012) | Present |
|---|---|---|---|
| 100 | 1 | 10.30 | 9.97 |
| 100 | 5 | 17.28 | 16.68 |
| 100 | 10 | 21.77 | 20.86 |
| 100 | 20 | 27.16 | 26.12 |
| 100 | 40 | 34.05 | 32.76 |
| 10 | 1 | 4.69 | 4.64 |
| 10 | 5 | 7.83 | 7.77 |
| 10 | 10 | 9.71 | 9.62 |
| 10 | 20 | 12.05 | 11.94 |
| 10 | 50 | 16.07 | 15.95 |
| 10 | 100 | 20.09 | 19.91 |

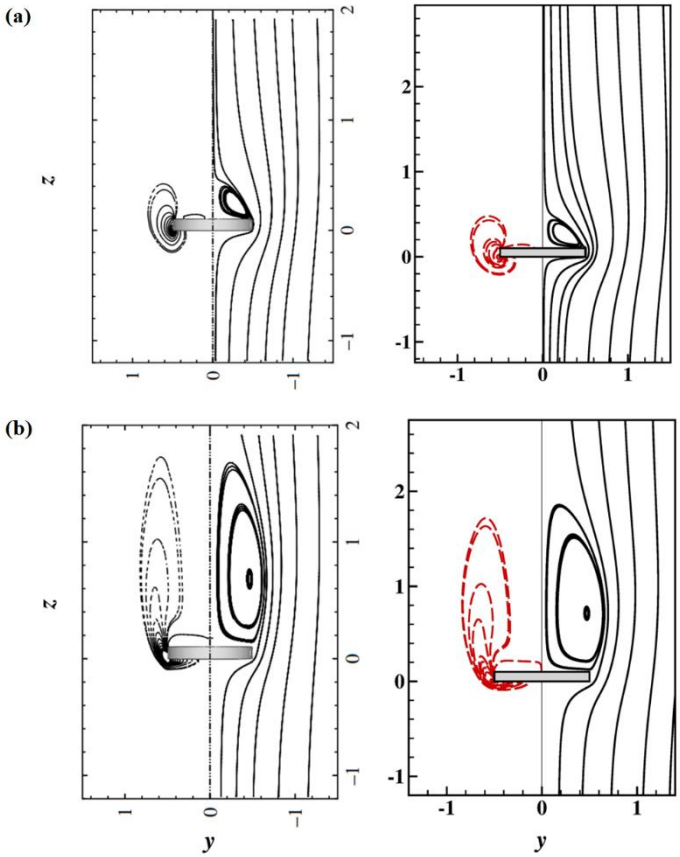


**Figure 4.22** Validation of steady axisymmetric flow with azimuthal vorticity (left half) and streamline (right half) Shenoy *et al.* (2008) (a) *Re* = 10 (b) *Re* = 100.

### 4.2.4 Results and discussion

Present work examines the effect of Reynolds number ($1 \leq Re \leq 100$) on the momentum and heat transfer characteristics of the steady flow of air ($Pr = 0.72$) past a heated spherical cap ($\alpha = 30°, 60°, 90°$) in the

confined tube with λ = 0.2, 0.5. The momentum and heat transfer characteristics have been studied and compared for spherical cap (α = 30°) with disc, and sphere having same projected area under identical conditions to establish a better understanding of the shape effect.

#### 4.2.4.1 Flow kinematics and heat transfer characteristics

The illustration of spatial variation of the velocity and temperature around the particle is customary to understand the effect of increasing Reynolds number. Streamline (left half) and isothermal contours (right half) are plotted for all three shapes α = 30°, 60° and 90° as shown in **Figs. 4.23-4.24** over the range of Reynolds numbers for λ = 0.2 and 0.5. Intuitively, the momentum and heat transfer rates increase significantly with the increase in inertial forces. Moreover, the shape plays a significant role in modulation of momentum and heat transfer rates. The shape of the particle particularly affects the formation of wakes at the rear end of the particle. For a fixed confinement, increase in Reynolds number results in acceleration in the flow which results in the flow separation and the wake formation. However, the increase in

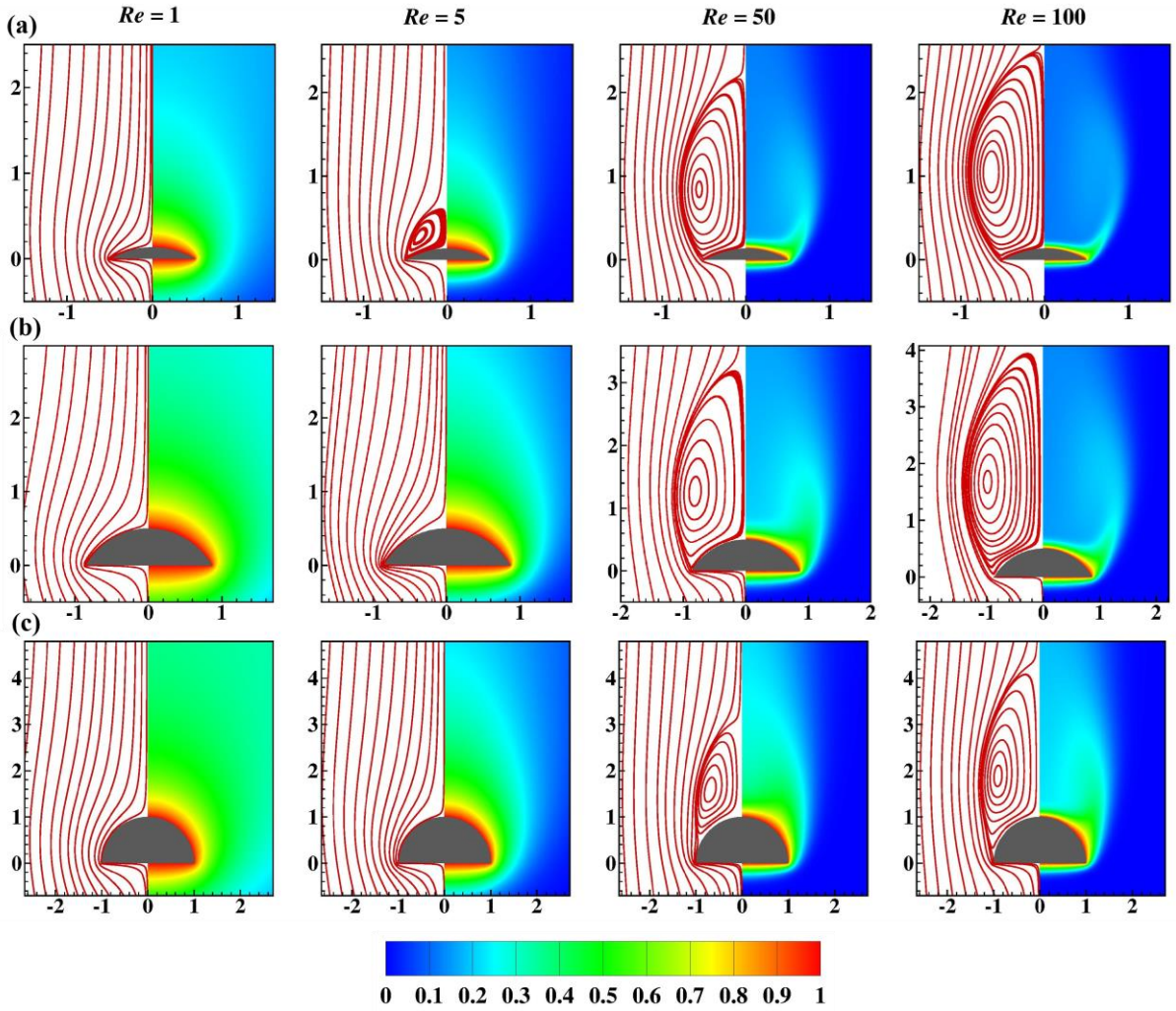


**Figure 4.23** Streamline (left half) and isotherm contour (right half) for spherical caps (a) α = 30°, (b) α = 60° and (c) α = 90° at confinement λ = 0.2.

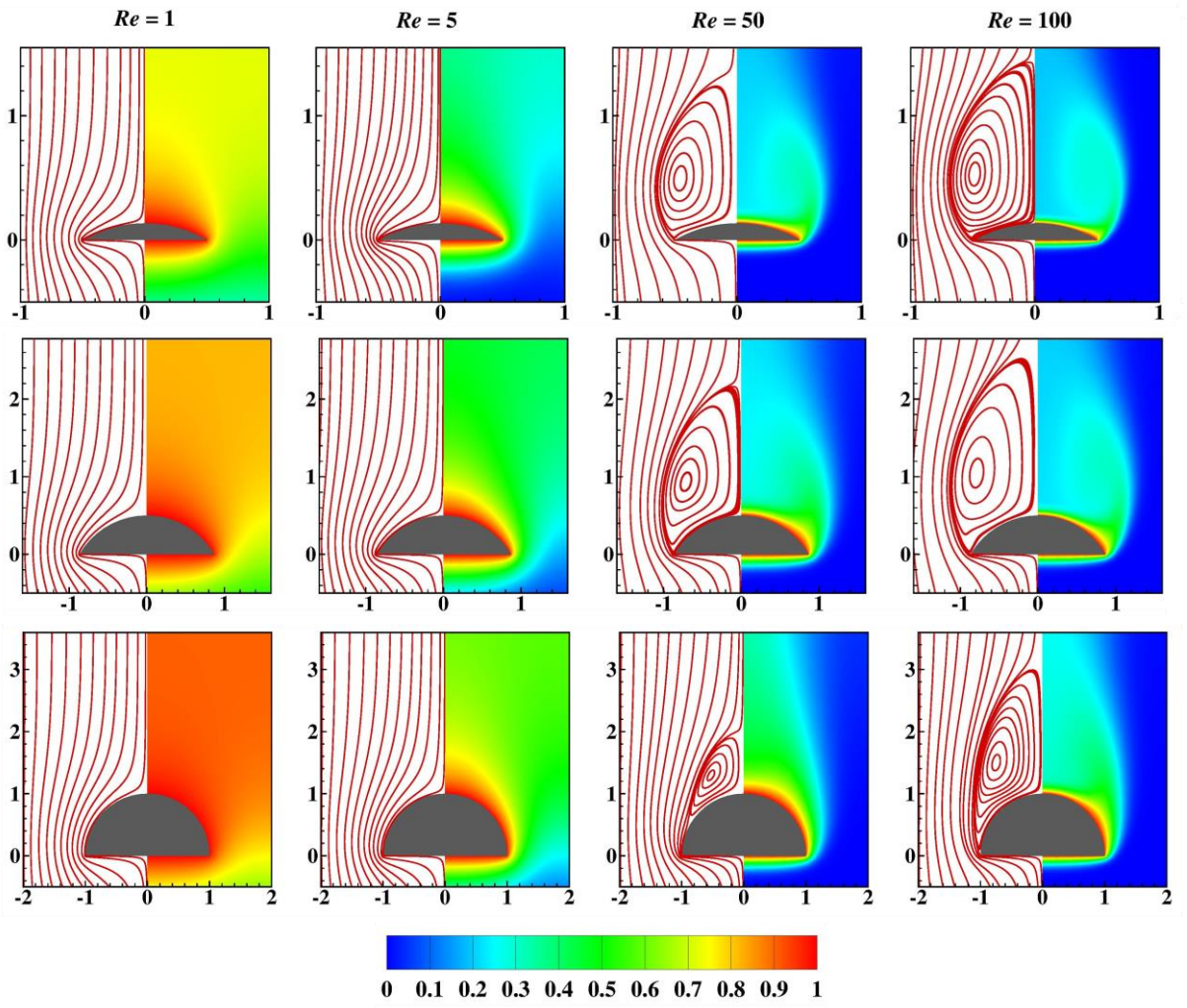


**Figure 4.24** Streamline (left half) and isotherm contour (right half) for spherical caps (a) α = 30°, (b) α = 60° and (c) α = 90° at confinement λ = 0.5.

confinement delays the wake formation due to stabilization in the flow. Thus, for a fixed Reynolds number and particle shape, the length of the wake decreases with the increase in the confinement. It is observed that for λ = 0.2, the wake is observed at *Re* = 5 for α = 30º which disappears with the further increase in confinement to λ = 0.5. **Figure 4.25** represents the velocity profiles at the rear side of the spherical caps for both confinement and at the extreme values of the Reynolds number. The dashed lines and the solid line represent the velocity profile of λ = 0.2 and 0.5, respectively. At low Reynolds numbers, *Re* = 1, the fluid velocity increases from zero to a constant velocity monotonically, which signifies no flow separation for both the confinements. However, as the confinement increases from 0.2 to 0.5 at the low Reynolds number, the velocity profiles for λ = 0.5, irrespective of the particle shape, attain to the constant fluid velocity earlier downstream of the particle as compared to λ = 0.2 due to wall effects that causes flow retardation. Furthermore, the velocity profiles also help to confirm the presence of the wake formation as the velocity magnitude downstream of the particle changes from negative to positive. It is also noticeable that the point of the change of velocity magnitude from negative to positive in the *z*-

direction moves closer to the rear stagnation point of the particle. It clearly suggests that the formation of the wake decreases with the increase in the confinement. Furthermore, the nondimensional distance between the rear stagnation point and the point of the change of the velocity magnitude for the highest Reynolds number, *Re* = 100 shows inverse dependence on shape factor α for both the confinement vales (**Fig. 4.25**).

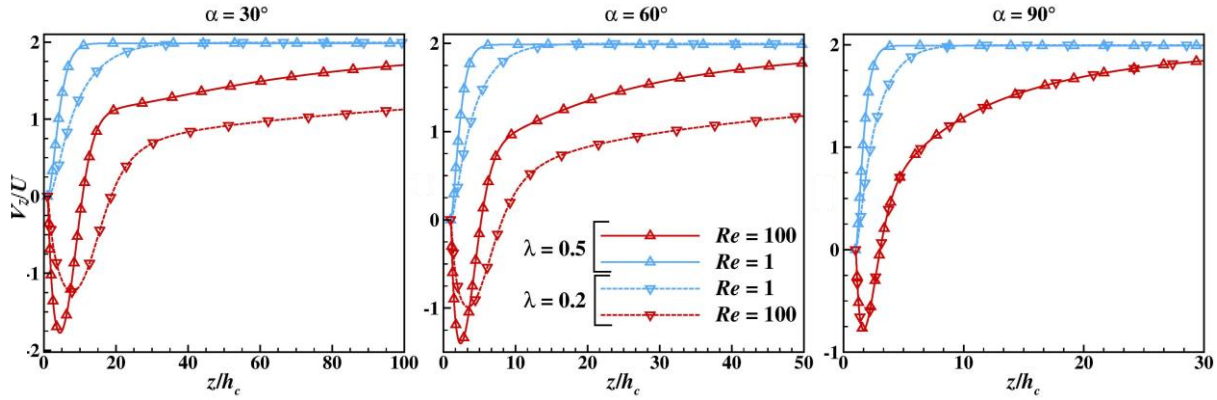


**Figure 4.25** Velocity profiles in the *z*-direction plotted downstream of the particle from the rear stagnation point. for all three shapes of the particle.

Isotherm contours plotted in **Figs. 4.23** and **4.24** help to delineate the variation of the temperature field around the spherical segments and results in indicating the hot and cold spot near the geometry in the confined flow. For a fixed confinement and low Reynolds number, *Re* = 1, heat transfer is mostly dominated by the conduction mechanism irrespective of the shape of the geometry. The convective heat transfer has been observed to be more predominant with the increase in Reynolds number, is manifested by the stretching of the contours in the downstream direction. Also, due to wake formation and thinning of thermal boundary layers, the heat transfer increases with the increase in Reynolds number. Maheshwari *et al*. (2006) reported that the rate of heat transfer increases with the increase in confinement. However, at low Reynolds number (*Re* = 1) and high confinement (λ = 0.5), the thermal boundary layer is observed to be much thicker than that observed for λ = 0.2 (**Fig. 4.24**). It appears that at low Reynolds number the heat transfer is dominated by the conduction mechanism and hence, the shape of the particle and percentage confinement to the flow, these two factors play intricate manner.

### 4.2.4.2 Drag Coefficient

Drag plays a vital role from the engineering point of view while dealing with applications involving particle-fluid interactions. **Figure 4.26** elucidates the relationship between the total and pressure drags experienced and the Reynolds number for α = 30˚, 60˚, 90˚ and λ = 0.2 and 0.5. The results of unconfined flow λ ≈ 0 are also included in the figure from the previous **section 4.1** in order to understand the transition of the global momentum and heat transfer parameters from unconfined to confined flow. The figure clearly depicts that both the drags experienced by the particle has an inverse relation with the Reynolds number. However, the increase in confinement not only increases the drag experience by the spherical

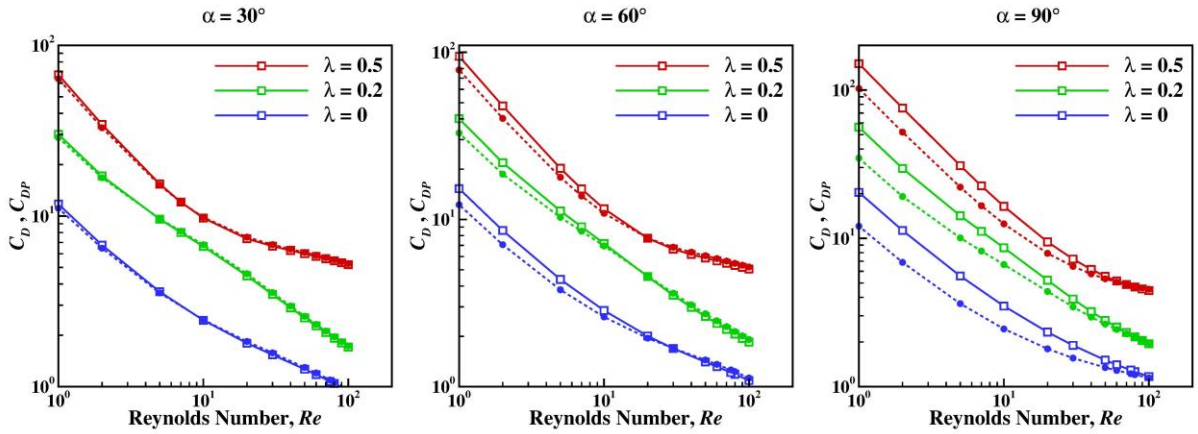


**Figure 4.26** Variation of the drag coefficient (solid line) and pressure drag coefficient (dashed line) over the range of Reynolds number and confinement ratios.

cap but at the same time it compels drag coefficients to drop faster as Reynolds number increases. The total drag experienced by the spherical cap is the resultant of both pressure and frictional forces collectively. The pressure drag coefficient (dotted line) is also plotted in **Fig. 4.26** which shows a similar trend with respect to the Reynolds number over the range of shape factors for both the confinements. The impact of the shape of the particle on the total drag coefficient can also be clearly observed in **Fig. 4.26**. The contribution of the pressure drag to the total drag gradually decreases as α decreases and/or Reynolds number increases irrespective to the flow confinement. At α = 30˚, foam drag dominates the total drag, as shown by the overlapping pressure and total drag coefficients in **Fig. 4.26**. Yet, the pressure drag values does not vary much with the increase in α under otherwise identical conditions. **Figure 4.27** plots the total drag coefficient, $C_D$, as a function of α, for two extreme values of Reynolds number The figure shows that the effect of α and λ on the total drag coefficient is more predominant at low Reynolds numbers.

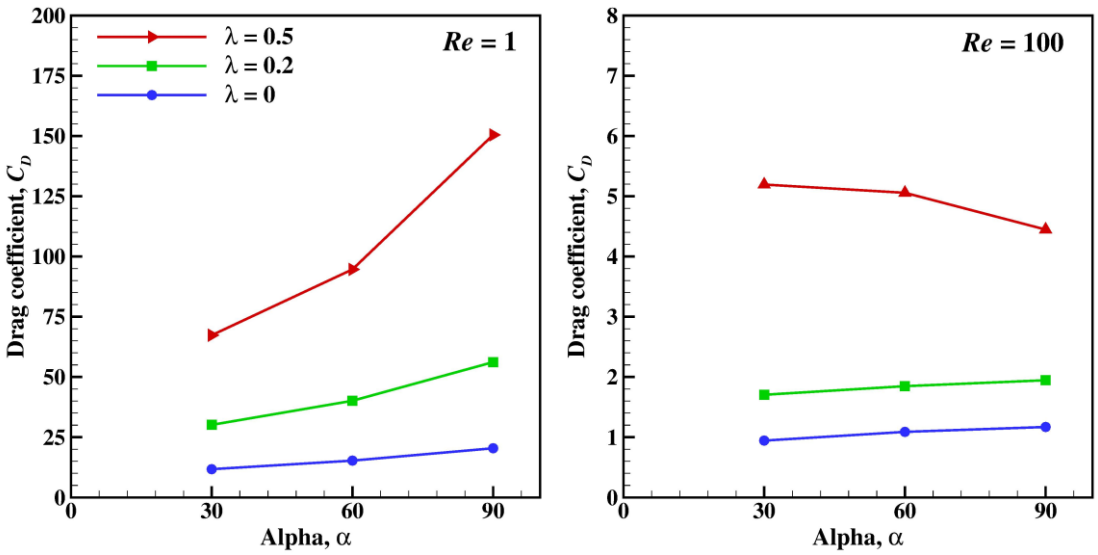


**Figure 4.27** Variation of drag coefficient over the range of shape factor and extreme values of Reynolds number.

The drag coefficient variation over the range of Reynolds number ($1 \leq Re \leq 100$) for spherical caps as a function of Reynolds number and two confinements, $\lambda = 0.2, 0.5$. can be represented as a modified form of Haider and Levenspiel (1989) correlation. The form of this correlation includes the contribution of shapes of the particle as shape factor $\psi$ which is found as a widely accepted shape descriptor for non-spherical particle. Hence, the shape of three particles considered in this work as $\alpha = 30^{\circ}$, $60^{\circ}$, and $90^{\circ}$ are incorporated in the proposed equation as $\psi = 0.424$, 0.663, and 0.84, respectively. The proposed form of the correlation is:

$$C_D = \frac{24}{Re}\left(1 + ARe^{p}\right) + B\left(\frac{Re}{Re + q}\right) \tag{4.8}$$

Where $A = exp\left(a + b\psi + c\psi^2\right)$ and $B = exp\left(d + e\psi + f\psi^2\right)$.

The **Eq. (4.8)** correlates total of 42 data for each value of $\lambda = 0.2$ and 0.5, respectively. The coefficients in the **Eq. (4.8)** for both the confinements over the range of shape factor and Reynolds number are tabulated in **Table 4.9** with their average and maximum percentage deviations from the numerical values of the drag coefficient.

Table 4.9 Coefficients for Eq. (4.8)

| | $a$ | $b$ | $c$ | $d$ | $e$ | $f$ | $p$ | $q$ | $\delta_{avg}$ | $\delta_{max}$ |
|---|---|---|---|---|---|---|---|---|---|---|
| $\lambda = 0.2$ | -3.952 | 5.696 | -1.060 | 0.046 | 2.662 | -3.414 | 0.115 | -0.608 | ~10% | ~ 31.6% |
| $\lambda = 0.5$ | 0.552 | -1.226 | 3.029 | 0.948 | 3.175 | -3.535 | -0.012 | 7.122 | ~1.5% | ~6.6% |

**Equation (4.8)** successfully correlates the drag coefficient for three spherical caps ($\psi$ = 0.424, 0.663, 0.84) at two confinement ratios over the range of Reynolds number range, $1 \leq Re \leq 100$. The maximum error arises in **Eq. (4.8)** is corresponding to the smallest spherical cap ($\alpha$ or $\psi$ = 30°or 0.424).

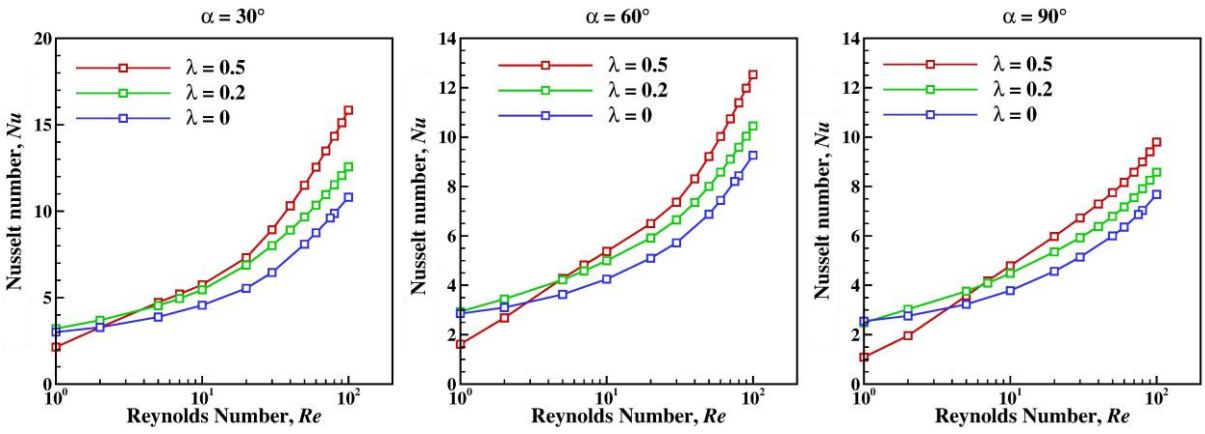


**Figure 4.28** Variation of the average Nusselt number over the range of Reynolds number and confinement ratios.

### 4.2.4.3 Nusselt number

Having prior knowledge of the heat transfer coefficient can be very helpful for process engineering calculations. Here, the heat transfer is only influenced by the change in fluid inertial force for each shape of the spherical cap. For a fixed value of $Pr$ = 0.72, the average Nusselt number is plotted for all three spherical caps over the range of Reynolds number ($1 \leq Re \leq 100$) in **Fig. 4.28** considering confined ($\lambda$ = 0.2 and 0.5) and unconfined flow conditions. It is observed that for low Reynolds number, initially as $\lambda$ increases from 0 to 0.2, heat transfer rates increase. However, it decreases for $\lambda$ = 0.5 due to the intervention between the thermal boundary layer and the proximity of the wall confinement. Furthermore, as Reynolds number increases, the thermal boundary layer thins, resulting in the increase in heat transfer being assisted by confinement. For $\alpha = 30°$, this flip over in the average Nusselt number over the range of Reynolds number occurs at $Re$ = ~5. Similar trends are also observed for the other two spherical caps, however, with the increase in $\alpha$, drop in the heat transfer coefficient for $\lambda$ = 0.5 at low Reynolds number is observed more. Also, the value of Reynolds number where the flip over in the average Nusselt number occurs, delays with increase in the shape factor $\alpha$. In order to get insight into the average Nusselt number variation with the confinement the results are plotted as a function of $\alpha$ as seen in **Fig. 4.29**. The average heat transfer coefficient has marginal variation for $\lambda$ = 0 and 0.2 as compared to $\lambda$ = 0.5 (lowest among three values of $\lambda$) at $Re$ =1 and all three shapes of the particle. While at $Re$ = 100 the trend of average Nusselt number with respect to $\lambda$ is reversed showing reasonable increase in the rate of heat transfer for $\lambda$ = 0.5 as compared to $\lambda$ = 0.2 and 0.

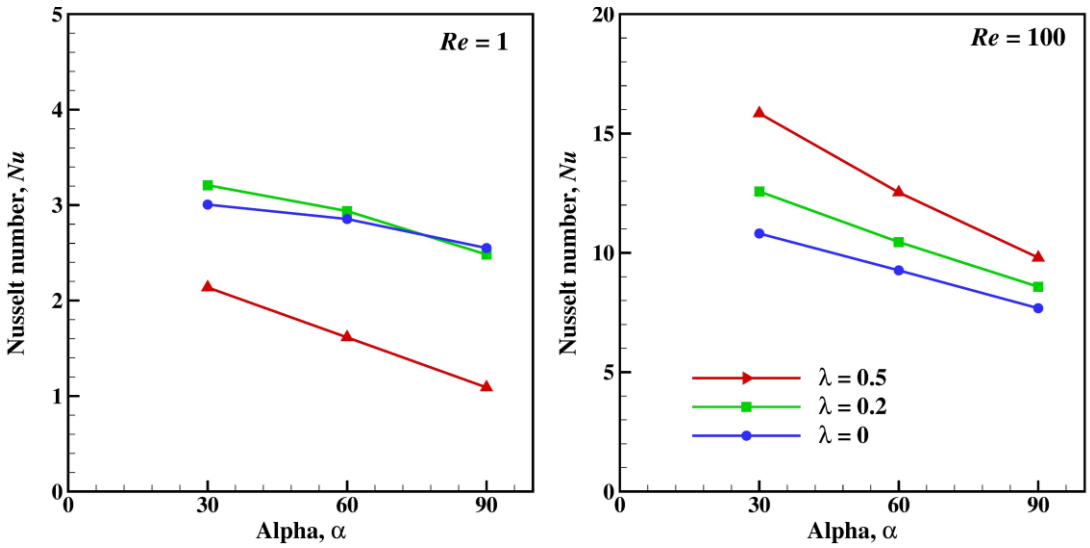


**Figure 4.29** Variation of the average Nusselt number over the range of shape factor and extreme values of Reynolds number.

Over the range of the shape factor ($0.424 \leq \psi \leq 0.84$) and Reynolds number ($1 \leq Re \leq 100$) the average Nusselt number has been correlated for air as a test fluid.:

$$Nu = a + b\left(\frac{\psi}{1+\psi}\right)^{c} Re^{d} \tag{4.9}$$

The **Eq. (4.9)** correlates total of 42 data for each value of confinement, λ = 0.2 and 0.5, respectively. The coefficients for **Eq. (4.9)** are tabulated in **Table 4.10** which includes the average and maximum % error in predicted results of average Nusselt number from the numerical results.

Table 4.10 Coefficients for Equation (4.9).

| | *a* | *b* | *c* | *d* | $\delta_{avg}$ | $\delta_{max}$ |
|---|---|---|---|---|---|---|
| λ = 0.2 | 1.980 | 0.382 | -0.988 | 0.463 | ~3% | ~ 13% |
| λ = 0.5 | -0.629 | 0.956 | -0.872 | 0.381 | ~7.3% | ~22.7% |

#### 4.2.4.4 Comparison of spherical cap with the corresponding shape of the circular disc

The effect of confined shape on the momentum and heat transfer characteristics in steady flow of air has been further explored by comparing the spherical cap with the circular disc having identical height and base diameter. For that spherical cap, α = 30° in the confinement, λ = 0.5 has been chosen from the previous discussion. Finally, the limiting case of the spherical cap, i.e., sphere having identical projected area has been included to broaden the scope of comparison of results. **Figure 4.30** compares the flow kinematics and isotherms of spherical cap with the circular disc. It illustrates that the curvature of the spherical cap delays the formation of wake to the high value of the Reynolds number than the circular disc. It is clearly seen that for a fixed confinement, wake is absent in case of spherical cap at *Re* = 5, while for circular disc the flow separation occurs due to the flat surface in the rear end of the circular disc where the fluid is not able to follow the body contour even with low inertial force. At high Reynolds number no such difference has been identified for two different shapes under identical conditions. The isotherms for both the shapes are also in close correspondence to each other.

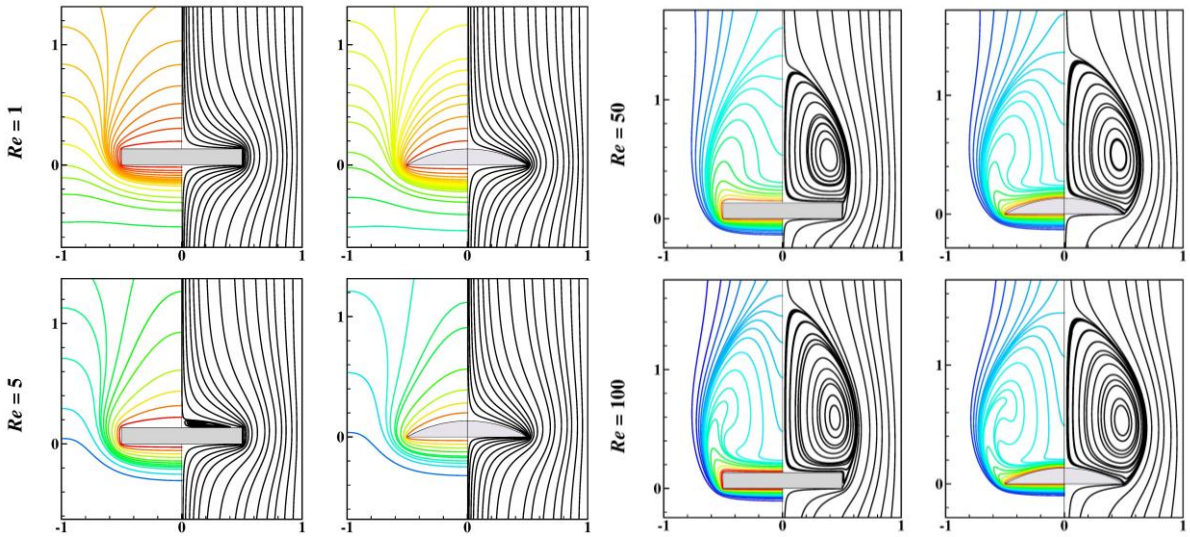


**Figure 4.30** Representation of isotherm (left) and Streamline (right) for circular disc and spherical cap (α = 30°) in a fixed confinement of λ = 0.5.

**Figure 4.31(a)** illustrates the relationship between the total drag of the particle and the Reynolds number. Interestingly, the spherical cap has experienced a higher drag than other geometries at high inertial flow. Despite having an identical projected area for the disc, sphere, and cap, at the low Reynolds number values, spherical cap experiences the lowest drag followed by disc. As the Reynolds number increases, the falling trend of the drag coefficient of spherical cap and disc flipped over at $Re \sim 30$. The drag coefficient for the sphere for $Re > 30$ continues to decrease. In **Fig. 4.31(b)** plots the ratio of drag experienced by particle to that of sphere with the identical projected area is plotted. It shows that the spherical cap experienced approx. ~1.4 times more drag than sphere at $Re = 100$. The three different shapes are defined with the sphericity as sphere, $\psi = 1$, circular disc $\psi = 0.541$, and spherical cap $\psi = 0.424$ for a confinement of $\lambda = 0.5$ are also correlated using the **Eq. (4.8)** as follows:

$$C_D = \frac{24}{Re}\left(1 + ARe^{-0.012}\right) + B\left(\frac{Re}{Re + 5.824}\right) \tag{4.10}$$

Where $A = exp\left(-2.792 + 10.153\psi - 5.169\psi^2\right)$ and $B = exp\left(2.928 - 3.548\psi + 1.127\psi^2\right)$.

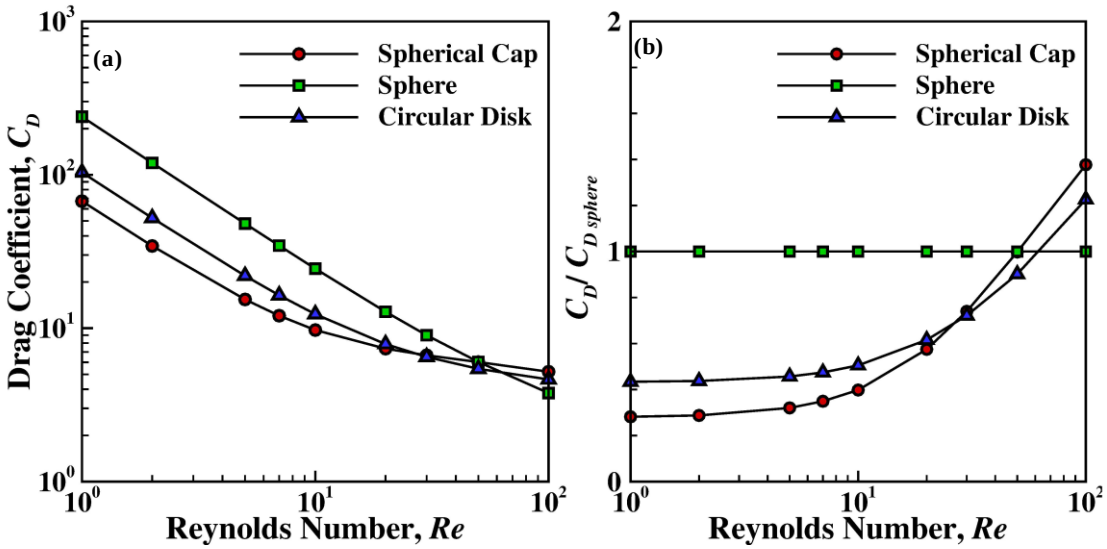


**Figure 4.31** Dependence of drag coefficient with the Reynolds number for axisymmetric bodies having similar projected area and a fixed confinement of $\lambda = 0.5$.

**Equation (4.10)** correlated the total data of 42 for each of the three shapes with an average error of ~1.1% and a maximum error of ~5.2%. The reliability of the proposed correlation is compared in **Table 4.11** with the literature data available for sphere (Song *et al.*, 2011) in the same confinement and it shows a good correspondence with less than ~1% error.

In addition to this case of similar projected area, if we also collaborate the data of other spherical caps ($\alpha = 60°$ and 90°) for a fixed confinement of $\lambda = 0.5$. The **Eq. (4.8)** can predict the drag coefficient of these spherical caps at high Reynolds number range ($30 \leq Re \leq 100$) with the maximum error of ~21%. However, for low Reynolds numbers this error can rise to ~60%. The previously reported simple **Eq.**

Table 4.11 Comparison of drag coefficient of sphere at λ = 0.5.

| *Re* | Present | Song *et al.* (2011) | Equation (4.8) |
|---|---|---|---|
| 1 | 238.86 | 236.94 | 239.12 |
| 5 | 48.09 | 48.19 | 47.72 |
| 10 | 24.44 | 24.17 | 24.35 |
| 50 | 6.03 | 6.08 | 6.07 |
| 100 | 3.78 | 3.82 | 3.84 |

**(4.4)** for the axisymmetric shapes in unconfined domain is also able to correlate all the shapes (three spherical caps, disc and sphere) for a confinement λ = 0.5 by just varying the coefficients.

$$C_D = 3.652 + \frac{224.2}{Re^{1.057}}\psi^{1.529} \tag{4.11}$$

The above coefficients for the **Eq. (4.11)** are proposed using 70 data points, whose sphericity range is $0.422 \leq \psi \leq 1$, with the average error of ~14% and maximum error of ~42%. There are only 6 data points whose errors are more than ~ 25%.

Next, Nusselt number for three geometries (sphere, circular disc, and spherical cap, α = 30°) over the range of Reynolds number ($1 \leq Re \leq 100$) are shown in **Fig. 4.32(a)**. Heat transfer is maximum for spherical cap than the other two considered shapes. At *Re* = 1, the heat transfer for spherical cap is almost ~3 times more than the sphere of having same projected area. This comparison of the average Nusselt number of the circular disc and spherical cap to the sphere is represented in **Fig. 4.32(b)**. The present numerical data for average Nusselt number have been correlated for three shapes by using the previous

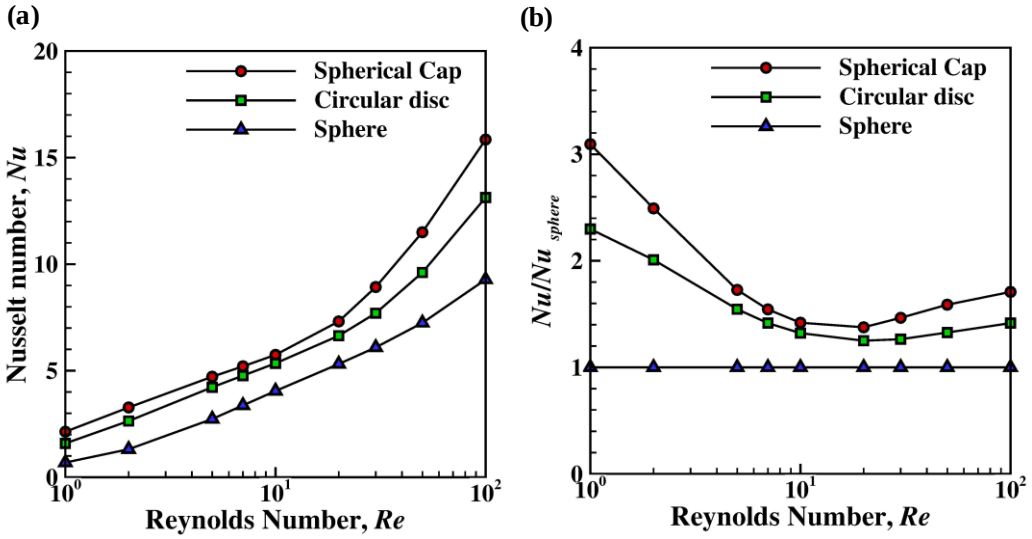


**Figure 4.32** Dependence of average Nusselt number with the Reynolds number for axisymmetric bodies having similar projected area and a fixed confinement of $\lambda$ = 0.5.

**Eq. (4.9)** and with the same coefficient of the spherical caps as mentioned in **Table 4.10** for $\lambda = 0.5$. Aforementioned **Eq. (4.9)** relates the sphericity and Reynolds number with the deviations of average ~6.0% and maximum ~62.3% over the range of Reynolds number ($1 \leq Re \leq 100$) for sphere, $\psi = 1$, circular disc $\psi = 0.541$, and spherical cap $\psi = 0.424$. The exclusion of the data of sphere for $Re \leq 2$ reduces the maximum error to ~11.6%.

## 4.3 Flow past non-spherical shapes in Bingham plastic fluid

This present study focuses on the momentum and heat transfer characteristics of the heated spherical segments in yield stress fluid whose range varies from pure Newtonian ($Bn = 0$) to high Bingham plastic fluid ($Bn = 100$) under forced convection regime. The wide range of Reynolds number ($0.1 \leq Re_B \leq 150$) and Prandtl number ($0.1 \leq Pr_B \leq 100$) are studied on the formation on the yielded/unyielded regions and variation of local (streamlines, velocity contours and profiles) and global parameters (drag coefficient, Nusselt number).

### 4.3.1 Previous work

In the previous **section 4.1** and **4.2**, we briefly reviewed the spherical and non-spherical shapes in the unconfined and confined Newtonian fluid. However, in industries as well as in natural processes, the various encountered fluids have viscoplastic nature (Hill and Shook, 1998; Chhabra and Richardson, 2008; Balmforth et al., 2014; Chhabra and Patel, 2023). In particulate flows and single particle studies, external flow past various spherical and non-spherical shapes always arises curious studies in the literature. Especially in the case of Bingham plastic flow where dual nature of fluid can be seen, these studies widely focus on the development of the yielded/unyielded regions around the particle and their influence on the drag, wake phenomena and heat transfer rates. In consideration of all different shapes, spheres and cylinders are one of the most studied particles due to its symmetry. Nirmalkar *et al*. (2013a, 2013b) have extensive studied the momentum and heat transfer studies for a sphere in unconfined Bingham and Herschel-Bulkley fluid under the wide range of Reynolds number ($1 \leq Re_B \leq 100$), Prandtl number ($1 \leq Pr_B \leq 100$) and Bingham number ($0 \leq Bn \leq 10^4$ in case of Bingham plastic fluid or $10^{-3} \leq Re_B \leq 10$ for Herschel-Bulkley fluid) numerically. The reported work strengthens the idea of delay in the wake formation under high yield stress of fluid, hence stabilizing the flow. On the other hand, the heat transfer shows the positive dependency on the Bingham number over the fixed values of Reynolds and Prandtl number. Similar studies are also found for the circular (Mitsoulis, 2004; Zisis and Mitsoulis, 2002; Roquet and Saramito, 2003; Tokpavi *et al*., 2008; Mossaz *et al*., 2010, 2012; Deglo de Besses *et al*., 2003; Nirmalkar and Chhabra, 2014; Sairamu *et al*., 2013) and non-circular cylinders (Nirmalkar *et al*., 2012; Patel and Chhabra, 2013; Bose *et al*., 2014; Tiwari and Chhabra, 2015). The increase in Reynold number and decrease in Bingham number yield more fluid-like behavior which furthermore also modulated by the shape of the body. On the other hand, the increase in yield stress shrinks these fluid-like regions and as a result the sharp gradients are observed near the surface of the object due to which increase in heat transfer rates are observed in such studies.

Subsequent, regular non-spherical particles having axisymmetric symmetry like disc, spheroid, cone and plate in the viscoplastic fluid also got some attention in the previous decade. Extensively, the researchers have studied the axisymmetric shapes like disc (Gupta *et al*., 2017), spheroid (Gupta and Chhabra, 2014) and cone (Sharma and Chhabra, 1991; Ahonguio *et al*., 2015; Mishra *et al*., 2019) are also studied under the effect of viscoplastic fluid. There is not much literature available for spherical segments but considering the hemisphere (Nalluri *et al*., 2015; Patel *et al*., 2015) is one of the spherical segments, had received much consideration to date in yield stress fluid for different orientation and thermal boundary conditions. The flat surface in the hemisphere leads to separate the fluid earlier in comparison to the sphere (Nalluri *et al*., 2015). In their work, Patel *et al*. (2015) found that the heat transfer rate is more prominent in case of inverted configuration of hemisphere and similarly constant heat flux thermal boundary yields more efficient results. They have further consolidated their numerical results by introducing the Colburn heat transfer *j*-factor and the modified definitions of the Reynolds and Prandtl numbers.

Hence, considering the pertinent literature, and as far as our knowledge spherical segments have received scant to very less engagement till date. The present work aimed to explore the effect of Bingham plastic fluid in case of spherical segments ($30° \leq \alpha \leq 180°$) over the wide range of parameters: Reynolds number ($0.1 \leq Re_B \leq 150$), Prandtl number ($0.1 \leq Pr_B \leq 100$) and Bingham number ($0 \leq Bn \leq 100$).

### 4.3.2 Problem formulation

In this present work the steady, two-dimensional and incompressible flow of a Bingham plastic fluid with the uniform velocity $U$ and temperature $T_c$ past heated spherical segment at temperature $T_h$ ($>T_c$) is studied as shown in **Fig. 4.33**. Five different spherical segments (as shown in **Fig. 4.1**) are considered in this work as previously discussed in **section 4.1.2**. It is also considered that, all the thermophysical properties of the Bingham plastic fluid (specific heat $C$, density $\rho$, thermal conductivity $k$, plastic viscosity $\mu_B$, yield stress $\tau_o$) are assumed to be constant. Over the range of chosen temperature difference, the ratio of the viscous dissipation to the conduction term in the energy equation is very small and thus it justified to neglect the viscous dissipation term in the energy equation. Furthermore, in order to circumvent the dual nature of the Bingham plastic fluid, Papanastasiou model is used primarily. However, some results of yielded/unyielded region obtained by Papanastasiou model are also compared with other regularization models in order to check the reliability of the chosen model.

In order to solve the governing equation in the considered domain, the following boundary conditions have been used in the present work:

At the inlet: $V_z = 1$; $V_r = 0$, and $\xi = 0$

At the surface of the spherical segment: $V_z = V_r = 0$; and $\xi = 1$

At the hypothetical cylindrical domain wall: $V_z = 1$ $V_r = 0$ and $\partial\xi/\partial r = 0$

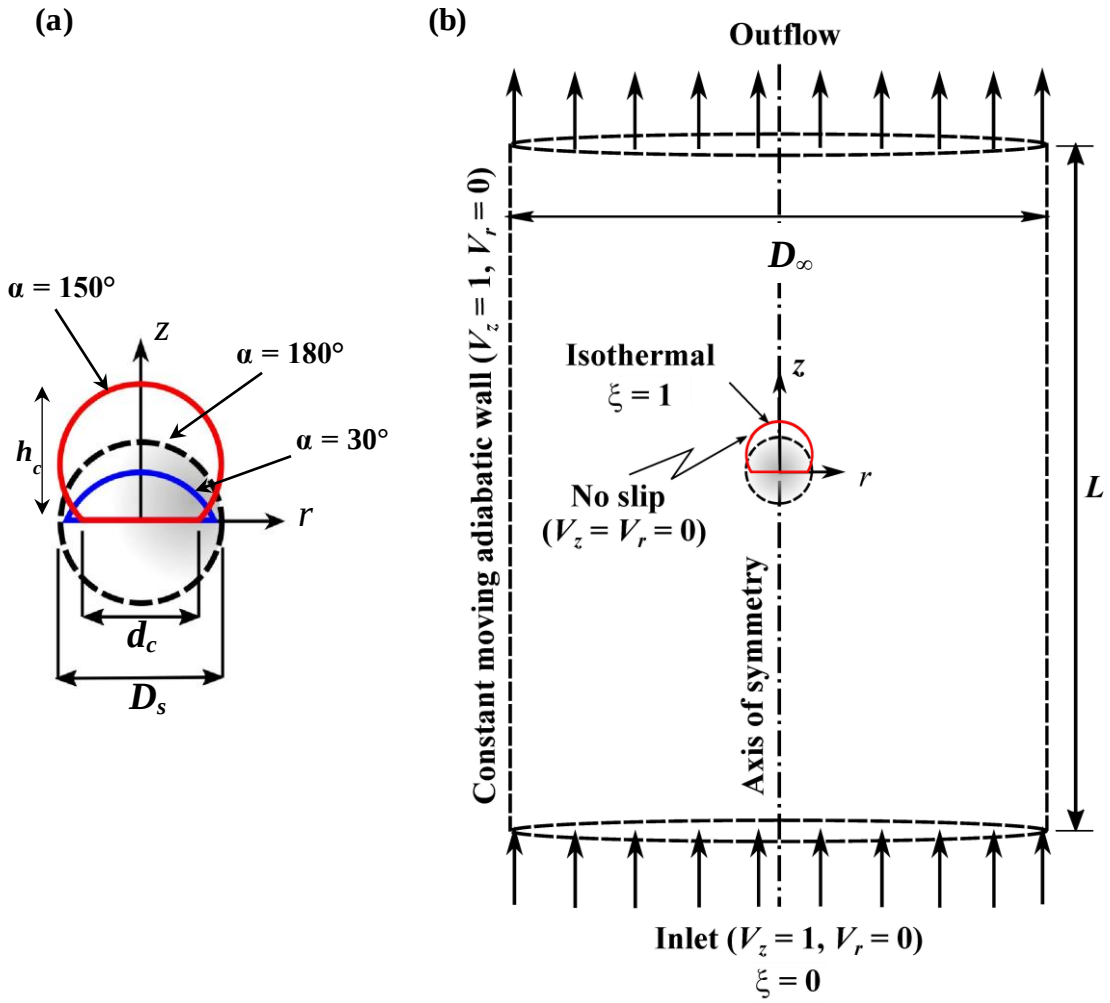


**Figure 4.33** Schematics of (a) geometries of spherical segment (b) computational domain of problem statement.

At the outlet (Neumann boundary condition): $\frac{\partial \zeta}{\partial z} = 0$ where $\zeta = V_z$, $V_r$, and $\xi$; $p = 0$

At the axisymmetric axis: $V_r = 0$, $\partial V_z/\partial r = 0$, $\partial \xi/\partial r = 0$

Where $\xi = = \frac{T - T_c}{T_h - T_c}$, non-dimensional temperature. The solution of **Eqs. (2.1) – (2.3)** yields the pressure ($p$), velocity ($V_r$, $V_z$), stress ($\tau$) and temperature ($\xi$) fields which are further post-processed to analyze in terms of streamlines, yielded/unyielded region, pressure coefficient ($C_{DP}$), frictional drag ($C_{DF}$), total drag coefficient ($C_D$), and average Nusselt numbers ($Nu$).

### 4.3.3 Choice of numerical parameter and validation

Numerically, the previously mentioned **Equations (2.1) - (2.3)** have been solved using finite element based commercial software, COMSOL Multiphysics (5.3a). The PARDISO solver discretizes the mass, momentum and energy equations in a sparse linear system which is further solved by LU decomposition

method. All the primitive variables ($p$, $V$, $T$) converge up to five significant digits and the yield surfaces converge as per von-Mises criterion with a relative tolerance of $10^{-6}$. All the present results are free from any numerical artifacts is ascertained by performing domain test, grid test and regularization test and their effect on drag coefficient, pressure coefficient, average Nusselt number and local Nusselt number is examined precisely. The boundary of the domain will have the maximum impact on the thick boundary layers i.e., for Newtonian fluids, as there the spatial variation in the primitive values is slower. Here, we have checked the domain of ref. (as previous **section 4.1**) for $Bn$ = 0, $Re_B$ = 0.1 and $Pr_B$ = 0.1 and it is found that it is suitable for the present chosen range of parameters. At the highest value of $Re_B$, $Pr_B$, and $Bn$ where both the hydrodynamic, thermal and stress boundary layers become thinner in the vicinity of the surface of the geometry, grids need to be refined to capture the steep changes in the velocity, temperature and stress gradients. Hence, near the surface of the geometry a very fine triangular grid has been generated and in the farther domain quadrilateral mesh has been used with the geometrical progressive spacing. Three different grids have been examined as G1, G2 and G3 for two extreme shapes of the spherical segments (α = 30° and α =180°) by varying the number of elements ($N_c \times N_f$) on the curved surface ($N_c$) and flat base ($N_f$) as tabulated in **Table 4.12**. The drag coefficients and average Nusselt numbers vary marginally as grid number increases from G2 to G3. Hence, G2 grid has been chosen to resolve the flow and thermal fields in this work. Furthermore, the variation of the local pressure coefficient and local Nusselt number is also plotted to gain confidence in the chosen Grid G2. **Figure 4.34** compares the local variation of pressure coefficient and Nusselt number for grids G2 and G3 for both shapes α = 30° and α =180° at $Re_B$ = 150 for extreme values of $Bn$ and $Pr_B$.

**Table 4.12** Grid impendence test at $Re_B$ = 150 $Bn$ = 100 $Pr_B$ = 100.

| **Grid** | ***Np*** | $N_T$ | $C_D$ | $C_{DP}$ | ***Nu*** |
|---|---|---|---|---|---|
| | | α = 180° | | | |
| G1 | 120 | 34400 | 21.246 | 15.055 | 119.15 |
| G2 | 260 | 91500 | 21.391 | 14.878 | 67.337 |
| G3 | 300 | 102500 | 21.402 | 14.934 | 67.758 |
| | | α = 30° | | | |
| **Grid** | $N_c \times N_f$ | $N_T$ | $C_D$ | $C_{DP}$ | ***Nu*** |
| G1 | 125 × 100 | 175759 | 17.952 | 17.14 | 35.21 |
| G2 | 175 × 150 | 372379 | 17.871 | 17.236 | 24.24 |
| G3 | 265 × 235 | 391368 | 17.85 | 17.286 | 23.475 |

The well merged plots of results for both G2 and G3 grids in **Fig. 4.34** further confirms the choice of grid G2 for present work Finally, the discontinuous nature of the Bingham plastic model for effective viscosity is regularized using the Papanastasiou regularization model widely reported in literature (Putz and Frigaard, 2005; Gupta and Chhabra, 2014). Nevertheless, to choose the suitable regularization parameter, $M$, for the chosen model, a detailed regularization test is performed at $Bn$ = 10 and $Re_B$ = 150 by comparing

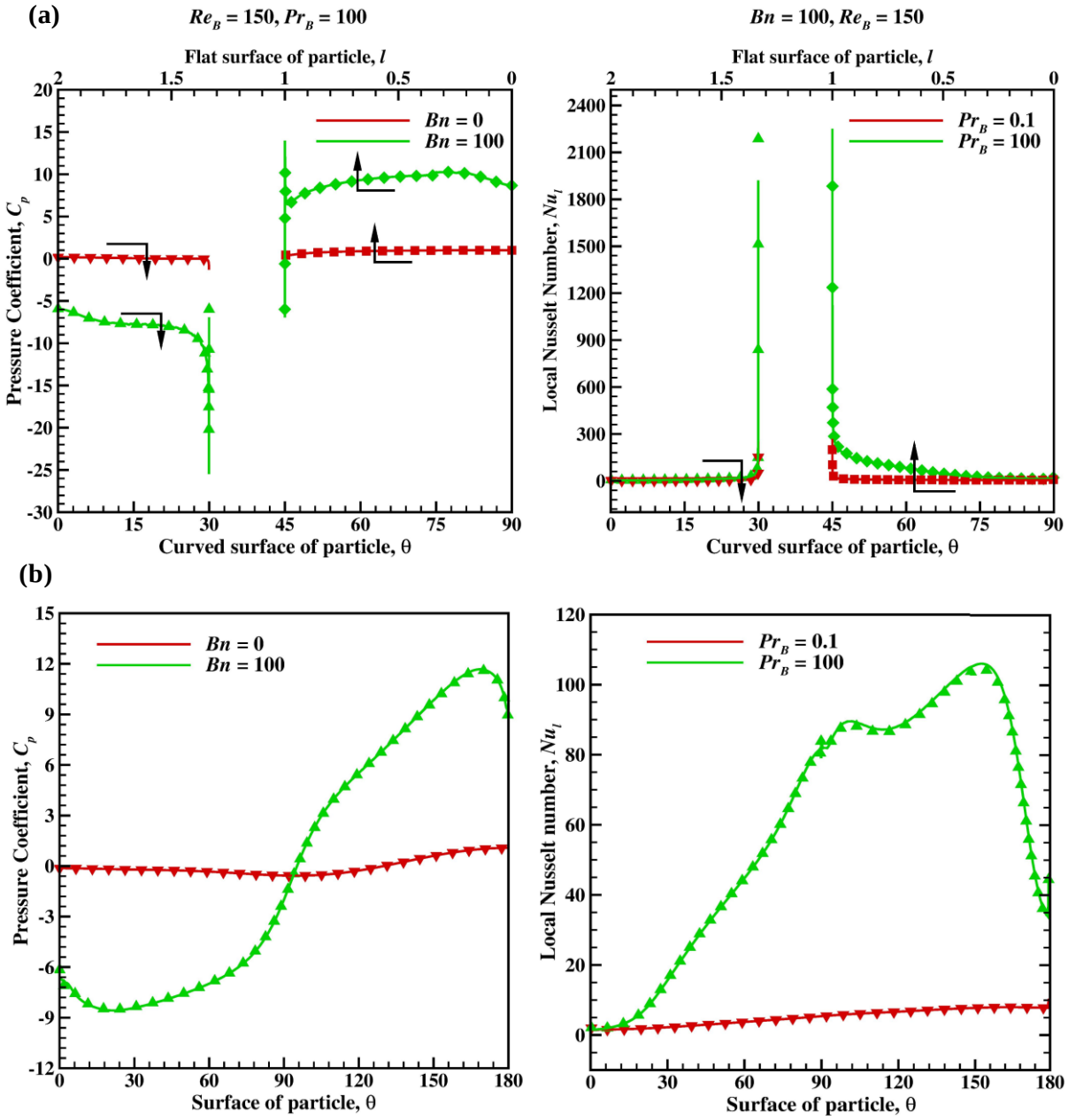


**Figure 4.34** Grid independence test G2 (symbol) and G3 (solid line) (a) α = 30° (b) α = 180°.

the yield surfaces. The effect of $M$ is studied for the three cases of spherical segment (α = 30°, 90° and 180°) as shown in **Fig. 4.35** by plotting the variation of the yield surfaces over range of $M$ values. The results show that as $M$ values increase from $10^6$ to $10^7$ the morphology of the yielded/unyielded regions remains undistinguished. In addition, some additional simulations were performed to scrutinize the chosen Papanastasiou regularization model with other available regularization models. **Figure 4.36** confirms the excellent agreement between results of yield surfaces of the three different regularizations models plotted for $Bn$ = 10 and $Re_B$ = 150 that lends credibility to the chosen Papanastasiou model. Hence, $M$ =$10^6$ is chosen as the regularization parameter for the Papanastasiou model. The convergence criterion

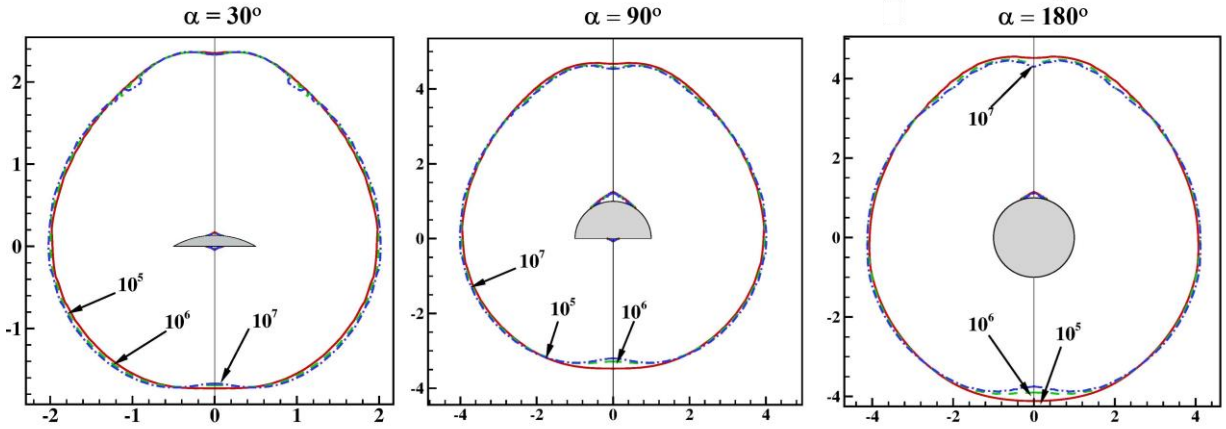


**Figure 4.35** Regularization test for different spherical segment at $Bn$ = 10 and $Re_B$ = 150.

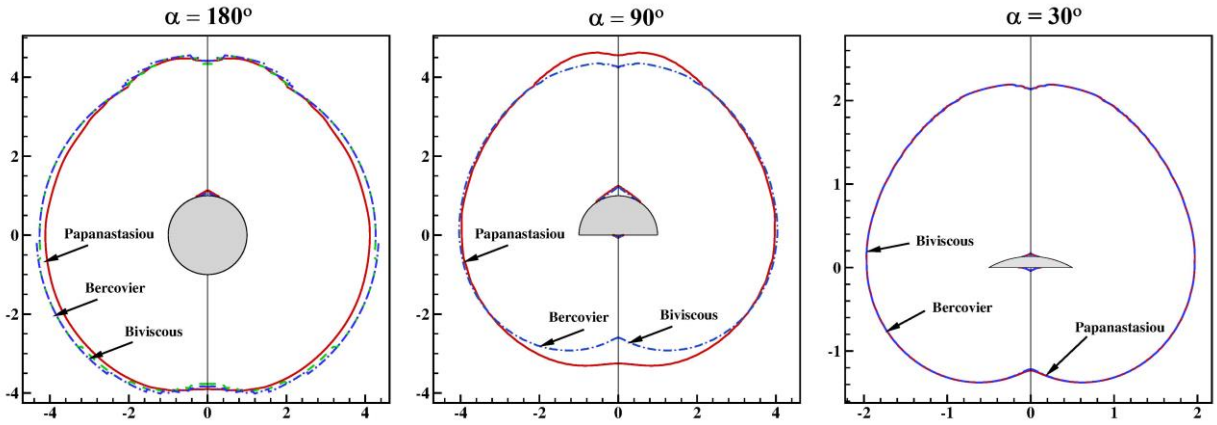


**Figure 4.36** Comparison of different Regularization models at $Bn$ = 10 and $Re_B$ = 150.

of $10^{-5}$ for continuity, flow and energy equations withing the domain has been established. It was found that employing a more stringent criterion had no apparent effect on the results.

The governing **equations (2.1) – (2.3)** are numerically solved to investigate the effect of the range of the parameters, i.e., Reynolds number ($0.1 \leq Re_B \leq 150$), Bingham number ($0 \leq Bn \leq 100$), Prandtl number ($0.1 \leq Pr_B \leq 100$) and shape factor ($30° \leq \alpha \leq 180°$) on the momentum and heat transfer characteristics in the steady forced convection regime. The chosen parameters for this study are based on the practical and numerical considerations found in the literature (Nalluri *et al.*, 2015; Patel *et al.*, 2015). Ongoing further comparison with the currently obtained results using the present numerical technique with the previous scant results have been discussed in the next section.

### 4.3.4 Results and discussion

Before discussing the new results, it is mandatory to establish the reliability and accuracy of the current numerical scheme and model by validating some previous benchmark solutions. Thus, the comparison with the currently obtained results using the chosen numerical technique with the previous scant results has been discussed in the next section. The sphere, $\alpha = 180°$, is one of the limiting cases of the present

range of the shape of the geometry studied in the present work in the literature for the forced convection in both Newtonian and Bingham plastic fluids. The numerically obtained results of the drag coefficient, pressure drag coefficient and Nusselt number for sphere by Nirmalkar *et al.* (2013a) are compared for Newtonian as well as Bingham plastic fluids in **Table 4.13** which shows excellent agreement with each other within 2-3% deviation. Similarly, the drag experience by sphere in Bingham plastic fluid is further compared with the available experimental results in the literature (Valentik and Whitmore, 1965; Pazwash and Robertson, 1971, 1975). Both results seem in fair agreement with each other as shown in **Fig. 4.37**. Finally, the surface variation of the Nusselt number for isothermal sphere is also compared in **Fig. 4.38** with the numerical results of Nirmalkar *et al.* (2013a) at $Bn$ = 0 and $Bn$ = 100 over a wide range

**Table 4.13** Validation of sphere with numerically evaluated data of Bingham plastic fluid.

| $Bn$ | $Re_B$ | Nirmalkar *et al.* (2013a) | | | Present | | |
|---|---|---|---|---|---|---|---|
| | | $C_D$ | $C_{DP}$ | $Nu_{avg}$ | $C_D$ | $C_{DP}$ | $Nu_{avg}$ |
| 0 | 1 | 27.333 | 9.148 | 5.772 | 27.181 | 9.064 | 5.806 |
| | 10 | 4.299 | 1.522 | 12.602 | 4.285 | 1.517 | 12.728 |
| | 50 | 1.578 | 0.654 | 24.289 | 1.567 | 0.658 | 24.113 |
| | 100 | 1.096 | 0.512 | 33.551 | 1.081 | 0.509 | 33.297 |
| 1 | 1 | 96.101 | 41.222 | 7.344 | 95.327 | 40.973 | 7.384 |
| | 10 | 10.023 | 4.349 | 15.068 | 9.928 | 4.314 | 15.129 |
| | 50 | 2.509 | 1.165 | 26.387 | 2.485 | 1.161 | 26.32 |
| | 100 | 1.503 | 0.756 | 33.814 | 1.499 | 0.751 | 33.875 |
| 10 | 1 | 433.55 | 248.92 | 8.872 | 430.14 | 247.96 | 8.908 |
| | 10 | 43.509 | 24.903 | 19.229 | 43.124 | 24.873 | 19.243 |
| | 50 | 9.021 | 5.199 | 32.989 | 8.943 | 5.206 | 33.175 |
| | 100 | 4.729 | 2.769 | 43.032 | 4.693 | 2.774 | 42.121 |
| 100 | 1 | 3208.1 | 2222.1 | 10.179 | 3179.7 | 2204 | 10.224 |
| | 10 | 320.49 | 222.14 | 24.545 | 317.98 | 220.42 | 24.511 |
| | 50 | 64.182 | 44.298 | 45.856 | 63.68 | 44.15 | 44.391 |
| | 100 | 32.184 | 22.035 | 58.942 | 31.952 | 22.165 | 57.301 |

of Prandtl number. The strong agreement between the two results adds credibility to the reliability of the findings presented in this work.

*4.3.4.1 Morphology of yielded/unyielded regions*

Bingham plastic fluids exhibit a unique characteristic where they manifest both solid-like (unyielded) and fluid-like (yielded) properties simultaneously under the prevailing shear stress field. Due to the steep velocity gradient near the surface of the spherical segment, fluid remains sheared. However, far from geometry these velocity gradients gradually decrease and cease at the critical yield stress value ($\tau_o$)

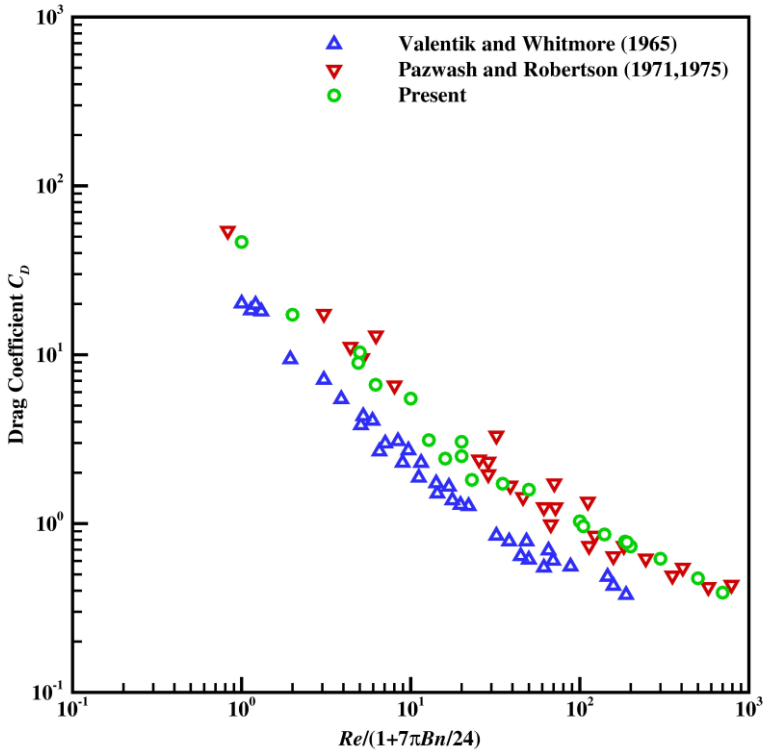


**Figure 4.37** Comparison of present drag experienced by sphere in Bingham plastic fluid with experimental data.

resulting in the formation of solid-like (unyielded) region. **Figure 4.39** represents the yielded/unyielded regions for three cases of spherical segment ($\alpha = 30°$, 90° and 150°) at three different values of Bingham number ($Bn$ = 1, 10, 100) and for two values of Reynolds number ($Re_B$ = 0.1, 150). The yield surfaces separate (stress contour plotted at yield stress value) the fluid-like and solid-like regions for the given set

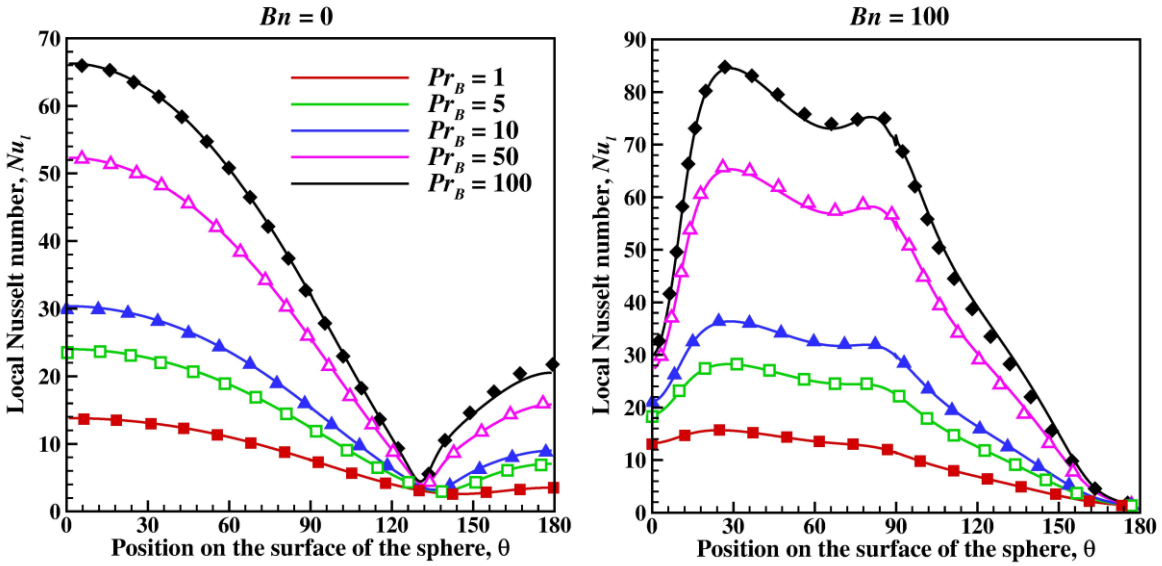


**Figure 4.38** Comparison of local Nusselt number of heated spheres in Bingham plastic fluid with numerically evaluated data of Nirmalkar *et al.* (2013a) at $Re_B$ = 100.

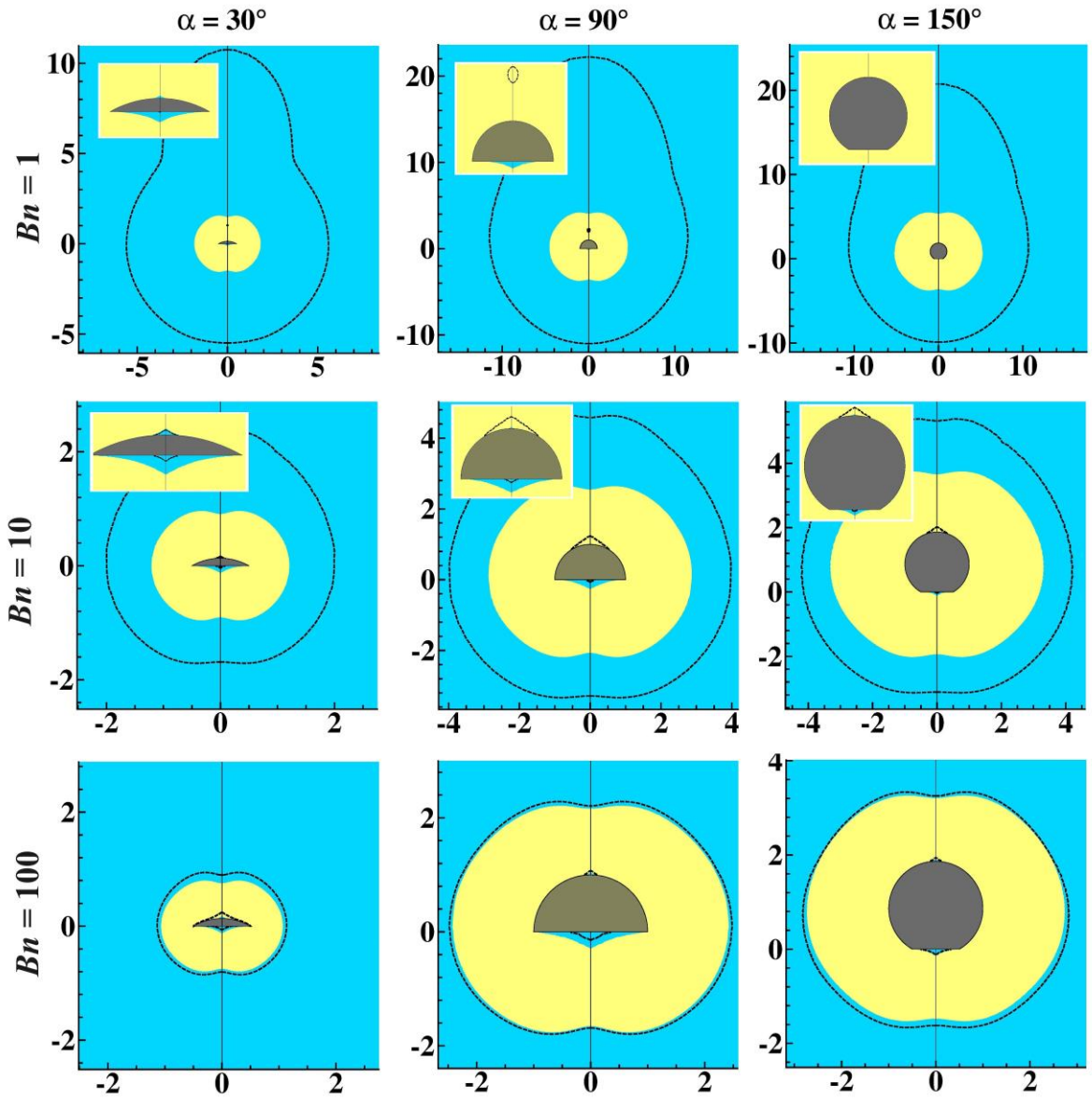


**Figure 4.39** Yielded/unyielded region at extreme Reynolds number $Re_B = 0.1$ (shaded regions) and $Re_B = 150$ (dotted line) (yellow color: yielded region; blue color: unyielded region).

of parameters. At low value of Reynolds number, i.e., $Re_B = 0.1$, it is observable that the fluid region (region shaded in yellow) remains encapsulated by the solid zone (region shaded in blue) follow the fore and after symmetry in the direction of the flow irrespective of the shape of the geometry and Bingham number. With the increase in Reynolds number $Re_B = 150$, the change in the shapes of the yielded/unyielded regions are represented by dotted lines as yield surfaces. **Figure 4.39** shows that with the increase in inertial force at high Reynolds number the yield surface elongates toward the flow direction resulting in pear-like shapes. The elongated fluid-like region downstream of the particle is more pronounced at high Reynolds numbers and low Bingham numbers. Furthermore, the shape of the particle has a significant effect on the elongated region. As particle segment shape moves closer to the spherical shape, it decreases the elongated region downstream of the particle with the radial expansion that has been clearly seen with the increase in the shape factor, α from 30° to 150°. However, for a fixed shape of

the particle, the increase in yield stress of the fluid suppresses the elongated fluid-like zone to enclose in the symmetric envelope in the vicinity of the particle over the range of the Reynolds number. Eventually, when the Bingham number or the yield stress of the fluid surpasses a critical threshold, the influence of the Reynolds number or inertia force is outweighed by the Bingham number or yield stress. Hence, at $Bn$ = 100, the yield surfaces for $Re_B$ = 0.1and 100 appear to be undistinguished.

The two static zones attached to the particle are also formed at the front and the rear stagnation points of the spherical segment which generally shrink in size with the increasing shape factor, α. At the fixed Reynolds number value, the front-end static zone grows in size with the increase in Bingham number while the size of rear end static zone decreases with the increase in Bingham number. At low plastic effect and high Reynolds number the static zone of the rear end of the geometry is formed far away from the geometry but eventually with the increasing plastic effect it forms closer to the spherical segment surface and at last adhere to the surface.

*4.3.4.2 Streamlines and wake formation*

The spatial variation of the flow field in terms of the nondimensional velocity contours and the streamlines have been visualized in **Figs. 4.40-4.42** to delineate the flow acceleration and wake formation around the spherical segments for two extreme shapes α = 30° and 150° including α = 90°. At low Bingham number $Bn$ = 0.01, in **Figs. 4.40-4.42** the fluid is able to negotiate with the body contour under low inertial force at $Re_B$ = 0.1 for all three shapes of the particle. However, with the increase in Reynold number at fixed Bingham number, $Bn$ = 0.01 due to the adverse pressure gradients associated with the sudden change in the body contour of the spherical segment leads to flow separation. It can be clearly seen that with the increase in Bingham number, the yield stress starts dominating inertial force by pacifying the flow. Hence, irrespective of the shape of the particle flow separation has been delayed with the increase in Bingham number for fixed value of the Reynolds number. Eventually, the wakes will cease to exist at $Bn$ = 100 can be seen in **Figs. 4.40-4.42.** Interestingly, attention is drawn to the fact that for a particular shape of the spherical segment, α = 60°, the evolution of the recirculation zones has been noticeable over the range of Reynolds number at fixed Bingham number. At $Bn$ = 5, the formation wake has been explored over the range of Reynolds number varying from 0.1 to 150 for α = 60° (**Fig. 4.43**). The formation of wake has been noticed in this work at $Re_B$ ~ 45. The visibly small size of wake observed at $Re_B$ = 60 in **Fig. 4.43**, however, the wake starts forming at $Re_B$ ~ 45 in a tiny size below which flow remains attached to the particle. The flow separation begins from the rear stagnation point of the particle on the curved surface instead of the sharp corner. In the case of Newtonian fluid, a similar trend of the wake formation has been reported for α = 60° (Suri and Patel, 2024). The separation bubbles formed at the rear end of the particle (primary bubbles) will grow with the increase in the Reynolds number. At the same time, the secondary separation bubbles emerge at the sharp corner of the particle (See in **Fig. 4.43** $Re_B$ = 75) eventually merge with the primary bubbles with the further increase in the Reynolds number can be seen at $Re_B$ = 80. Eventually, the merged separation bubbles grow radially to engulf the curved surface of the particle as

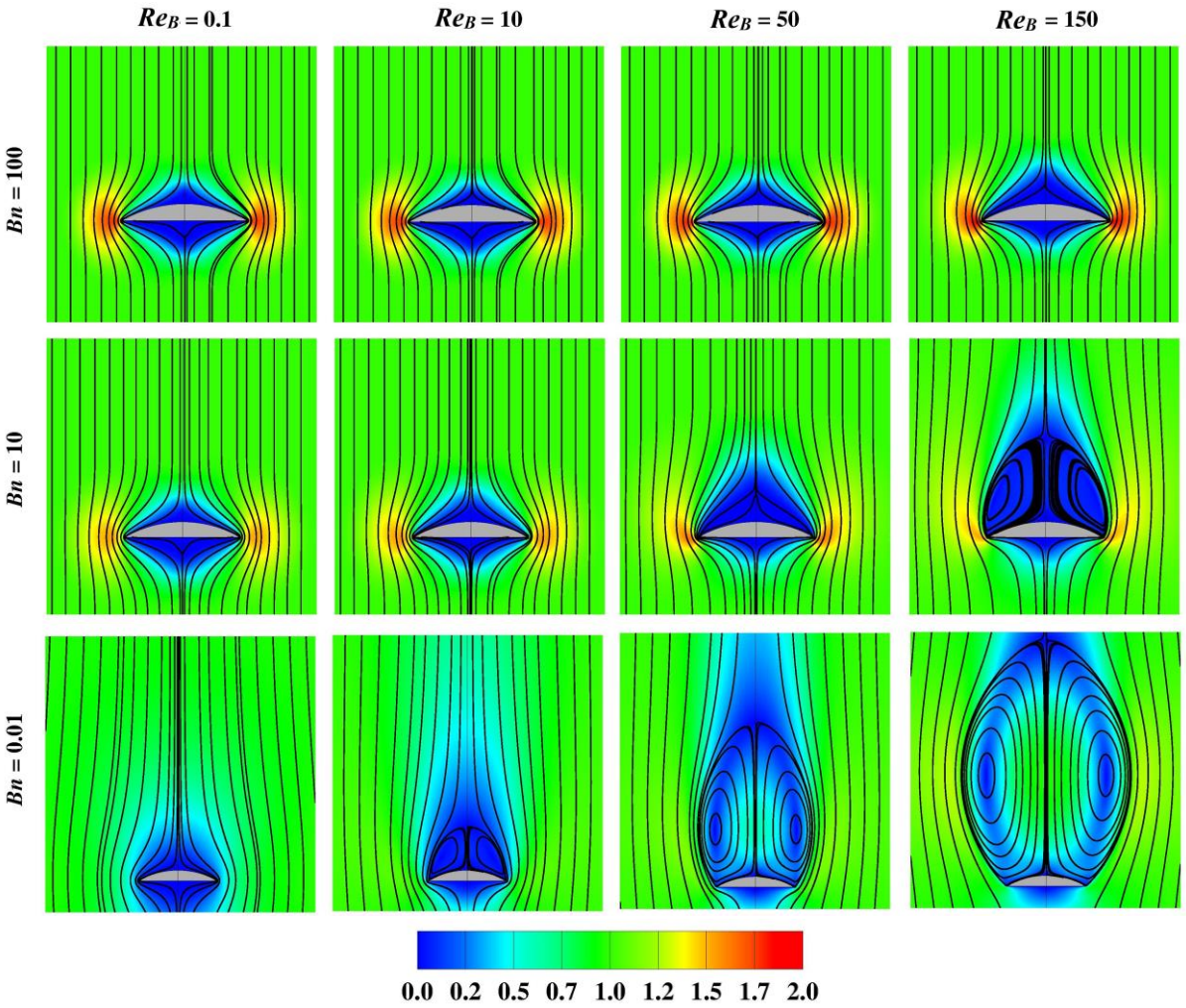


**Figure 4.40** Formation of wakes as a function of Reynolds number and Bingham number for α = 30° (lines: streamlines; color contours: velocity magnitude).

Reynolds number increases (for instance at $Re_B$ = 100 for α = 60°) followed by growing in the *z*-direction of the flow. Hence, for each shape of the particle there exists a critical Bingham number for a fixed Reynolds number or vice versa.

In **Fig. 4.44**, the combination of Reynolds number and Bingham number at the critical condition has been mapped to determine the presence or absence of wake for the given shape. By moving along each of the dotted lines connecting the data points, it can be inferred that at the fixed value of Bingham number on the *x*-axis, the flow separation has started at a Reynolds number that can be extrapolated on the *y*-axis. It also points out the Bingham number for the given shape delays the flow separation to the higher values of Reynolds number. The dotted line indicates the Reynold number at which the wake is present/absent for a particular Bingham number.

At the same time, the color contours in **Figs. 4.40-4.42** represent the dimensionless velocity magnitudes in the vicinity of the particle over the range of the parameters. For a fixed Reynolds number, as the Bingham number increases, the fluid velocity is observed to be increased while flowing past the particle. The solid-like regions enlarge due to increase in yield stress effect and, hence, the fluid-like zone

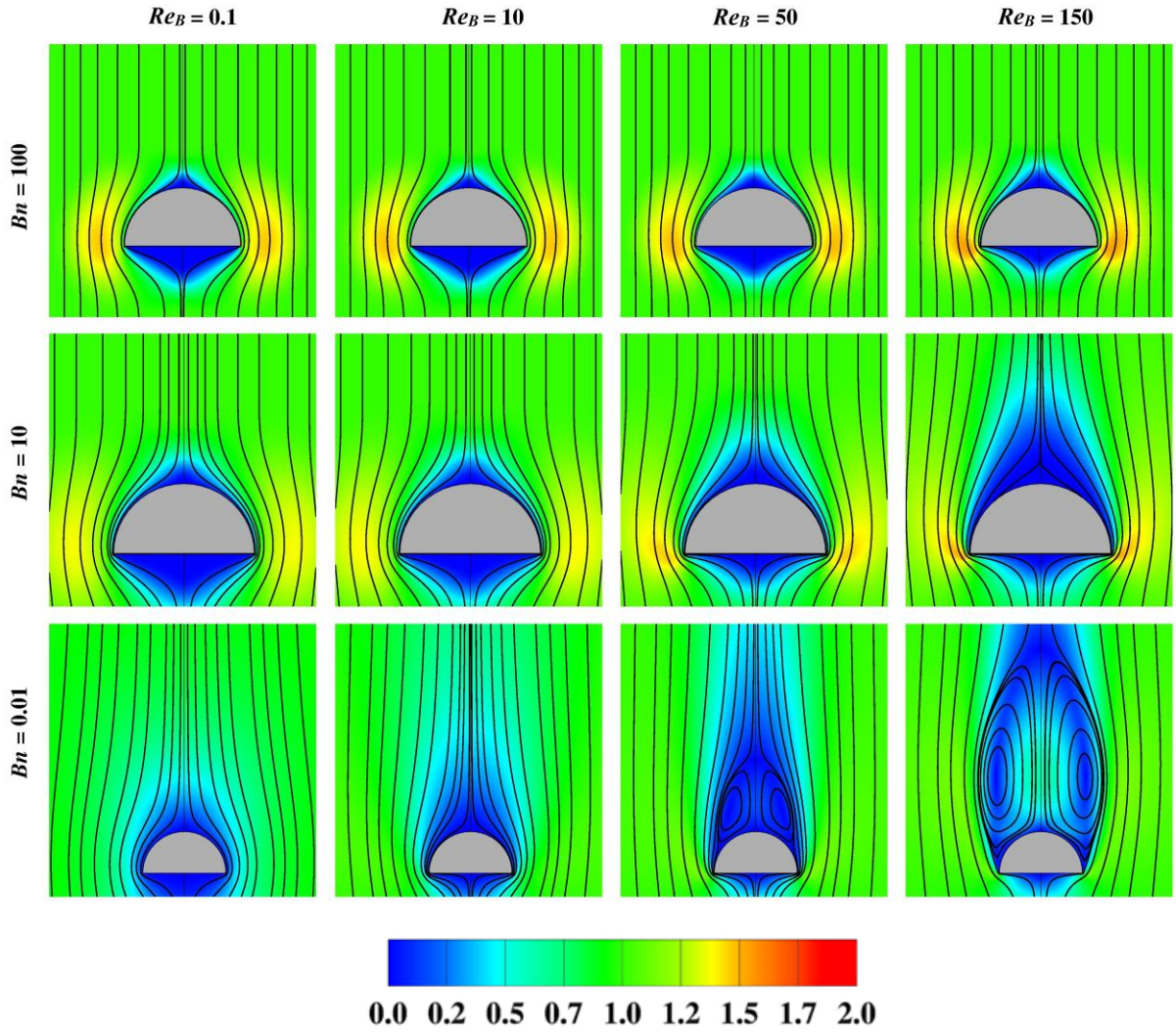


**Figure 4.41** Formation of wakes as a function of Reynolds number and Bingham number for α = 90° (lines: streamlines; color contours: velocity magnitude).

encapsulating the particle shrinks in size. As a result, the fluid flowing through the high shearing region experiences acceleration in velocity in the fluid-like zone as it has to satisfy the conditions of zero-velocity on the particle wall and free-stream. In summary, **Figs. 4.40-4.42** depict the effect of shapes by indicating that the velocities are higher in case of smallest spherical segment (α = 30°) and lowest in case of largest spherical segment (α = 150°).

*4.3.4.3 Velocity profiles and shear rate contours*

Plotting the velocity magnitude profiles and shear rate contours in close proximity to the particle can provide a better understanding of the flow field around the spherical segment. **Figures 4.45** and **4.46** plot the variation of the non-dimensional *z*-velocity component ($V_z$) in both the *r*- and the *z*- directions from the particle surface, respectively. **Figures 4.40-4.42** have shown that the flow past the particle accelerates with the Bingham number increases, as demonstrated by the velocity magnitude. In **Fig. 4.45** the non-dimensional *z*-velocity component, $V_z/U$, is plotted in the radial direction for three different spherical segments (α = 30°, 90° and 150°) at *Bn* = 100 over the range of Reynolds number. The radial distance is

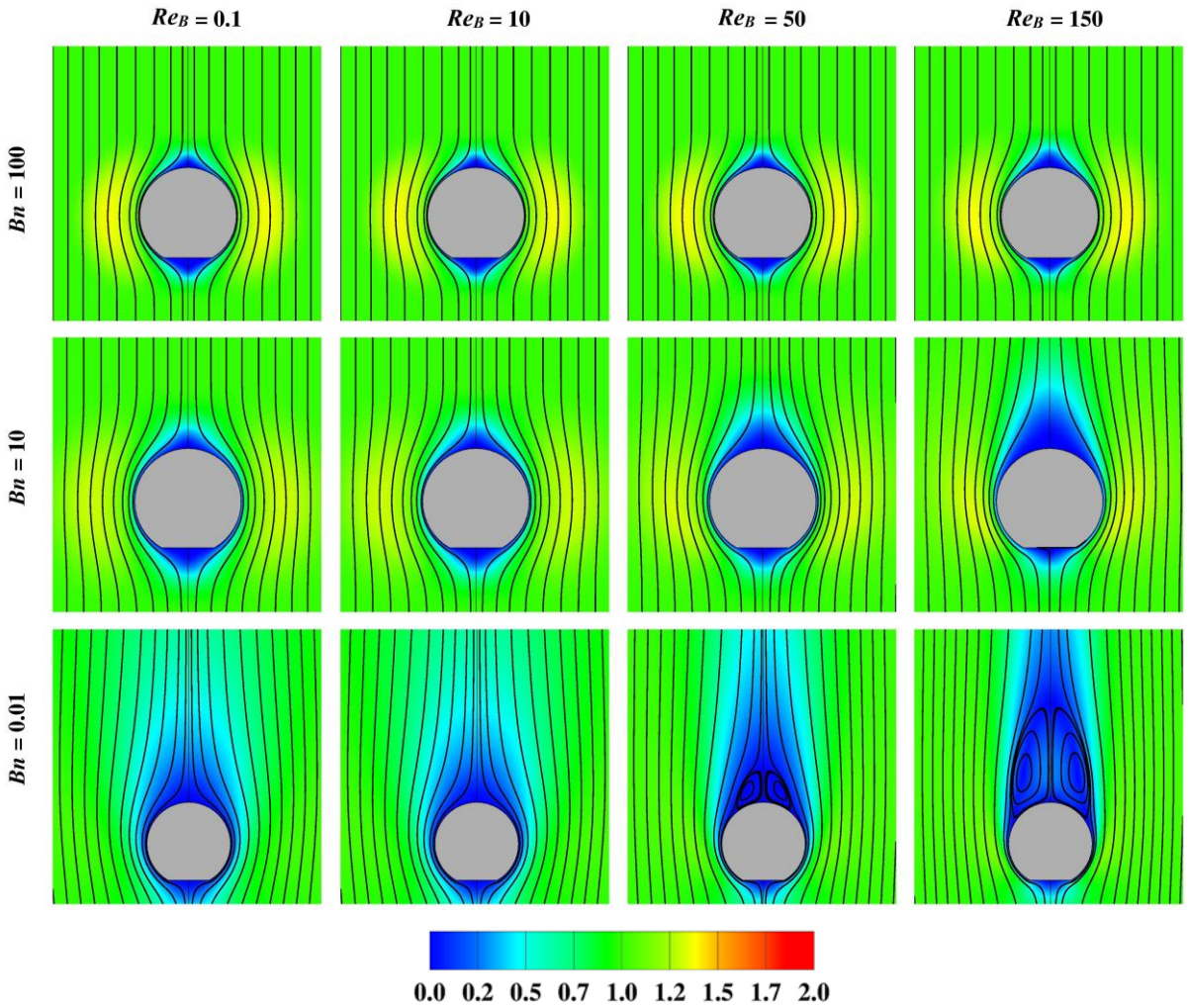


**Figure 4.42** Formation of wakes as a function of Reynolds number and Bingham number for α = 150° (lines: streamlines; color contours: velocity magnitude).

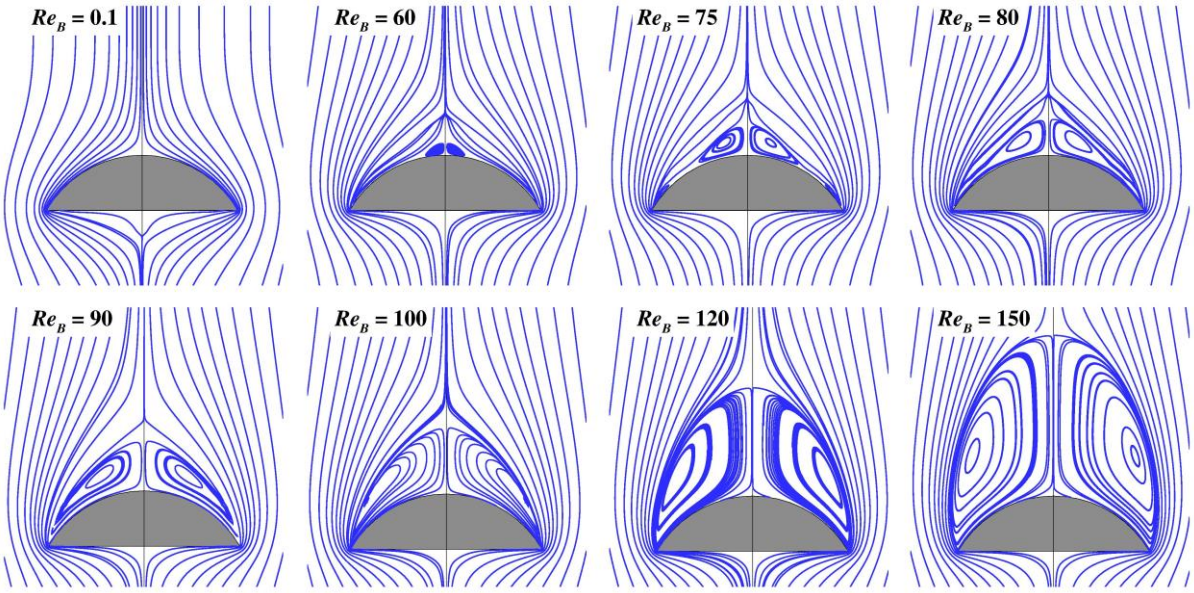


**Figure 4.43** Effect of Reynolds number and fixed Bingham number ($Bn$ = 5) on streamlines of α = 60° spherical segment.

measured from the largest cord length of the particle. Hence, it has been measured from the base of the

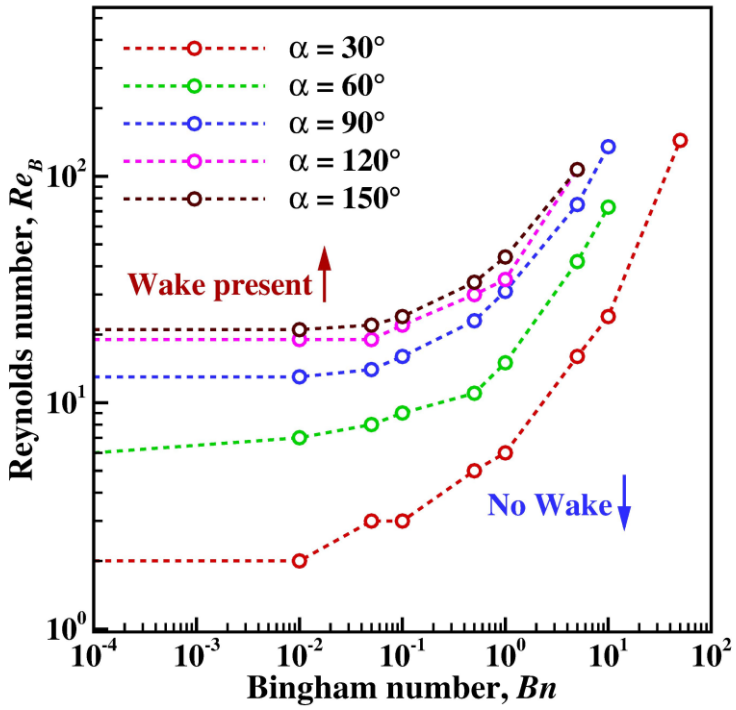


**Figure 4.44** Effect of Bingham number on the critical Reynold number of the spherical segment.

particle for α = 30° and 90°while for α = 150° it is measured from the largest cord length of segment that is diameter of the spherical particle from which the segment is dissected rather than the base of the segment. The reduction in the size of the fluid zone encapsulated particle has been observed to be maximum at the highest plastic effect at *Bn* = 100 in this study (see **Fig. 4.40**). The hump observed in the $V_z/U$ profile from the particle surface (zero-velocity) plotted in the *r*-direction indicates the increase in velocity of the fluid in the radial direction of the spherical segment followed by decrease to free stream velocity the in the plug flow region over the range of Reynolds number. The increase in the peak of the hump shows positive dependence of velocity on the Reynolds number within the yielded region.

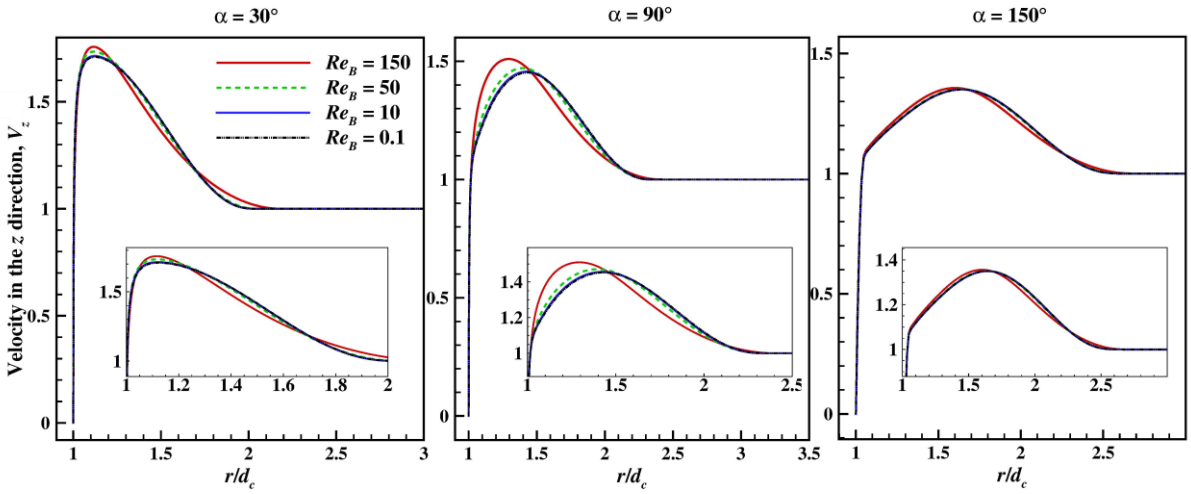


**Figure 4.45** Non-dimensional velocity in the radial direction of the spherical segment at *Bn* = 100.

Furthermore, the effect of shape is also noticeable on the velocity profile, with the increase in the shape factor. The hump broadens in width in the radial direction significantly otherwise under identical conditions denotes the positive effect of shape on the size of yielded encapsulated zone (see **Fig. 4.40**). In the extreme cases of the α = 30° and α = 150° the velocity increases almost ~1.76 times and ~1.36 times the free stream fluid velocity of the fluid, respectively, as shown in **Fig. 4.45** at $Re_B$ = 150 and *Bn* = 100 which consistent with the observations marked for the velocity contours in **Figs. 4.40-4.42**.

Non-dimensional velocity $V_z/U$ is further plotted at the rear end of the spherical segment in the *z*-direction over a range of Reynolds number at the extreme values of Bingham number (*Bn* = 0 and 100) for three different spherical segments (α = 30°, 90° and 150°). For the Newtonian fluid (*Bn* = 0) and $Re_B$ = 0.1 for all three shapes the velocity profile starts from zero at the rear stagnation point and monotonically increases to achieve its asymptotic value of free stream velocity for low inertial flow. However, the increase in the inertial force due to increase in Reynolds number creates the adverse pressure gradient

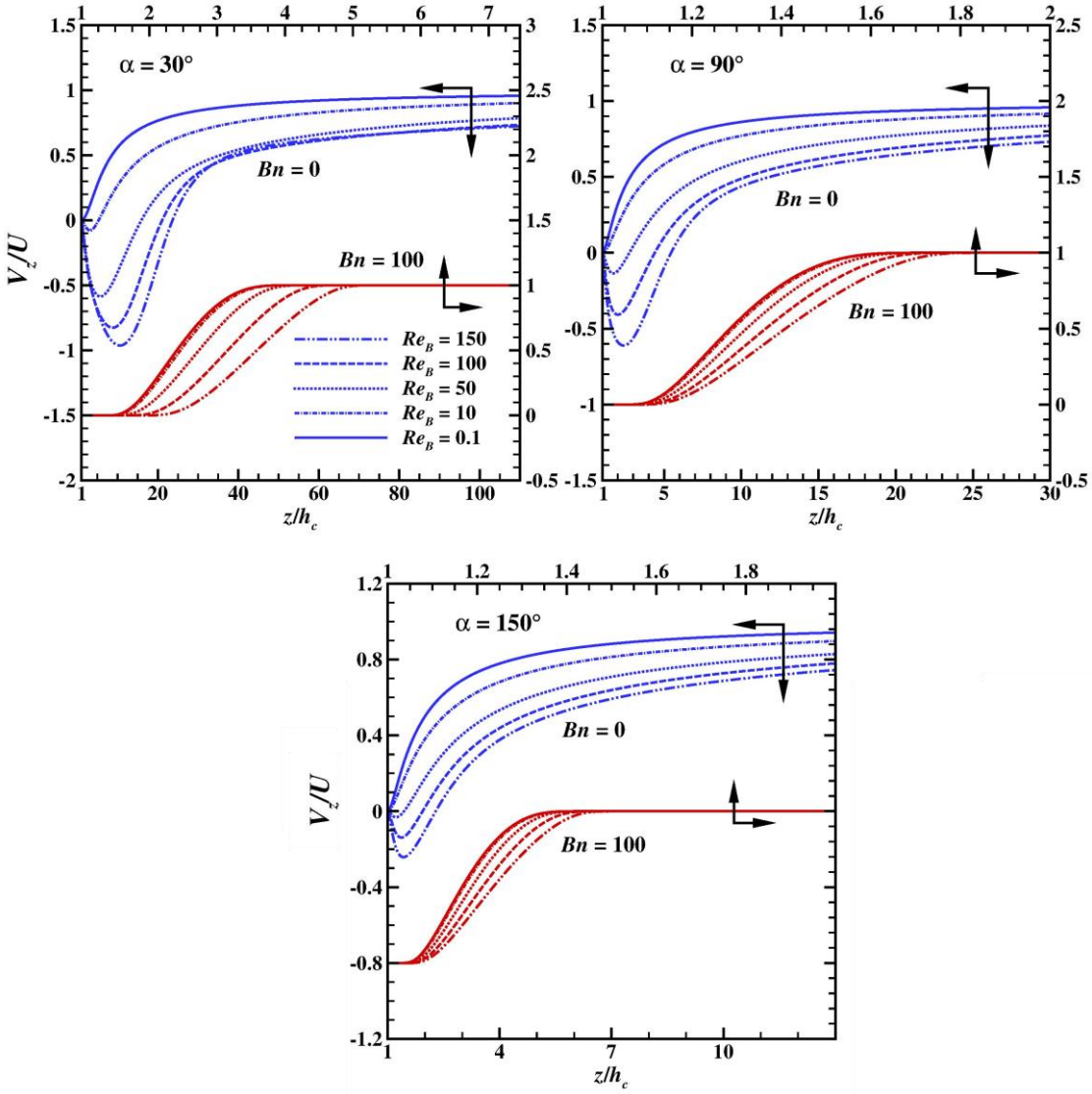


**Figure 4.46** Non-dimensional velocity in the flow direction (*r* = 0) of the spherical segment.

leads to flow separation from the particle surface. Thus, wakes are formed at the rear end of the spherical segment. The negative velocities in the velocity profiles signify the presence of recirculation zone at the rear side of the segments. Furthermore, these velocity profiles provide insight into the effect of the shape and other nondimensional parameters on wake length. The distance between the rear stagnation points and confluence point (magnitude of the velocity becomes zero while changing from negative to positive) measures the wake length. **Figure 4.46** demonstrates for the case of Newtonian fluids; wake length decreases with the increase in the shape factor from $\alpha = 30°$ to $150°$ for fixed value of the Reynolds number. At the same time, the effect of Reynolds number for each shape observed to be increase in wake

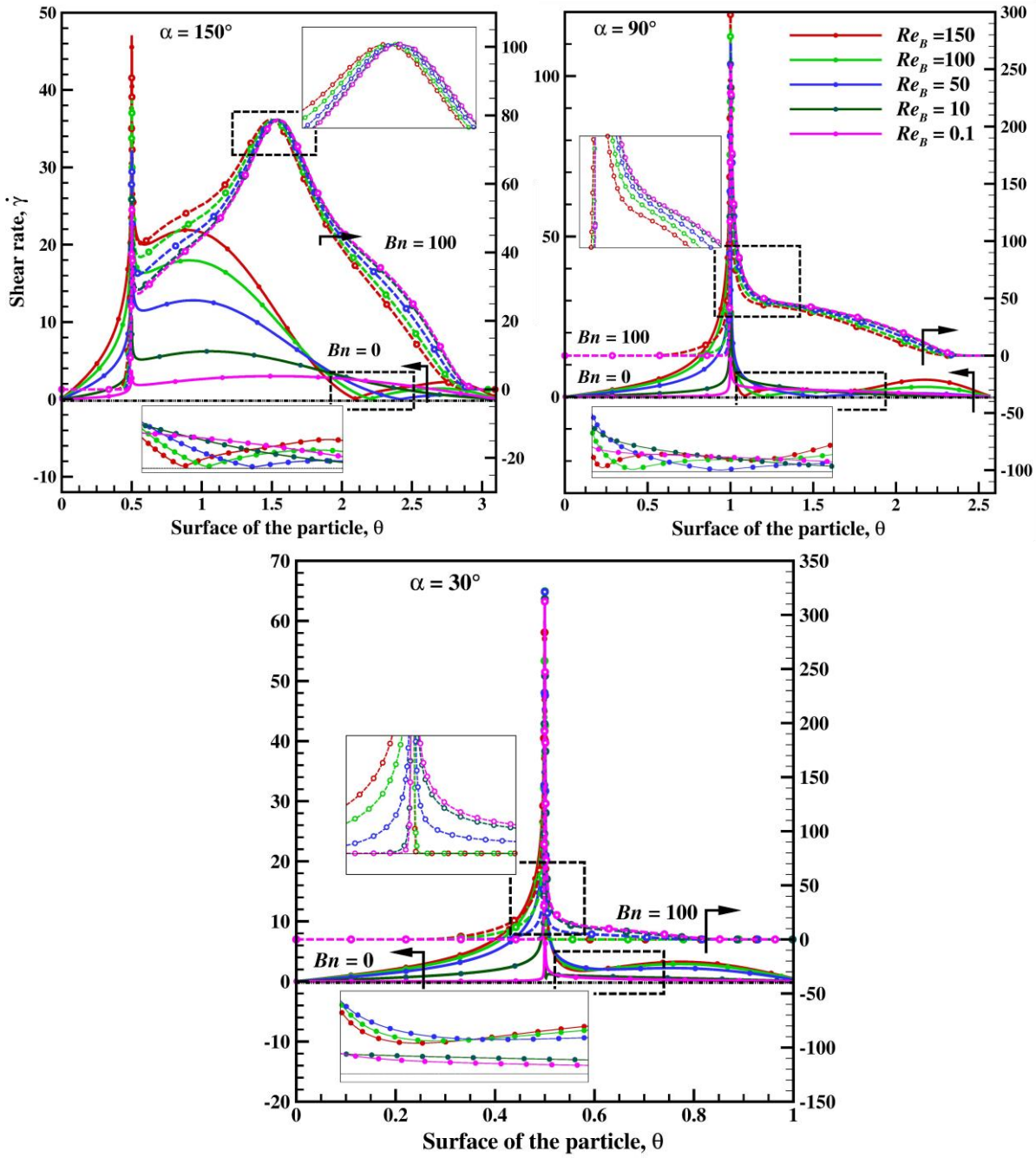


**Figure 4.47** Non-dimensional shear rate profiles at the surface of the spherical segment.

length. Following the effect of Bingham number on the non-dimensional velocity ratio, $V_z/U$, three sections can be distinguished denoted as I, II, III in **Fig. 4.46**. The first constant section of velocity profile (I) indicates the presence of the static zone attached to the rear end of spherical segment also shown in **Fig. 4.40**. For a fixed Bingham number and shape factor, the size of these static zones increases as the Reynolds number increases that can clearly be seen in **Fig. 4.46**. The second section (II) that monotonically increases also known as shearing zone shows the similar behavior as Newtonian fluid since here Bingham plastic fluid show fluid like behavior and it tries to approach the free stream velocity. However, here the magnitude of nondimensional velocity shows transition from zero to unity even at the high Reynolds number which supports the results of the streamlines having no wakes present at $Bn = 100$. With increasing Reynolds number, the slope of section II decreases due to the enlargement of the fluid zone in the *z*-direction (refer to **Fig. 4.40**). The last section (III) indicates the presence of solid rigid zone where the fluid will flow with the translation plug flow velocity. The increase in the shape factor significantly reduces the size of the first two sections and quickly approaches the constant plug flow velocity.

In **Fig. 4.47** non-dimensional shear rates are plotted at the surface of the spherical segment over the range of the Reynolds number and extreme values of Bingham number $Bn = 0$ and 100. In the case of Newtonian fluid ($Bn = 0$); at the front stagnation point the fluid is stagnant, hence, the velocity gradient becomes zero, hence, shear rate vanishes. Moving from the front stagnation point on the flat base of the spherical segment due to shearing of the fluid shear rate increases and eventually it achieves the peak value at the point of the sharp corner of the spherical segment due to the singularity. On the curved surface, the shear rate gradually decreases to zero and then increases again. The location of flow separation is manifested by the zero-shear rate on the surface of the particle. With the increase in Reynolds number, the location of zero shear rate on curved surfaces moves closer to the base confirming the early flow separation. The separation of the fluid from the surface of the spherical segment is suppressed by an increase in Bingham number due to yield stress dominating over fluid inertial force. Evidently, at $Bn = 100$, there is no drop in the shear rate values that can be seen confirms no flow separation. However, the fluctuation of the shear rate is thought to be solely due to the particle shape and the size of the unyielded cap on the curved surface of the particle.

*4.3.4.4 Drag coefficient*

Drag experienced by any bluff body is generally combination of the two different stress components known as normal stress and the shear stress. Both the stresses correspondingly contribute as a foam drag and viscous drag in the total drag experienced by the body. **Figure 4.48** shows the dependency of the total drag (hollow symbols) and the pressure drag (solid symbols) over the range of the Reynolds and Bingham number for three shape factors, $\alpha = 30°$, 90° and 150°. For each shape, the drag coefficient follows the standard inverse and positive dependency on Reynolds and Bingham number, respectively. In **Fig. 4.49** both drag coefficients, total (hollow symbol) and the pressure (solid symbol), are plotted as a function of shape factor over the range of Reynolds number and Bingham number. The total drag

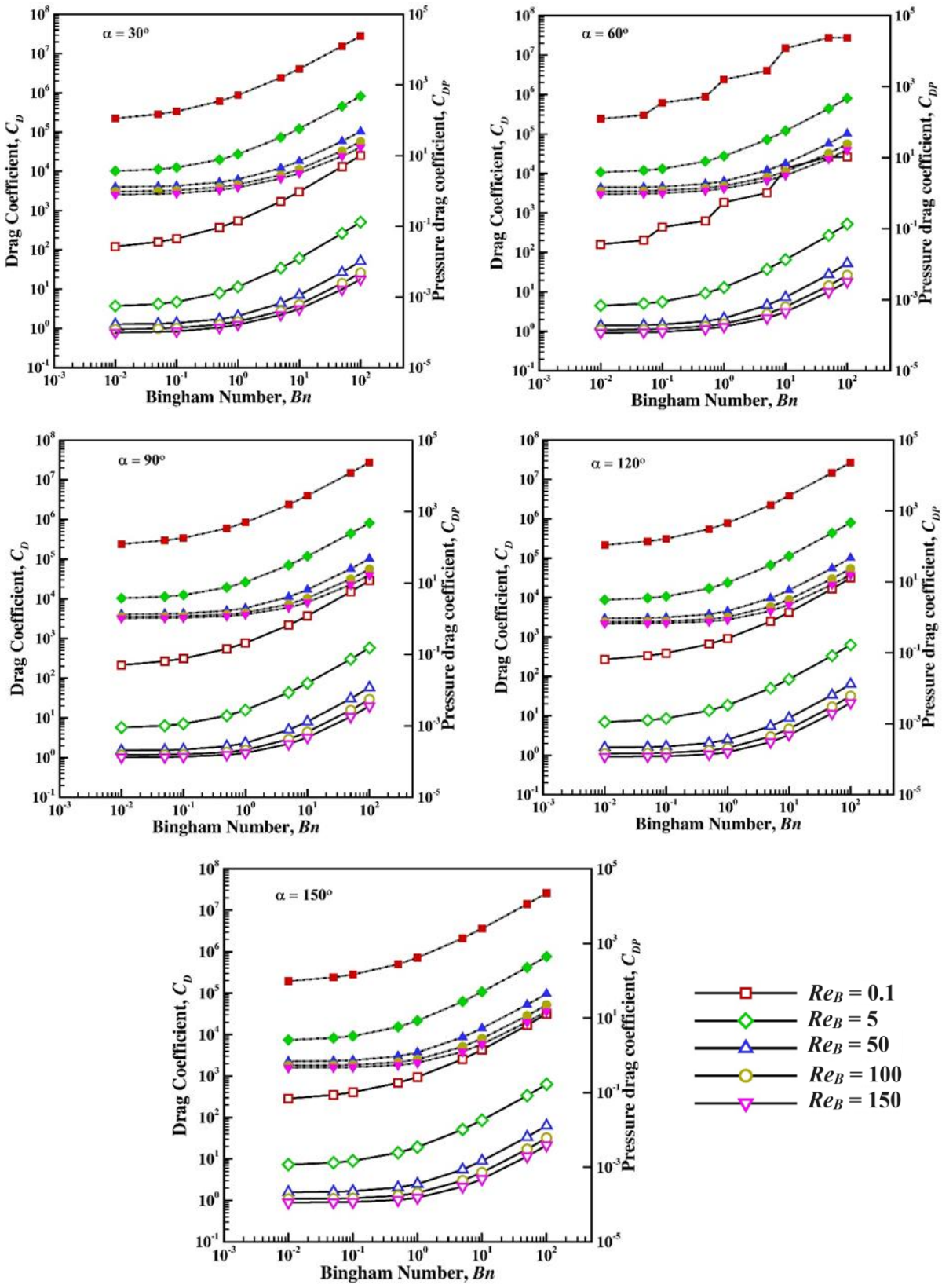


**Figure 4.48** Effect of Bingham number on the drag and pressure drag coefficient over the range of Reynolds number (hollow symbols: total drag coefficient; solid symbols: pressure drag coefficient).

experienced by the spherical segments are increasing with the increase in shape factor irrespective of the Bingham number for a fixed Reynolds number and eventually it becomes almost constant for the largest

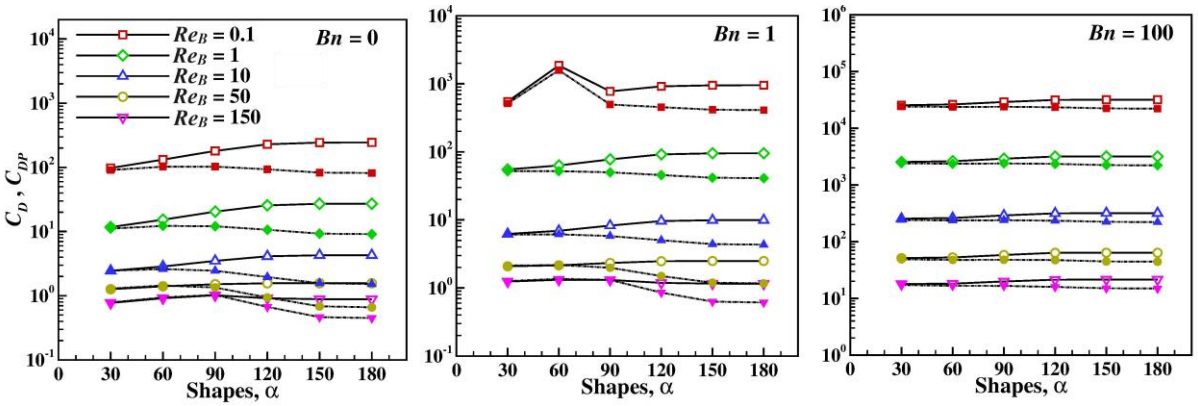


**Figure 4.49** Effect of the shape of spherical segment on the drag (Hollow symbol) and pressure drag (Solid symbol) coefficient over the range of Reynolds and Bingham number.

spherical segment (α = 150°) and the sphere (α = 180°). On the other hand, at low Bingham number the pressure drags increases with the increase α from 30° to 90° as the projected area of these shapes increase with the α values. As the angle α increases from 90° to 180°, the curved surface area of the spherical segment continues to increase. However, the projected area (i.e., the diameter of the parent sphere) remains constant, resulting in a more contribution of foam drag compared to pressure drag. This ultimately leads to an increase in the total drag experienced by the spherical segment. Finally, for the highest Bingham number (*Bn* = 100), the pressure drag coefficient becomes almost constant over the range of the shape factor and Reynolds number.

In order to compare the drag experienced by the different spherical segments with respect to sphere, the ratio of the drag coefficient, $C_{D\alpha}/C_D$ sphere, is plotted in **Fig. 4.50**. At the low Reynolds number, the ratio of the drag experienced by the spherical segment α = 30° is generally smallest while it is close to unity for α = 150° as it has almost similar geometrical feature as a sphere. The drag ratio shows strong dependence on Reynolds number above certain critical value of $Re_{B(\text{critical})}$, for instance, $Re_{B(\text{critical})}$ = 0.5 at

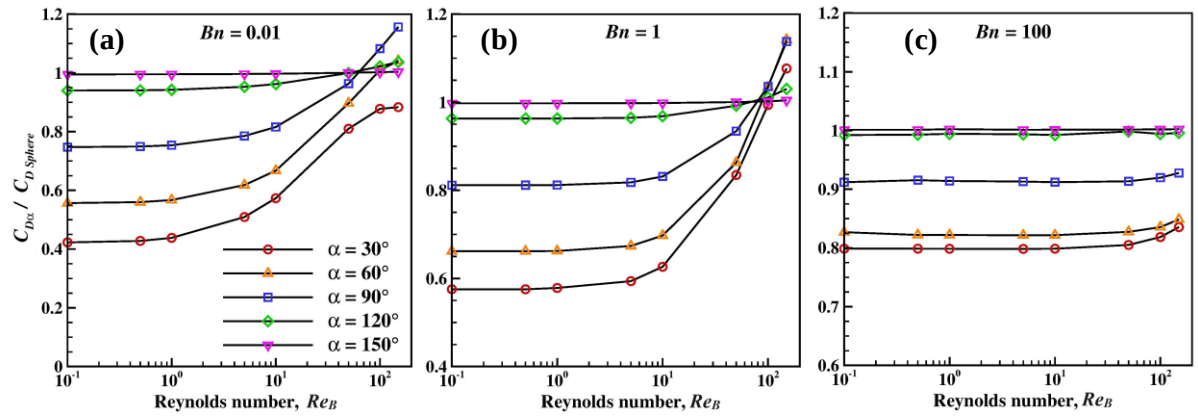


**Figure 4.50** Variation of ratio of drag coefficient to the sphere with Bingham and Reynolds number.

$Bn$ = 0.01 (**Fig. 4.50a**). The increase in Bingham number shifts this critical Reynolds to the higher value of Reynolds number can be seen in **Figs. 4.50b** and **4.50c**. For $Re_B$ = 150, the $C_{D\alpha}/C_D$ sphere is maximum for the hemispherical segment. Finally, for the ease of application, the drag coefficient is correlated as a function of $Re_B$ ($0.1 \le Re_B \le 150$), $Bn$ ($0 \le Bn \le 100$), $\psi$ ($0.424 \le \psi \le 1$) and $d_c/h_c$ ($1 \le d_c/h_c \le 7.463$) using two different proposed correlations. Here, the effect of the shape is considered in the form of shape factor, $\psi$ ($0.424 \le \psi \le 1$) rather than $\alpha$ ($30° \le \alpha \le 180°$) which is most widely employed and practical measured shape factor, specifically for nonspherical particles.

For $Re_B < 1$:

$$C_D = \left(\frac{0.123}{Re_B}\right) + 14.201 Re_B^{-1.021} \psi^{0.556} \left(1 + 5.793 Bn^{0.772}\right) \left(\frac{d_c}{h_c}\right)^{0.145} \tag{4.12}$$

**Equation (4.12)** is proposed using 120 data point with the average and maximum error of 22% and 63%, respectively. However, only a few data points, i.e., 19 show the error greater than 40%.

For $Re_B \ge 1$:

$$C_D = 0.602 + 25.94 Re_B^{-1.001} \psi^{-0.196} \left(1 + 1.294 Bn^{0.929}\right) \left(\frac{d_c}{h_c}\right)^{-0.215} \tag{4.13}$$

**Equation (4.13)** is proposed for $Re_B \ge 1$with the total data point of 359. It shows the average and maximum error of 23% and 75%, respectively, where only 3 data points have errors of more than 38%.

*4.3.4.5 Isotherm contour*

The isothermal contours generally help to visualize the local temperature fields while indicating the hot and cold spot in the surrounding media**. Figures 4.51** and **4.52** represent the isothermal plots for three spherical segments ($\alpha$ = 30°, 90°, 150°) and Bingham number ($Bn$ = 1, 10, 100) over the extreme combinations of Reynolds and Prandtl number. The left half illustrates the isothermal contours at $Pr_B$ = 0.1 and the right half illustrates the contours for $Pr_B$ = 100.

At lowest Peclet number ($Pe_B$ = 0.01) when the convection is very weak, fluid adheres to the surface of the spherical segments. Hence, the isotherms show aft and forth symmetry in the direction of the flow and the heat transfer is mainly governed by the conduction mechanism seen in **Fig. 4.51**. Next, with the increase in Prandtl number the thinning of the thermal boundary layer, isotherms lose their symmetry in the upstream and downstream direction of the flow. Thus, it clustered in the front end of the spherical segment while stretched at the rear end of the spherical segment (see right half of **Fig. 4.51**), hence, the rate of heat transfer increases. However, the increase in Bingham number has not significant effect at low Peclet number.

Now, as the Reynolds number increases or high inertial forces, heat is mainly transferred by convection. **Figure 4.52** depicts that as the Reynolds number increases due to recirculation zones at the rear end of the spherical segments, isotherms become denser towards the surface of the spherical segment. Hence,

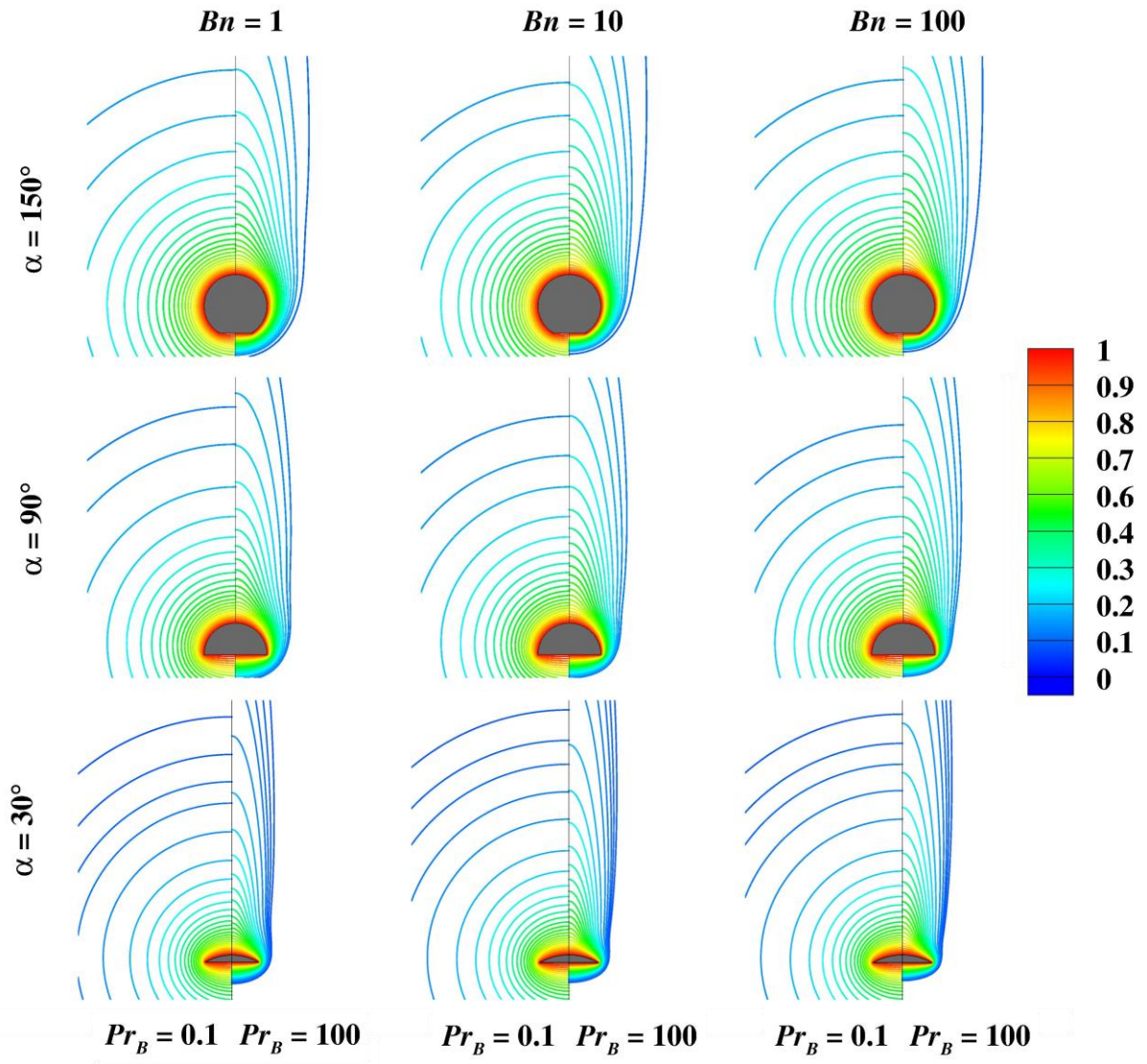


**Figure 4.51** Representation of isothermal contours at $Re_B$ = 0.1 at two Prandtl number $Pr_B$ = 0.1 (left half) and $Pr_B$ = 100 (right half).

promotes mixing and the heat transfer rates. The further increase in Prandtl number creates the distortion of the isotherms and crowded near the surface with high temperature gradients that further enhance the heat transfer rates. In yield stress fluid heat transfer have strong dependency on the yielded/unyielded regions. As in the unyielded region heat is mostly transferred by conduction while in the yielded region by convection. Thus, the increase in Bingham number suppresses the flow circulation as it progressively reduces the yielded region (see **Fig. 4.39**) which further reduced the thermal boundary layer and the steep temperature gradients exist near to the surface.

The shape of the spherical segment also plays a crucial role in the heat transfer. Due to abrupt variation in the surface of lowest spherical segment (α = 30°), flow separation is more prominent (see in **Fig. 4.44**) hence, the heat transfer is higher. With the increase in shape factor (α), the spherical segment becomes streamlined which further delays the flow detachment and thermal boundary layers thicken indicating the

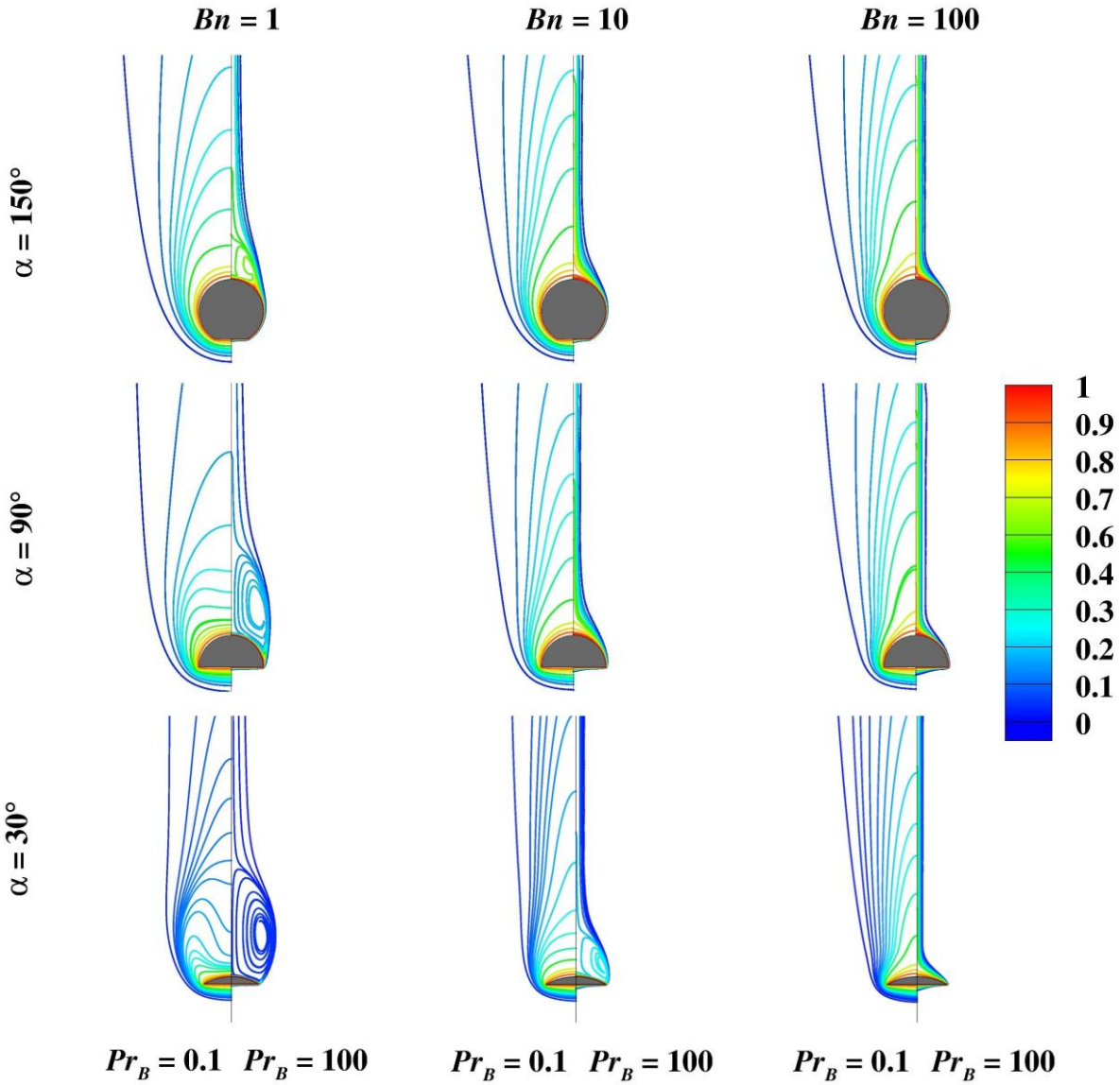


**Figure 4.52** Representation of isothermal contours at $Re_B$ = 150 at two Prandtl number $Pr_B$ = 0.1 (left half) and $Pr_B$ = 100 (right half).

low heat transfer in comparison to α = 30°. Thus, it is fair to postulate here that the heat transfer shows a combined behavior as a function of Reynolds, Prandtl and Bingham number. Certainly, these complex interplays between the parameters are widely studied for the average Nusselt number in the next section.

*4.3.4.6 Nusselt number*

The average or mean Nusselt number is often required for various engineering applications such as fluidization and processing of particulate products. Thus, the dependence of the Nusselt number is studied as a function of four non-dimensional parameters, namely, $Re_B$, $Pr_B$, $Bn$, and α. For the Newtonian fluid, it is readily acknowledged in the literature that the Nusselt number has a positive dependence on both Reynolds and Prandtl number due to the progressive thinning of the thermal boundary layer. The same analogy can also be applied here in the case of the spherical segments. **Figure 4.53** shows the effect of Reynolds number on the average Nusselt number over the range of the Prandtl number for α = 30°, 90°

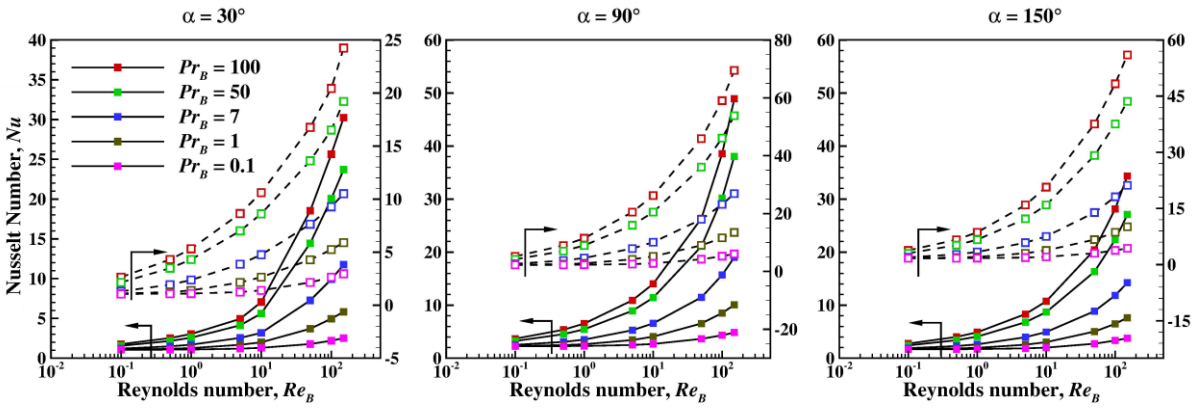


**Figure 4.53** Variation of Nusselt number with the Reynolds number at $Bn$ = 0 (solid lines) and $Bn$ = 100 (dashed line) over the range of Prandtl number.

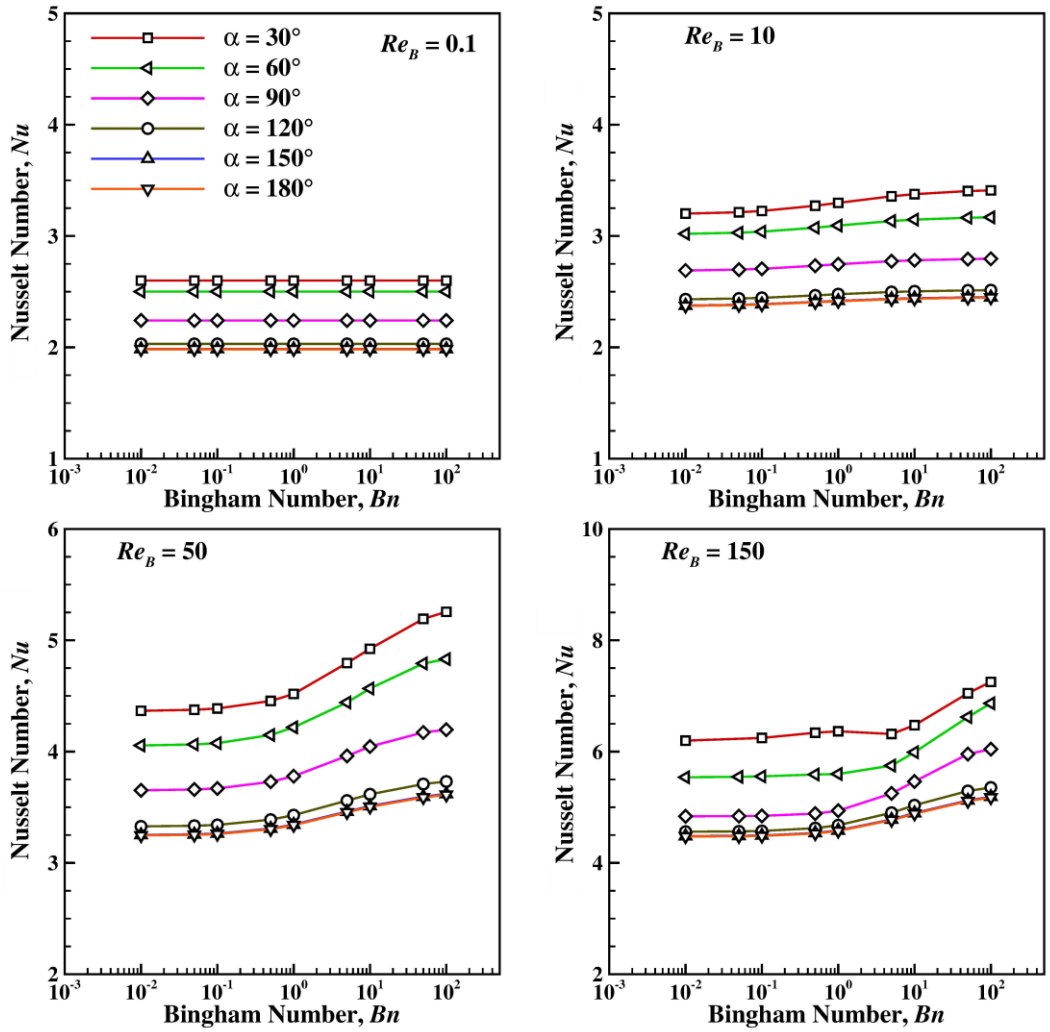


**Figure 4.54** Variation of Nusselt number for different spherical segment with the Bingham number at $Pr_B$ = 0.1

and 150°. The solid lines indicate Newtonian fluid ($Bn$ = 0) and the dashed line indicates the Bingham plastic fluid ($Bn$ = 100). For all three cases of the spherical segments, the average Nusselt number

compared for the Bingham plastic fluids to Newtonian fluids indicates the overall positive dependence of Nusselt number on $Pr_B$ and $Bn$ numbers.

In **Figs. 4.54** and **4.55**, the average Nusselt number is plotted as a function of Bingham number over the range of the shapes of spherical segment and Reynolds number for the two cases of Prandtl number, i.e., $Pr_B = 0.1$ and $Pr_B = 100$. At low Peclet number ($Pe_B = Pr_B \times Re_B = 0.01$), the effect of Bingham number is not significant; however, with the increase in the Peclet number the effect of Bingham number becomes more pronounced can be seen in **Fig. 4.54** and **4.55**. For fixed $Pr_B = 0.1$, the increase Reynolds number above $Re_B = 0.01$ progressively thins the thermal boundary layer resulting in the increase in the overall heat transfer rate for all cases of spherical segments. As the Peclet number increases, above $Pe_B = 15$ the combined effect of $Re_B$, $Bn$ and $Pr_B$ shows complex behaviour depending upon the yielded/unyielded zones formed around the spherical segments can be seen in **Fig. 4.55**. At high Peclet, $Pe_B = 5\times10^3$ and $15\times10^3$ for high Prandtl number and/or Reynolds number, the Nusselt number shows weak dependence

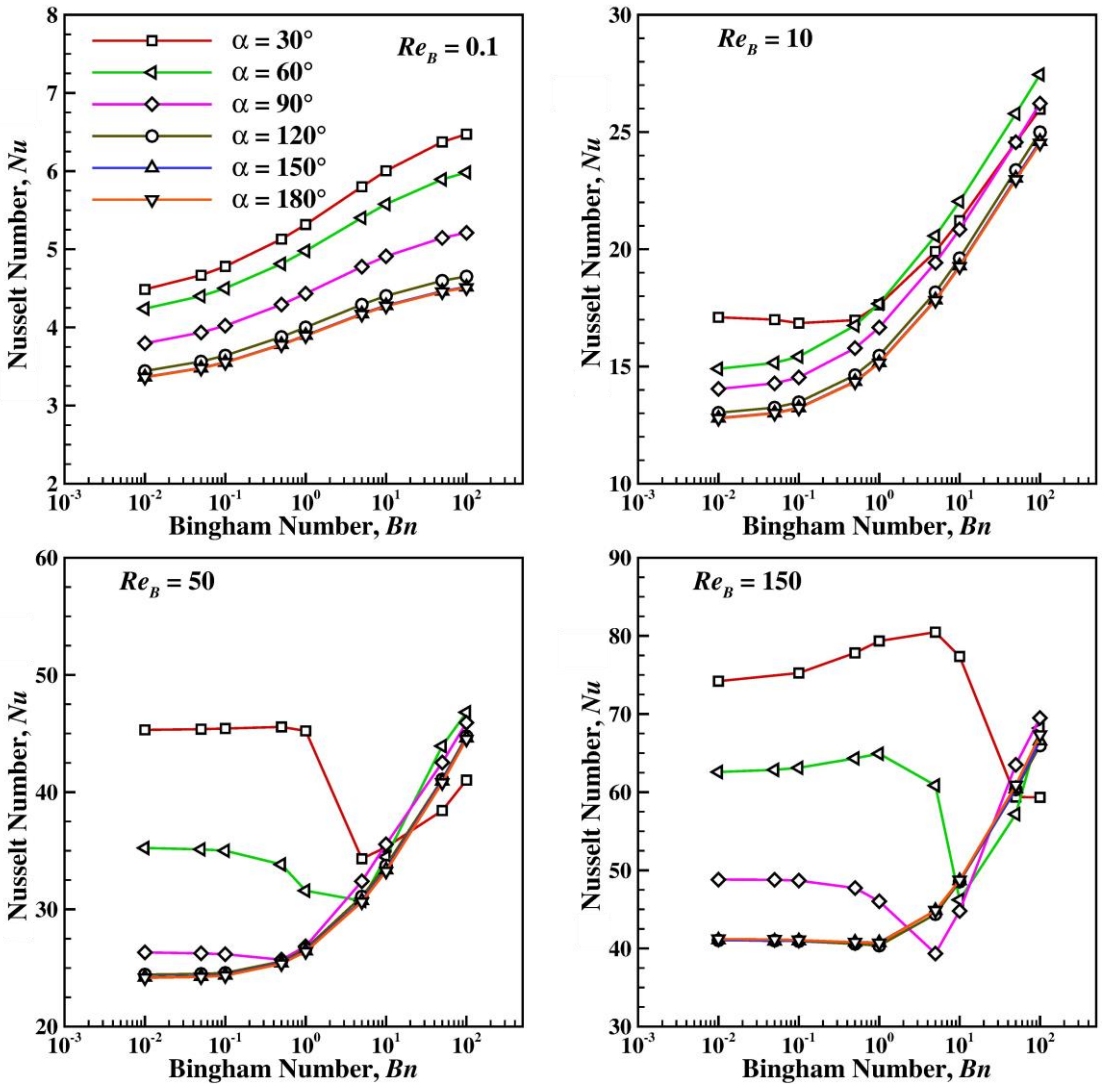


**Figure 4.55** Variation of Nusselt number for different spherical segment with the Bingham number at $Pr_B = 100$.

on the Bingham number initially. Furthermore, a sharp drop in Nusselt number is observed particularly for α = 30° to 90° that and increases with the increase in Bingham number The drop in the Nusselt number is observed as a function of the shape factor, α. It can be seen in **Fig. 4.55** that for α = 30°, *Nu* drops at *Bn* ~ 50 while for α = 90°, it moves to smaller value of the Bingham number *Bn* ~ 5. Intuitively, the decrease in the Nusselt number is possibly due to the formation of the solid zones attached to the surface of the spherical segment. For α = 60°, the value of Nusselt number is dropped to its minimum at *Bn* = 10. To gain further insight into the significant decrease in the Nusselt number, we plotted the yielded/unyielded region alongside the local variation of the strain rate in **Figure 4.56** for α = 60° and $Re_B$ = 150 for three Bingham number values of 1, 10 and 100.

**Figure 4.56** depicts that initially at low Bingham number *Bn* = 1, the heat is being transferred by convection from the surface of the geometry to the encapsulated fluid. The further increase in *Bn* number, *Bn* = 10, reduces the fluid-like zone at the same time there is a formation of the solid zone adhering to the rear end of the spherical segment. Thus, the heat transfer to the surrounding fluid from the hot surface of the particle impeded by the presence of the solid zone attached to the particle surface and heat is only transferred by the conduction from the curved surface to the solid-like material. This causes the drop in the rate of heat transfer, hence, Nusselt number. Eventually, the solid zone starts to disappear with the increasing Bingham number which further increases the heat transfer rates.

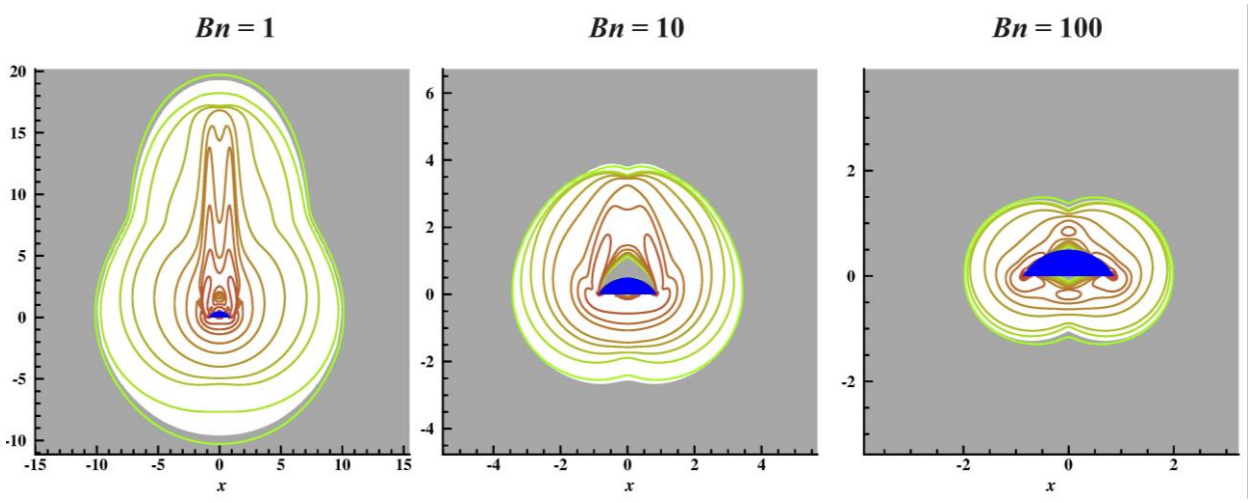


**Figure 4.56** Effect of Bingham number on the formation of the yielded/unyielded region and local strain rate for α = 60° at $Re_B$ = 150.

The variation in Nusselt number with respect to the shape is plotted in **Fig. 4.57**. It exhibits that overall, the smallest spherical segment (α = 30°) shows a high rate of heat transfer. The increase in shape factor steadily reduced the average Nusselt number and eventually it becomes constant.

In the case of high Peclet and Prandtl numbers, some cases are observed where Nusselt number is not high for the smallest segment. A possible reason for this is the presence of the solid zones as discussed

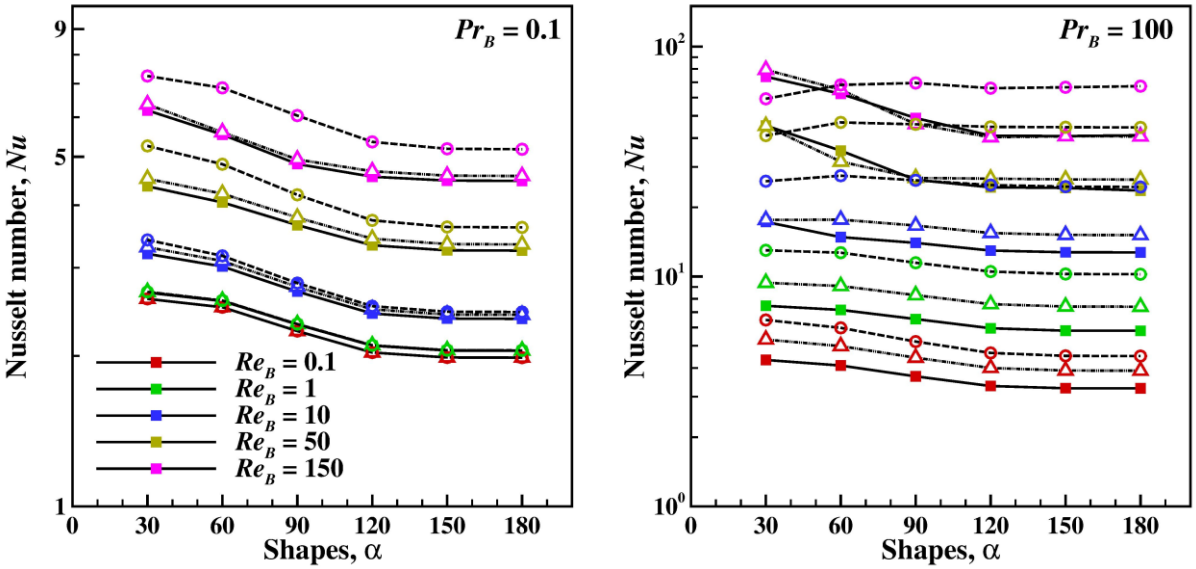


**Figure 4.57** Effect of shape on the Nusselt number at (a) $Bn$ = 0 (square symbol) (b) $Bn$ = 1 (Delta symbol) (c) $Bn$ = 100 (circle symbol).

for **Fig. 4.56**. Finally, a generalized correlation for the average Nusselt number is proposed as a function of $Pr_B$ ($0.1 \le Pr_B \le 100$), $Re_B$ ($0.1 \le Re_B \le 150$), $Bn$ ($0 \le Bn \le 100$) and $\psi$ ($0.424 \le \psi \le 1$) is given below:

$$Nu = a\left(1+Bn\right)^{b} + cRe^{d}Pr^{e}\psi^{f}\left(1+Bn\right)^{g} \tag{4.14}$$

The parameters of the **Eq. (4.14)** have splitted for the two ranges of $Pe_B$ (= $Pr_B \times Re_B$) number are given in the **Table 4.14** as follows:

Table 4.14 Coefficient for Eq. (4.14)

| | $a$ | $b$ | $c$ | $d$ | $e$ | $f$ | $g$ | $\delta_{avg}$ | $\delta_{max}$ |
|---|---|---|---|---|---|---|---|---|---|
| $Pe_B \le 15$ | 2 | -0.013 | 0.593 | 0.481 | 0.471 | -0.719 | 0.096 | 10.6% | 32% |
| $Pe_B > 15$ | 1.27 | 0.215 | 0.887 | 0.431 | 0.374 | -0.473 | 0.043 | 8.9% | 39% |

For $Pe_B \le 15$ and $Pe_B > 15$, total 1559 and 2273 data points, are used where only 16 and 24 data points show more than 30% error, respectively. For both the cases the maximum error arises in the case of smallest spherical segment α = 30°.

# Chapter 5
# Free convection

In this chapter, we focus on the natural convection from spherical and non-spherical bodies in non-Newtonian fluid under steady flow conditions. In the first section, both momentum and heat transfer characteristics are studied for the heated single and twin sphere for power-law fluid have been examined at very low Grashof number. The effect of gap between the twin spheres is also briefly explored for the hydrodynamic interference in between them. Next in the subsequent section, the thermal characteristics of spherical segments in Bingham plastic fluid have been explored. The obtained results are presented in form of streamlines, isothermal contours, yielded/unyielded region, local and average Nusselt number as a function of wide range of rheological and kinematic parameters.

## 5.1 Free convection from a single and twin sphere in power-law fluids at low Grashof number

### 5.1.1 Previous work

Much of the pertinent literature relates to the prediction of the thermal characteristics of an isothermal sphere at small Grashof numbers in Newtonian fluids (Martynenko and Khramtsov, 2005; Patel *et al.*, 2017; Amato and Tien, 1972; Jafarpur and Yovanovich, 1992). While the early approximate analyses were based on the series expansion methods at low Grashof numbers (Fendell, 1968; Hossain and Gebhart, 1970; Hieber and Gebhart, 1969; Mahony,1957) which are supplemented by the boundary layer results at high Rayleigh and Grashof numbers. Thus, for instance, Hieber and Gebhart (1969) reviewed the prior analytical studies (Fendell, 1968; Hossain and Gebhart, 1970; Hieber and Gebhart, 1969; Mahony,1957; Elenbass, 1942) in their work on the mixed convection from a sphere in a Newtonian fluid ($Pr = 1$) which delineated the contribution of the forced- and free- convection to the total drag coefficient. They used the matched asymptotic expansion in the so-called inner and outer fields within the range of the Grashof number to the order of $Re^2$ (both $Gr$ and $Re \to 0$). In the limit of the pure natural convection (large Richardson number $Ri = Gr/Re^2$), their analysis suggests the following expression for drag on a sphere in the limit of $Gr \to 0$:

$$C_D = \frac{24\phi(Pr)}{\sqrt{Gr}} \tag{5.1}$$

**Equation (5.1)** has a striking similarity with the Stokes drag equation by recognizing that $Re \sim \sqrt{Gr}$. Similarly, for the surface average Nusselt number Hieber and Gebhart (1969) reported the following correlation up to the second-order correction in Grashof number as:

$$Nu = 2 + Gr + Gr^2\left(0.139 - 0.4519Pr + 1.1902Pr^2\right) \tag{5.2}$$

They divided the flow region into three sub-domains: close to the sphere, there exists a Stokes-like region characterized by feeble flow (low momentum) and large body force. Beyond this region, when the fluid velocity reaches its maximum value, all terms in the governing equations (momentum, viscous, body force, and pressure effects) are relevant, and the fluid velocity eventually approaches zero far away from the sphere. **Equation (5.2)** was stated to be valid under the conditions of $Gr \leq \sim 1$ and $Pr \sim 1$. Their analysis also suggests that up to $Gr = 0.01$, the local Nusselt number is nearly constant ($Nu \sim 2$) over the entire surface of the sphere whereas at $Gr = 0.40$, convection sets in the front of the sphere thereby augmenting the value of the local Nusselt number beyond its conduction value of $Nu = 2$. Stewart (1971) considered the free convection from a sphere and other three-dimensional shapes within the framework of boundary layer equations for Newtonian fluids, which is a further extension of Acrivos (1960) analysis in power-law fluids. For Newtonian fluids, this analysis predicts the drag coefficient for a sphere, as:

$$C_D = \frac{K}{\pi}\left(Gr\ Pr\right)^{-1/4} \tag{5.3}$$

The value of $K$ ranges from 21 for $Pr = 0.72$ to 27.4 for $Pr = 1000$, though for $Pr \geq 10$, it varies only from 25.15 to 27.4. Notwithstanding the minor differences in the numerical constants, **Eqs. (5.1)** and **(5.3)** differ significantly in terms of the role of the Grashof number. This is like the role of Peclet number in the forced convection regime. Subsequently, Geoola and Cornish (1981;1982) have numerically studied the natural convection in air from a sphere over the range $0.05 \leq Gr \leq 50$. They have also studied time-dependent natural convection to delineate the time-delay in the onset of buoyancy-induced flow and they observed weak convective current close to the outer boundary even at extremely small values of Grashof number (Geoola and Cornish, 1982). Owing to the relatively short computational domain ($12d$), their results are presumed to be less reliable (Jia and Gogos, 1996a; 1996b; Yang *et al*., 2007). However, more reliable results and over a somewhat wider range of Grashof number ($10 \leq Gr \leq 10^8$) and Prandtl number (= 0.72 and 7) have been reported by Gogos and co-workers (Jia and Gogos, 1996a; 1996b; Yang *et al*., 2007). These studies also confirm the scaling of the drag coefficient (non-dimensional total drag) as $C_D \sim (Gr\ Pr)^{-1/4}$, in line with the analysis of Stewart (1971), given here by **Eq. (5.3)**. Subsequently, a comprehensive study on drag coefficient of a sphere in free convection flows over wide ranges of Grashof and Prandtl numbers has been reported in Newtonian as well as in power-law fluids (Prhashanna and Chhabra, 2010). However, no attempt was made to develop a correlation between the hydrodynamic drag force and the Rayleigh number. There have been parallel experimental developments in the measurement of drag on a single sphere in natural convection and mixed convection regimes. For instance, Dudek *et al*. (1988) measured the drag force on 10–250 μm sized spheres in air, $N_2$, and $CO_2$ at very small Grashof numbers ($0.002 \leq Gr \leq 0.03$). Based on their experiments, they proposed the following drag correlation for a sphere:

$$\log C_D = 1.054 - 0.960x - 0.097x^2 \qquad (5.4)$$

where $x = \log Gr$

**Equation (5.4)** was stated to be valid in the range $0.69 \leq Pr \leq 0.78$. Also, these results agree with the numerical predictions of Yang *et al.* (2007) and the value of the ratio ($C_{DF}/C_{DP}$) was found to be ~ 2 at such low Grashof numbers, like in the case of the Stokes flow regime. A few other studies on drag measurements are also available, but most of these relate to the cross-buoyancy flow (Ziskind *et al.*,2001) or aiding or opposing buoyancy mixed-convection conditions (Mogarbi *et al.*, 2002), etc. Also, these studies span relatively small values of *Gr* and *Re* which are way below the currently available numerical results, and it is thus not possible to make a direct comparison between the predictions and observations. An experimental study involving the measurement of velocity and temperature in the vicinity of an isothermal sphere has been reported by Hossain (1966) over the range of conditions $0.01 \leq Gr \leq 2.54$ for a wide range of Prandtl numbers. Similarly, Tsubouchi *et al.* (1959) have documented the values of the average Nusselt number for nearly spherical particles in air at low Grashof numbers ($0.01 \leq Gr \leq 4$). At such low Grashof numbers, their Nusselt number values do seem to approach the expected limiting value of $Nu = 2$. All in all, as noted above, there is a paucity of results for low Grashof number in general, for both Newtonian and power-law fluids even for the case of an isolated sphere.

The relevant literature for free convection from vertically aligned two spheres is even more scant. For instance, Chamberlain *et al.* (1985) correlated their experimental results on average Nusselt number for two vertically touching spheres by adding the expected conduction limiting value and the boundary layer predictions (thin boundary layer) over the range $10 \leq Ra \leq 10^7$ for air. Similarly, Raithby and Hollands (1976) and Hassani and Hollands (1989) identified a linear characteristic dimension for complex shaped objects to consolidate their experimental results for two touching spheres obtained in air as the working medium. In addition to the above-noted limited experimental studies, Musong *et al.* (2016) numerically investigated free convection heat transfer in air from two spheres with air as the working fluid. In particular, their results for vertically aligned two spheres are of direct relevance to the present work. Their results are however limited to a single value of $Gr = 100$ (and $Pr = 0.71$) but for centre-to-centre spacing varying from 1 (touching) to 10. Subsequently, Zhang *et al.* (2019) have also studied interactions between two vertically aligned spheres in air for a fixed value of the Rayleigh number, $Ra = 10^5$ and for the centre-to-centre spacing ranging from 2 to 24. The interference between the two spheres progressively decreased with the increasing gap, though the behavior of the upper sphere is influenced by the mixed flow impinging on it and due to the preheating of the fluid by the lower sphere.

As far as known to us, no prior results are available on free convection heat transfer for two vertically aligned spheres immersed in power-law fluids. The present study focuses on obtaining reliable results of total drag and average Nusselt number for a heated isolated sphere and for vertically aligned two spheres under free convection regime. Numerical studies are performed for both Newtonian ($n = 1$) and power-

law fluid ($0.1 \leq n \leq 2$ for a single sphere and $0.1 \leq n \leq 1.5$ for a pair of spheres), at low Grashof numbers ($10^{-4} \leq Gr \leq 10$) and high Prandtl numbers ($0.72 \leq Pr \leq 1000$) which considerably extends the range of previously reported results for a single sphere (Prhashanna and Chhabra, 2010) and for two vertically aligned spheres (Musong *et al.*, 2016; Zhang *et al.*, 2019). For the vertically aligned twin sphere case, centre-to-centre spacing between two spheres defined as gap ratio, $l/d$, three values of 1, 4 and 6 have been used to explore the hydrodynamic interference between the two spheres. Furthermore, the present results are compared with the scant experimental data as far as possible, especially at low Grashof numbers for the isolated sphere as well as the twin sphere case.

### 5.1.2 Physical model and mathematical formulation

**Figure 5.1a** and **5.1b** show the schematics of the two configurations studied herein and the corresponding computational domains employed in this work. Since the coupled momentum and thermal equations and the boundary conditions employed herein are identical to that used in ref. (Prhashanna and Chhabra, 2010) for the isolated sphere, these are presented here in brief. For both cases, the velocity and the temperature fields are governed by the momentum and energy equation written in their dimensionless form as **Eqs. (2.1) – (2.3).**

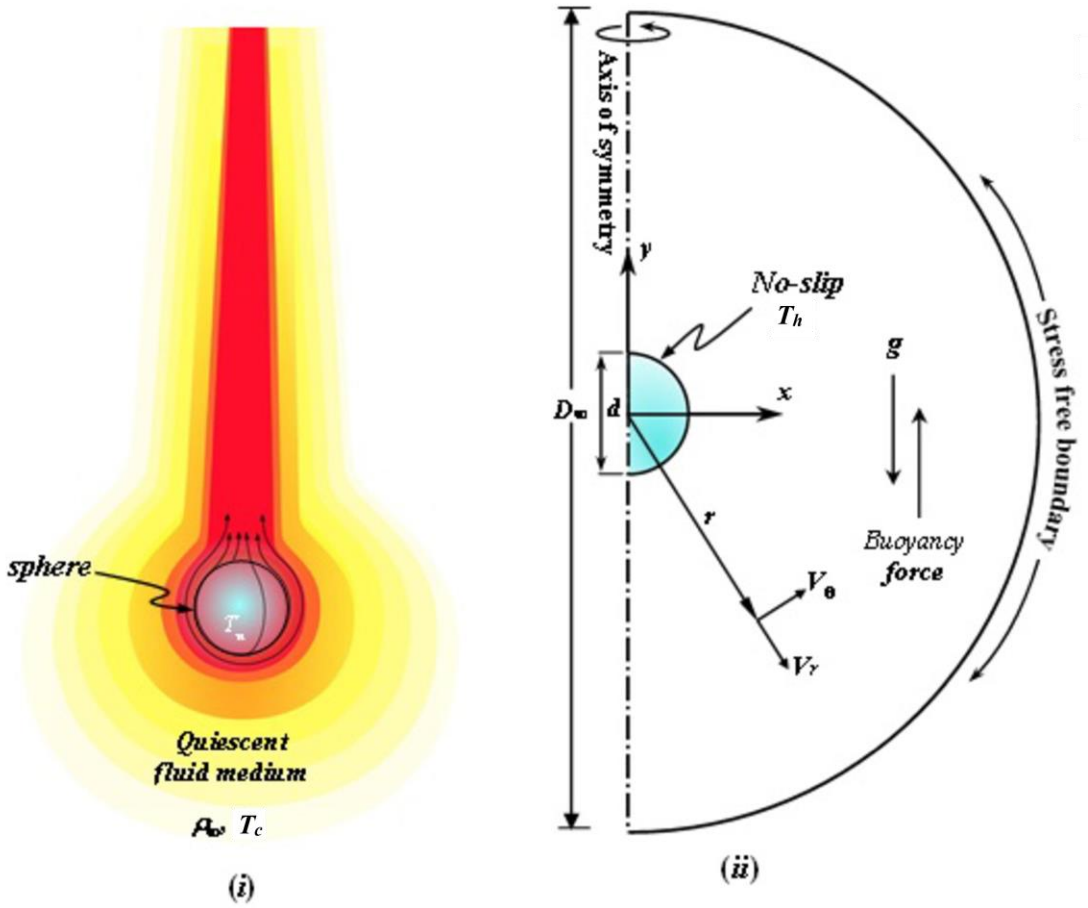


**Figure 5.1a**. Schematics of (i) physical model and (ii) computational domain for a single sphere.

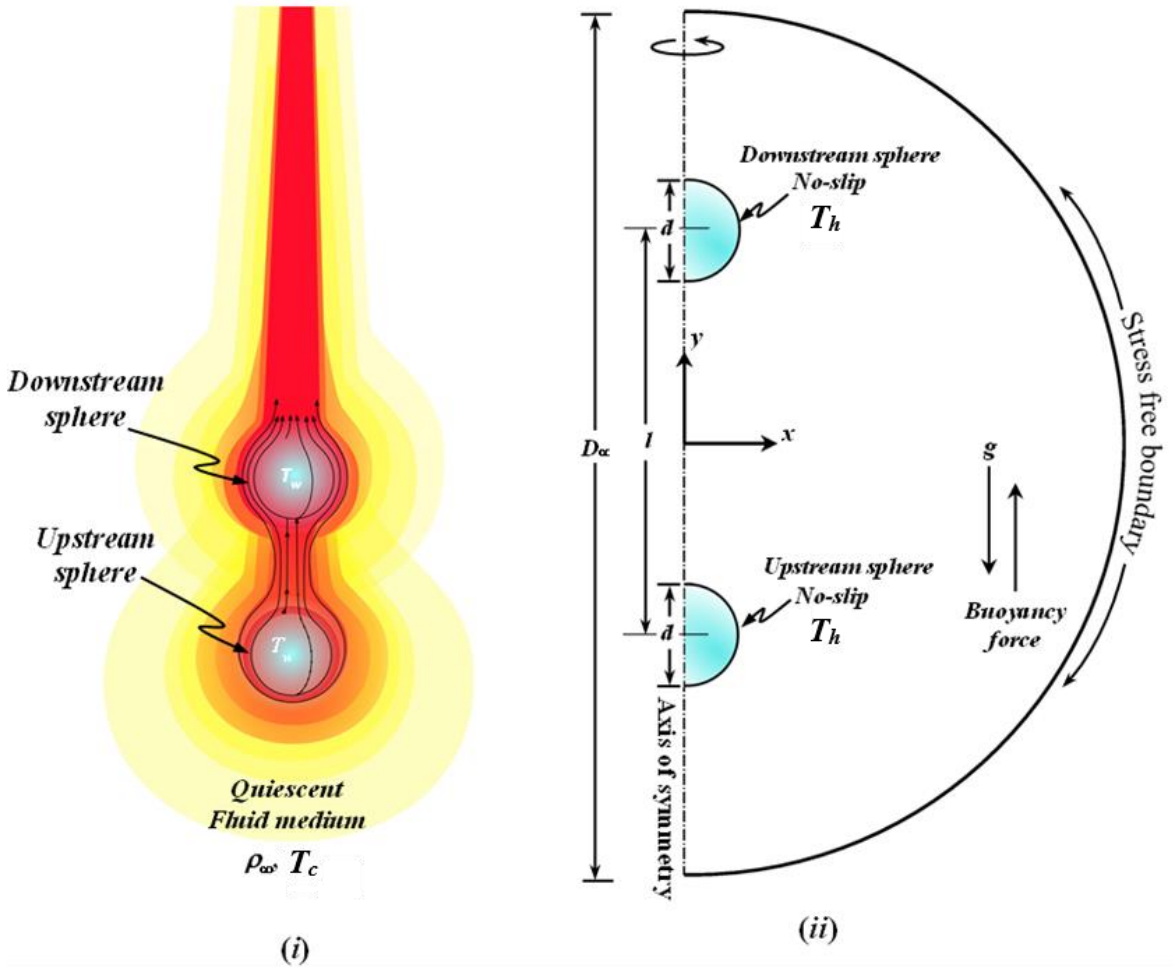


**Figure 5.1b.** Schematics of (i) physical model and (ii) computational domain for a twin sphere.

**Equations (2.1 – 2.3)** have been rendered dimensionless using $R$ and $V_c$ as the characteristic length and velocity scales, respectively. Thus, pressure and the stress components, respectively, have been scaled as $\rho V_c^2$ and $m(V_c/R)^n$ and whereas the non-dimensional temperature is defined as $\xi = (T - T_c)/(T_h - T_c)$. The physically realistic boundary conditions for the flow are that of no-slip and constant temperature on the surface of solid sphere for both configurations and for temperature at the far away boundary (fictitious spherical envelope of diameter $D_\infty$), $\frac{\partial \xi}{\partial r} = 0$ (Neumann type). The fluid velocity is expected to have dropped to zero, but the more commonly used condition is that of no stress, similar to Neumann type conditions, which ensure that the rate of change of $\theta$-velocity in the radial direction is zero whereas the radial velocity itself approaches zero. It is appropriate to add here that the far-away boundary conditions exert very little influence on the results for sufficiently large values of $D_\infty$ (Saitoh *et al.*, 1993; Prhashanna and Chhabra, 2011) such as that used here.

For the case of the twin- spheres also, the usual no-slip condition for velocity and constant temperature for energy equations are implemented on the surface of the spheres. At the faraway spherical boundary,

the stress-free boundary condition has been applied as explained above. The surface of the spheres is maintained at a constant temperature $\xi = 1$ whereas the radial temperature gradient is applied at $r = D_\infty/2$. For both the cases of single and twin spheres, the flow remains steady over the range of parameters spanned here and hence, the problem has been solved for by assuming axisymmetric flow.

The coupled field of **Eqs. (2.1) to (2.3)** with the constitutve **Eq. (2.5)** have been solved here using the finite element based COMSOL Multiphysics (Version 5.3a), as detailed in a later section. The velocity and temperature fields can be post-processed to deduce the value of the heat transfer coefficient and hydrodynamic force exerted on the sphere.

### 5.1.3 Choice of numerical parameter and validation

As the numerical solution methodology is described in detail in ref. (Prhashanna and Chhabra, 2010), only the key features are presented here. Parameters such as domain size and the number of grid elements in the flow domain influence the accuracy and reliability of the numerical results. Bearing in mind the fact that at small Grashof numbers and/or Prandtl numbers, the feeble buoyancy-induced flow field decays slowly and hence a large domain is required for numerical simulations as noted by others also in the context of Newtonian fluids (Dudek *et al.*, 1988). For this purpose, the value of $D_\infty/d$ was varied from 20 to 3000 and the resulting values of $C_D$ and $Nu$ in Newtonian fluids are shown in **Fig. 5.2**. Clearly, the Nusselt number necessitates a much shorter computational domain (**Fig. 5.2b**) than that needed for the corresponding drag values to stabilize, as also noted by Dudek *et al.* (1988). Indeed, smaller the value of the Grashof number, the larger the value of $D_\infty/d$ required to obtain reliable values of $C_D$. **Figure 5.3** shows this effect much more clearly with reference to the results of Dudek *et al.* (1988). Their numerical values are based on $D_\infty/d = 40$. The present values of $Nu$ included here are based on $D_\infty/d = 1000$. Two

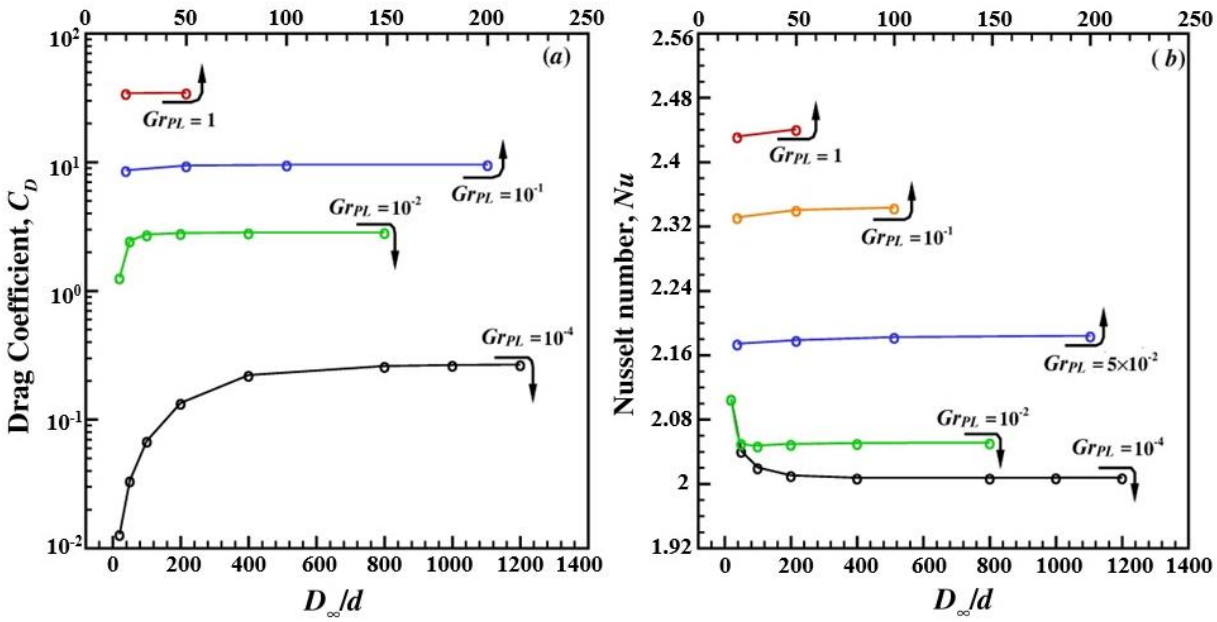


**Figure 5.2** Effect of outer boundary on the drag coefficient and Nusselt number for $Pr_{PL} = 0.72$ for a single sphere.

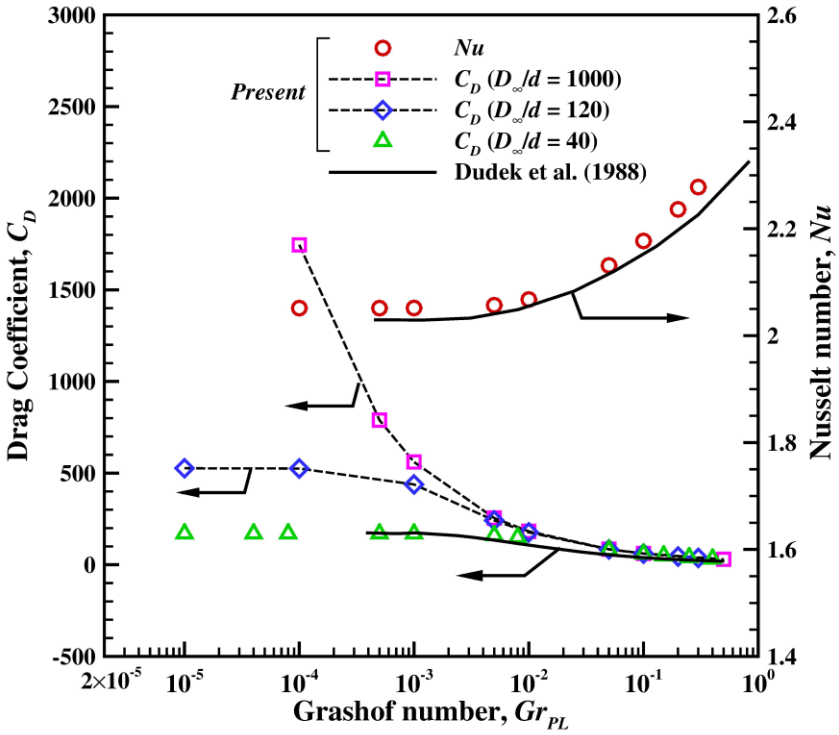


**Figure 5.3** Validation of drag coefficient and Nusselt number for $Pr_{PL}$ = 0.72 for a single sphere.

observations are in order here. Firstly, the Nusselt number is robust with respect to the size of the computational domain, and the Nusselt number is within 0.05% of the expected conduction limit of $Nu$ = 2 at $Gr = 10^{-4}$. On the other hand, the present drag values (obtained using $D_\infty/d$ = 1000) agree with that of Dudek *et al.* (1988) obtained with $D_\infty/d$ = 40 only up to about $Gr$ = 0.05. In order to further explore this aspect, additional simulations have been performed here using $D_\infty/d$ = 40 (same as that used in reference (Dudek *et al.* (1988)) for $10^{-5} \leq Gr \leq 0.05$ (shown as green symbols in **Fig. 5.3**) and irrespective of the value of the Grashof number, the value of the drag is seen to approach a constant value. Consequently, to capture both the thickest momentum and thermal boundary layers for $n$ = 0.1 and for $n$ = 1 at the lowest value of $Pr$ = 0.72 in this work, two domain sizes were chosen as $D_\infty/d$ = 3000 and 1000 for the Grashof number ranges $10^{-4} \leq Gr \leq 0.9$ and $0.9 < Gr \leq 10$, respectively. Further increase in the value of ($D_\infty/d$) for the aforementioned range of parameters changed the values of $C_D$ and $Nu$ by less than 1%. Moreover, for the extreme values of the Prandtl number ($Pr$ = 0.72, 1000) and power-law index ($n$ = 0.1, 2), the values of drag coefficient and average Nusselt number in both domains were examined at an intermediate value of $Gr$ = 0.9 and the difference between these values obtained with the two domains is also less than 1%. In a similar fashion, by varying the number of nodes on the surface of the sphere ($N_p$), the effect of the grid density on the values of $C_D$ and $Nu$ has been explored (**Table 5.1a** and **5.1b**). In the case of a single sphere, quadrilateral grids have been used in both domains (**Fig. 5.4a**). There is only a marginal difference observed as the number of nodes ($N_p$) is increased on the surface of the sphere from 250 to 300 on drag coefficient and Nusselt number values (**Table 5.1.1a** and **5.1.1b**). Furthermore, the adequacy of the computational grids used herein has been verified by comparing the Nusselt number

**Table 5.1a** Grid independence test for a single sphere for $Gr_{PL} \leq 0.9$.

| $D_\infty/d$ | $Gr_{PL}$ | $N_p$ = 250, $N_{pd}$ = 1425,00* | | | | $N_p$ = 300, $N_{pd}$ = 204,000# | | | |
|---|---|---|---|---|---|---|---|---|---|
| | | $Pr_{PL}$ = 0.72 | | $Pr_{PL}$ = 1000 | | $Pr_{PL}$ = 0.72 | | $Pr_{PL}$ = 1000 | |
| | | $n$ = 0.1 | $n$ = 2 | $n$ = 0.1 | $n$ = 2 | $n$ = 0.1 | $n$ = 2 | $n$ = 0.1 | $n$ = 2 |
| | | $C_D$ | | | | $C_D$ | | | |
| 3000 | $10^{-4}$ | 2777.8 | 509.69 | 1343.9 | 22.786 | 2776.8 | 510.31 | 1342.7 | 22.811 |
| | 0.9 | 27.028 | 20.763 | 7.0608 | 1.7051 | 27.014 | 20.784 | 7.0729 | 1.7148 |
| | | $Nu$ | | | | $Nu$ | | | |
| | $10^{-4}$ | 2.0009 | 2.0363 | 2.034 | 3.4511 | 2.0008 | 2.0363 | 2.0339 | 3.4509 |
| | 0.9 | 2.3558 | 2.4529 | 5.7636 | 9.2896 | 2.3558 | 2.4528 | 5.7637 | 9.2881 |

distribution on the surface of the sphere for the extreme values of the governing parameters in both domains, as shown in **Fig. 5.5**. It clearly depicts that the values of the Nusselt number overlap for the two cases of the nodes on the surface of the sphere from $N_p$ = 250 and $N_p$ = 300. The present results are, hence, based on the $N_p$ = 250 and the total grid elements in the computational domain $N_{pd}$ = 142,500 (Grid G1)

**Table 5.1b** Grid independence test for a single sphere for $Gr_{PL} \geq 0.9$.

| $D_\infty/d$ | $Gr$ | $N_p$ = 250, $N_{pd}$ = 116,250* | | | | $N_p$ = 300, $N_{pd}$ = 139,500# | | | |
|---|---|---|---|---|---|---|---|---|---|
| | | $Pr$ = 0.72 | | $Pr$ = 1000 | | $Pr$ = 0.72 | | $Pr$ = 1000 | |
| | | $n$ = 0.1 | $n$ = 2 | $n$ = 0.1 | $n$ = 2 | $n$ = 0.1 | $n$ = 2 | $n$ = 0.1 | $n$ = 2 |
| | | $C_D$ | | | | $C_D$ | | | |
| 1000 | 0.9 | 27.013 | 20.768 | 7.6474 | 10.511 | 27.103 | 20.789 | 7.6744 | 10.522 |
| | 10 | 6.9375 | 1.7051 | 2.0959 | 1.0154 | 6.9473 | 1.7073 | 2.097 | 1.0167 |
| | | $Nu$ | | | | $Nu$ | | | |
| | 0.9 | 2.3549 | 2.4529 | 3.4862 | 2.7917 | 2.3549 | 2.4529 | 3.4861 | 2.7917 |
| | 10 | 5.7238 | 9.2895 | 10.535 | 12.979 | 5.7235 | 9.2892 | 10.529 | 12.978 |

* Grid G1, # Grid G2 in computational domain

and 116,250 (Grid G2) for $D_\infty/d$ = 3000 and $D_\infty/d$ = 1000, respectively for a single sphere.

For the case of twin spheres, the domain size chosen above for a single sphere has been found adequate for the highest gap ratio $l/d$ = 6. On the other hand, a grid independence study has been performed for the extreme values of $l/d$ = 1 and $l/d$ = 6 separately. The flow domain has been discretized using triangular grids in the vicinity of the spheres and using quadrilateral cells in the remaining faraway regions as shown in **Figs. 5.1.4b** and **5.1.4c**. The case of the touching spheres ($l/d$ = 1) requires a dense grid on the surface ($N_p$ = 400 for each sphere) to capture the steep gradients due to a single point of contact. For $l/d$ = 4 and

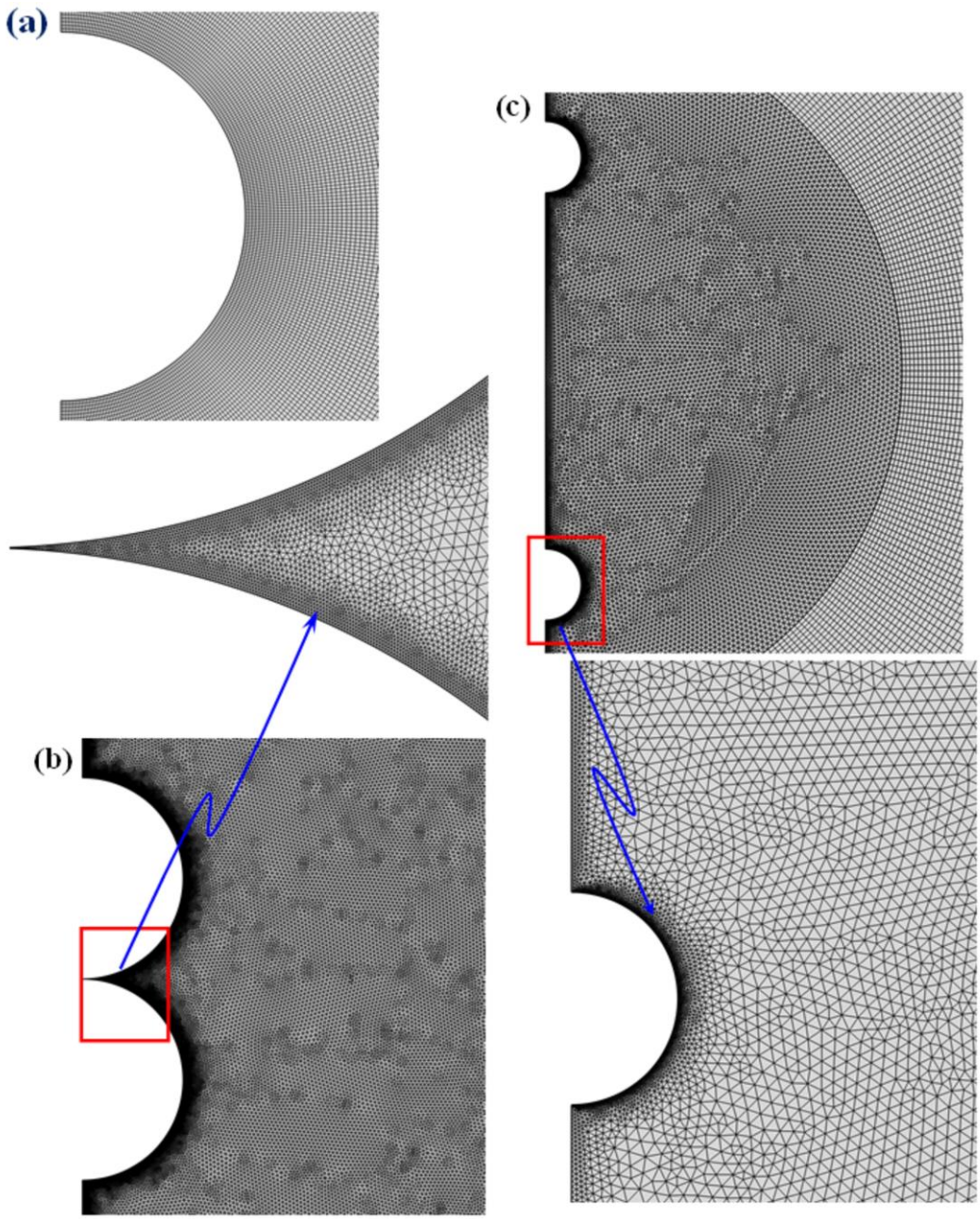


**Figure 5.4.** Grid structure for (a) single sphere (b) twin sphere at $l/d$ = 1 (c) twin sphere at $l/d$ = 6.

$l/d$ = 6, the number of nodes has been found identical to the single sphere, i.e., $N_p$ = 250. As a result, the total number of cells in the domain ranges from $N_{pd}$ = 384,500 for $l/d$ = 1 to $N_{pd}$ = 130,000 for $l/d$ = 6.

The finite-element numerical scheme adopted in this work by employing COMSOL Multiphysics® (Version 5.3a) discretizes the **Eqs. (2.1) - (2.3)** in a sparse linear system. PARDISO (Parallel Sparse Linear Direct Solver) has been used for the steady, 2-D axisymmetric, laminar flow and heat transfer modules to solve for the flow and temperature fields. Based on extensive exploratory simulations, the relative convergence criterion of $10^{-5}$ for the continuity, momentum and thermal energy equations has been set for all the field variables in the flow domain for simulations to have converged. Adequacy of the

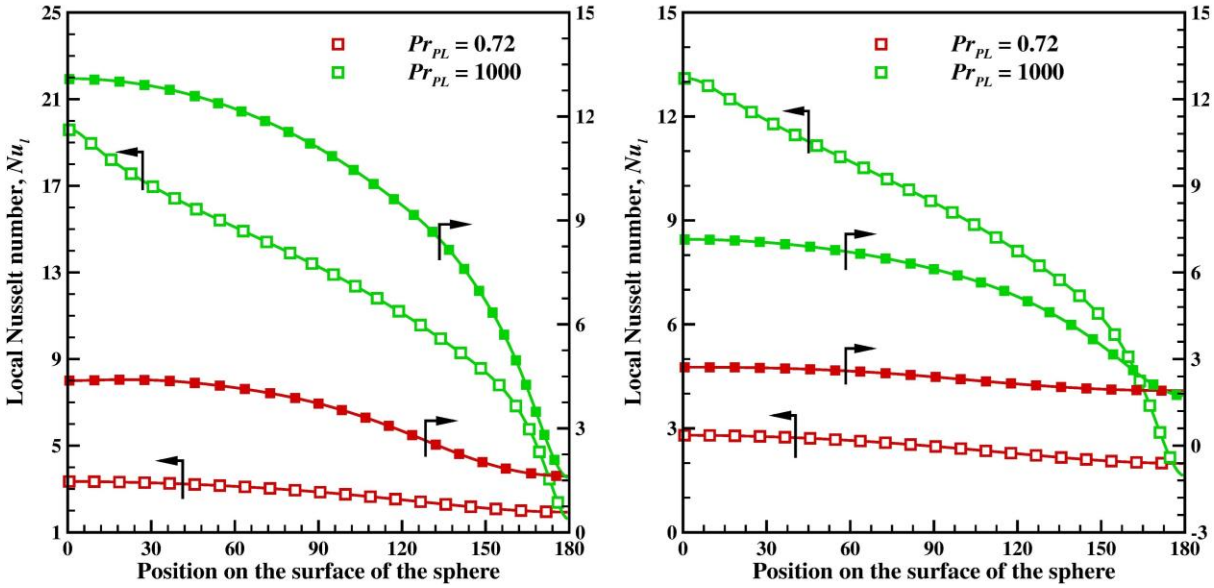


**Figure 5.5** Effect of grids on the variation of Nusselt number on the surface of the sphere at $n$ = 0.1 (filled symbols) and $n$ = 2 (hollow symbols) (a) $D_\infty/d$ = 1000 at $Gr_{PL}$ = 10 (b) $D_\infty/d$ = 3000 at $Gr_{PL}$ = 0.9 (symbols: Grid G1; lines Grid G2, see details in **Table 5.1**).

numerical parameters detailed above is further illustrated by way of presenting detailed comparisons with the previous numerical and experimental studies culled from the literature.

In **Fig. 5.6**, the present values of the local Nusselt number are compared with that of Singh and Hasan (1983) for air over the range of Grashof number $0.01 < Gr < 1$. They used the value of $D_\infty/d$ in the range 20 to 80. The agreement between the two results is fair in the overlapping range of conditions. Also, the isotherms shown in **Fig. 5.7**, are in good agreement with each other for $Gr \geq 0.1$. Furthermore, the present predictions of temperature profiles are compared in **Fig. 5.8** with the experimental results of Hossain (1966). The agreement is seen to be reasonable in the range $0.023 \leq Gr \leq 2.54$ and $125 \leq Pr \leq 1000$. Finally, the present numerical and experimental results for the average Nusselt number, $Nu$ of a single sphere culled from various sources over the range of $10^{-4} \leq Gr \leq\sim 6$ and $0.7 \leq Pr \leq 1000$ have been compared with each other in **Fig. 5.9**. Included here also the predictions of the widely used correlation of Churchill and Churchill (1975) given below:

$$Nu = 2 + \frac{(1.6Ra)^{1/4}}{\left[1+\left(\frac{0.5}{Pr}\right)^{9/16}\right]^{4/9}} \tag{5.4}$$

The correspondence between the present and previous results in **Fig. 5.9** is seen to be excellent. The preceding comparisons coupled with those reported in ref. (Prhashanna and Chhabra, 2010) for $Gr$ >10 lend credibility to the new results included here which are regarded to be reliable to within 1–2%. It is

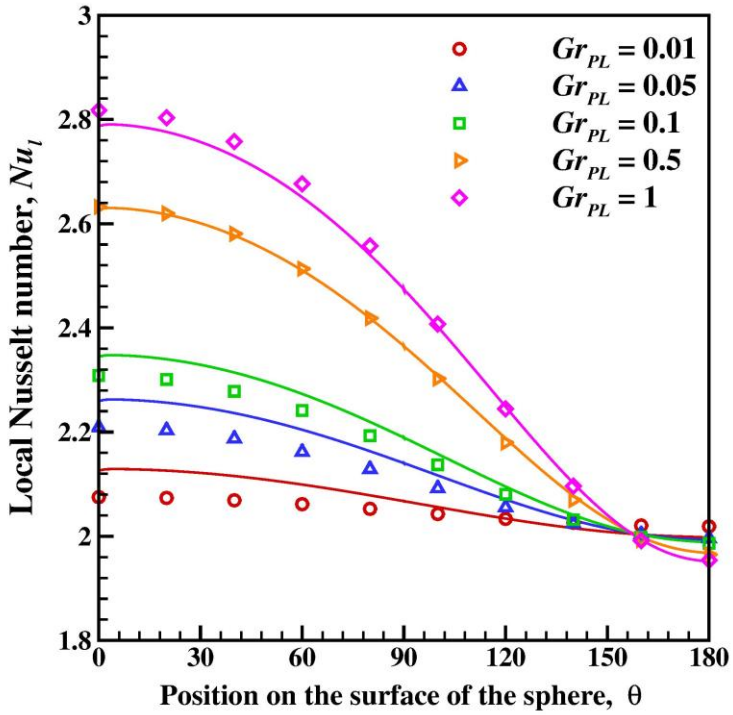


**Figure 5.6.** Validation of the present results (line) of local Nusselt number with that of Singh and Hassan (1983) (symbols) at $Pr_{PL}$ = 0.7 for a single sphere.

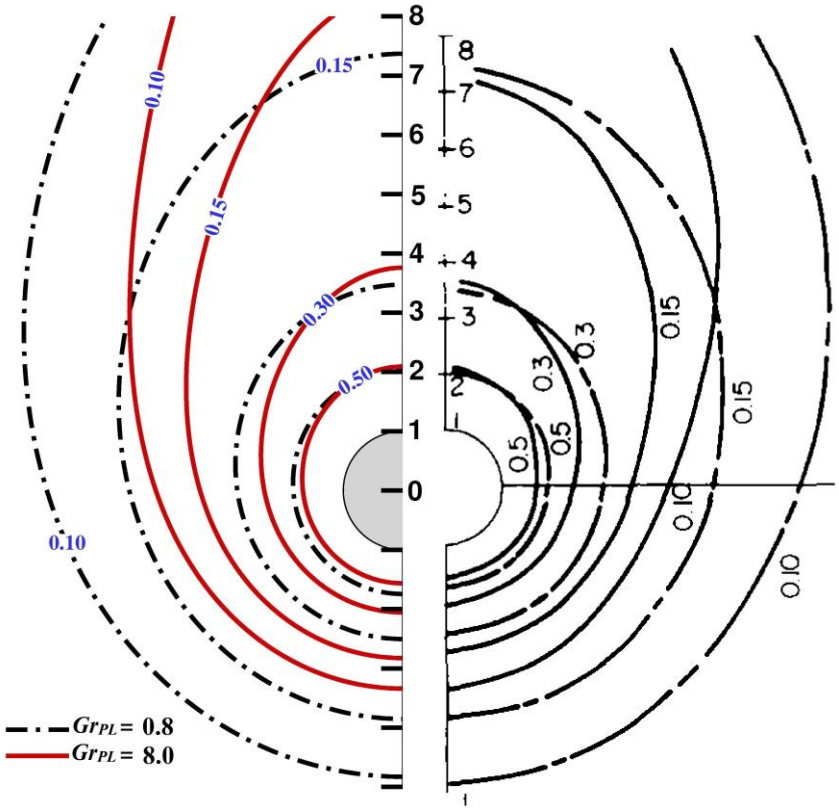


**Figure 5.7.** Comparison of isotherms at $Pr_{PL}$ = 0.7 with the results of Singh and Hassan (1983) for a single sphere.

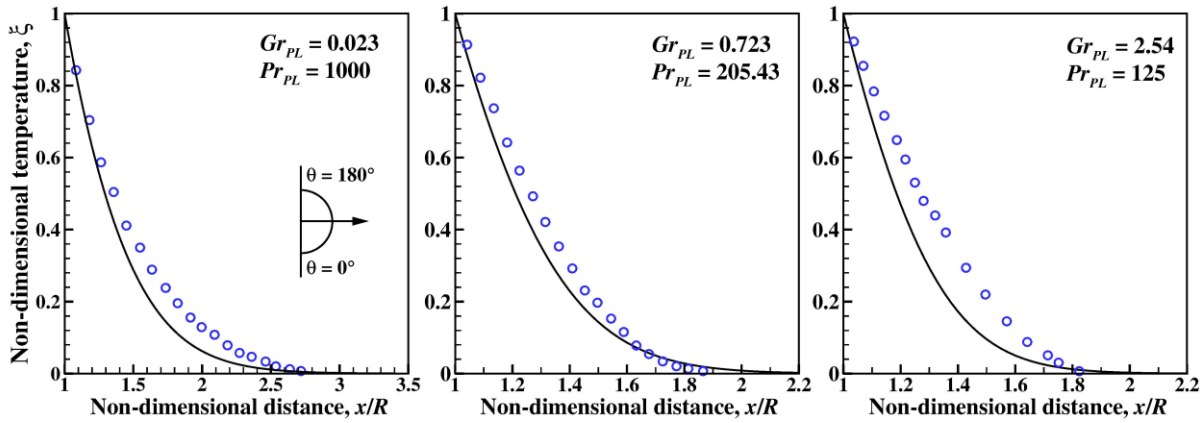


**Figure 5.8** Comparison of present temperature profiles (line) at θ = 90° with the experimental results of Hossain and Gebhart (1966) (symbols) for a single sphere.

useful to mention here that in the limit of $Ra \rightarrow 0$, the conduction limit for a sphere $Nu = 2$ is seen to be approached here. For instance, the present numerical results approach this limit at about $Ra \sim 10^{-4}$ within about 2%. The experimental results from Tsubouchi *et al.* (1959) shown in **Fig. 5.9** also seem to show such a levelling off. Also, it is not at all easy to achieve the pure free convection regime in an experimental study. Finally, it is also not always possible to approach the unconfined sphere limit in numerical simulations at low Grashof numbers as that used here. All these factors will yield higher values of the Nusselt number than that expected in the free convection regime. Also, the experimental errors in this limit can be as high as 50% as can be gaged from the scant experimental results (Amato and Tien, 1976; Liew and Adelman, 1975) included in **Fig. 5.9**. For low Rayleigh number, only Chamberlain *et al.* (1985) have reported limited experimental results for twin spheres ($l/d = 1$). **Table 5.2** shows a comparison between their and the present results for air ($Pr = 0.72$); once again, an excellent agreement exists

**Table 5.2** Comparison of the average Nusselt number for air ($Pr_{PL} = 0.72$) for the two touching spheres $l/d$ =1.

| $Gr_{PL}$ | $Ra_{PL}$ | $Nu_{avg}$ | |
|---|---|---|---|
| | | Present | Chamberlain *et al.* (1985) |
| - | $Ra \rightarrow 0$ | 1.387 | 1.386 |
| 0.0001 | $7.20 \times 10^{-5}$ | 1.3955 | 1.4148 |
| 0.0005 | $3.60 \times 10^{-4}$ | 1.4059 | 1.4321 |
| 0.001 | $7.20 \times 10^{-4}$ | 1.4133 | 1.4419 |
| 0.005 | $3.60 \times 10^{-3}$ | 1.4418 | 1.4726 |
| 0.01 | $7.20 \times 10^{-3}$ | 1.4610 | 1.4901 |
| 0.05 | $3.60 \times 10^{-2}$ | 1.5305 | 1.5447 |

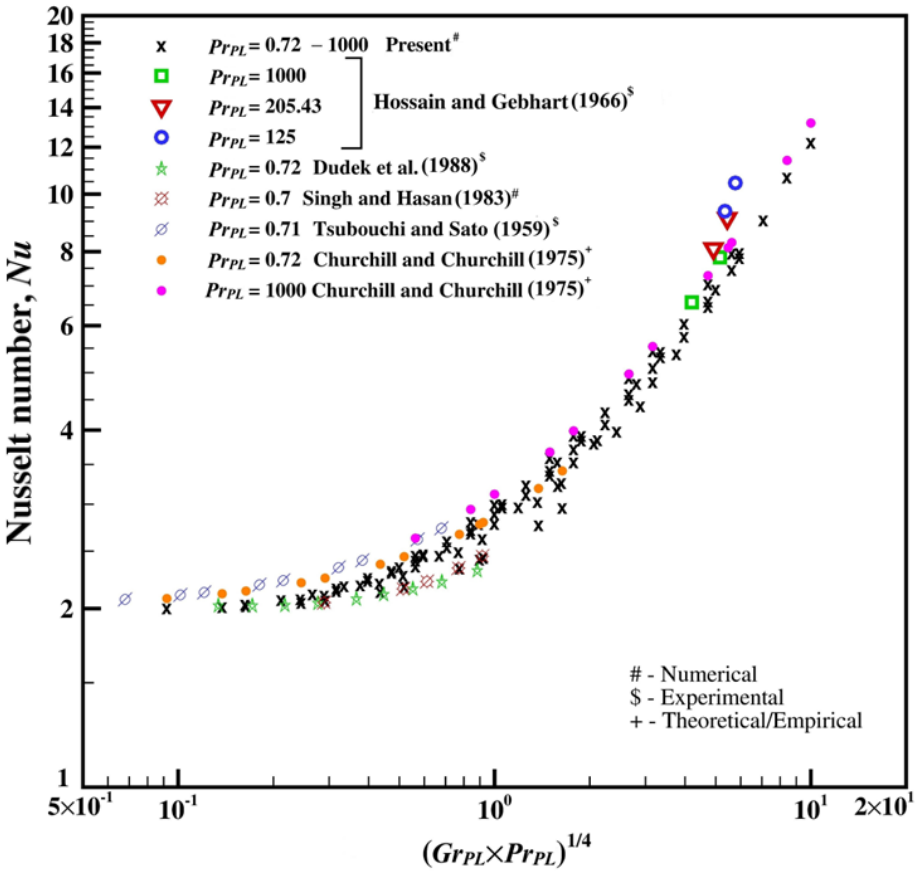


**Figure 5.9** Comparison of average Nusselt number with the literature for a single sphere.

between the two results. Finally, the present values of the average Nusselt number for two spheres arrangement have been compared with the experimental results of Hassani and Holland (1989) and the numerical results of Musong *et al.* (2016) for air at $Ra > 50$ for varying gap ratios (**Fig. 5.10**). The close correspondence seen in this case also lends credibility to the present solution methodology. Suffice it to

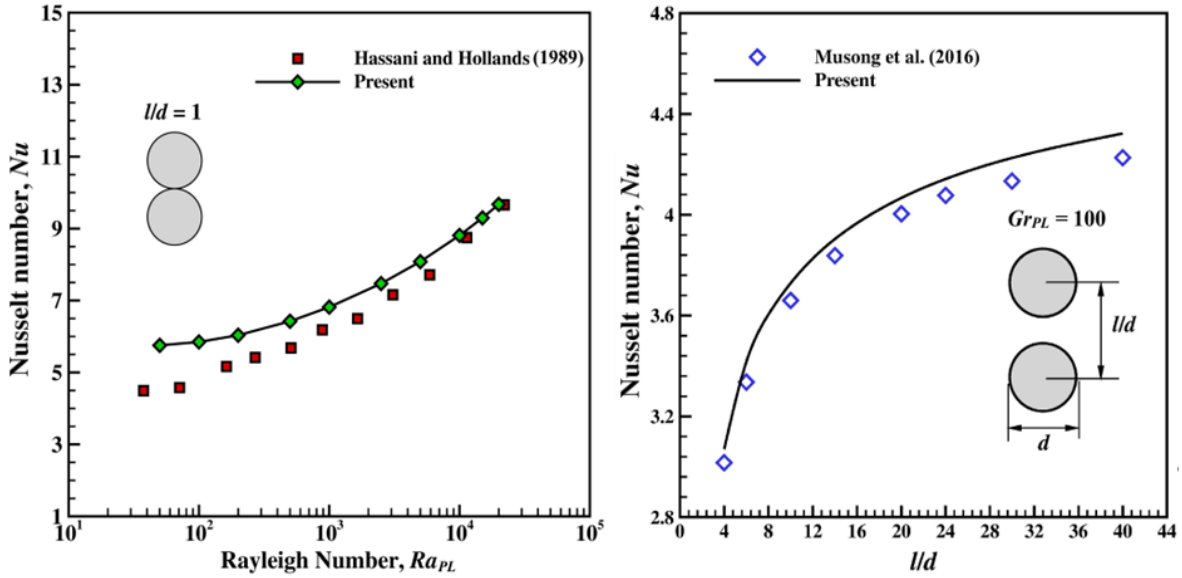


**Figure 5.10** Validation of the average Nusselt number for twin spheres with the varying gap ratios in air ($Pr_{PL}$ = 0.72).

say here that additional validation and comparison with experimental data on local temperature and velocity profiles in power-law fluids are reported in Ref. (Prhashanna and Chhabra, 2010) and hence these are not repeated here.

### 5.1.3 Results and discussion

Altogether, nearly 2000 individual numerical results for single and 4600 for twin-spheres denoting different combinations of the values of $Gr_{PL}$, $Pr_{PL}$, $n$ and $l/d$ have been obtained in this work; these results extend over the following ranges of parameters, $Gr_{PL}$ ($10^{-4}$, $10^{-3}$, $5 \times 10^{-3}$, $10^{-2}$, $5 \times 10^{-2}$, $10^{-1}$, $5 \times 10^{-1}$, 1, 10), $Pr_{PL}$ ($0.72 \leq Pr \leq 1000$), $n$ ($0.1 \leq n \leq 2$ for a single sphere and $0.1 \leq n \leq 1.5$ for a pair of spheres), and $l/d$ (1, 4, 6). These have been used to delineate the influence of each of these parameters on free convection from an isolated sphere and from two identical spheres aligned vertically.

*5.1.3.1 Isolated sphere*

*A. Drag on sphere*

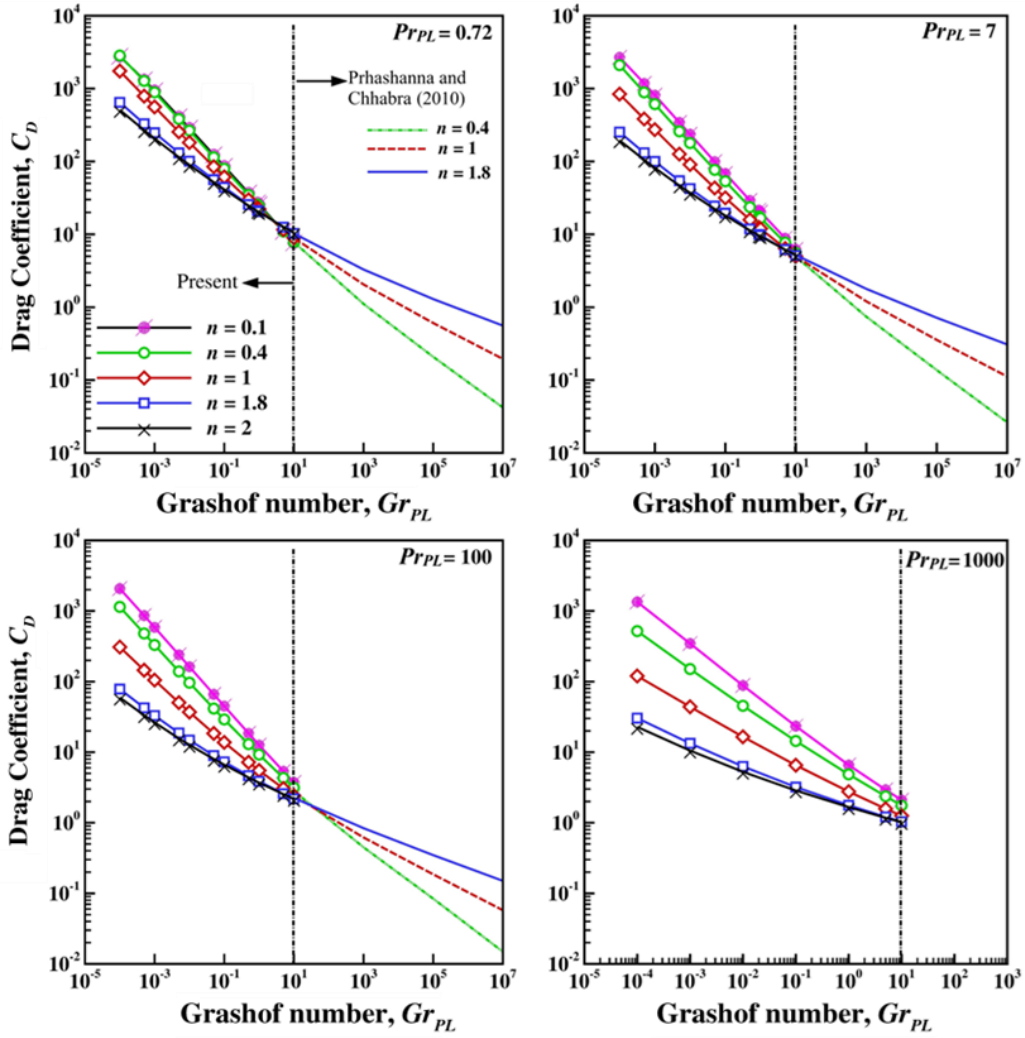


**Figure 5.11** Variation of drag coefficient as a function of Grashof number ($Gr_{PL}$), Prandtl number, ($Pr_{PL}$) and power-law index ($n$) for a single sphere.

**Figure 5.11** plots the drag coefficient, $C_D$ experienced by the sphere for scores of values of the power-law index ($n$), Grashof number ($Gr_{PL}$), and Prandtl number ($Pr_{PL}$). This figure also includes the previous results of Prhashanna and Chhabra (2006) for Grashof number $Gr_{PL} \geq 10$. Interestingly, **Fig. 5.11** shows that the effect of the power-law index, $n$ on $C_D$ is flipped over between $2 < Gr_{PL} < 15$; for instance, for $Pr_{PL} = 0.72$, this flip-over occurs at $Gr_{PL} \sim> 3$. For $Gr_{PL} < 2$, **Fig. 5.11** shows varying extents of drag augmentation in pseudoplastic fluids ($n < 1$) whereas it decreases in dilatant fluids ($n > 1$) with reference to the corresponding value in a Newtonian fluid over the range of Prandtl number $0.72 \leq Pr_{PL} \leq 1000$. This observation is in stark contrast to the behavior at $Gr_{PL} > 15$ reported by Prhashanna and Chhabra (2006). Similar trends for a sphere in the forced convection regime (Dhole *et al.*, 2006) have also been reported for power-law fluids. The possible reasons for the varying role of shear-thinning and shear-thickening behavior on the total drag may be attributed to the varying contributions of the friction and form drags which scale differently with the velocity and power-law index, e.g., frictional force scales as $\sim V_c^n$ whereas the inertial forces scale as $\sim V_c^2$. **Figure 5.12** quantifies the contribution of the individual

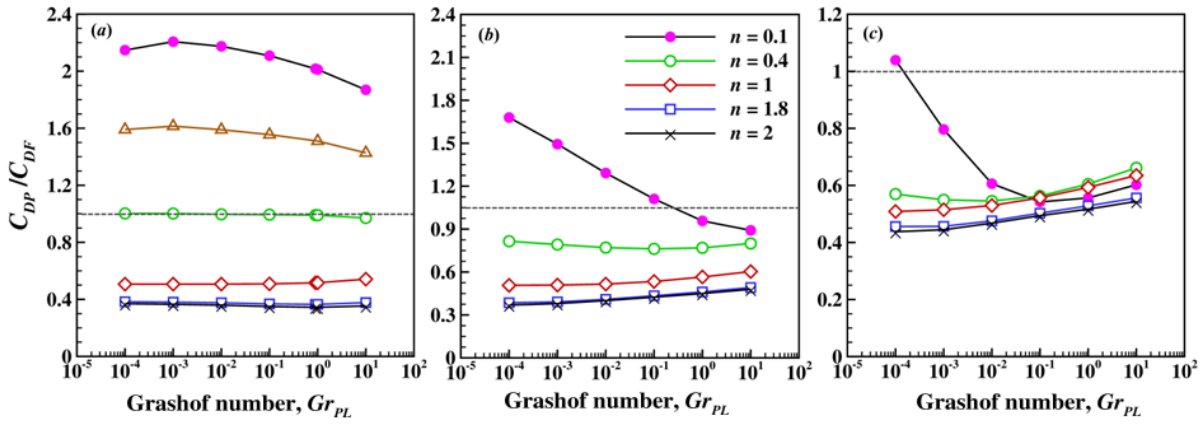


**Figure 5.12** Effect of power-law index on pressure and frictional drag ratio for a single sphere at (a) $Pr_{PL} = 0.72$ (b) $Pr_{PL} = 100$ (c) $Pr_{PL} = 1000$.

components to the total drag coefficient which is seen to be strongly influenced by the values of the Prandtl and Grashof numbers, and the flow behavior index, thereby confirming the foregoing assertion based on the scaling of the individual drag coefficients. For instance, at $Pr_{PL} = 0.72$, the ratio $C_{DP}/C_{DF}$ is below unity up to about $n \geq \sim 0.4$ whereas it exceeds unity for $n \leq \sim 0.2$ thereby suggesting that $C_{DF}$ rises less steeply than $C_{DP}$. Qualitatively similar trends, though less severe, are seen at $Pr_{PL} = 100$ whereas this effect is virtually absent at $Pr_{PL} = 1000$. Returning to **Fig. 5.11**, the increasing value of the Prandtl number reduces the total drag otherwise under identical conditions. To elucidate the effect of power-law index on the total drag in an unambiguous fashion, the drag ratio $Y(n)$ defined as the total drag in a power-law fluid normalized by the corresponding value in a Newtonian fluid at given values of $Gr_{PL}$ and $Pr_{PL}$, is plotted in **Fig. 5.13**. It confirms the tendency of the Grashof number to modulate the effect of power-law index on the total drag. **Figure 5.13** also shows that with the increasing Prandtl number, the onset of flip over

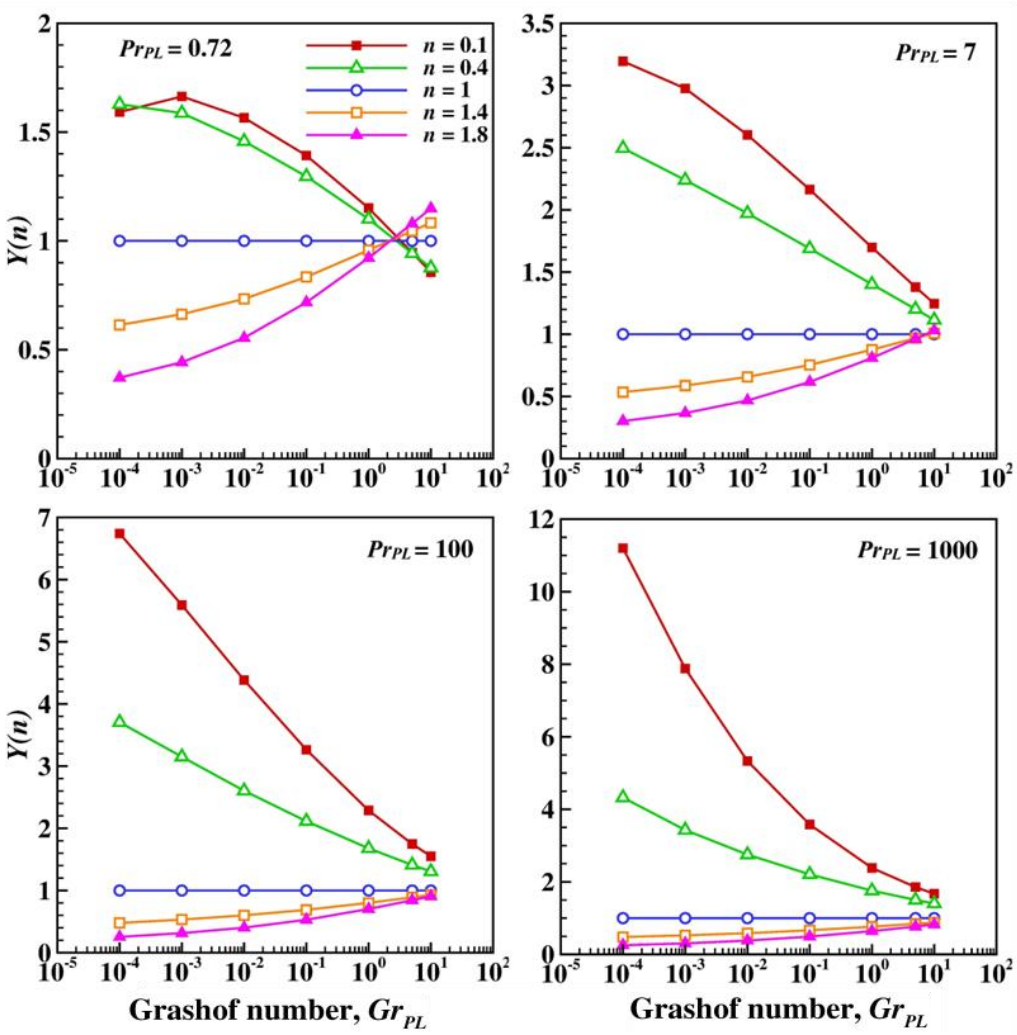


**Figure 5.13** Variation of drag correction factor, $Y(n) = C_{Dn} / C_{Dn=1}$ with Grashof number, $Gr_{PL}$, Prandtl number, $Pr_{PL}$ and power-law index, $n$ for a single sphere.

of the dependence of $C_D$ on the power-law index shifts towards a higher Grashof number, as also seen in **Figs. 5.11** and **5.12**. It is useful to recall here that the drag correction factor is a function of the power-law index only in the forced convection Stokes regime and it ranges from about $Y(n) \sim 0.261$ at $n = 1.8$ to $Y(n) \sim 1.354$ at $n = 0.1$, with its maximum value of $Y(n) \sim 1.458$ at $n = 0.4 - 0.5$ (Dhole *et al.*, 2006; Chhabra and Richardson, 2008). In contrast, this factor shows a strong dependence on the Grashof and Prandtl numbers in the free convection regime, as can be seen at $Pr_{PL} = 7$ and $Pr_{PL} = 100$ thereby suggesting that even such low values of $Gr_{PL}$ do not necessarily correspond to the "creeping flow approximation" in the free convection regime. The effect of shear-thinning viscosity ($n < 1$) on $C_D$ as well as $Y(n)$ appears to be more pronounced than that of the dilatant fluid viscosity ($n > 1$).

In an extensive experimental investigation on free convection heat transfer from an isothermal sphere in power-law fluids by Amato and Tien (1976), two flow regimes have been identified based on the value of the modified form of the Rayleigh number defined as:

$$\Omega = Gr_{PL}^{\frac{1}{2(n+1)}} Pr_{PL}^{\frac{n}{(3n+1)}} \tag{5.5}$$

Within the margin of experimental errors, Amato and Tien (1976) argued that for $\Omega < \sim 10$, $Nu = 2$ and for $\Omega > 10$, the Nusselt number exhibited a linear positive dependence on $\Omega$, $Nu \approx \Omega$. This trend was also supported by the subsequent numerical results available in the literature (Prhashanna and Chhabra, 2010). However, the present results seem suggest that the conduction limit $Nu = 2$ approaches only for $\Omega < \sim 1$ instead of $\Omega = 10$. Due to the coupling between the flow and thermal fields in the free convection regime, the thickness of both the hydrodynamic and thermal boundary layers are determined by the value of $\Omega$,

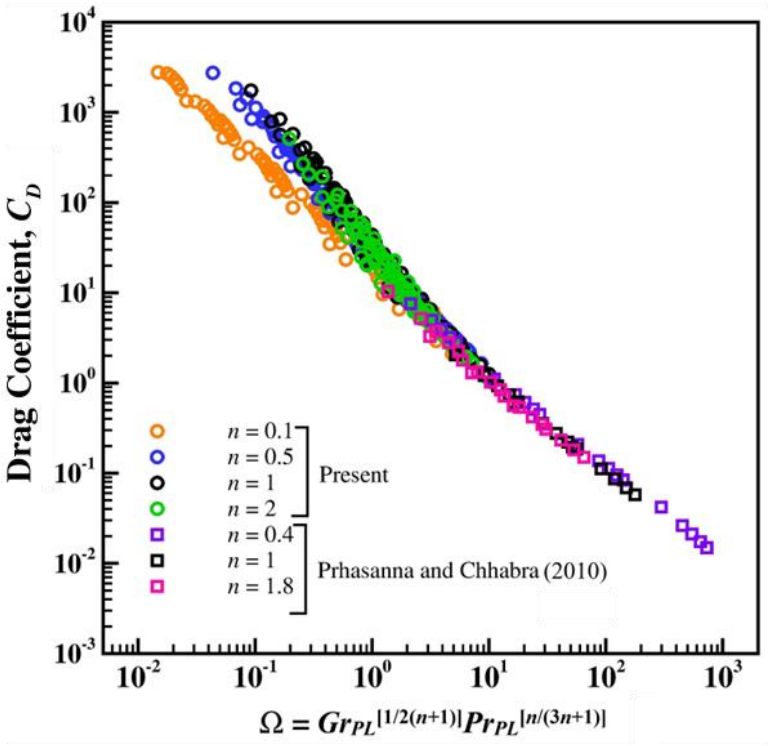


**Figure 5.14** Drag coefficient as a function of $\Omega$ over the range of power-law index for a single sphere.

one would expect the total drag to exhibit an inverse dependence on $\Omega$. Indeed, this inference is supported by the results shown in **Fig. 5.14** where the present results ($0.0148 \leq \Omega \leq 10.58$) and that of Prhashanna and Chhabra (2010) spanning the range $10 \leq \Omega \leq 10^3$ are included. With the increasing value of $\Omega$, the effect of power-law index progressively diminishes due to the gradual weakening of the viscous forces. On the other hand, there is a distinct effect of power-law index for $\Omega < \sim 5$–$10$, in line with the previous discussion in the context of **Figs. 5.11** to **5.13**. In other words, the composite parameter $\Omega$ can be interpreted as the effective Reynolds number here.

*B. Nusselt number*

**Figure 4.15** shows the variation of the local Nusselt number, $Nu_l$ on the surface of the sphere encompassing a range of combinations of parameters, namely, $Pr_{PL}$, $Gr_{PL}$, and $n$. As expected, at low

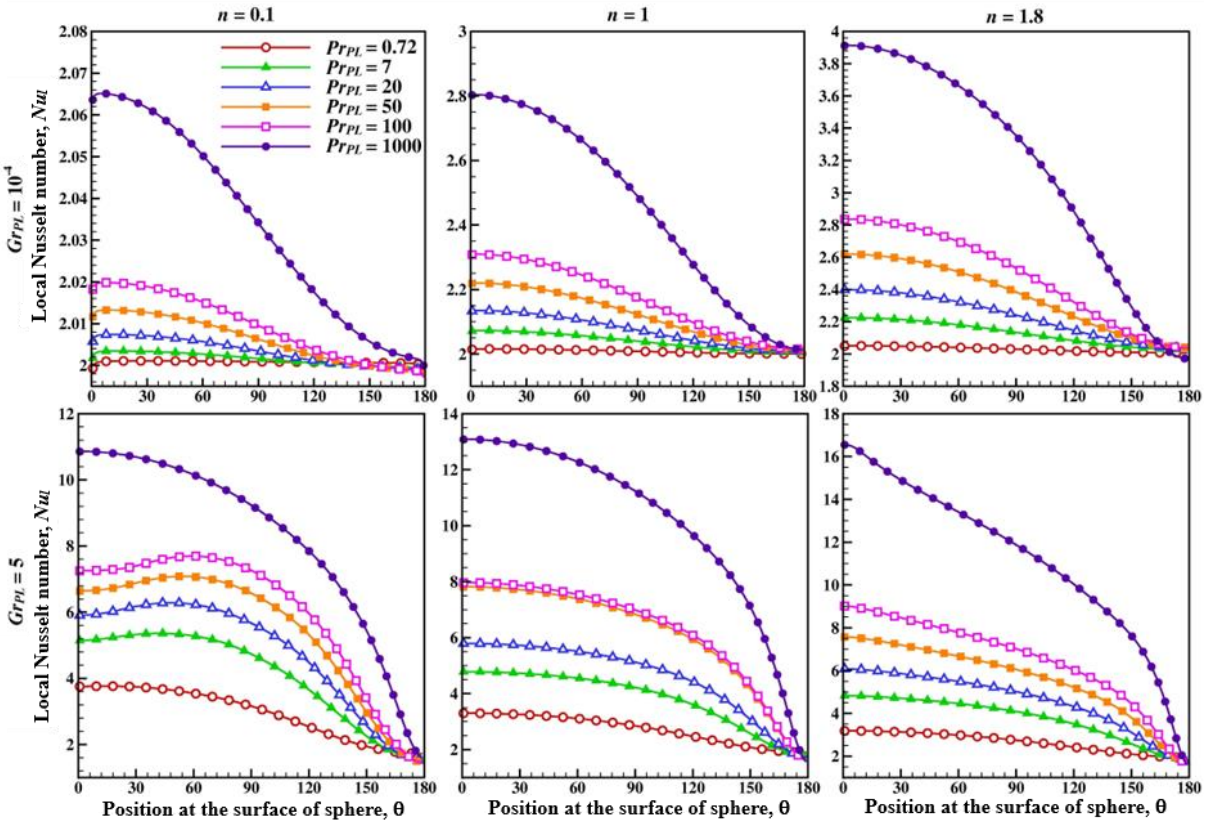


**Figure 5.15** Local Nusselt number on the surface of sphere over the range of $Pr_{PL}$ and $n$ at $Gr_{PL}$ = $10^{-4}$ and $Gr_{PL}$ = 5 for a single sphere.

Grashof numbers, (e.g., $Gr_{PL} = 10^{-4}$) and Prandtl number ($Pr_{PL} = 0.72$), the local Nusselt number varies very little over the entire surface of the sphere being close to the conduction value of $Nu_l = 2$ and it remains independent of the values of the power-law index. This is so because the conduction heat transfer is influenced only by the thermal conductivity of the fluid and the viscous (flow) properties are irrelevant in this regime. This is in line with the approximate analysis of Hossain and Gebhart (1970). However, a gradual increase in Prandtl number and/or Grashof number raises the Nusselt number by varying amounts indicating the onset of convection in the front of the sphere, e.g., see the results in the first row of **Fig. 5.15** and the same effect is further intensified at $Gr_{PL} = 5$ (bottom row). In Newtonian and dilatant fluids ($n \geq 1$), the local Nusselt number exhibits a peak at the front stagnation point ($\theta = 0$). In contrast, for $n$ = 0.1 (highly shear-thinning fluid), the peak value shifts slightly downstream from the front stagnation point. These results are also in agreement with the previous work at high Grashof numbers (Prhashanna and Chhabra, 2010). The shift of the peak of the local Nusselt number from the front stagnation point on the sphere surface depends on the critical Rayleigh number ($Gr_{PL} \times Pr_{PL}$) or on the value of Ω which is a strong function of the power-law index (Prhashanna and Chhabra, 2010). The present results also confirm that for $n$ = 0.1, the shift of local maxima for Nusselt number is observed at $Ra_{PL} = 35$ for $Gr_{PL} = 5$ in **Fig. 5.15** whereas it was observed for $n$ = 0.4 by Prhashanna and Chhabra (Prhashanna and Chhabra, 2010)

only after $Ra_{PL} \sim 7 \times 10^3$ for $Gr_{PL} \sim 10^3$. At the front stagnation point, the shear rate is maximum which corresponds to maximum (or minimum) viscosity depending upon the value of the power-law index. The temperature gradient is also maximum at this point. However, both the shear rate and temperature gradients decrease along the surface of the sphere. Such a viscosity variation along the surface leads to local values of $Gr_{PL}$ and $Pr_{PL}$ which can be significantly different from those based on the scaling of $R$ and $V_c$. This coupled with the variable temperature gradient determines the local value of the Nusselt number. Both the velocity and temperature gradients are strongly influenced by the power-law index. For small values of $n$, the dependence of viscosity on the shear rate is weakened and hence this effect is observed only in highly shear-thinning fluids, i.e., small values of $n$. Finally, the currently available numerical results (Prhashanna and Chhabra, 2010) for $\Omega > 10$ and experimental results (Amato and Tien, 1976; Liew and Adelman, 1975) are consolidated in **Fig. 5.16** along with the present results. As expected,

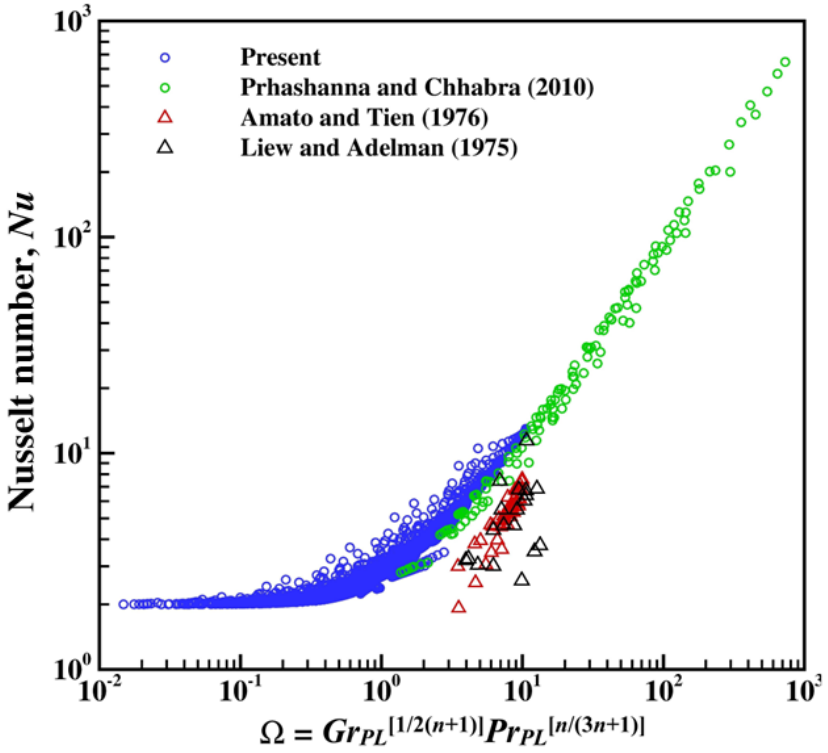


**Figure 5.16** Comparison of the present values of Nusselt number with the previous numerical and experimental results for a single sphere.

the Nusselt number gradually approaches the limiting value of $Nu = 2$ for $\Omega < \sim 0.1$ regardless of the type of fluid, Newtonian or power-law ($0.1 \leq n < 2$). Similarly, at the other end, $\Omega > \sim 10$, the results for different values of the power-law index seem to collapse onto a single curve, given by $Nu \sim \Omega$, in line with the suggestion of Amato and Tien (1976) and Liew and Adelman (1975) in the range of the power-law index $0.3 \leq n \leq 1$. However, in between these two limits corresponding to the onset of convection, the results exhibit slightly greater dispersion around the mean value. However, no trend is discernible with respect to $Gr_{PL}$, $Pr_{PL}$, $\Omega$, or the value of $n$ in this regime. The difference between the numerical and experimental results seen here is well within the margin of errors inherent in the experimental results, as

indicated by the values of $Nu < 2$ in a few cases. Finally, similar to the flipping over seen in drag results with respect to the role of power-law index, the average Nusselt number shows qualitatively similar behavior at values of the Grashof number of the order of 5–10 depending on the values of the power-law index and Prandtl number when the present results are plotted along with that from ref. (Prhashanna and Chhabra, 2010), though these are not included here.

*5.1.3.2 Twin sphere*

The twin heated spheres aligned vertically in a buoyancy driven flow exhibit dramatic changes in the overall flow and heat transfer phenomena on three counts: firstly, the plume of the heated fluid rising from the upstream sphere impinges on the downstream hot sphere thereby exposing it to the effectively buoyancy-assisted mixed convection regime. Secondly, the rising plume expands radially, thereby lowering its upward velocity in compliance with the equation of continuity. Both these effects are strongly modulated by the gap between the two spheres and the strength of the flow. For instance, for small value of $l/d$, the rising plume will slow down much less than that for large value of $l/d$. For closely-placed spheres, this effect will tend to increase the rate of heat transfer from the downstream sphere, but this effect will weaken with the increasing separation between the two spheres. Finally, due to the preheating of the fluid by the upstream sphere, the driving force for heat transfer from the downstream sphere is lower than that of the upstream sphere. This will lower the rate of heat transfer from the downstream sphere. These three factors influence the hydrodynamics (drag) and heat transfer (Nusselt number) of the trailing sphere. The relative strengths of these three factors themselves are strongly influenced by the values of $Gr_{PL}$, $Pr_{PL}$, $l/d$ and n in a complex manner. Furthermore, due to the coupled flow and heat transfer phenomena, the drag experienced by the downstream sphere differs from that for an isolated sphere otherwise under identical conditions. Based on these considerations, only three values of $l/d$ have been employed here which represent strong to moderate interference between the two spheres as the values of $l/d$ is varied from $l/d = 1$ to $l/d = 6$. These interactions can also be viewed in terms of the boundary layers formed on both spheres and the boundary layer thickness are determined by the values of these parameters.

The ratio of drag coefficients of the downstream sphere ($C_{D1}$) to the upstream sphere ($C_{D2}$) is plotted as a function of the Grashof number in **Fig. 5.17** for $l/d = 6$ and $l/d = 1$. It is observed that the drag ratio ($C_{D1}/C_{D2}$) has not exceeded 1 over the range of parameters for twin spheres indicating that the downstream sphere has a drag coefficient equal to or less than the upstream sphere. This is due to the effectively augmented flow around the downstream sphere, (i.e., effectively high Rayleigh number) which lowers the drag coefficient. Moreover, the ratio becomes more sensitive to power-index as the Grashof number increases over the range of Prandtl numbers due to enhanced advection. In other words, for a fixed value of $Pr_{PL}$, the drag values vary for both the spheres at low Grashof numbers, e.g., $10^{-4}$ over the range of $0.8 <\sim C_{D1}/C_{D2} <\sim 1$. As the Grashof number increases, their ratio $C_{D1}/C_{D2}$ decreases while with the increase in Prandtl number, it shows a decrease for the case of $l/d = 6$. On the contrary, for $l/d = 1$ the effect of the Prandtl number has been observed to be the other way around. In this case, it is possible that the plume

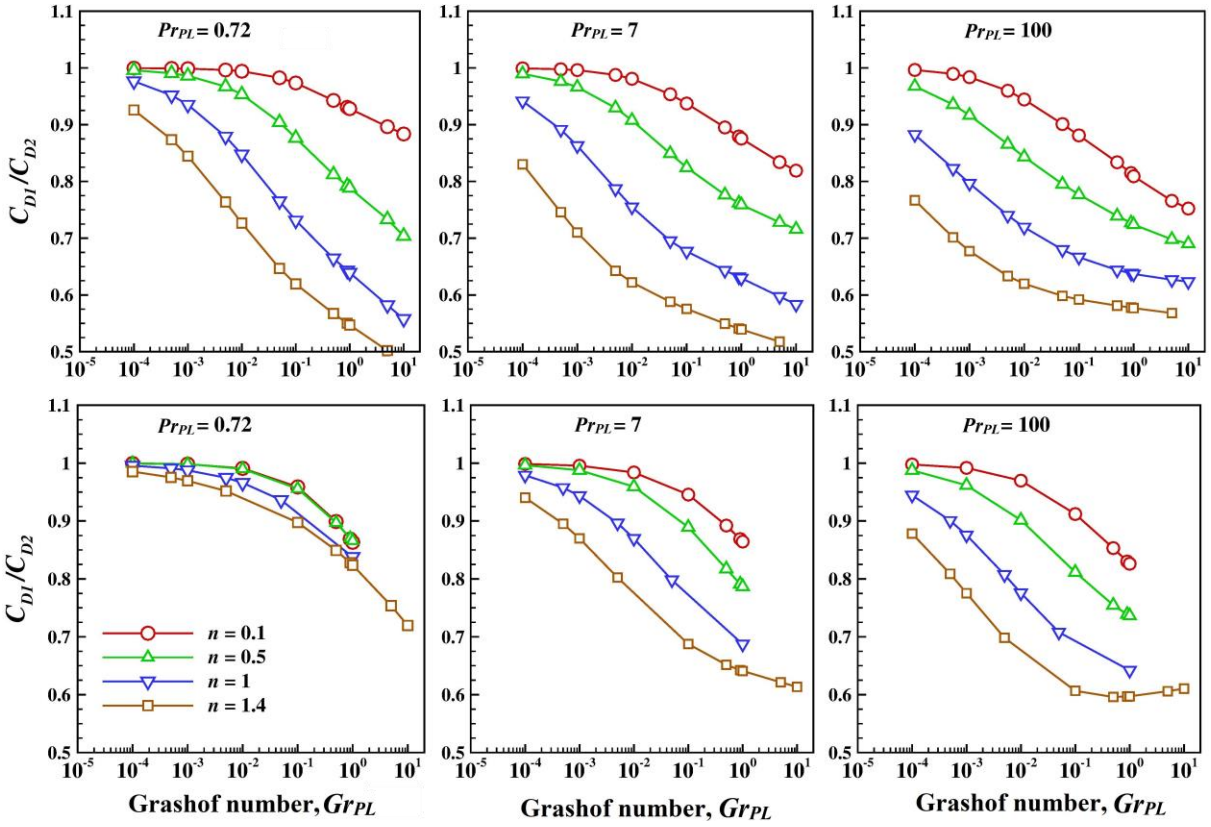


**Figure 5.17** Effect of gap ratio on drag coefficient (Top row: $l/d$ = 6; bottom row: $l/d$ = 1).

from the upstream sphere encapsulated the downstream sphere partially or completely thereby effectively behaving as a single body.

The heat transfer characteristics for the twin spheres have been examined in terms of the average Nusselt number, as shown in **Fig. 5.18**. It can be seen that the average Nusselt number values for both spheres increase with the increasing gap ratio; however, they remain higher for the upstream sphere ($Nu_1$) compared to the downstream sphere ($Nu_2$) for $l/d$ = 1 over the range of the parameters as shown in **Fig. 5.19**. In this case, possibly the preheating of the fluid by the upstream sphere dominates the behavior of the downstream sphere. As, the gap ratio increases presumably due to the mixed-convection flow experienced by the downstream sphere, specifically shear-thinning fluids show a complete flip over this behavior (i.e., $Nu_1/Nu_2 < 1$) as the Grashof number increases above ~1. In this case, the mixed-convection effect outweighs the preheating effect. On the other hand, in the case of Newtonian and shear-thickening fluids, the ratio of $Nu_1/Nu_2$ seems to be a function of the Prandtl number. With the increase in the Prandtl number, e.g., at $Pr_{PL}$ = 100 the ratio of the average Nusselt number, $Nu_1/Nu_2$ remains greater than 1 for these fluids. Interestingly, the Nusselt numbers for both spheres seem to approach the limiting (conduction) value of the Nusselt number as the Grashof number decreases over the range of parameters considered in this work (**Fig. 5.18**). For $l/d$ = 1, the two touching spheres thus forming a single particle in a quiescent power-law fluid have a limiting average Nusselt number ~ 1.387

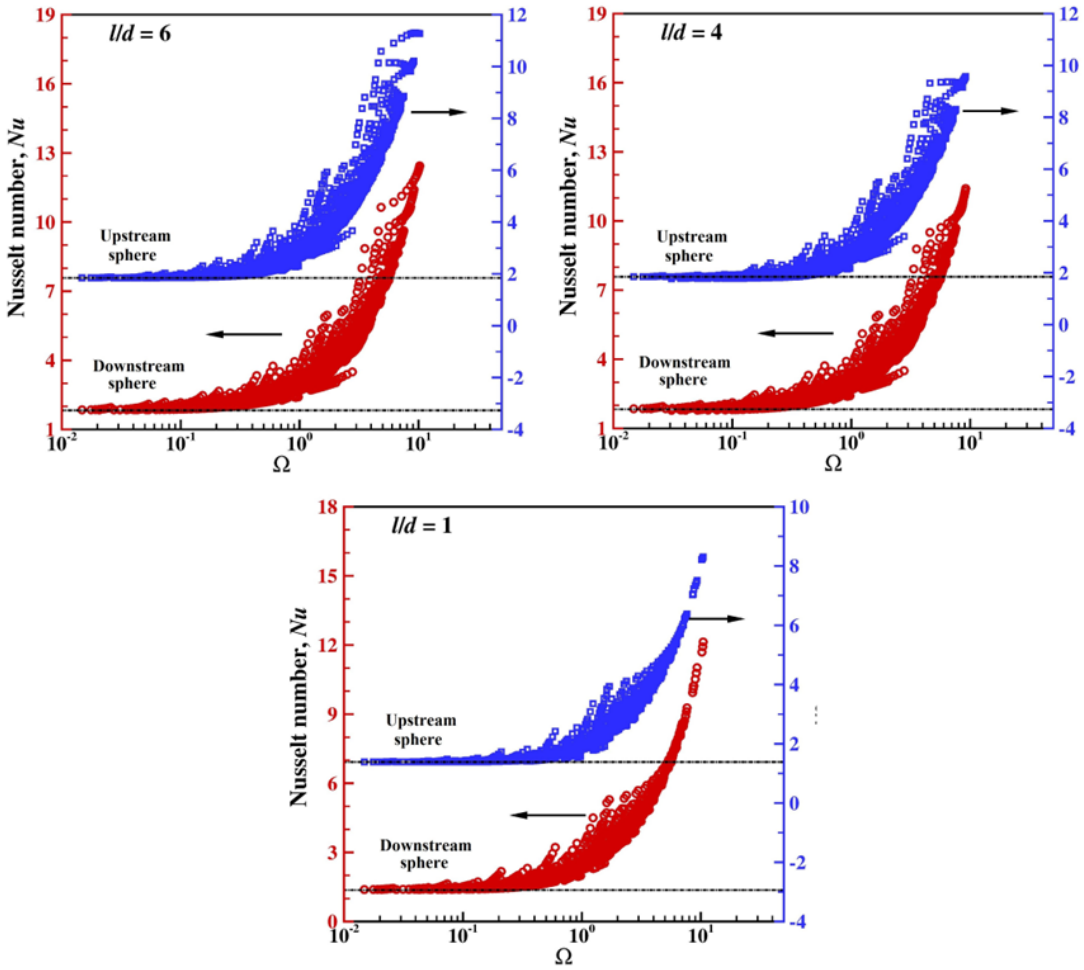


**Figure 5.18** Effect of gap ratio on average Nusselt number (a) $l/d$ = 6 (b) $l/d$ = 4 (c) $l/d$ = 1.

which is lower than the limiting average Nusselt number value of $Nu$ = 2. However, this value increases with the increasing value of $l/d$. For instance, for $l/d$ = 4 and 6, these values are 1.783 and 1.849, respectively thereby indicating the weakening of the interference in the pure conduction limit. However, the single sphere limit cannot be possibly reached for the downstream sphere in the presence of convection due to the preheating of the fluid, though the interference between the two spheres diminishes with the increasing value of $l/d$. The present study shows that the gap required to make both spheres act independently will certainly be much greater than the gap ratio $l/d$ = 6.

*5.1.3.3 Practical application*

For an isolated sphere, as noted earlier, the drag coefficient exhibits an inverse dependence on Ω (modified Rayleigh number) as shown in **Fig. 5.11** for an isolated sphere. Clearly, two regimes exist roughly separated at Ω ~ ≤ 10. For Ω ~> 10, over the range of the power-law index, the results from Prhashanna and Chhabra (2010) seem to collapse onto a single curve and the effect of the power-law index becomes gradually significant as Ω decreases below Ω ≤ 10.

For Ω ≤ 10, the relationship between $C_D$ and Ω is of the form as:

$$C_D = a\Omega^b \tag{5.6}$$

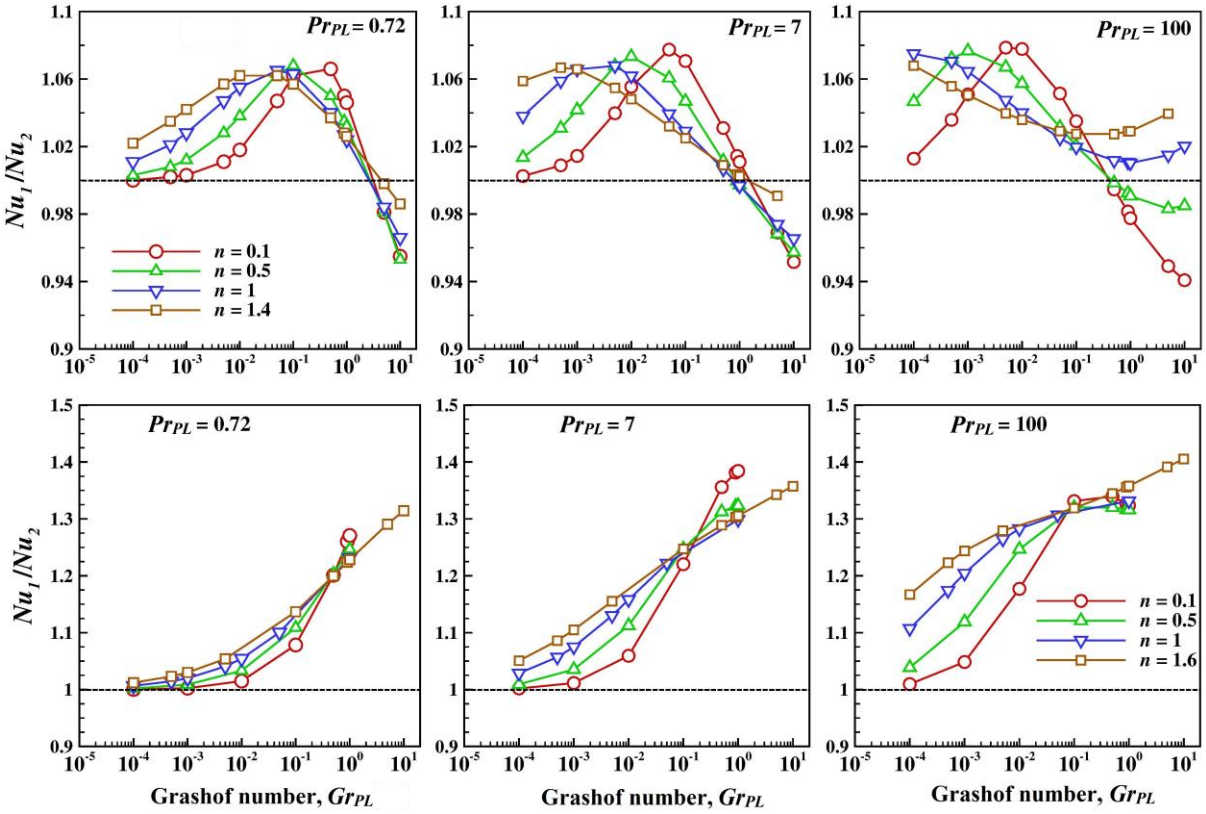


**Figure 5.19** Effect of gap ratio on the ratio of Nusselt number of upstream ($Nu_1$) to downstream ($Nu_2$) sphere (Top row: $l/d$ = 6; bottom row: $l/d$ = 1).

For a single sphere: $a = 11.270n^{1.47}\left(\frac{4.318}{n^{1.096}} - 1\right)$ and $b = \frac{0.576}{0.584 + n} - 2.060$

The results for Prandtl number of 0.72 are not included in **Eq. (5.6)** as they are of little interest in the context of power-law fluids. This equation predicts 1600 individual values of the drag coefficient with a mean error ($\delta_{avg}$) of 18% which rises up to a maximum ($\delta_{max}$) of 53% for a single sphere. Further analysis of the results shows that the maximum errors were observed for extreme values of the power-law index $n$ = 0.1 and $n$ = 2. For $\Omega \geq 10$, the drag coefficient values of Prhashanna and Chhabra (2010) are also well approximated by **Eq. (5.6)** with the coefficient values, $a$ = 15.580 and $b$ = −1.120 with the mean and maximum deviations of 11% mean and 36% respectively for 140 individual data points. It is worthwhile to mention here that for $n$ = 1, the value of $b$ is sufficiently close to the value of unity suggested by the analysis of Stewart (1971), **Eq. (5.3)** here whereas the value of $a$ = 15.58 is about 30% lower than their proposal. Similarly, at low Rayleigh numbers, our drag results are approximately in line with **Eq. (5.1)** in so far that $C_D$ scales as $\sim Ra_{PL}^{-1/2}$ as suggested by **Eq. (5.1)**.

Similar correlations have been also proposed here for the twin sphere system. **Equation (5.6)** can also be used to predict the drag coefficient for both spheres adequately. However, the coefficients in **Eq. (5.6)** are much more involved in this case as, $a = a_1 n^{a_2}\left[\left(a_3/n^{a_4}\right) - 1\right]$ and $b = \left[b_1/\left(b_2 + n\right)\right] - b_3$. The values of

$a_1$, $a_2$, $b_1$, $b_2$, etc. along with the maximum and average deviations are tabulated in **Table 5.3** (excluding data for $Pr_{PL}$ = 0.72). In each case, the results for the downstream sphere entail greater uncertainty than the first sphere. This is obviously due to the mixed convection flow over the downstream sphere and the

**Table 5.3** Coefficients of **Equation (5.6)** $a = a_1 n^{a_2}\left[\left(a_3/n^{a_4}\right)-1\right]$ and $b=\left[b_1/\left(b_2+n\right)\right]-b_3$ for the case of twin spheres.

| Coefficient | ***l/d* = 6** | | ***l/d* = 4** | | ***l/d* = 1** | |
|---|---|---|---|---|---|---|
| | **Downstream** | **Upstream** | **Downstream** | **Upstream** | **Downstream** | **Upstream** |
| $a_1$ | 8.249 | 4.597 | 6.015 | 4.365 | 3.825 | 3.545 |
| $a_2$ | 2.152 | 2.65 | 2.484 | 2.719 | 2.657 | 2.727 |
| $a_3$ | 5.857 | 12.866 | 7.322 | 12.722 | 8.501 | 11.338 |
| $a_4$ | 1.747 | 2.237 | 2.124 | 2.329 | 2.265 | 2.319 |
| $b_1$ | 0.294 | 0.296 | 0.212 | 0.219 | 0.161 | 0.108 |
| $b_2$ | 0.35 | 0.393 | 0.26 | 0.306 | 0.191 | 0.154 |
| $b_3$ | -1.871 | -1.762 | -1.802 | -1.699 | -1.755 | -1.578 |
| $\delta_{avg}$ | 12.04 | 9.01 | 12.57 | 9.88 | 11.72 | 9.84 |
| $\delta_{max}$ | 53.62 | 36.15 | 50.19 | 33.75 | 58.03 | 46.12 |
| # data | 1971 | 1971 | 1765 | 1765 | 900 | 900 |

preheating effect which are not being accounted for here.

Next, a simple expression has been postulated for estimating the average Nusselt number for a single sphere as:

$$Nu = 2 + 0.9\Delta^{0.358}\Omega^{1.07} \tag{5.7}$$

where, $\Delta = \left(\frac{3n+1}{4n}\right)$

Here also, the results of $Pr_{PL}$ = 0.72 are not included. **Equation (5.7)** predicts the average Nusselt number with the mean and maximum deviations of 4% and 35% respectively. All in all, 74 data points out of 1600 show deviations of more than 10%, specifically, at $Pr_{PL} = 10^3$ for $n \leq 0.3$ and $Gr_{PL} \geq 0.05$. It is worthwhile to add here that the present results for $Pr_{PL}$ = 0.72 over the low Grashof number range $10^{-4} \leq Gr_{PL} \leq 10$ are close to the available experimental results within the margin of experimental uncertainty. In particular, the present numerical results for air ($Pr_{PL}$ = 0.72) have been found to be in excellent agreement with the available correlations based on experimental results (Campo, 1980; Yuge, 1960; Churchill, 1983). In view of the wide acceptance of the correlation due to Churchill (1983) for Newtonian fluids, an attempt has been made to correlate the average Nusselt number for power-law fluids as a

function of the modified Rayleigh number proposed.

$$Nu = 2 + \frac{0.589\Omega^{a}}{\left[1+\left(\frac{0.43}{Pr_{PL}}\right)^{9/16}\right]^{4/9}} \tag{5.8}$$

This equation correlated the present data of power-law fluids over wide ranges of the modified Rayleigh number, $0.0148 \le \Omega \le 731$ for $0.1 \le n \le 2$, $10^{-4} \le Gr_{PL} \le 10^{7}$ and $0.72 \le Pr_{PL} \le 1000$, including the results of Prhashanna and Chhabra (2010). The resulting values of the parameter $a$ in **Eq. (5.8)** are as follows:

$a$ = 1.32 for $0.0148 \le \Omega < 10$ (% Error: mean = 8%, maximum = 46%, #data = 1846)

$a$ = 1.073 for $10 \le \Omega \le 731$ (% Error: mean = 17%, maximum = 28%, # data = 100)

For $n$ = 1, **Eq. (5.8)** approaches the original form of the expression proposed by Churchill (1983) with $\Omega = Ra^{1/4}$ and $a$ = 1. Finally, the trends seen in **Fig. 5.18** suggest that the correlation for the isolated sphere, **Eq. (5.7)**, might be useful to predict the average Nusselt numbers for the twin spheres also with the appropriate coefficients. The coefficients in **Eq. (5.7)** can be represented for the twin spheres as:

$$Nu = c_1 + c_2\Delta^{c_3}\Omega^{c_4} \tag{5.9}$$

**Table 5.4** summarizes the values of the fitting parameters for the twin sphere system along with the average and maximum percentage errors for each case excluding the data for $Pr_{PL}$ = 0.72. The coefficient $c_1$ captures the limiting average Nusselt number that is the function of purely gap ratio. For $l/d$ = 1 touching spheres, the limiting average Nusselt number. i.e., 1.387, matches with the reported value of 1.386 by Chamberlain *et al.* (1985).

**Table 5.4** Coefficients of **Equation (5.9)** for the case of twin spheres.

| Coefficient | ***l/d* = 6** | | ***l/d* = 4** | | ***l/d* = 1** | |
|---|---|---|---|---|---|---|
| | **Downstream** | **Upstream** | **Downstream** | **Upstream** | **Downstream** | **Upstream** |
| $c_1$ | 1.849 | 1.849 | 1.783 | 1.783 | 1.387 | 1.387 |
| $c_2$ | 1.080 | 1.030 | 1.126 | 0.943 | 1.018 | 0.561 |
| $c_3$ | 0.977 | 0.979 | 0.957 | 0.985 | 1.016 | 1.112 |
| $c_4$ | 0.381 | 0.485 | 0.356 | 0.456 | 0.556 | 0.663 |
| $\delta_{avg}$ | 4.3 | 3.7 | 4.63 | 4.26 | 3.94 | 3.27 |
| $\delta_{max}$ | 40.2 | 42.03 | 37.77 | 39.77 | 31.62 | 40.39 |
| # data | 1971 | 1971 | 1765 | 1765 | 900 | 900 |

Before leaving this section, it is worthwhile to add here that the modified Rayleigh number, Ω, employed here also captures the varying roles of the Grashof and Prandtl numbers modulated by the value of the

flow behavior index ($n$). For $n$ = 1, it predicts the expected scaling of $Nu \sim Ra_{PL}^{1/4}$, i.e., identical roles of Grashof and Prandtl number in determining the value of the Nusselt number. For $n$ = 0.1 (highly shear-thinning fluid), $\Omega = Gr_{PL}^{0.45} Pr_{PL}^{0.077}$ thereby implying a much stronger influence of the Grashof number than that of the Prandtl number. At the other extreme of a highly shear-thickening fluid (e.g., $n$ = 2), the modified Rayleigh number, $\Omega = Gr_{PL}^{0.167} Pr_{PL}^{0.29}$, weaker influence of Grashof number is evident here with reference to that for $n \leq 1$. While it is not easy to delineate the individual roles of Grashof number, Prandtl number and the flow behavior index due to their entwined definitions via the power-law index. However, limited analysis of the drag and Nusselt number results confirms these conjectures apart from the expected positive dependence of the Nusselt number on the Grashof and Prandtl numbers as suggested above. For fixed values of $Gr_{PL}$ and $Pr_{PL}$, boundary layers are expected to be thinner in shear-thinning fluid ($n$ < 1) than that in Newtonian fluids thereby fostering heat transfer in moderately shear-thinning fluids under the strong flow conditions. This suggestion is also supported by the previous results (Prhashanna and Chhabra, 2010).

## 5.2 Free convection from spherical segments in Bingham plastic fluids

### 5.2.1 Previous work

The literature pertaining to natural convection from *a sphere in Newtonian and power-law* fluids has been reviewed in the previous **section 5.1.1**. However, the spherical segments are the least focused geometry found in the literature for Newtonian fluids, let alone non-Newtonian fluids in free convection regime. This section reviews the literature on free convection form segment of sphere in both Newtonian and Non-Newtonian fluids. In the case of spherical segments, researchers have only given attention to the hemisphere as a limiting case. Jaluria and Gebhart (1975) have conducted experimental studies for both upright and inverted hemisphere over two boundary conditions of uniform temperature and uniform heat flux in free convection regime The study revealed fundamental findings regarding the nature of separation in natural convection and the effect of buoyancy force on the orientation of the geometry. The results suggested that the inverted hemisphere has weak velocity field and thinner boundary regions than the upright hemisphere which provides more insight into the boundary region fluid. Heat transfer from the three isothermal hemispherical segments from a sphere placed on a horizontal plate were experimentally studied by Stewart and Johnson (1985) for the upright configuration. Over the range of $Ra$ number ($2.8\times10^5 \leq Ra \leq 2.8\times10^7$) and fixed Prandtl number ($Pr \sim 0.7$) they proposed that all the zones show a slight variation from the standard correlation of the isothermal sphere i.e., $Nu = CRa^{0.25}$. Subsequently, Cieslinski and Pudlik (1988) extended this work for high values of Prandtl number which suggests the influence of the flat base on the overall heat transfer. Their theoretical results were found in good agreement with their own experimental results of aqueous glycerin solutions ($680 \leq Pr \leq 1700$). Lewandowaki *et al*. (1996) investigated analytically and experimentally isothermal laminar natural convection from upright hemisphere in air which shows a good agreement with each other and the

previous literature. Numerically, Liu *et al*. (2018) also have investigated the heat transfer from a hemisphere in laminar natural convection regime by implying the isothermal curved surface and adiabatic bottom flat surface over the range of Grashof number ($10 \leq Gr \leq 10^6$). Although the plane is adiabatic, at low Grashof number the temperature boundary layer still exists in the vicinity of the plane and the local Nusselt number for the hemispherical surface is greater than the isothermal condition for different Grashof number. Since the scant literature all the above-mentioned studies have only considered the Newtonian fluid so far. Sasmal and Chhabra (2014) have studied the two configurations of hemisphere in power-law fluid under laminar free convection numerically. The study implied that with respect to Newtonian fluid shear-thinning power-law fluid enhances the heat transfer rates while shear-thickening fluid plays an adverse role. There are limited results available for the hemisphere segment in yield stress fluid, i.e., Bingham plastic examining the effect of buoyancy-driven heat transfer. Only one work reported in literature by Nalluri *et al*. (2015) has studied the mixed convection from a heated hemisphere in a Bingham plastic fluid and provides a functional correlation in term of modified Reynolds and Prandtl number. The results explored over the broad range of the parameters: Reynolds number, $1 \leqslant Re \leqslant 100$, Prandtl number, $1 \leqslant Pr \leqslant 100$, Richardson number, $0 \leqslant Ri \leqslant 10$ and Bingham number, $0 \leqslant Bn \leqslant 100$ covers natural convection dominating flow regime at high Richardson number. The prior discussion clearly implies that no studies have been conducted to investigate the effects of the yield stress fluid for the geometry of spherical segment. In the present numerical work five spherical segments ($\alpha = 30°$, 60°, 90°, 120°, 150°) are studied over the wide range of Grashof number ($1 \leq Gr_B \leq 10^4$), Prandtl number ($1 \leq Pr_B \leq 100$), and Bingham number ($0 \leq Bn \leq 10^4$).

### 5.2.2 Physical model and mathematical formulation

**Figure 5.20** shows the schematics of the spherical segment herein and the corresponding computational domains employed in this work. The isothermal heated spherical segment at temperature, $T_h$ is placed in unconfined steady, incompressible, Bingham plastic fluid at temperature, $T_c$ ($<T_h$). The hypothetical unconfined fluid is simulated here by enclosing the fluid surrounding the spherical segment within the sufficiently large spherical envelope imposing a stress-free boundary on the periphery. All the thermophysical properties of the fluids are assumed to be constant and the viscous dissipation term in the energy equation is assumed to be negligible over the range of parameters considered in this work. Moreover, the flow is assumed to be axisymmetric under the steady state flow conditions. The temperature gradients between the hot surface of the spherical segment and the cold fluid results in the movement of the fluid which aids the heat transfer by free convection.

To solve the proposed problem, under the aforementiond assumptions **Eqs. (2.1 – 2.3)** have been rendered dimensionless using $d_{eq}$ and $V_c$ as the characteristic length and velocity scales, respectively. Thus, pressure and the stress components, respectively, have been scaled as $\rho V_c^2$ and $m(V_c/R)^n$ and whereas the non-dimensional temperature is defined as $\xi = (T - T_c)/(T_h - T_c)$. In the momentum equation, boussinesq approximation is plugged into the body force to to account the variation of density with temperature

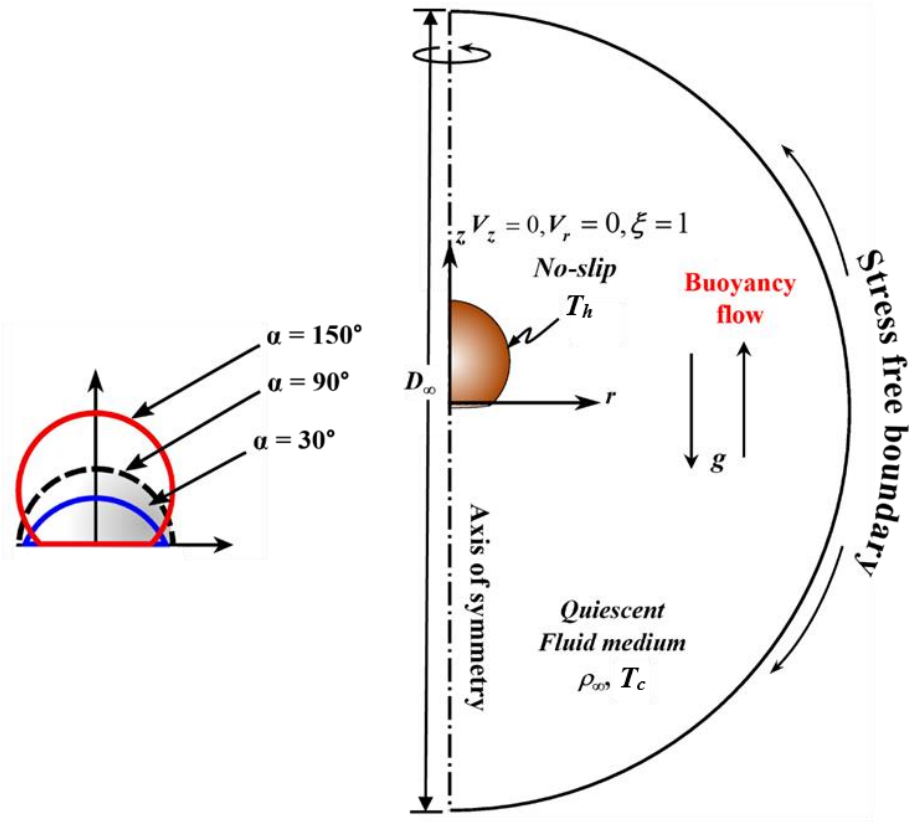


**Figure 5.20** Schematics (i) physical model and (ii) computational domain for spherical segment.

where temperature differece surmises to be small . However, everywhere else density is assume to be constant.The physically realistic boundary conditions of no-slip and constant temperature are imposed on the surface of spherical segmentwhile at the far away on the evelope surface (fictitious spherical envelope of diameter $D_\infty$), stress free boundary and radial gradint of temperature, $\frac{\partial \xi}{\partial r} = 0$ (Neumann type) are applied. The flow and heat transfer are governed by the dimensionless parameters:Bingham number (*Bn*), Prandtl number ($Pr_B$), Grashof number ($Gr_B$) and Rayleigh number ($Ra_B = Gr_B \times Pr_B$) that evolved while deriving the nondimenstional equations, i.e, **Eq. (2.1)-(2.3)** in this considered problem. Furthermore, the discountinuous behaviour of the Bingham plastic fluid is rendered by using Papanastasiou model as discussed in Chapter 2, Section 2.1, **Eq. (2.8)**.

### 5.2.3 Choice of numerical parameters

The accuracy and reliability of the numerical results are influenced by parameters such as the domain size and the number of grid elements in the flow domain. To ensure the results derived are free from any artifact of the domain size, the computational domain has to be chosen based on the assumption of axisymmetric flow for the domain size $D_\infty$ as shown in **Fig. 5.20**. The outer boundary of the domain is carefully chosen by conducting the systematic domain test for the extreme values of the shape factor (α = 30° and 150°) $Pr_B = 0.72$ and $Gr_B = 1$ for $Bn = 0$ (Newtonian) and 100, since both the momentum and thermal boundary layers are thickest at the lowest value of the Prandtl and Grashof numbers. After the

detailed examination of the variation in the average Nusselt numbers (**Table 5.5**), $D_\infty$ = 130 has been chosen in this work as further increase in size of the domain has marginal, less than 1%, change in the values of *Nu*.

The abrupt change in geometry of spherical segment from flat base area to the curved rear surface, the velocity and temperature gradients exhibit a sharp peak at the corner that is not present with spherical

**Table 5.5** Domain Independence Test for $Pr_B$ = 0.72 and $Gr_B$ = 1

| $D_\infty$ | $Gr_B$ | $Pr_B$ | $Bn$ | α = 30° | α = 90° | α = 150° |
|---|---|---|---|---|---|---|
| | | | | *Nu* | | |
| 80 | 1 | 0.72 | 0 | 2.965 | 2.490 | 2.198 |
| | 1 | 0.72 | 100 | 2.640 | 2.304 | 2.055 |
| **130** | **1** | **0.72** | **0** | **2.969** | **2.493** | **2.202** |
| | **1** | **0.72** | **100** | **2.610** | **2.286** | **2.035** |
| 300 | 1 | 0.72 | 0 | 2.971 | 2.497 | 2.205 |
| | 1 | 0.72 | 100 | 2.603 | 2.269 | 2.017 |

shape. Hence, in order to capture these steep gradients, a very fine mesh is required in the vicinity of the spherical segment. With the gradual increase in the number of grid element on the surface of spherical segments (α = 30°, 90°, 150°), three grids have been studied at the highest values of Prandtl and Grashof numbers ($Pr_B$ = 100 and $Gr_B$ = $10^4$) for $Bn$ = 0 (Newtonian) and 100. The effect of grids G1, G2 and G3 are examined on the variation of the local (**Fig. 5.21**) and average (**Table 5.6**) Nusselt number. **Figure 5.21** clearly shows that both grids G2 and G3 seem to be indistinguishable. Evidently, G2 is chosen as the computational grid for the present work.

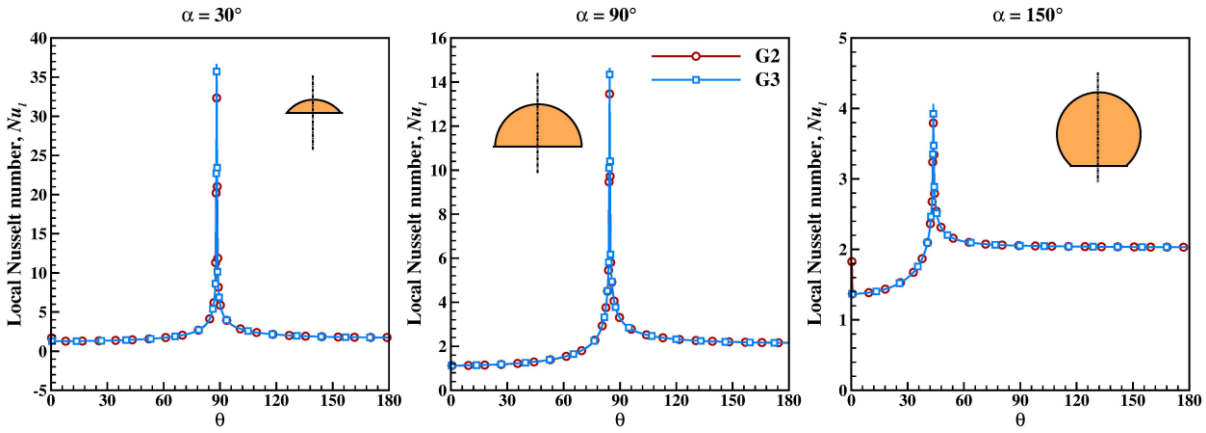


**Figure 5.21** Grid independent test at $Gr_B$ = $10^4$, $Pr_B$ = 100 and $Bn$ =$10^4$.

The discontinuous nature of Bingham plastic fluid having a coexistence of solid-like and fluid-like zones simultaneously in the flow is rendered here by using the Papanastasiou model. It is evident for **Eq. 2.8** that as the value of *M* approaches infinite, the regularized model predictions attend the ideal Bingham plastic fluid characteristics. Hence, in order to examine the effect of the value of *M* on the

yielded/unyielded regions, regularization test is performed by varying its value at $Gr_B$ = 100, $Pr_B$ = 1 and $Bn$ = 1 for three shape parameters where the presence of both yielded/unyielded regions are obvious as shown in **Fig. 5.22**. The yielded/unyielded regions seem to overlap for regularization parameters $M = 5 \times 10^6$ and $10^7$ can be seen in **Fig. 5.22**. Hence, $M = 5 \times 10^6$ is considered to be satisfactory over the range of conditions spanned here.

**Table 5.6** Grid Independence Test at $Gr_B = 10^4$, $Pr_B = 100$

| Grid | $N_c$ | $N_f$ | $N_T$ | $Nu$ | |
|---|---|---|---|---|---|
| | | | | $Bn = 0$ | $Bn = 10^4$ |
| | | | α = 30° | | |
| G1 | 90 | 65 | 55099 | 27.898 | 2.639 |
| G2 | 165 | 125 | 118354 | 27.616 | 2.636 |
| G3 | 200 | 175 | 162713 | 27.579 | 2.635 |
| | | | α = 90° | | |
| G1 | 60 | 40 | 39827 | 22.329 | 2.288 |
| G2 | 190 | 150 | 90355 | 22.084 | 2.287 |
| G3 | 275 | 225 | 144750 | 22.073 | 2.287 |
| | | | α = 150° | | |
| G1 | 90 | 25 | 38140 | 20.178 | 2.036 |
| G2 | 150 | 70 | 93730 | 20.063 | 2.035 |
| G3 | 260 | 100 | 157886 | 20.064 | 2.035 |

However, prior to study the detailed results and discussion of the new outcomes for spherical segments, the validity of the adapted computational scheme and numerical parameters has been demonstrated by presenting a few benchmark comparisons with the prior studies available in the literature. In literature results are found for the two-limiting cases of spherical segments i.e., sphere and hemisphere. The results of the sphere in Newtonian fluid under free convection regime are already discussed in the previous **section 5.1**. Hence, the validations for natural convection from a sphere in Bingam plastic fluids and form a hemisphere in Newtonian fluid have been added in this section. The results of the local variation of Nusselt number and surface vorticity at the surface of the sphere in Bingham plastic fluids are compared

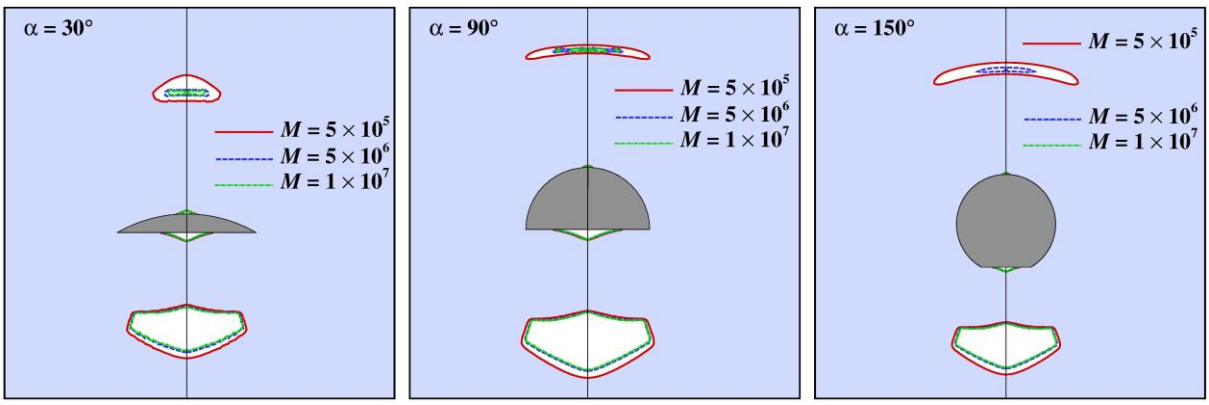


**Figure 5.22** Regularization test for Papanastasiou model at $Gr_B$ = 100, $Pr_B$ = 1 and $Bn$ =1.

with that of reported by Nirmalkar *et al*. (2014) in their numerical work in **Fig. 5.23** and **5.24**, respectively. The results are in excellent agreement with each other. The experimental results of Lendawoski *et al*. (1996) are compared in **Table 5.7** for Newtonian fluid over three values of Prandtl number, $Pr$ = 6, 700, and 1200. The agreement between the present results and the literature values are seen to be excellent with the deviation of the order ~ 10%. Finally, the numerical results of average Nusselt numbers for free convection from a hemisphere in Newtonian fluids by Sasmal and Chhabra (2014) are compared with the present results in **Table 5.8** shown good correspondence with each other. Confidence in the reliability and precision of the new results is inspired due to the close correspondence between the present and literature results, which are within ~3%.

### 5.2.4 Results and Discussion

The present numerical results have delineated the effect of shape of spherical segments ($30° \le \alpha \le 150°$) on the thermal characteristics in Bingham plastic fluids over wide ranges of parameters: $0 \le Bn \le 10^4$,

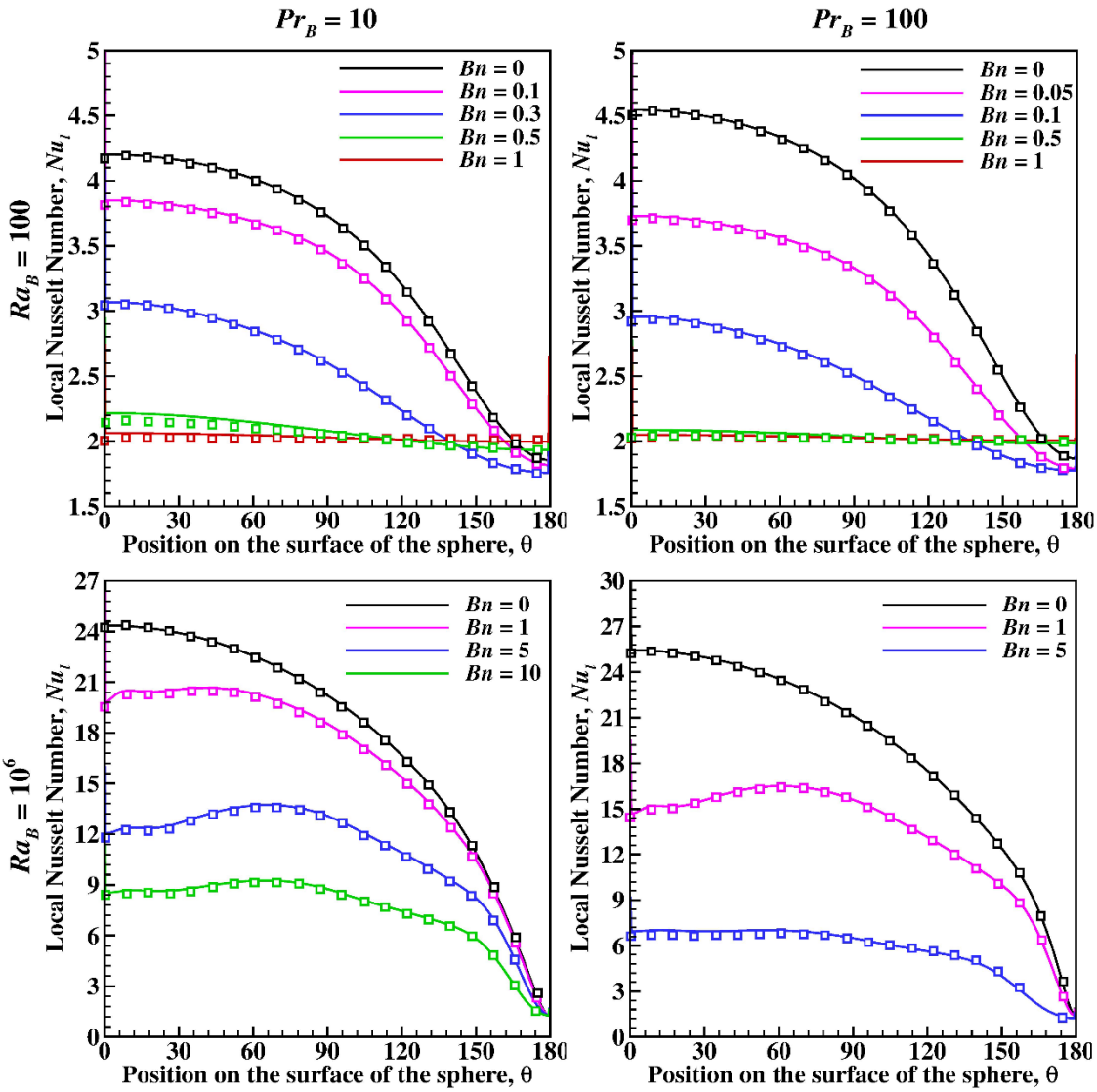


**Figure 5.23** Comparison of Local variation of Nusselt number for various Grashof number for sphere in Bingham Plastic fluids (Line: present results; symbols: Nirmalkar *et al*. (2014)).

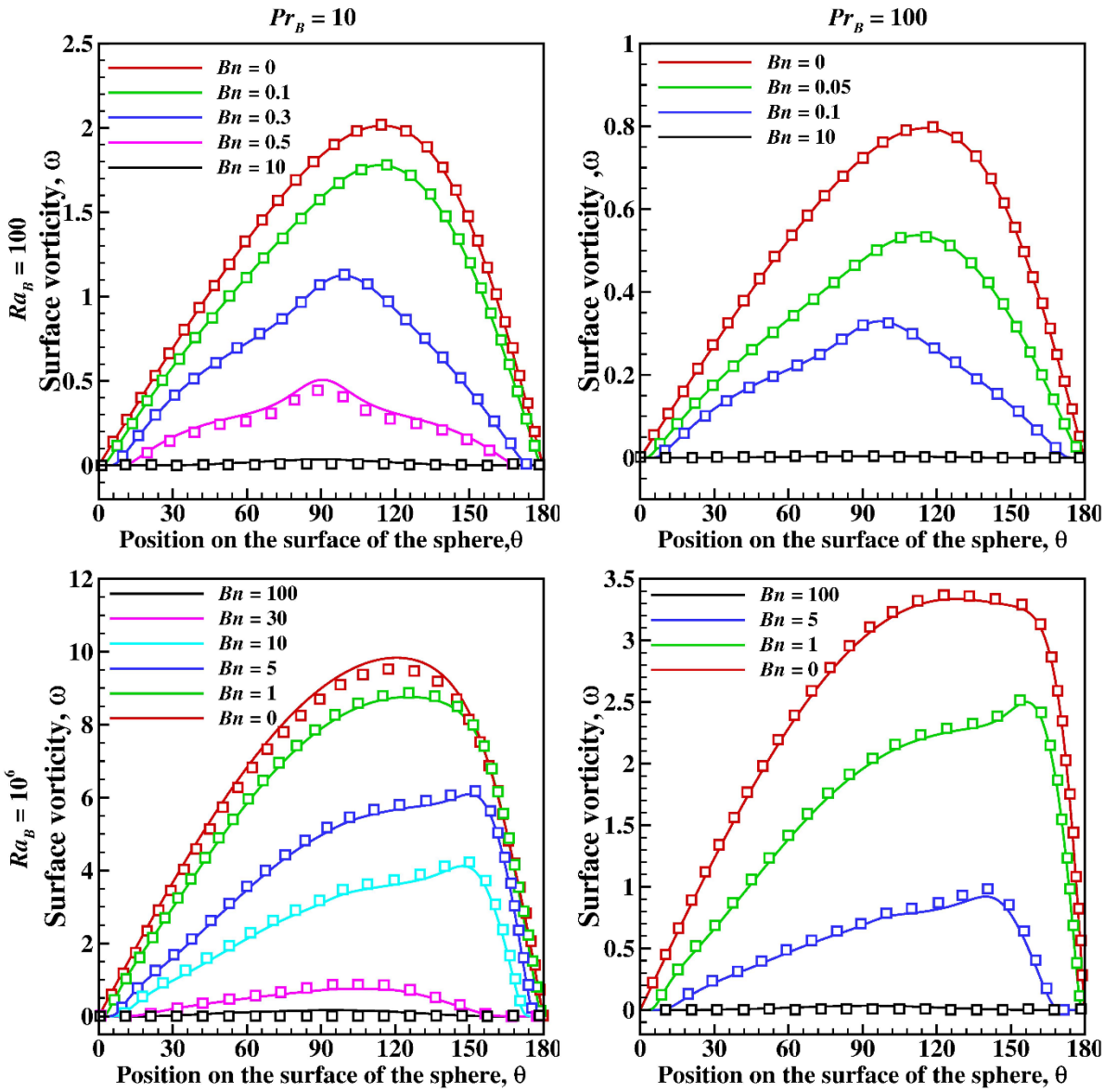


**Figure 5.24** Comparison of local surface vorticity for various Grashof number for sphere In Bingham Plastic fluids (Line: present results; symbols: Nirmalkar *et al*. (2014)).

$0.72 \le Pr_B \le 100$, $1 \le Gr_B \le 10^4$ in the steady free convection regime. The detailed momentum and thermal characteristics of fluid are represented in terms of streamlines, isothermal contours and yielded/unyielded regions. The functional relationship of average Nusselt number dimensionless parameters ($Gr_B$, $Pr_B$, $Bn$) and shape factor is also explored in this study.

### 5.2.4.1 Streamline and isotherm contour

The heat transfer from the heated spherical segment to the fluid is strongly influenced by the velocity and the temperature gradients on/near the surface of the spherical segment. **Figure 5.25-5.28** represents the streamlines (right half) and isothermal contours (left half) for three cases of spherical segments ($\alpha = 30°$, 90°, 150°) over the extreme values of Prandtl and Grashof numbers. At the lowest combination of $Pr_B$ and $Gr_B$ number as shown in **Fig. 5.25**, the heat transfer is mostly governing by conduction mechanism under the weak buoyancy force, thus, the streamlines follow the body contour while uniformly spread

**Table 5.7** Comparison of the average Nusselt number with the experimental literature data

| $Ra_B$ | Lewandowski et al. (1996) | Present |
|---|---|---|
| | $Pr_B$ = 6 | |
| $10^4$ | 4.440 | 4.861 |
| $5 \times 10^4$ | 6.639 | 6.579 |
| $5 \times 10^5$ | 11.807 | 11.137 |
| $10^6$ | 14.041 | 13.602 |
| | $Pr_B$ = 700 | |
| $10^4$ | 5.010 | 5.504 |
| $5 \times 10^4$ | 7.492 | 7.545 |
| $5 \times 10^5$ | 13.322 | 12.944 |
| $10^6$ | 15.843 | 16.257 |
| | $Pr_B$ = 1200 | |
| $10^4$ | 5.100 | 5.519 |
| $5 \times 10^4$ | 7.626 | 7.589 |
| $5 \times 10^5$ | 13.562 | 13.140 |
| $10^6$ | 16.128 | 16.596 |

isotherms confirm the conductive heat transfer. Even at the lowest values of the Grashof number, the increase in Prandtl number results in high rate of heat transfer as it makes the thermal boundary layer and the rising plume thinner clustering close to the surface of the particle (**Fig. 5.26**). The cold fluid is mostly dragged from beneath spherical segments towards the hot spherical segment as the Prantl number increases. On the other hand, the increase in yielded force broadens the size of the plume and allows to transfer the heat by conduction only.

At the high value of Grashof or Rayleigh number (**Fig. 5.27-5.28**), the heat transfer is promoted by advection in the fluid and as a result, more cold fluid entrained from the sides of the spherical segment. Both the momentum and thermal boundary layers become thinner and thinner with the increase in Prandtl

**Table 5.8** Comparison of the average Nusselt number for hemisphere in Newtonian fluids

| $Pr_B$ | Sasmal and Chhabra (2014) | Present | Sasmal and Chhabra (2014) | Present |
|---|---|---|---|---|
| | $Gr_B$ = 10 | | $Gr_B$ = 1000 | |
| 0.72 | 2.697 | 2.699 | 4.226 | 4.223 |
| 10 | 3.750 | 3.733 | 7.321 | 7.243 |
| 20 | 4.165 | 4.153 | 8.510 | 8.388 |
| 50 | 4.847 | 4.826 | 10.417 | 10.210 |
| 100 | 5.469 | 5.439 | 12.166 | 11.869 |

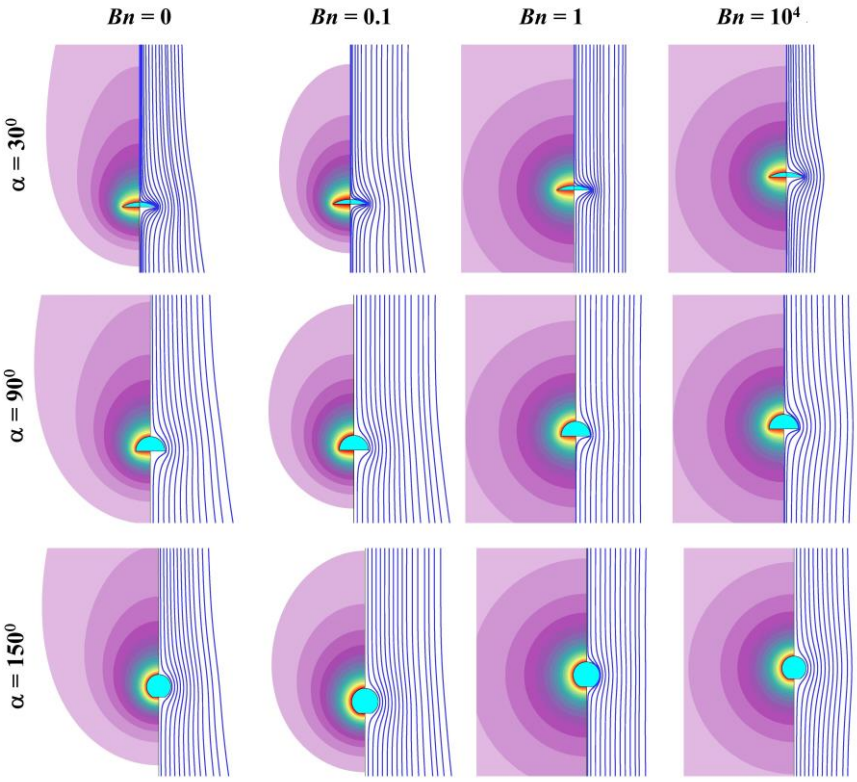


**Figure 5.25** Isotherm (left half) and Streamlines (right half) contours at $Pr_B$ = 0.72 and $Gr_B$ = 1.

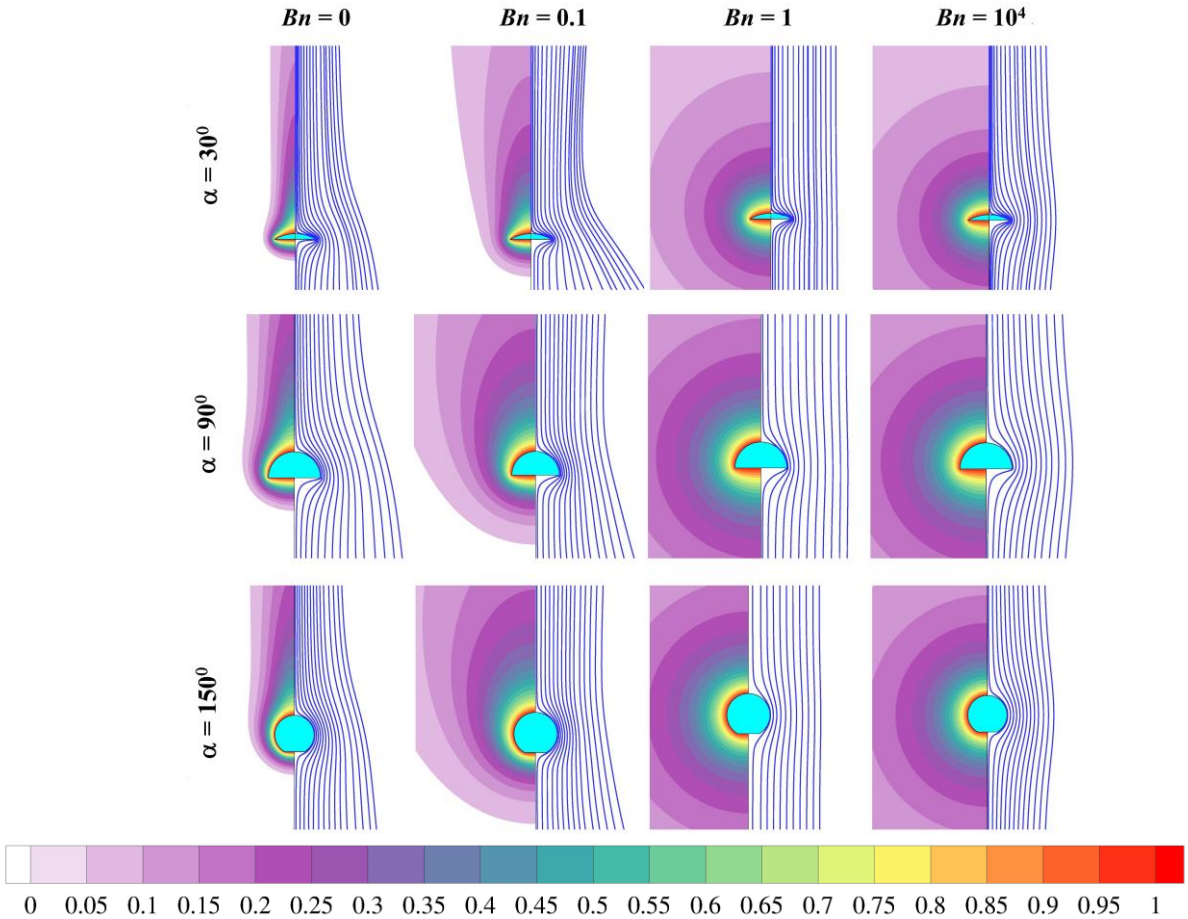


**Figure 5.26** Isotherm (left half) and Streamlines (right half) contours at $Pr_B$ = 100 and $Gr_B$ = 1.

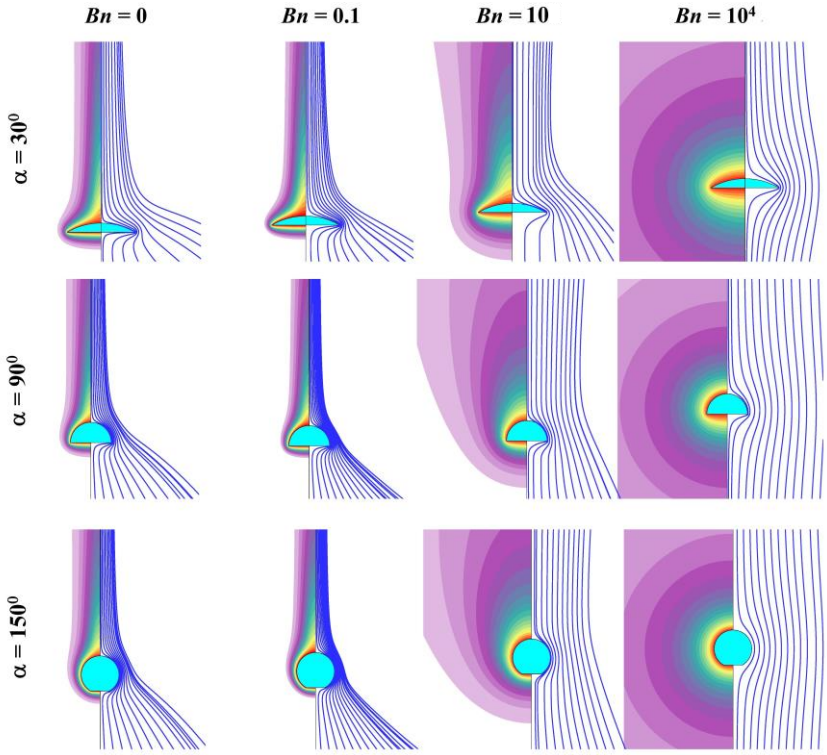


**Figure 5.27** Isotherm (left half) and Streamlines (right half) contours at $Pr_B$ = 0.72 and $Gr_B$ = $10^4$.

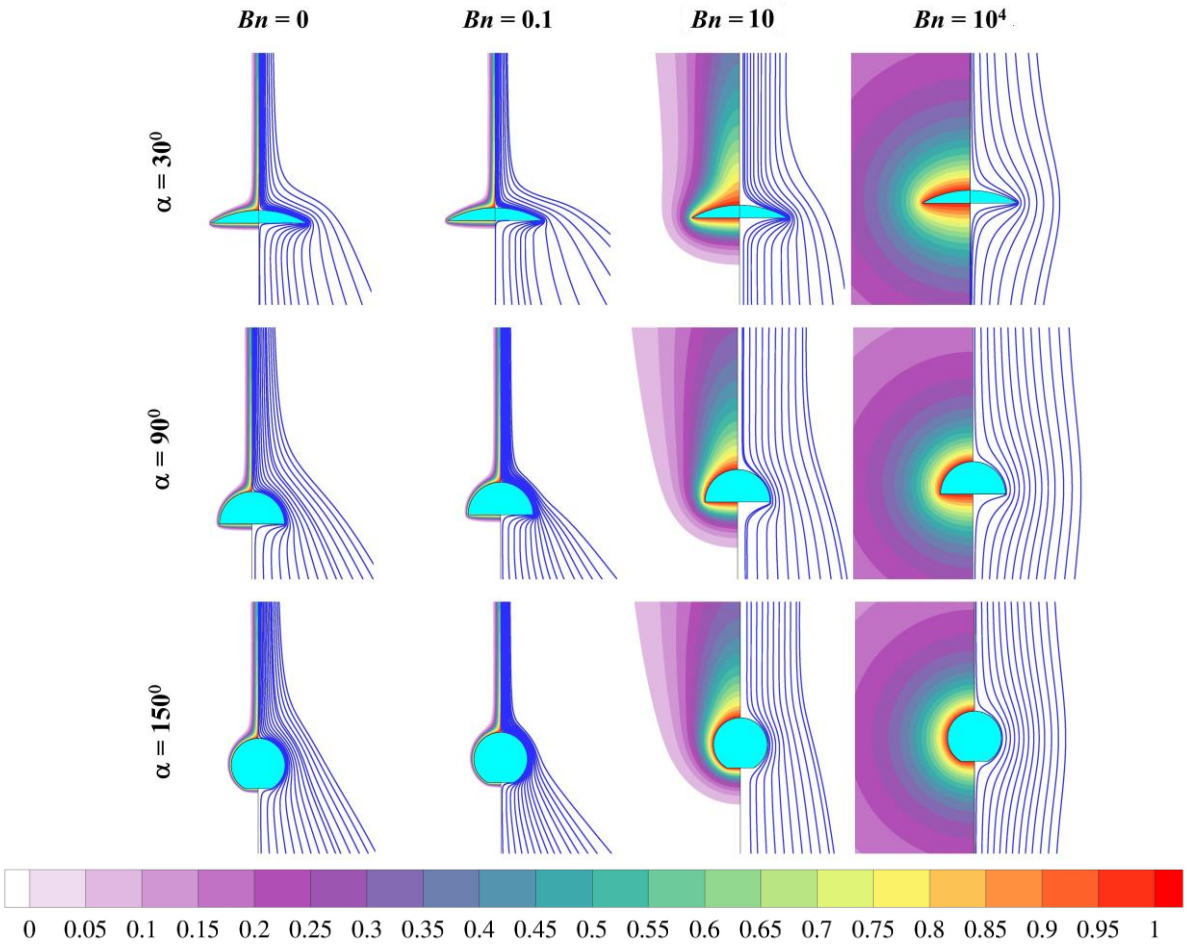


**Figure 5.28** Isotherm (left half) and Streamlines (right half) contours at $Pr_B$ = 100 and $Gr_B$ = $10^4$.

number (**Fig. 5.27-5.28**), the isotherms get more clustered at the front stagnation point due to strong buoyancy force effect. However, these forces are further suppressed by the high yield forces with the increase in Bingham number and make the contours more symmetrical in the upward and the downward directions similar to the low Grashof and Prandtl number cases.

The effect of the shape on the streamlines and temperature contours is not much differentiable. However, the sharp corner of the spherical segment results in the sudden changes in the streamline and isothermal contours which promote advection. Though the increase in shape factor tends to make the geometry more and more spherical the shape of the contours gets more broadened indicating comparative low heat transfer rate as compared to the smallest spherical segment.

### 5.2.4.2 Morphology of yielded/unyielded region

The key feature of the Bingham plastic fluid is their dual behavior of simultaneous existence of both solid-like (unyielded) and fluid-like (yielded) zones. The yielded/unyielded region are illustrated in **Figures 5.29 and 5.30** for three cases of spherical segment ($\alpha = 30°, 90°$ and $150°$) at two extreme values of the Grashof numbers, $Gr_B = 1$ and $10^4$. At low Bingham number $Bn = 0.1$, most of the fluid is yielded

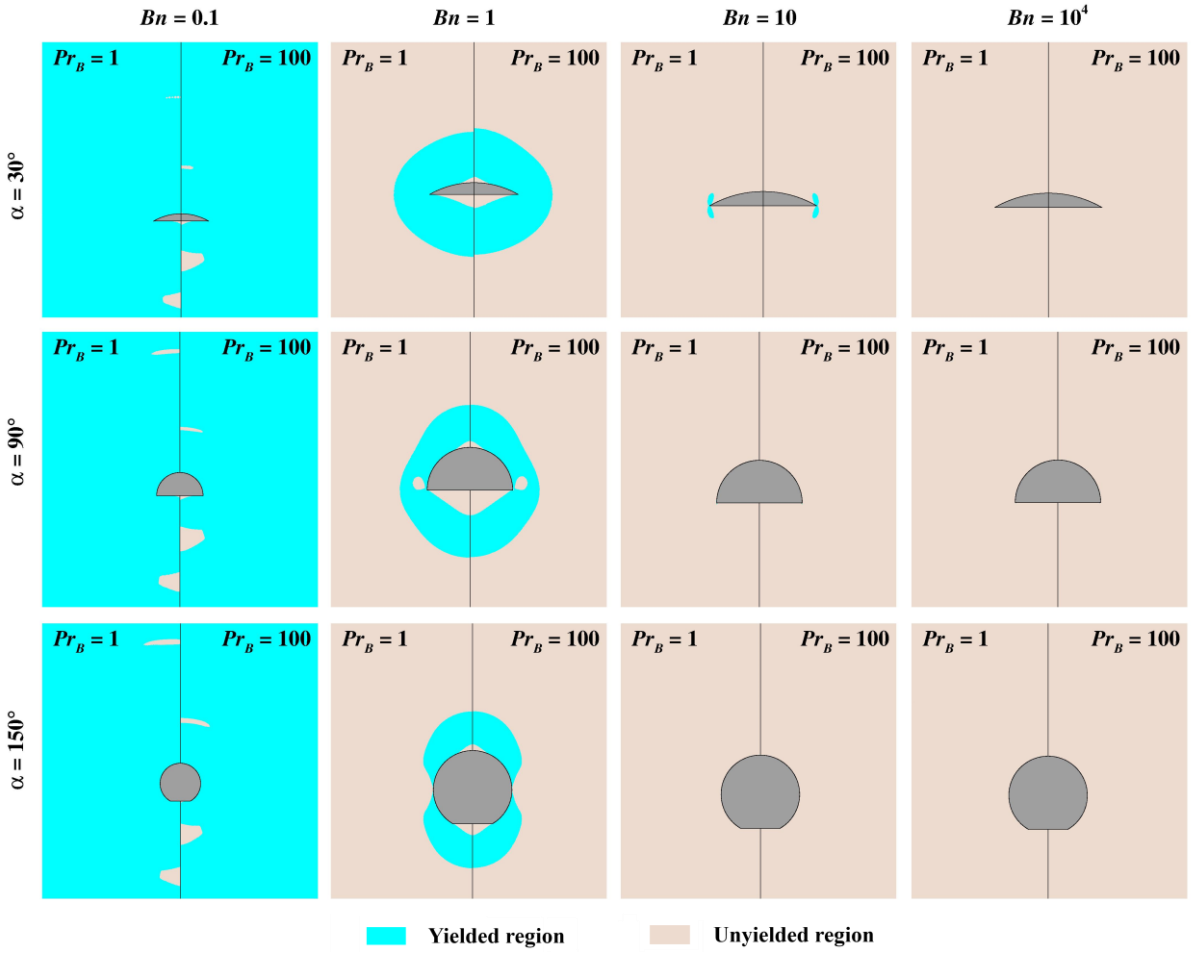


**Figure 5.29** Delineate of yielded/unyielded region at $Gr_B = 1$.

and two unyielded regions are observed at the upstream and downstream of the spherical segment which further moves closer to the geometry with the increase in Prandtl number (**Fig. 5.29**). Eventually, these

zones move towards the geometry surface and adhere to the surface of the spherical segments with the increase in Bingham number at fixed Grashof and/or Prandtl number. Due to the advection effect the unyielded regions at the front stagnation are generally observed larger due to flat surface than that of the rear end. Also, the increase in Bingham number l confines the yielded region in the envelope surrounding the spherical segment and eventually fluid-like regions disappear completely at the high value of Bingham number ($Bn \geq 10^4$). The shape of the fluid like zone specifically depends on the shape of spherical segments.

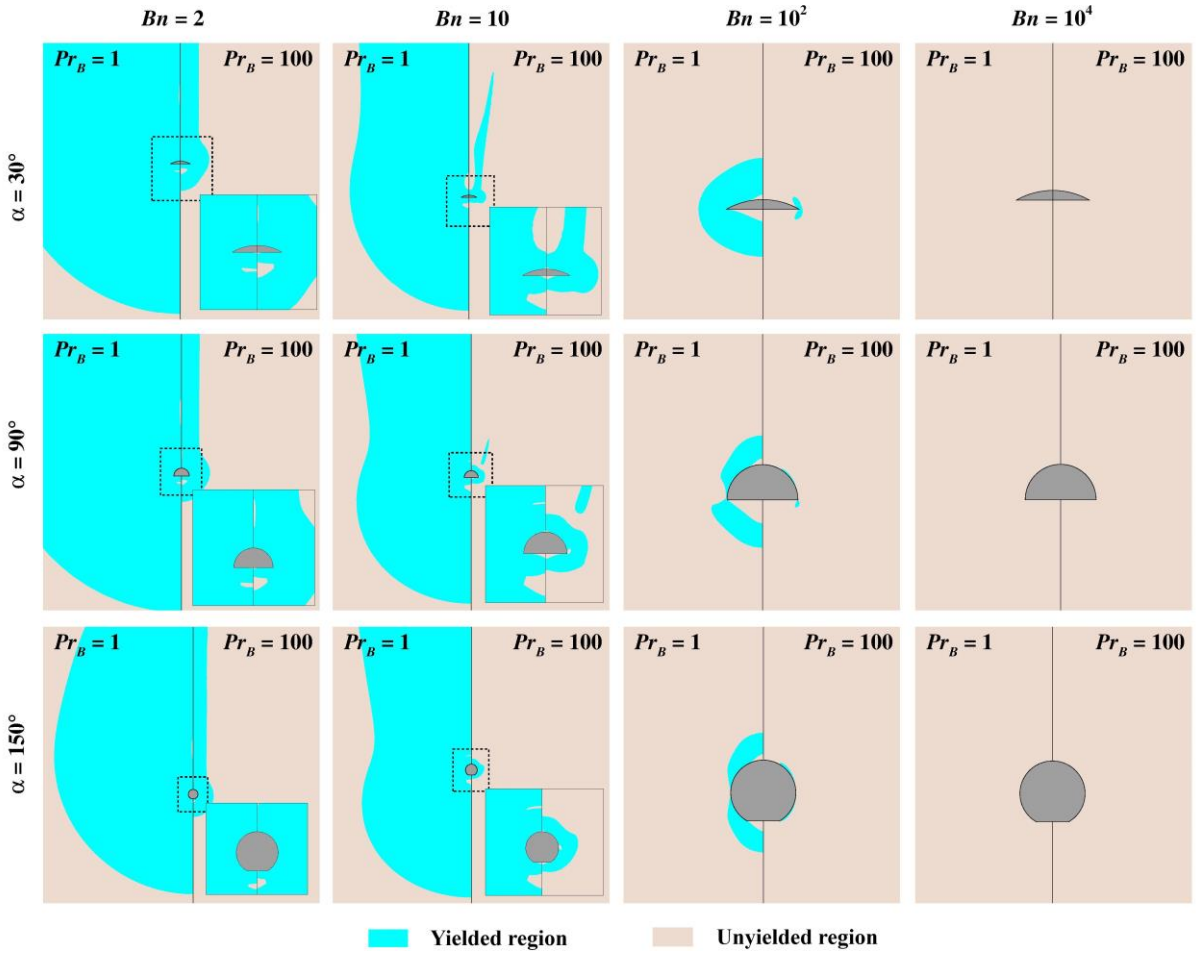


**Figure 5.30** Delineate of yielded/unyielded region at $Gr_B = 10^4$.

Due to the high buoyancy forces, the fluid gets more inertia; as a result, the yielded region increases in size and eventually requires high yield stress value or Bingham number to attain the perfect solid regions see **Fig. 5.30**. For the $Gr_B = 10^4$, the effect of Prandtl number is more noticeable here. The fluid zone becomes thinner and stretches upward with the increase in Prandtl number which is consistent with the isotherm contours.

The Grashof number has a similar effect in the natural convection as the Reynolds number in the forced convection. Similarly, it enhances the heat transfer in free convection for low Bingham number where fluid can be easily yielded. This suggests that the heat transfer is highest for low Bingham number (*Bn*

→ 0) and eventually decreases to the conduction limit as all the fluid gets frozen at high Bingham number ($Bn \rightarrow \infty$) which is clearly seen in **Fig. 5.30** for $Bn = 10^4$.

**Fig. 5.31** shows the variation of the non-dimensional *z*-component of the velocity from base of the particle ($\alpha = 30^o$) in the *r*-direction for two extreme values of Grashof numbers ($Gr_B = 1$ and $10^4$) and Prandtl ($Pr_B = 0.72$ and 100) number over the range of Bingham number. The velocity rises quickly to a maximum and then decays very slowly to lower values. For Newtonian fluid, $Bn = 0$, the velocity tapers off very slowly giving a thickest boundary layer. As Bingham number increases, the fluid will be enclosed in the vicinity of the particle by solid-like region which is moving with a constant velocity. Hence, it can be clearly observed that as the Bingham number increases the velocity profiles quickly approach to lowest value showing the decrease in the momentum boundary layer. Furthermore, for the constant Bingham number, increase in Prandtl number and/or Grashof number has similar effects which makes the boundary

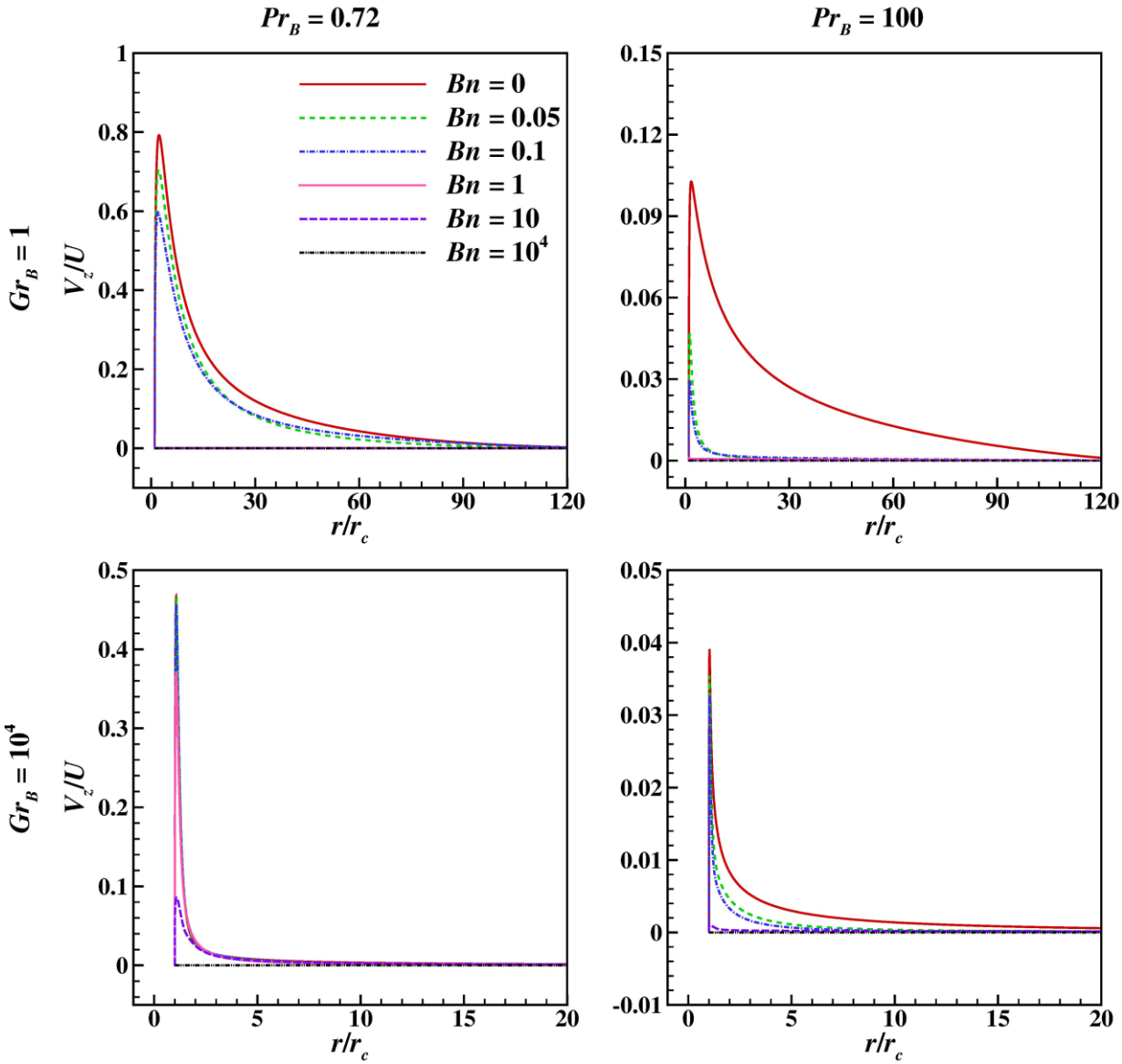


**Fig.5.31** Velocity profiles over the range of Bingham number in the *r*- direction from the base of the spherical segment for $\alpha = 30^o$

layer thinner. The plots for the two other cases of spherical segment (α = 90º and 150º) are mentioned in Appendix **A2**.

### 5.2.4.3 Local Nusselt number

The local variation of Nusselt number over the surface of the spherical segment has contributed to understanding the contribution of the different surfaces of the geometry. Even though the surface of the spherical segment is maintained at the isothermal condition the temperature gradient normal to the surface varies from point to point. **Figures 5.32** show the effect of $Gr_B$, $Pr_B$, $Bn$ and α on the variation of local Nusselt number considering the lowest value of $Gr_B$ = 1 and to extreme values of $Pr_B$ number i.e., $Pr_B$ = 0.72 and 100. It is evident that the heat transfer is governed by conduction at lower values of $Ra_B$ number i.e., $Ra_B$ = 0.72. For $Gr_B$ = 1, the local Nusselt number profiles over the range of Bingham number show marginal variation irrespective of the shape factor. However, it is noticeable here that the local value of the Nusselt number is observed to be lower at front stagnation point than the rear one. For the range of $Bn$ number values greater than 0.1 in **Fig. 5.32**. This is due to the formation of the unyielded zone at the front stagnation point as discussed in the previous **section 5.2.4.2**. While the Bingham number $Bn \leq 0.1$ the trend of local Nusselt number is observed similar to Newtonian fluids having local Nusselt number is always higher at front stagnation point than rear stagnation point. In **Fig. 5.32**, as Rayleigh number

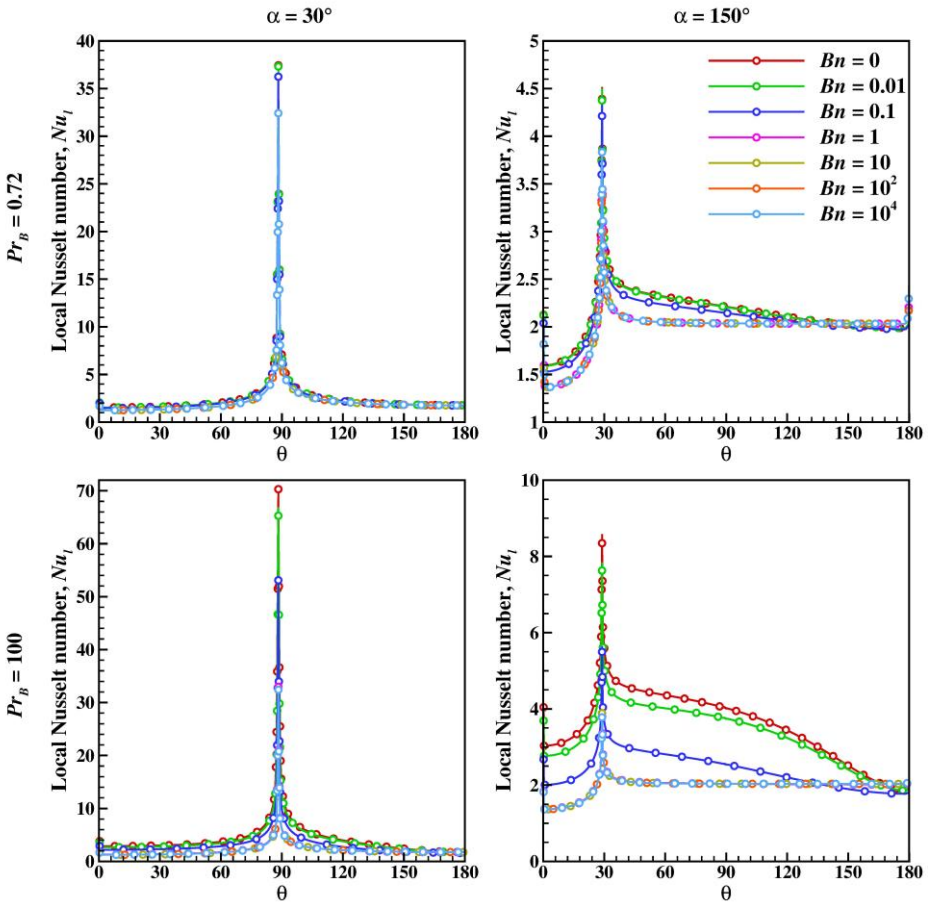


**Figure 5.32** Variation of local Nusselt number with Bingham number at $Gr_B$ = 1.

increases to $Ra_B$ = 100 for $Gr_B$ = 1. The increase in Prandtl number enhanced the rate of heat transfer which is more visible for $Bn \leq 0.1$ for both the extreme values of shape factors.

With the gradual increase in Rayleigh number in **Fig. 5.33,** i.e., $Ra_B = 72 \times 10^2$ and $10^6$, the role of increase in Prandtl number is observed to be similar as discussed before. However, the increase in $Ra_B$ postpones the conduction limit to the high Bingham number values due to advective heat transfer.

Finally, the effect of the shape of the spherical segment on the local Nusselt number is more visible on the curved surface for the Bingham number values below the conduction limit, particularly at high Grashof and Prandtl number values. For α = 30° and 150°, the Nusselt number shows maximum at the edge of the base of the spherical segment due to abrupt bending of the streamline and isotherm contours to negotiate the body contour of the geometry. As discussed in **section 5.2.4.1**, the streamlines and isotherms seem to be bent severely due to the shape of the particle at α = 30° which gradually becomes smooth on the surface of the particle as the alpha increases to 150°. This clearly reflects the highest value of the local Nusselt number of the particle which is observed higher for α = 30° than a α = 150°.

In summary, the local Nusselt number shows the positive dependence on the Grashof and Prandtl number, however, this dependence is weak with respect to Prandtl number as compared to Grashof number. Moreover, the progressive increase in Bingham number from the Newtonian behavior gradually

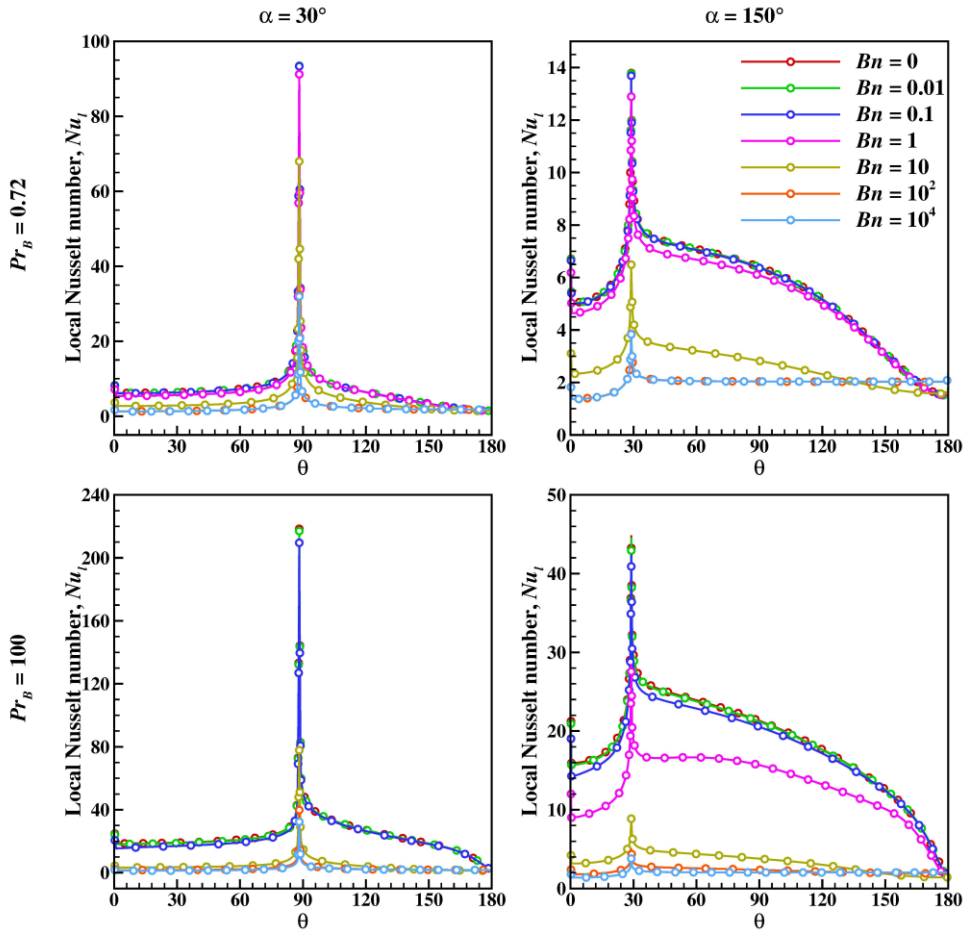


**Figure 5.33** Variation of local Nusselt number with Bingham number at $Gr_B = 10^4$.

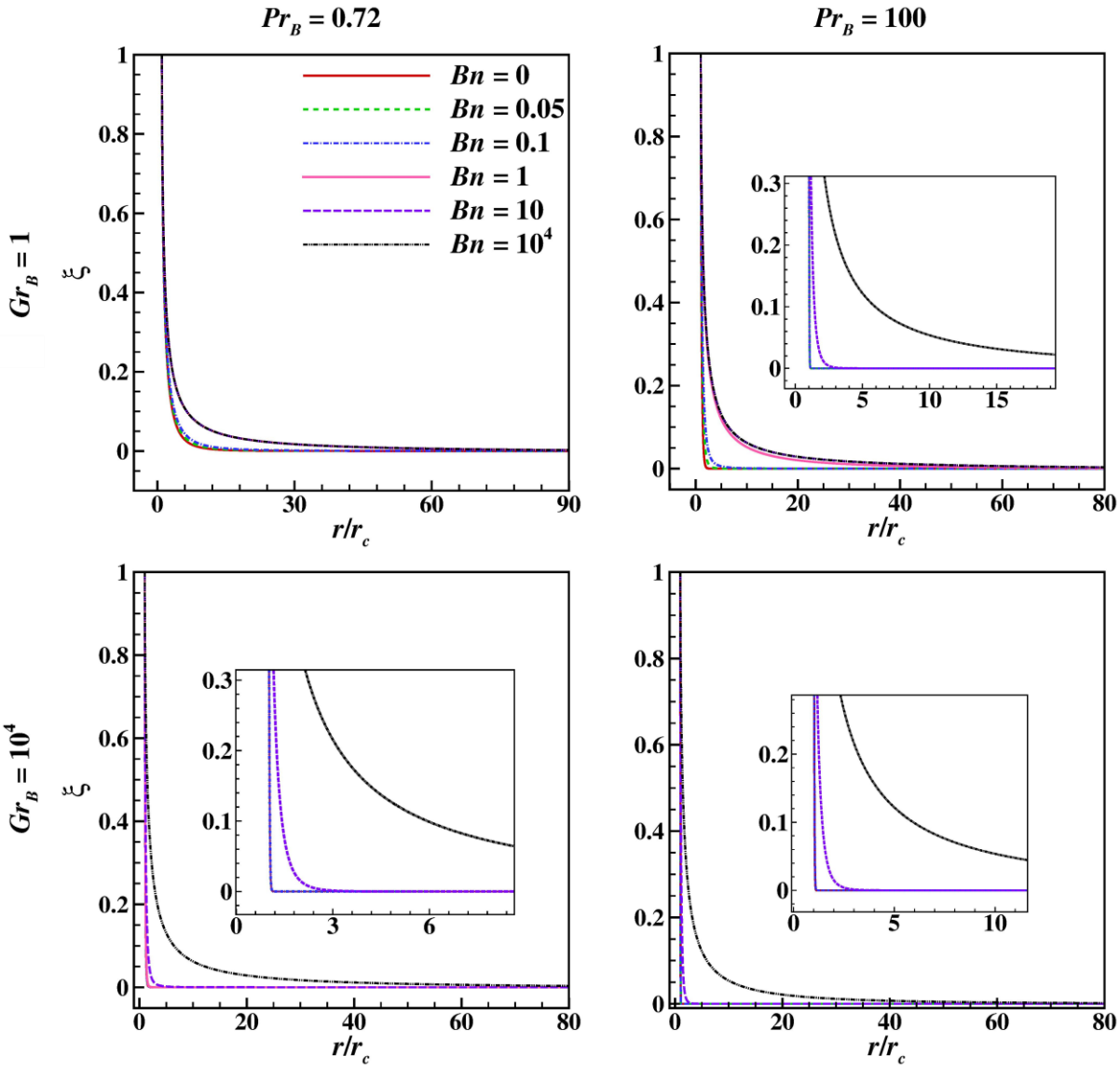


**Fig.5.34** Temperature profiles over the range of Bingham number in the *r*- direction from the base of the spherical segment for α = 30º.

deteriorates the heat transfer due to disappearance of yielded regions. Eventually the heat transfer is governed by purely conduction at the limit of Bingham number tends to infinite, which is found to be function of $Gr_B$, $Pr_B$ and α.

The non-dimensional temperature profiles or thermal boundary layer in the radial direction for smallest spherical segment (α = 30º) from its base are plotted in **Fig. 5.34**. A general trend can be seen where the thermal boundary layer is observed to be thinnest for the Newtonian fluids and it gradually increases as the Bingham number increases.

### 5.2.4.4 Average Nusselt number

Finally, it is worthwhile to analyze the rate of heat transfer in terms of gross parameter i.e., average Nusselt number and its dependance on $Ra_B$ (= $Gr_B \times Pr_B$), $Pr_B$, $Bn$ and α. The representation of the functional dependance of average Nusselt number as $f(Gr_B, Pr_B, Bn, \alpha)$ are frequently demanded in the various process engineering calculation. **Figures 5.35-5.37** illustrate the variation of average Nusselt

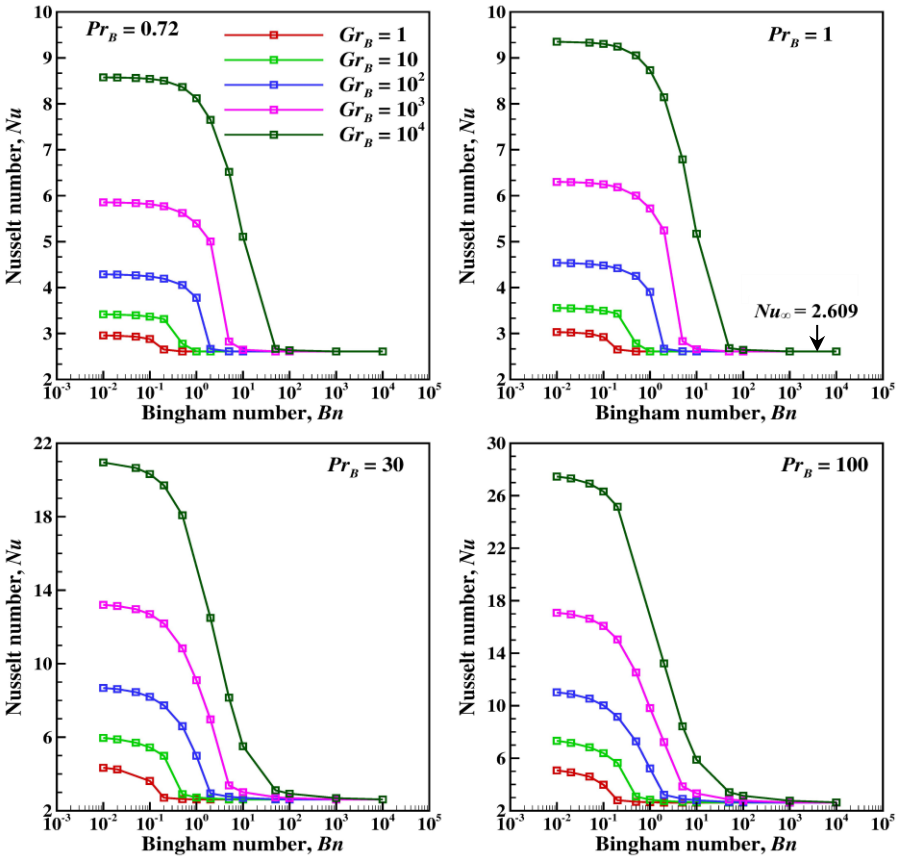


**Figure 5.35** Variation of Nusselt number with Bingham number for α = 30°.

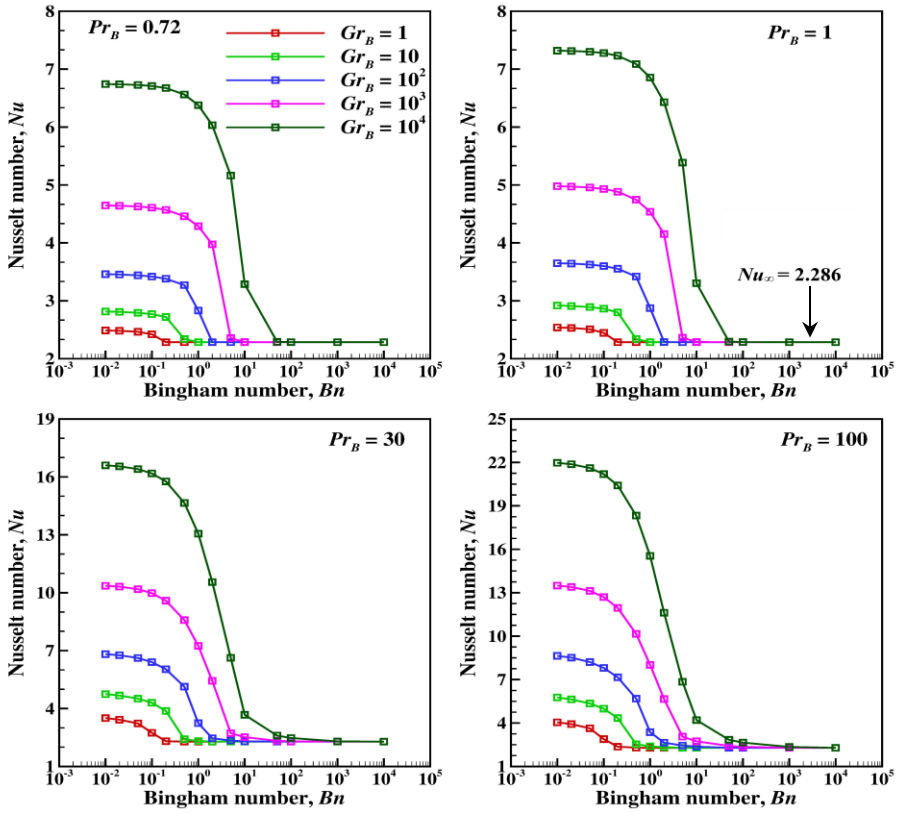


**Figure 5.36** Variation of Nusselt number with Bingham number for α = 90°.

number with the Bingham number over the range of $Gr_B$ and $Pr_B$ for α = 30°, 90° and 150°. The plots

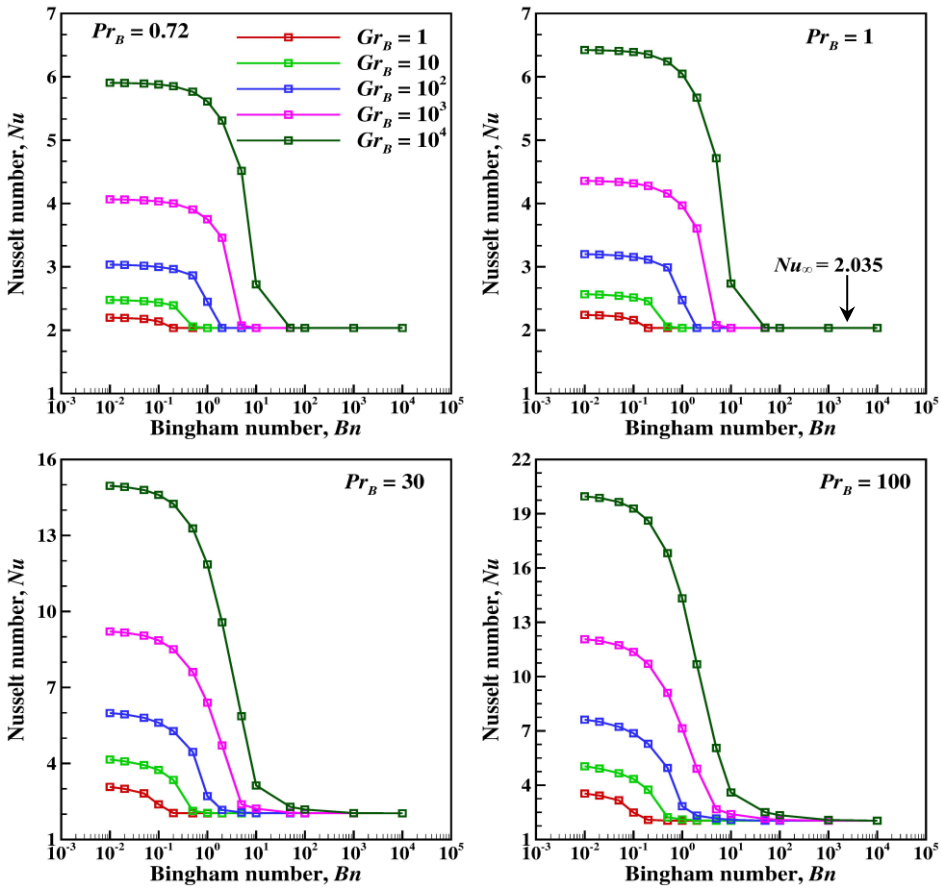


**Figure 5.37** Variation of Nusselt number with Bingham number for α = 150°.

reveal the positive dependence of average Nusselt number on Rayleigh number (= $Gr_B \times Pr_B$) and Prandtl number, while inverse dependence on the Bingham number for the fixed value of alpha. However, the average Nusselt number approaches the limiting value of Nusselt number ($Nu_\infty$) as Bingham number increases where the heat transfer is solely governed by the pure conduction. The maximum value of the Bingham number ($Bn_{max}$) corresponding to the pure conduction limit ($Nu_\infty$) delays with the increase in Rayleigh number.

Furthermore, the examination of **Figs. 5.35-5.37** over the range of $Ra_B$, $Pr_B$ and $Bn$ exhibits the inverse dependence of average Nusselt number on the α, otherwise under identical conditions. To gain further insight into the effect of shape of the particle on the rate of heat transfer, the average Nusselt number has plotted as a function of alpha as shown in **Figs. 5.38-5.40**. The effect of shape on the average Nusselt number is more prominent for α ≤ 120° as shown in **Figs. 5.38-5.40**. Also, it is evident from **Fig. 5.39** that to reach the conduction limit for α = 30°, the Bingham number has to be higher as compared to any other alpha value over the range of Rayleigh and Prandtl number considered in this study.

Finally, have function dependence of the average Nusselt number on $Gr_B$, $Pr_B$, and $Bn$ for spherical segments has been proposed in the form of correlation. It is essential to recall here that in the limit of $Bn \rightarrow \infty$, the heat transfer is governed by purely conduction mechanism approaching to the conduction limit of the heat transfer. Hence, the limiting average Nusselt number needs to be included in the predictive

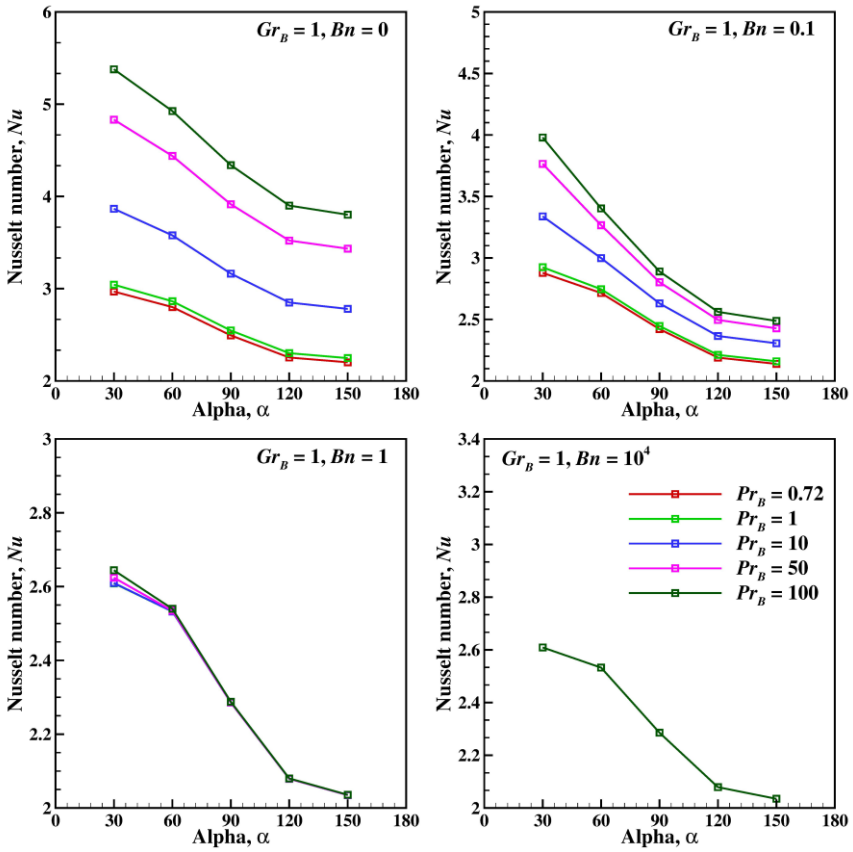


**Figure 5.38** Variation of average Nusselt number with shape factor (α) at $Gr_B$ = 1.

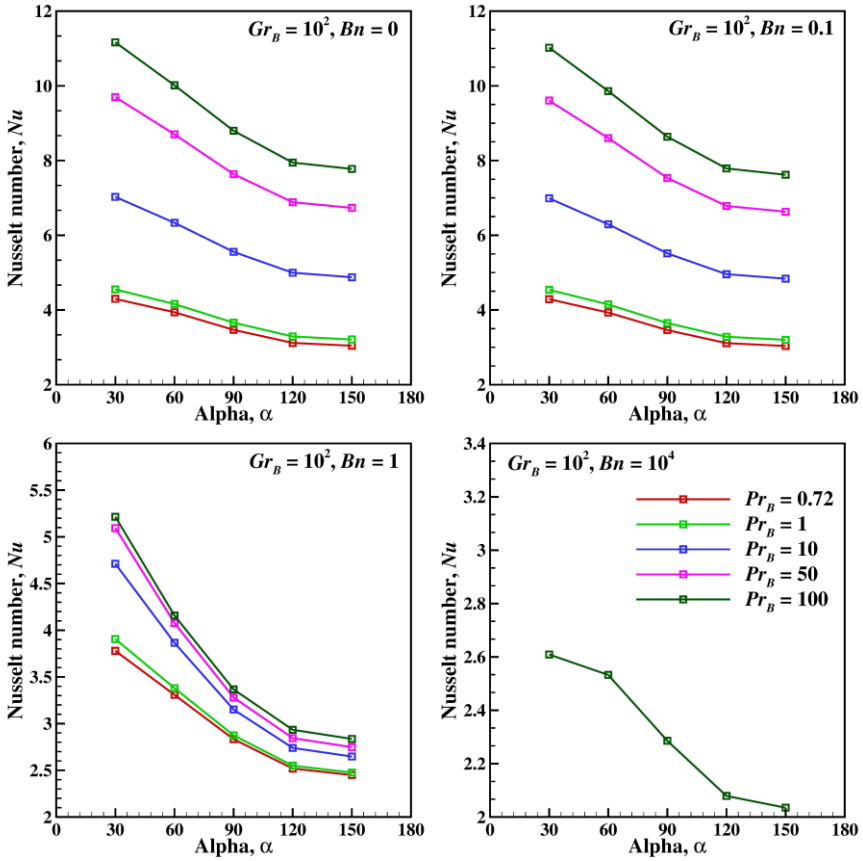


**Figure 5.39** Variation of average Nusselt number with shape factor (α) at $Gr_B$ = 100.

equation. Using the preceding heuristics, we can establish a satisfactory correlation with the numerical

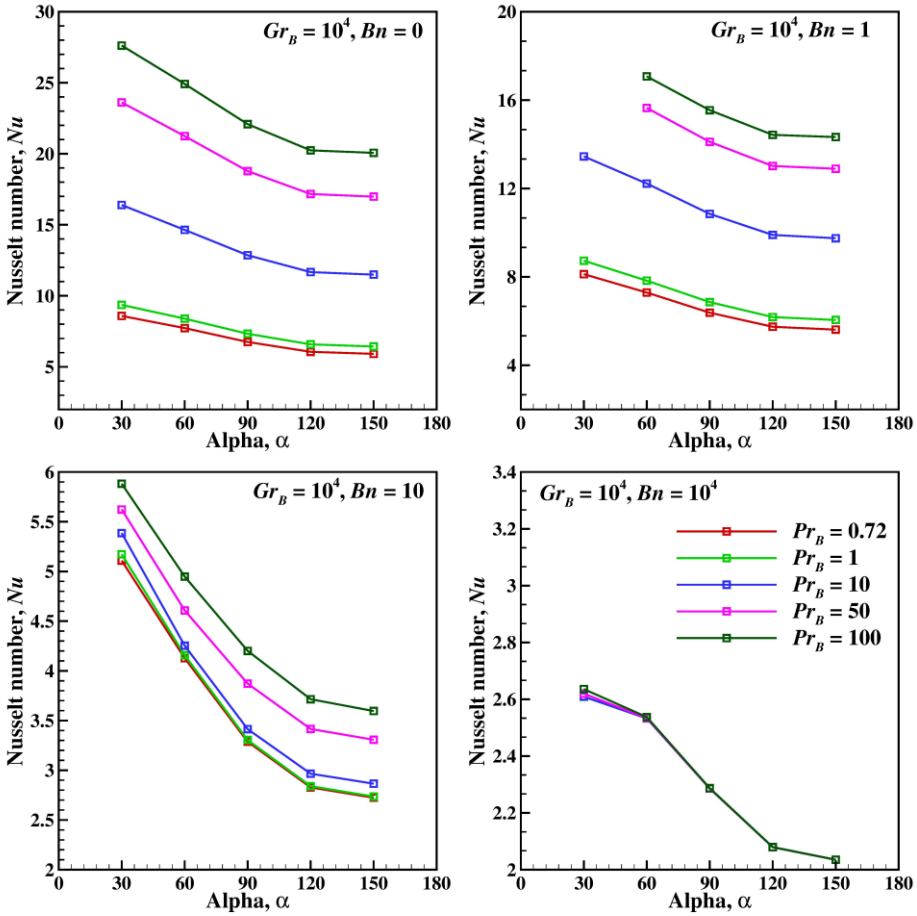


**Figure 5.40** Variation of average Nusselt number with shape factor (α) at $Gr_B = 10^4$.

data at hand.

For $Bn < Bn_{max}$ :

$$Nu = Nu_{\infty} + a\ Gr_B Pr_B^{\ 0.25}\left(1-\left(\frac{Bn}{Bn_{\max}}\right)^{b}\right)1+Bn^{\ -c} \tag{5.10}$$

For $Bn \geq Bn_{max}$ :

$$Nu = Nu_{\infty} \tag{5.11}$$

**Table 5.9** Coefficient for **Eqs. (5.10) and (5.11)**

| α | $Nu_{\infty}$ | $a$ | $b$ | $c$ | % $\delta_{avg}$ | % $\delta_{max}$ | # data |
|---|---|---|---|---|---|---|---|
| 30 | 2.609 | 0.735 | 0.218 | 0.894 | 11.8 | 60.0 | 580 |
| 60 | 2.532 | 0.623 | 0.304 | 0.728 | 12.5 | 64.3 | 539 |
| 90 | 2.286 | 0.500 | 0.319 | 0.730 | 13.9 | 65.7 | 524 |
| 120 | 2.079 | 0.438 | 0.318 | 0.730 | 14.5 | 58.5 | 513 |
| 150 | 2.035 | 0.412 | 0.344 | 0.730 | 15.2 | 57.9 | 504 |

The **Eqs. (5.10)** and **(5.11)** is valid for the range of parameters: Grashof number ($1 \leq Gr_B \leq 10^4$) and Prandtl number ($0.72 \leq Pr_B \leq 100$), Bingham number ($0 \leq Bn \leq 10^4$) and shape factors α = 30°, 60°, 90°,

120° and 150°. The coefficients of **Eqs. (5.10)** and **(5.11)** have been tabulated in **Table 5.9** including number of correlated data for each geometry, maximum and average percentage deviations of the predicted values from the numerical values.

Upon detailed analysis, it was discovered that approximately 10 % of the data points for each geometry show deviation greater than 30% in **Eq. (5.10)**, indicating no noticeable trends.

# Chapter 6

# Falling ball method (FBM) for determining zero-shear and shear-dependent viscosities of power-law fluids

The falling ball method (FBM) is one of the well-established techniques for measuring the viscosity of Newtonian liquids at the room as well as at elevated temperatures and pressures. Owing to its simplicity and low cost, the possibility of extending its range of application to non-Newtonian systems including virgin and filled polymer melts, composites, polymer-solutions, etc. is explored here. In this chapter, we have used theoretical results for the flow of power-law fluids past a sphere to extract the values of the zero-shear viscosity and shear-dependent viscosity in the low shear rate limit. The theoretical scheme outlined in this work has been validated by presenting comparisons with experimental results for scores of polymer solutions for which both Newtonian and power-law fluid.

## 6.1 Previous work

Owing to its simplicity and ease of operations, and low cost the falling ball method (FBM) is a well-established technique for measuring the viscosity of Newtonian fluids under ambient conditions as well as at elevated temperatures and pressures, e.g., see References (Elahi *et al*., 2012; Gupta, 2014; Kono, 2018; and Cartwright, 2020) for a broad spectrum of applications of the FBM. Furthermore, Brizard *et al*. (2005a, b) and Sutterby (1973) have discussed detailed designs, various corrections and the precision of the viscosity values for Newtonian fluids obtained by this method. With a suitable design and careful operation, it is possible to achieve a relative uncertainty of ~ 0.1% in the value of the measured viscosity at ambient temperatures.

The basic equation used in the FBM is the so-called Stokes law which is written as follows for a sphere falling under its own weight,

$$\mu = \frac{gd^2\left(\rho_s - \rho\right)}{18U} \tag{6.1}$$

In **Eq. (6.1)**, $\mu$ is the viscosity of the liquid, $\rho_s$ and $\rho$ are the density of the sphere and the liquid, respectively, $d$ is the diameter of the sphere, $g$ is the acceleration due to the gravity. The only measured quantity in **Eq. (6.1)** is the terminal falling velocity, $U$ of the sphere. The main assumptions underpinning the validity of **Eq. (6.1**) include the steady, incompressible, isothermal, creeping flow regime (negligible inertial effects << viscous effects) and unconfined fluid. The relative importance of the inertial and viscous forces is ascertained by calculating the value of the familiar Reynolds number, $Re$, defined as

$$Re = \frac{\rho U d}{\mu} = \frac{Inertial\ force}{Viscous\ force} \tag{6.2}$$

Evidently, vanishingly small values of $Re \rightarrow 0$ indicate negligible inertial effects. In practice, this condition is reached by, $Re <\sim 1$. One can always choose a sphere of appropriate size and density to meet this criterion. Since the experimental determination of the terminal falling velocity $U$ is often carried out in cylindrical tubes of a finite diameter $D$ and height $L$ with its bottom end closed, therefore, it is necessary to correct the experimentally measured value the terminal falling velocity $V_m$ of the sphere for the wall and end effects. The wall correction is often applied by using the wall correction factor $f_w$ defined as:

$$f_w = \frac{V_m}{U} \tag{6.3}$$

In the creeping flow regime, this factor $f_w$ is only a function of $(d/D)$. One widely used expression is given by (Faxen, 1923 and Bohlin, 1960)

$$f_w = 1 - 2.10443\frac{d}{D} + 2.08877\left(\frac{d}{D}\right)^3 + ..... \tag{6.4}$$

**Equation (6.4)** is valid for $Re << 1$ and $(d/D) \leq 0.6$. Numerous other expressions of varying complexity and forms for the wall correction factor spanning the full ranges of the Reynolds number and confinement ratio $(d/D)$ are available in the literature though the high Reynolds number results are of no interest here; for the falling ball experiments aimed at measuring the viscosity must be carried at small Reynolds numbers. (Chhabra, 2006). In contrast, only scant information is available regarding the end effects on the falling velocity, albeit this effect is known to be indeed negligible (Brizard *et al*., 2005a, b). Using the analytical results of Tanner (1963) and Kono (2018) prescribed the measured velocity to be multiplied by the end correction factor $E$ given by

$$E = 1 + \frac{9}{18}\left(\frac{d}{2z}\right) + \left[\frac{9}{8}\left(\frac{d}{2z}\right)\right]^2 \tag{6.5}$$

where $z$ is the distance from the bottom end of the tube to the section where the falling sphere velocity of the sphere is measured. Within the distance of ten-times the diameter, i.e., $z/d = 10$, **Eq. (6.5)** predicts $E = 1.0256$, **Eq. (6.5)** is applicable. Clearly, for $z/d \geq 20$ this correction becomes negligible. **Equation (6.1)** can now be written as

$$\mu = \frac{gd^2(\rho_s - \rho)}{(V_m / f_w)E} \tag{6.6}$$

**Equation (6.6)** thus forms the basis of the FBM for measuring the viscosity of Newtonian fluids as a function of temperature and pressure by using the value of the fluid density $(\rho)$ at the relevant temperature and pressure. Finally, smaller is the value of the Reynolds number, better should be the result due to strict compliance with the condition of inertial forces being negligible. Conversely, the viscous effects progressively diminish with the increasing Reynolds number, i.e., the falling velocity shows a dependence

weaker than $\mu^{-1}$. This condition is similar to the requirement of operating U-tube and capillary viscometers in the laminar flow regime.

Next, we turn our attention to the application of the FBM for evaluating the zero-shear viscosity of polymer melts, solutions and loaded systems. Since in this regime, the shear viscosity is expected to be a constant irrespective of the value of the shear rate induced by a falling sphere, the fact that the shear rate varies from one point to another on the surface of the sphere is of no significance, akin to that in the case of Newtonian fluids. Thus, all that is required is the falling sphere data is obtained in the constant viscosity region for the system of interest. Though this range is not known a priori, one can obtain data with a few spheres (different size and/or density) to calculate the value of $\eta$ sing **Eq. (6.6)** to check whether the resulting values of $\eta$ are identical to each other within the margin of experimental uncertainty. Scaling arguments suggest the shear-rate to be of the order of ($U/d$) and indeed for a Newtonian fluid, the local value of $\dot{\gamma}_{r\theta}$ ranges from 0 to ($3U/d$) on the surface of the sphere yielding the surface mean value of ($2U/d$) (Bird *et al.*, 2002; Uhlherr *et al.*, 1976). Thus, by using a few spheres tests, one can ascertain whether the sphere is settling in the constant viscosity ($\eta_0$) region or not. In any case, the falling velocity in a viscous fluid is very small and therefore the resulting values of the surface average shear rate ($2U/d$) are generally small, and one can even extrapolate these results to extract the value of $\eta_0$ as demonstrated elsewhere (Bird *et al.*, 2002; Chhabra and Uhlherr, 1980; Chhabra, 2006; Tanner, 1963; Uhlherr *et al.*, 1976). Beyond this region, however, **Eq. (6.6)** can still be used to obtain a value of $\eta$ for a given fluid-ball system which is often employed to monitor the uniformity and consistency of a product, though the apparent viscosity-shear rate curve cannot be constructed because neither the shear stress nor the shear rate is known a priori in the shear-thinning region. This issue is explored in detail in the next section.

## 6.2 Creeping flow of power-law past a sphere

The creeping flow around a sphere is non-viscometric and therefore the shear rate $\left(\dot{\gamma}_{r\theta}\right)$ varies on the surface of the sphere, i.e., $\dot{\gamma}_{r\theta}\left(R,\theta\right)$ from one point to another. This, in turn, depends upon the corresponding velocity $U(r, \theta)$ field. In principle, the velocity and pressure fields can be obtained by numerically solving the governing differential equations for a specific fluid model such as Newtonian, power-law, Ellis model, etc. to obtain an expression equivalent of **Eq. (6.1)**, though its specific form will depend upon the choice of the specific viscosity model. For an incompressible power-law fluid, the $r$-$\theta$ component of the extra stress tensor, $\tau_{r\theta}$ is related to the corresponding component of the rate of strain tensor $\dot{\gamma}_{r\theta}$ as:

$$\tau_{r\theta} = \left[2\eta\left(\dot{\gamma}\right)\right]\dot{\gamma}_{r\theta} \tag{6.7a}$$

For a power-law fluid, the viscosity is given by the expression:

$$\eta(\dot{\gamma}) = m(\dot{\gamma})^{n-1} \tag{6.7b}$$

For a general flow, the shear rate $\dot{\gamma}$ is evaluated as:

$$\dot{\gamma} = \sqrt{2\dot{\gamma}_{ij}\dot{\gamma}_{ji}} \tag{6.8}$$

In **Eq.** (6.8), $\dot{\gamma}_{ij}$ are the components of the rate of deformation tensor (Bird *et al.*, 2002). Here, $m$ and $n$ are the power-law constants. For $n = 1$, **Eq. (6.7b)** reduces to a Newtonian fluid of viscosity $m = \mu$. Due to the axisymmetric nature of the flow, the $\dot{\gamma}_{r\theta}$ component of the rate of deformation tensor, $\dot{\boldsymbol{\gamma}}$ in turn is related to the velocity component $V_r$ and $V_\theta$ as (Bird *et al.*, 2002):

$$\dot{\gamma}_{r\theta} = r\frac{\partial}{\partial r}\left(\frac{V_\theta}{r}\right) + \frac{1}{r}\frac{\partial V_r}{\partial \theta} \tag{6.9}$$

One can now combine **Eq**. **(6.7)** to **(6.9)** to obtain the value of $\tau_{r\theta}$ for a fixed value of $\dot{\gamma}_{r\theta}$ Thus, a knowledge of the velocity field is required to evaluate ($\tau_{r\theta}$, $\dot{\gamma}_{r\theta}$) on each point on the surface of the sphere. The fact that both these quantities vary on the surface of the sphere is of no consequence for Newtonian fluids due to their constant shear viscosity (independent of shear rate). But this is not so for a power-law fluid. Despite this complexity, the simplicity of this method has received some attention in the literature to explore the possibility of extending the FBM to characterize power-law fluids. In order to appreciate the intrinsic difficulty in this endeavor, it is instructive to first revisit the issue of constructing the steady shear flow curve for a Newtonian fluid using FBM data. For the sake of simplicity, it is assumed hereafter that the terminal falling velocity of the sphere is free from wall and end effects and the Reynolds number of flow is small. Our analysis begins with the celebrated analysis of the Stokes stream function for the creeping flow of a Newtonian flow around a sphere which can be used to write the following expressions for $\dot{\gamma}_{r\theta}$ and $\tau_{r\theta}$(Bird *et al.*, 2002):

$$\tau_{r\theta} = \frac{3}{2}\frac{\mu U}{R}\left(\frac{R}{r}\right)^4 \sin\theta \tag{6.10a}$$

$$\dot{\gamma}_{r\theta} = \frac{3}{2}\frac{U}{R}\left(\frac{R}{r}\right)^4 \sin\theta \tag{6.10b}$$

The component of the viscous force $F_V$ along the direction of the sphere fall is calculated as:

$$F_V = \int_o^\pi \left(\tau_{r\theta|r=R}\sin\theta\right) 2\pi R^2 \sin\theta d\theta \tag{6.11}$$

Substituting from **Eq. (6.10a)** into **Eq. (6.11)** and evaluating the integral yields:

$$F_V = 4\pi\mu RU = 2\pi\mu Ud \tag{6.12}$$

It is also known that $F_V$ is (2/3) of the total drag force, $F_D$ exerted on the sphere for a Newtonian fluid. For the case of the steady settling of a sphere under the influence of gravity, the total drag force $F_D$ is given as:

$$F_D = \frac{\pi d^3}{6}(\rho_s - \rho)g \tag{6.13}$$

And hence

$$F_V = \frac{2}{3}F_D = \frac{\pi d^3}{9}(\rho_s - \rho)g \tag{6.14}$$

One can now introduce a surface average shear stress $< \tau_w >$ for a Newtonian fluid such that

$$F_V = \langle\tau\rangle_N \pi d^2 \tag{6.15}$$

**Eq. (6.13)** and **Eq. (6.14)** combine to yield,

$$\langle\tau\rangle_N = \frac{gd}{9}(\rho_s - \rho) \tag{6.16}$$

This equation applies to Newtonian fluids. Now rearranging **Eq. (6.1)** as

$$\langle\tau\rangle_N = \mu\langle\dot{\gamma}\rangle_N \tag{6.17}$$

It is clearly seen that the average shear rate for a Newtonian fluid $\langle\dot{\gamma}\rangle_N$ is given by ($2U/d$). i.e.,

$$\langle\dot{\gamma}\rangle_N = \frac{2U}{d} \tag{6.18}$$

This can also be obtained by averaging $\dot{\gamma}_{r\theta}$, **Eq. (6.10b)**, on the surface of the sphere (Bird *et al.*, 2002). Thus, a series of data point obtained from falling sphere tests can be used to construct a flow curve in terms of $\langle\tau\rangle_N$, $\langle\dot{\gamma}\rangle_N$ which will be a straight line of slope equal to $\mu$ and it should pass through the origin provided the experimental results are free from wall and end effects and $Re$ < ~ 1 or so.

In order to parallel this treatment for power-law fluids, one must know the corresponding velocity (i.e., stream function) and pressure field to evaluate the drag force on the sphere, equivalent of **Eq. (6.12)** and the ratio of the viscous drag to the overall drag force. In spite of the fact that significant literature has accrued on this subject, (Chhabra, 2006; Song *et al*., 2009, 2011; Sun *et al*., 2020; Okesanya, 2020) much of the literature is concerned with the prediction of the total drag force experienced by a sphere in

generalized Newtonian fluids, or viscoelastic fluid in the limit of creeping flow. This body of knowledge has been thoroughly revised by Agwu *et al*. (2018). Most of these studies either relate to high Reynolds number ($Re_{PL} > 1$) and/or are concerned with the development of empirical correlation for predicting the terminal falling velocity of a sphere of known size and density in a non-Newtonian liquid of known rheology. Therefore, this body of knowledge is of little utility in the present context.

Dimensional considerations of this flow suggest that even in the creeping flow regime, the flow field to be a function of the power-law index and consequently, as demonstrated by Uhlherr *et al*. (1976) and Cho and Hartnett (1983), the ratio of the viscous-to-total drag force is expected to be a function of the power-law index $n$ and hence the average shear stress and shear rate will also depend upon the value of the power-law index ($n$). Conversely, one can think of applying a correction factor to the corresponding Newtonian values as follows:

$$\langle \tau \rangle = \langle \tau \rangle_N \; f_1(n) \tag{6.19a}$$

$$\langle \dot{\gamma} \rangle = \langle \dot{\gamma} \rangle_N \; f_2(n) \tag{6.19b}$$

Neither of this information is available in the above-mentioned previous numerical or experimental studies. Much of the limited effort to date has been directed at establishing the form of the two correction factors, $f_1(n)$ and $f_2(n)$ only in an approximate manner in order to use the FBM for power-law fluids in the shear-thinning region. The earliest attempt is this direction is due to (Hirota and Takada, 1959) who presented the following empirical expression for the maximum shear rate on the surface of the sphere:

$$\dot{\gamma}_R = \left(\frac{3U}{d}\right)\left[1 + 2.5\left(n' - 2\right) - 0.75\left(n' - 2\right)^2\right] \tag{6.20}$$

where $n' = \dfrac{d \ln U}{d \ln R}$

The corresponding maximum shear stress (in Newtonian fluids) is given by:

$$\tau_{max} = \frac{gd\left(\rho_s - \rho\right)}{6} \tag{6.21}$$

For a Newtonian fluid in the Stokes regime, $n' = 2$ ($U \sim R^2$) and thus **Eq. (6.20)** leads to the maximum value of the shear rate at the equator, i.e., ($3U/d$). Hirota and Takada (1959) reported that their predictions are in good agreement with the capillary viscometer data for a few polymer solutions. Clearly, this development is not based on a solution of the continuity and momentum equations and thus must be seen as an entirely empirical approach. However, in the limit of the Newtonian fluid behaviour ($n' = 2$), this method is identical to **Eq. (6.1).** In contrast, Uhlherr *et al*. (1976) made use of the approximate drag results based on the application of variational calculus. Since the upper bound calculation of the drag on a sphere

hinge on a trial velocity profile which merely satisfies the continuity equation and the boundary conditions, this may or may not satisfy the corresponding momentum equation (Slattery, 1962; Wasserman and Slattery, 1964). Notwithstanding this limitation, they proposed two methods, namely, i.e., either $f_1(n)$ or $f_2(n)$ is needed. Thus, if $f_1(n)$ is used, then $f_2(n) = 1$ and vice versa if $f_2(n)$ is used, $f_1(n) = 1$. However, this analysis is also limited to a rather narrow range of conditions as $0.76 \leq n \leq 1.0$, as the fully converged solution was not feasible for values of the power-law index $n < 0.76$ (Slattery, 1962). Subsequently, Cho and Hartnett (1983) and Cho *et al.* (1984) improved upon the numerical results of (Slattery, 1962 and Wasserman and Slattery, 1964) but their results still denote approximate upper and lower bounds on the total drag over the complete range of conditions $0.1 \leq n \leq 1$. The two bounds deviate appreciably with the decreasing value of the power-law index and are limited to shear-thinning fluids only.

In essence, they have used **Eq. (6.7)** to obtain the functional forms of $\tau_{r\theta}(r, \theta, m, n)$ and $\dot{\gamma}_{r\theta}(r, \theta, m, n)$ to obtain their surface average values. For the upper bound, one can calculate $\tau_{r\theta}$ by substituting the values of $I_2$ and $\dot{\gamma}_{r\theta}$ obtained from the trial stream function whereas the lower bound calculation is based on the trial stress profile (i.e., $\tau_{r\theta}$ is known) and one can thus calculate $\dot{\gamma}_{r\theta}$. However, it needs to be emphasized here that these results are based on an incomplete solution of the governing momentum and continuity equations. The variational principal approach is concerned with the total energy dissipation, and it is therefore neither possible nor justified to delineate the contribution of the viscous and form drags to the total drag force within the framework of this approach, i.e., the ratio of $F_V$ to the total drag force $F_D$ is not known.

They presented empirical expressions for $f_1(n)$ and $f_2(n)$ as polynomials in the power-law index containing terms up to $n^3$ or $n^4$ (Cho and Hartnett, 1983). Two observations are in order here. Firstly, as noted earlier, the upper bound calculation does not satisfy the momentum equation. Similarly, the lower bound calculation does not satisfy the conservation of mass! Secondly, the two bounds coincide only for Newtonian fluids ($n = 1$), and the two bounds increasingly deviate from each other with the decreasing value of the power-law index, e.g., see **Fig. 6.1**. For instance, the two bounds differ from each other by ~ 40% for $n = 0.3$ which rises to ~ 80-90% for $n = 0.1$. Finally, the variational principles are not applicable for $n > 1$. More detailed discussion regarding the deficiencies of the previous work on the use of the FBM for power-law fluids is available in the literature (Chhabra, 2006). In summary, no reliable method is available as of now for testing the validity of the FBM for power-law fluids and this work aims to bridge this knowledge gap.

Admittedly, as noted previously, this problem has attracted a lot of attention, e.g., see recent works (Song *et al.*, 2009, 2011; Sun *et al.*, 2020; Okesanya, 2020; Agwu *et al.*, 2018) but most of these studies relate either to the intermediate value of the Reynolds number or have not provided the values of the individual

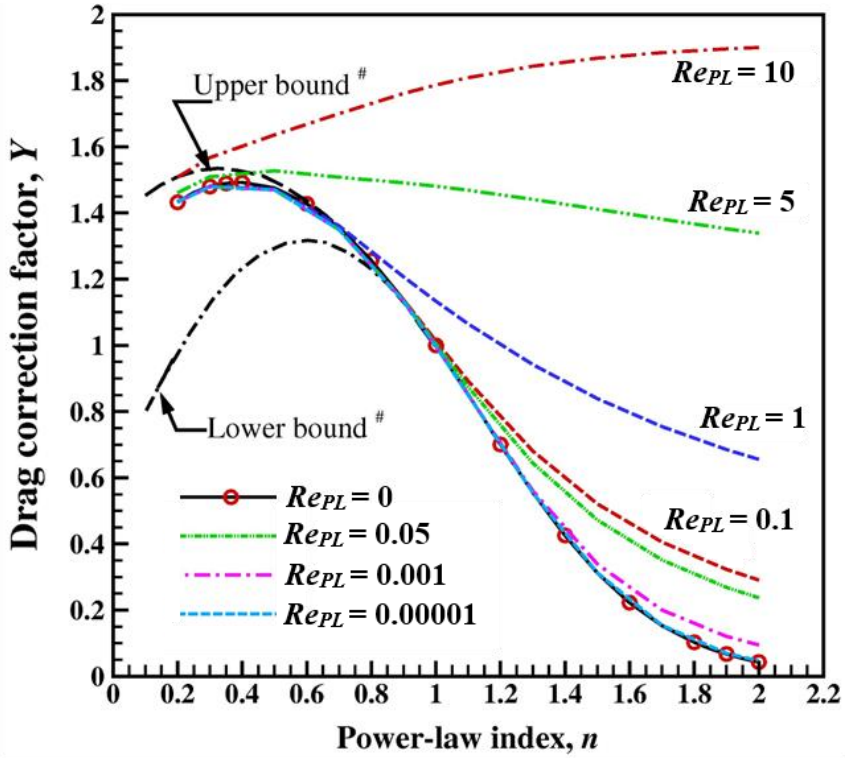


**Figure 6.1** Comparison of shear rate over the range of power-law index (Lines represent results of Cho and Hartnett (1983) for $n \leq 1$).

drag components or have not presented the surface average value of $\tau_{r\theta}$ or $\dot{\gamma}_{r\theta}$. In order to extract this information, fresh simulations have been conducted here.

This objective is accomplished here by numerically solving the partial differential equations describing the creeping flow ($Re_{PL} = 0$) of a power-law fluid past a sphere. This allows us to examine the variation of the shear stress ($\tau_{r\theta}$), and viscosity ($\eta$) on the surface of the sphere. Using the present numerical results, theoretical forms of $f_1(n)$ and $f_2(n)$ are developed and presented considering the dependence of the ratio of the viscous-to-total drag force on the power-law index. Finally, the numerical predictions presented here are compared with the experimental results to demonstrate the validity of FBM for power-law fluids in the shear-thinning region. Limited results are also included here for finite values of the Reynolds number in order to delineate the range of the validity of the FBM outlined here.

## 6.3 Numerical methodology

The creeping flow of a power-law fluid over an unconfined sphere are available in the literature, the major thrust of such studies has been on developing the standard drag curve in terms of the drag coefficient-Reynolds number-power-law index relationship (Chhabra, 2006; Song *et al.*, 2009; 2011). As noted earlier, no attempt has been made to delineate the individual drag contribution and/or to evaluate the surface average shear stress and shear rate as functions of the power-law index. Hence, low Reynolds number (creeping flow) simulations have been carried out here using the Multiphysics finite element solver COMSOL version 5.3a. In order to reach the unconfined flow approximation, the outer boundary

was set at 1400*d*. This choice was arrived at by varying the location of the boundary from 1000 to 1400 times the diameter of the sphere. Similarly, an optimal numerical mesh was chosen for these results to be free from the numerical artefacts following the strategy similar to that of previous studies (Song *et al.*, 2009; 2011).

## 6.4 Analysis of results

At the outset, the present values of the drag correction factor *Y*, defined below, are compared with the previous results in **Table 6.1** where a good agreement is evident. This lends credibility to the precision and reliability of the present results.

$$Y = \frac{Drag\ in\ power-law\ fluid}{Stokes\ drag} = \frac{C_D Re_P}{24} \tag{6.22}$$

Where $C_D = \frac{8F}{\rho U^2 \pi d^2}$ and $Re_{PL} = \frac{\rho U^{2-n} d^n}{m}$ for a power-law fluid.

Clearly, for $n = 1$, the drag correction factor $Y$ will be equal to the unity. An excellent agreement is seen to exist between the present and previous results thereby inspiring confidence in the reliability and precision of the present results (**Table 6.1**). Next, the present values are shown in **Fig. 6.1** where it is clearly seen that these are far off from the lower bound of Cho and Hartnett (1983), and the present results are also consistently lower than their upper bound. This clearly elucidates the major deficiencies of the correction factors $f_1(n)$ and $f_2(n)$ put forward by Uhlherr *et al.* (1976), Cho and Hartnett (1983, 1984) which have been subsequently used by others (Kanchanalakshana and Ghajar, 1986). Included here are the results for a few values of the Reynolds number. Clearly, the results for $Re = 1$ superimpose on the

**Table 6.1:** Values of Drag correction factor ($Y$)

| Values of $n$ | Values of $Y$ | |
|---|---|---|
| | Present | Ref. (Song *et al.*, 2009) |
| 0.20 | 1.432 | 1.434 |
| 0.25 | 1.461 | - |
| 0.30 | 1.480 | 1.485 |
| 0.35 | 1.480 | - |
| 0.40 | 1.492 | 1.497 |
| 0.50 | 1.476 | - |
| 0.60 | 1.428 | 1.417 |
| 0.70 | 1.355 | - |
| 0.80 | 1.257 | 1.258 |
| 0.90 | 1.137 | - |
| 1.00 | 1.006 | 1.0183 |

creeping flow results for $n \leq 1$, this limit appears to be $Re \sim 10^{-5}$ for shear-thickening fluids. As expected, the drag correction factor is now a function of the power-law index and the Reynolds number thereby rendering FBM unsuitable beyond the creeping flow regime.

**Figure 6.2** shows the relationship between the contribution of the viscous drag (due to $\tau_{r\theta}$) to the total drag and the power-law index. This ratio is seen to vary from ~ 0.33 to ~ 0.74 as the value of the power-law index ranges from $n = 0.1$ to $n = 2$ and as expected it is seen to be (2/3) for a Newtonian fluid. Results are included here for $1 \leq Re \leq 10$ in this figure show that $F_V/F_D$ moves closer to the results for $Re = 0$ as the Reynolds number decreases and has a marginal difference for $Re = 1$ over the range of the power-law index.

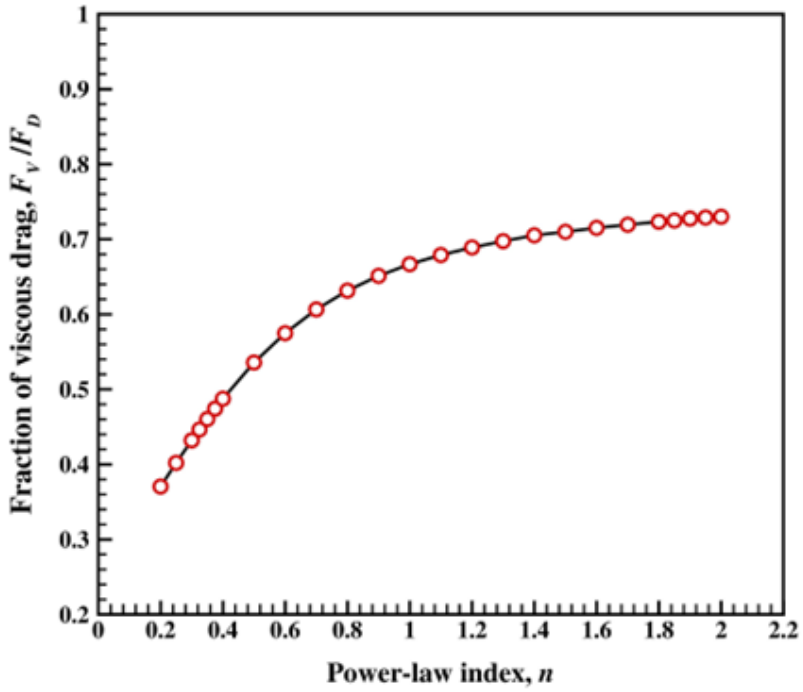


**Figure 6.2** Dependence of the ratio $F_V/F_D$ on power-law index ($n$).

**Figures 6.3** and **6.4** show the influence of the power-law index on the distribution of the viscosity, $\eta$ (normalized using $m(U/d)^{n-1}$) and shear stress, respectively, on the surface of the sphere for $Re_{PL} = 0$. Evidently, most of the sphere surface is exposed to a nearly uniform viscosity in **Fig. 6.3a** except for the small regions near the front and rear stagnation points ($0 \leq \theta \leq 15°$ and $165 \leq \theta \leq 180°$). However, smaller the value of $n$, lower is the viscosity and it is always below the Newtonian value ($n = 1$) except in small regions in the vicinity of the stagnation points. On the other hand, in shear-thickening fluids ($n > 1$), the viscosity is also always lower than that the Newtonian value, but it shows much greater variation on the surface of the sphere, **Fig. 6.3b**. The variation flattens with the increasing value of the power-law index. The corresponding local shear stress distribution follows qualitatively similar pattern except for the fact that the shear stress shows a greater variation. Except the smaller regions near the front and rear stagnation points, the bulk of the sphere surface is exposed to a uniform shear stress which decreases with the

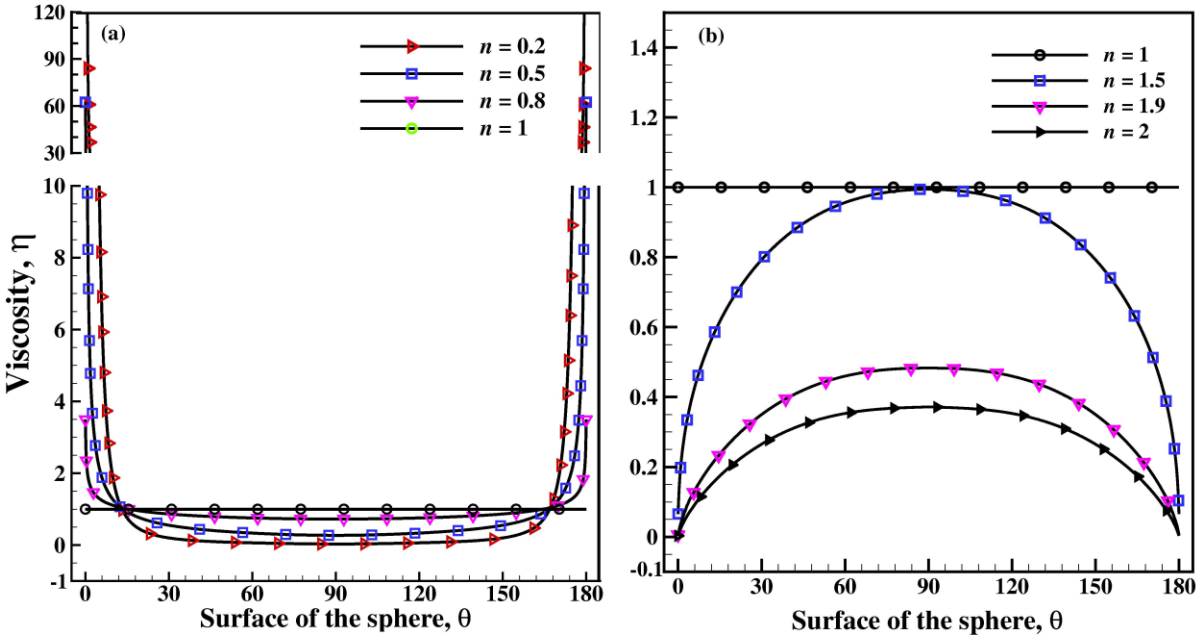


**Figure 6.3** Viscosity distribution on the surface of the sphere as a function of power-law index (*n*). θ = 0 corresponds to the front stagnation point.

increasing degree of shear-thickening fluid behaviour. Using these results, one can also construct the corresponding shear rate distribution plots, but these are not shown here for the sake of conciseness. Next, one can average the shear stress and shear rate distribution over the surface of the sphere and their dependence on power-law index is shown in **Figs. 6.5** and **6.6** as functions of *n* for a range of values of

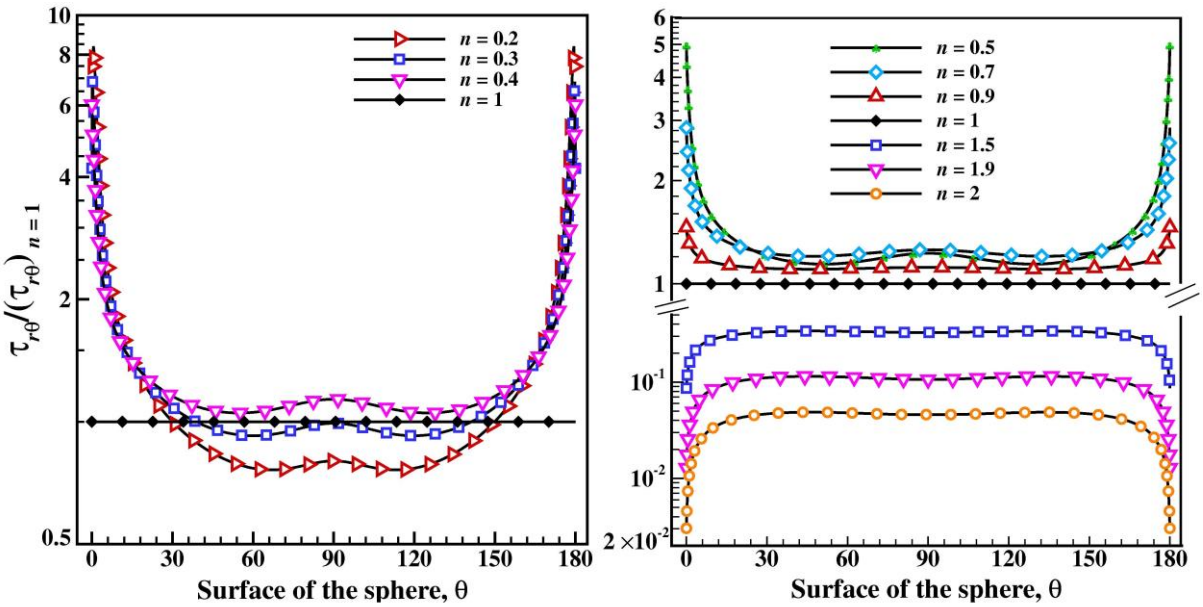


**Figure 6.4** Shear stress distribution on the surface of the sphere as a function of power-law index (*n*). θ = 0 corresponds to the front stagnation point.

the Reynolds number. In these figures, the shear stress and shear rate have been normalized using the corresponding Newtonian values given by $\langle \tau \rangle_N$ and $\langle \dot{\gamma} \rangle_N$, respectively.

Thus, the ordinates in **Figs. 6.5** and **6.6** are simply $f_1(n)$ and $f_2(n)$, introduced in **Eqs. (6.19a)** and **(6.19b)**, respectively. The maximum in **Fig. 6.6** at about $n \approx 0.375$ is not predicted by previous studies due to the approximate nature of their solution. Both $f_1(n)$ and $f_2(n)$ can be well approximated by the following simple expression:

$$f_1(n) = 1.238 \exp\left[ -\frac{(n-0.667)^2}{0.527} \right] \tag{6.23}$$

$$f_2(n) = \frac{3.54}{1+\exp\left[ -\frac{(n-0.248)}{0.0215} \right]} \qquad 0.2 \le n < 0.375 \tag{6.24a}$$

$$f_2(n) = 7.437 \exp(-1.970n) - 0.0153 \qquad .375 \le n \le 2 \tag{6.24b}$$

**Equation (6.23)** correlates the present numerical results with the mean deviation of 1.6% which rises to a maximum of 9%. Similarly, the mean and maximum errors for **Eq. (6.24a)** and **Eq. (6.24b)** are ~4% and ~9% respectively. However, for $n = 1$, $f_1 = 1$ and $f_2 = 1.02$ which are sufficiently close to their expected

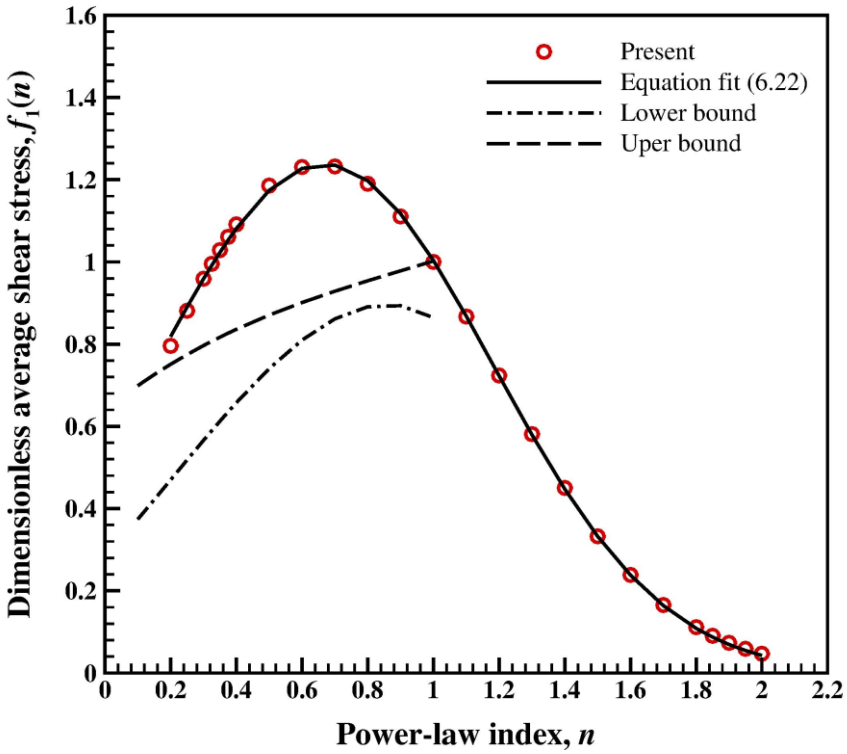


**Figure 6.5** Dependence of the average shear stress on power-law index (Lines represent results of Cho and Hartnett, (1983, 1984)).

values of one. **Figures 6.5** and **6.6** also include the results of Cho and Hartnett (1983, 1984). Evidently, the present results, especially of shear stress, deviate significantly from that of Cho and Hartnett (1983).

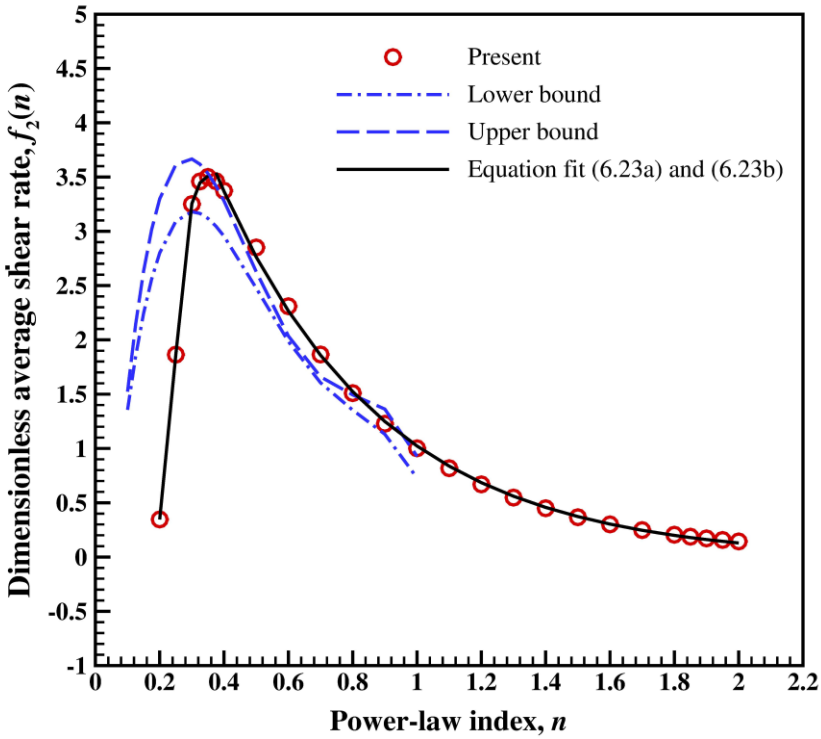


**Figure 6.6** Comparison of shear rate over the range of power-law index (Lines represent results Cho and Hartnett, 1983, 1984).

In view of the highly approximate nature of their results, the present results are considered to be more reliable than theirs. Also, this really casts doubts about the validity of their method for determining the shear stress-shear rate curves by using FBM. The applicability of the new method proposed herein is demonstrated in the next section by way of presenting a few comparisons with experiments.

## 6.5 Comparison with experiments

Admittedly a significant body of experimental data exists on the falling sphere experiments in aqueous solutions of chemically different polymers (Chhabra, 2006). However, not all authors have presented sufficient details for their results to be recalculated in the format required here. For instance, most authors have not reported individual value of $V$, $d$, $\rho_s$, etc. and/or the resulting value of the Reynolds number are above unity. In some of the analytical and experimental studies, viscoelastic constitutive models and/or viscoelastic fluids have been used and clearly, these results also cannot be used here. A thorough search of the literature reveals only very limited data which can be used to validate the present predictions. At the outset, it is worthwhile to recall here the key assumptions which must be met by the experiments: low Reynolds number ($\leq \sim 0.01$), steady flow, no wall and end effects and power-law fluid behaviour. Bearing in mind these factors, we begin with the case of Newtonian fluids, followed by the determination of the zero-shear viscosity and finally the shear-thinning viscosity curves for power-law fluids obtained by

the FBM. For this purpose, much of the data used here is taken from the extensive compilations of Chhabra (Chhabra, 1980, 2006) as we could not find other data in which the complete information was available for the results to be recalculated in the format required here.

### 6.5.1 Flow curve for Newtonian fluids

**Figure 6.7** compares the true steady shear stress-shear rate data for corn syrup and silicon oil with that calculated using the FBM through **Eqs. (6.16)** and **(6.17)**. The two results are seen to be virtually indistinguishable from each other in the overlapping range of shear rates. Furthermore, the two values of the Newtonian viscosities of these two fluids are also extremely close to each other. For instance, the viscosity values of the corn syrup of 11.49 and 11.41 Pa.s obtained from the cone-and-plate rheometer and the FBM respectively are within 0.7% of each other. The corresponding values for the silicon oil are: 24.11 an 24.02 Pa.s respectively. Such a close agreement between the two values inspires confidence in the experimental protocol followed in conducting these experiments.

### 6.5.2 Estimation of zero-shear viscosity

As noted earlier, the critical value of the shear rate marking the onset of shear-thinning behaviour is not known a priori. Therefore, one must perform falling ball tests with a few spheres (different size and/or density) to evaluate the zero-shear viscosity. In essence, one must use the Stokes expression, **Eq. 6.1** to calculate the value of $\eta$ and if the resulting values corresponding to different balls are constant within the

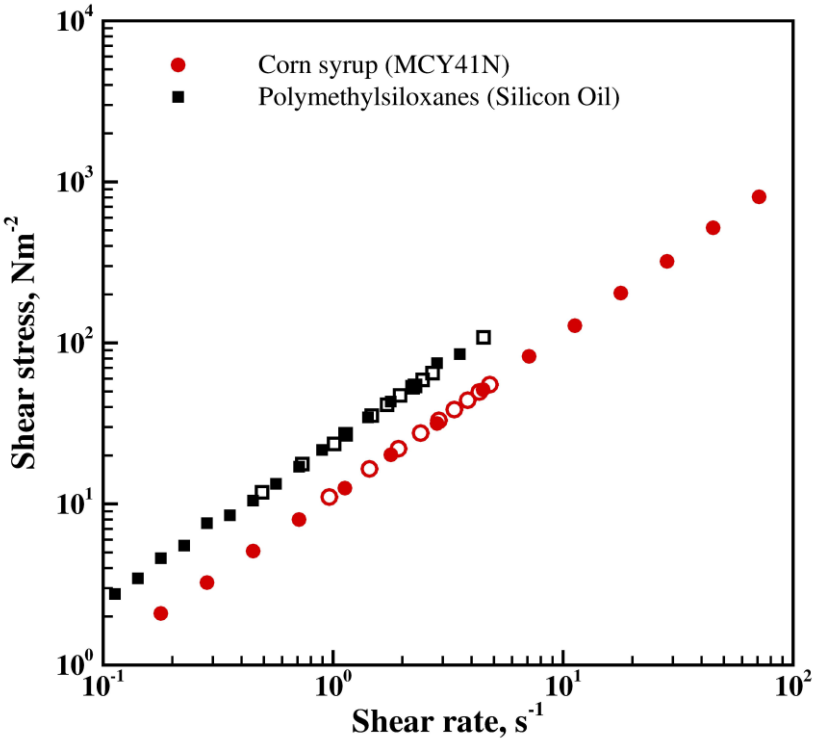


**Figure 6.7** Comparison between the predicted (hollow symbols: FBM) and Rheometrical measurements (filled symbols) of shear stress and shear rate in Newtonian fluids (Chhabra, 1980).

margin of experimental errors, this will confirm that these are the values of the zero-shear viscosity and one can thus evaluate the average shear rate as ($2U/d$). Such data are indeed very scare in the literature. **Table 6.2** presents the results for a few polymer solutions. The results shown in **Table 6.2** confirm the expectation that the FBM can yield reliable values of the zero-shear viscosity provided the sphere drop data fall in the constant viscosity region. The mean values of $\eta_0$ obtained with the FBM are generally within ~ 2-3% of the rheometrical values of the zero-shear viscosity. The values of the surface average shear rate $\langle \dot{\gamma} \rangle_N$ are also included in this table as are the corresponding value of the Reynolds number which all are < 1. In summary, it is thus possible to evaluate the zero-shear viscosity using the FBM even for non-Newtonian fluids.

**Table 6.2** FBM results for zero-shear viscosity evaluation (Chhabra, 1980)

| 1.46% Methocel in water ($\rho$ = 1003 kg/m$^3$) | | | | | |
|---|---|---|---|---|---|
| $d$ (mm) | $\rho_p$ (kg/m$^3$) | $U$ (mm/s) | $2U/d$ (s$^{-1}$) | Zero-shear viscosity (Pa.s) | |
| | | | | FBM | Cone & Plate |
| 12.686 | 1415 | 11.1 | 1.75 | 3.26 | |
| 11.115 | 1490 | 10.3 | 1.85 | 3.18 | |
| 10.30 | 1492 | 8.62 | 1.68 | 3.28 | 3.31 |
| 6.35 | 2500 | 10 | 3.15 | 3.29 | |
| 1.59 | 7790 | 2.85 | 3.60 | 3.27 | |
| 1.25% Polyacrylamide in water ($\rho$ = 1005 kg/m$^3$) | | | | | |
| $d$ (mm) | $\rho_p$ (kg/m$^3$) | $U$ (mm/s) | $2U/d$ (s$^{-1}$) | Zero-shear viscosity (Pa.s) | |
| | | | | FBM | Cone & Plate |
| 9.51 | 1190 | 0.42 | 0.093 | 20.7 | |
| 11.065 | 1190 | 0.607 | 0.11 | 20.34 | 19.9 |
| 12.686 | 1190 | 0.820 | 0.13 | 19.80 | |
| 6.368 | 1397 | 0.460 | 0.14 | 18.90 | |
| 1.5% Polyacrylamide in water ($\rho$ = 1014 kg/m$^3$) | | | | | |
| $d$ (mm) | $\rho_p$ (kg/m$^3$) | $U$ (mm/s) | $2U/d$ (s$^{-1}$) | Zero-shear viscosity (Pa.s) | |
| | | | | FBM | Cone & Plate |
| 8.749 | 1350 | 0.263 | 0.055 | 58.58 | |
| 10.3 | 1492 | 0.460 | 0.09 | 60.08 | 59.0 |
| 11.115 | 1490 | 0.560 | 0.101 | 57.23 | |
| 12.686 | 1415 | 0.590 | 0.093 | 59.61 | |
| 0.17% Polyacrylamide in 8.2/91.8% Water-corn syrup solvent ($\rho$ = 1300 kg/m$^3$) | | | | | |
| $d$ (mm) | $\rho_p$ (kg/m$^3$) | $U$ (mm/s) | $2U/d$ (s$^{-1}$) | Zero-shear viscosity (Pa.s) | |

| | | | | FBM | Cone & Plate |
|---|---|---|---|---|---|
| 1.59 | 2500 | 0.127 | 0.16 | 13.01 | |
| 3.175 | 2500 | 0.512 | 0.323 | 12.88 | 13.0 |
| 1.59 | 4010 | 0.295 | 0.371 | 12.66 | |
| 0.24% Polyacrylamide in 11/89% water/corn syrup ($\rho$ = 1310 kg/m$^3$) | | | | | |
| $d$ (mm) | $\rho_p$ (kg/m$^3$) | $U$ (mm/s) | $2U/d$ (s$^{-1}$) | Zero-shear viscosity (Pa.s) | |
| | | | | FBM | Cone & Plate |
| 1.59 | 2500 | 0.097 | 0.122 | 16.903 | |
| 3.175 | 2500 | 0.388 | 0.244 | 16.85 | 16.9 |
| 1.590 | 4010 | 0.232 | 0.292 | 16.04 | |
| 2.00 | 4010 | 0.363 | 0.363 | 16.21 | |
| 0.07% Polyacrylamide in 8/92 % water/Maltose syrup ($\rho$ = 1310 kg/m$^3$) | | | | | |
| $d$ (mm) | $\rho_p$ (kg/m$^3$) | $U$ (mm/s) | $2U/d$ (s$^{-1}$) | Zero-shear viscosity (Pa.s) | |
| | | | | FBM | Cone & Plate |
| 1.59 | 4010 | 0.44 | 0.55 | 8.45 | |
| 2.00 | 4010 | 0.70 | 0.70 | 8.41 | |
| 1.59 | 2500 | 0.19 | 0.24 | 8.63 | 8.5 |
| 6.35 | 2500 | 3.125 | 0.98 | 8.46 | |
| 1.59 | 7790 | 1.04 | 1.31 | 8.59 | |

### 6.5.3 Shear-rate dependent viscosity

In order to establish and demonstrate the validity of the approach presented here to extract flow curve for power-law fluids using FBM, one must first evaluate the value of the power-law index, $n$. For this purpose, one must plot log $\langle\tau\rangle_N$ versus log $\langle\dot{\gamma}\rangle_N$, as shown in **Figure 6.8** for a series of polymer solutions. Indeed, over the range of conditions, linear variation on double logarithmic coordinates is evident in each case. The slope of these curves is simply the value of the power-law index, in line with the suggestion of Uhlherr *et al*. (1976) and Cho and Hartnett (1983, 1984). This value can, in turn, now be employed to evaluate the correction factors $f_1$ ($n$) and $f_2$ ($n$), **Eqs. (6.22)** and **(6.23)**, respectively. One can now evaluate the shear stress and shear rate values via **Eq. 6.18** using the falling sphere data.

**Figure 6.9** shows representative results for four different polymer solutions. Included in these figures are also the corresponding shear data obtained using the cone-plate system in a rheogoniometer. Indeed, the

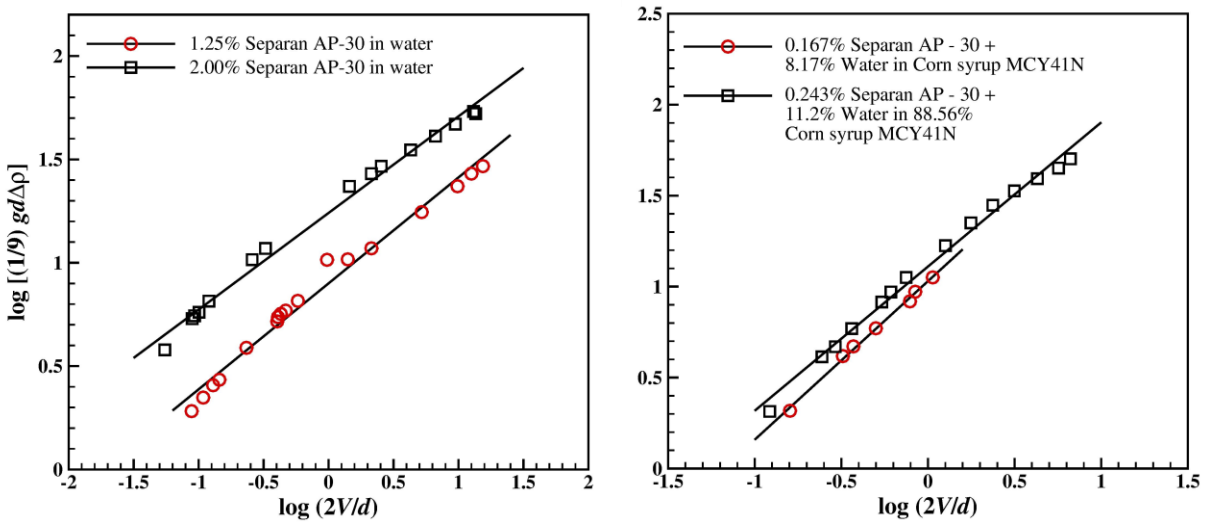


**Figure 6.8** Estimation of power-law index from log and log $\langle\dot{\gamma}\rangle_N$.

falling sphere data and rheological measurements literally superimpose within the overlapping range of conditions with the margin of experimental errors.

The minor differences seen here are possibly due to the fact that a single constant value of *n* has been used here in analyzing the falling sphere data. This lends credibility to the validity of the FBM to evaluate the flow curves for power-law fluids, especially in the low-shear rate range which is not always accessible in rotational viscometer. While the limited validations shown here all pertain to polymer solution, unfortunately to the best of our knowledge, no such data is available for filled system and composites in the open literature. In principle, the scheme obtained here should work equally well for loaded system and composites provided the assumption of continuum is justified, i.e., size of the ball is larger than the

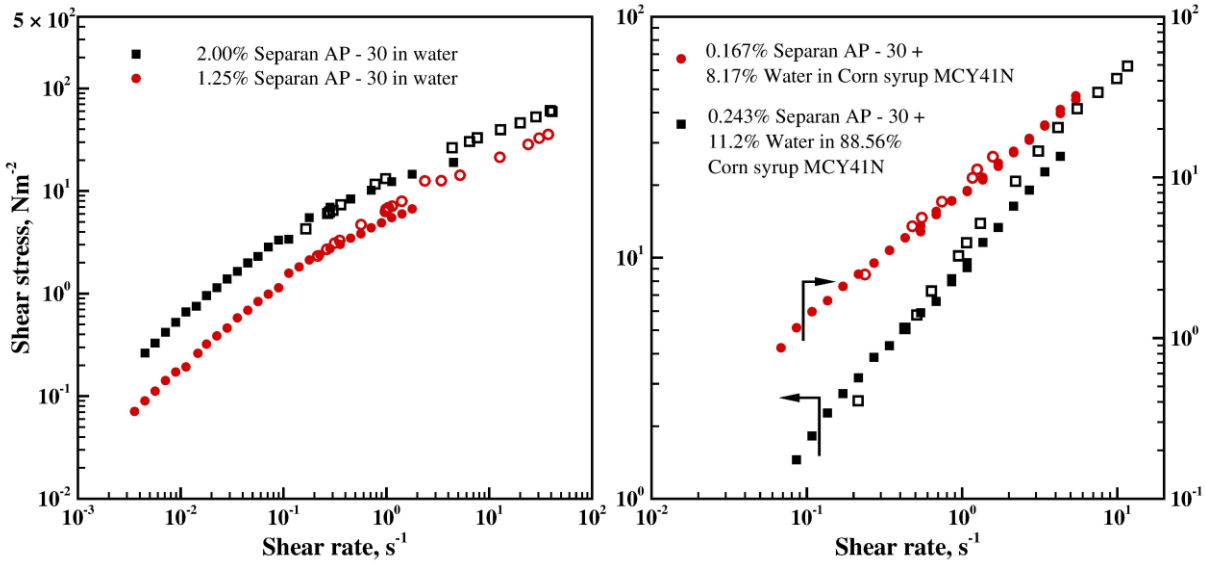


**Figure 6.9** Comparison between the predicted (hollow symbols: FBM) and Rheometrical measurements (filled symbols) of shear stress and shear rate (Chhabra, 1980).

size of the additives. In practice, this condition is generally met. This is indeed demonstrated by the limited experimental results reported by Milliken et al. for the suspensions of microspheres and rods in viscus Newtonian solvents (Metzner and Reed ,1955; Milliken *et al.*, 1989).

In summary, therefore, it is possible to use the FBM for evaluating the zero-shear viscosity and the shear-dependent viscosity of composites, polymeric melts and solutions provided the falling sphere data is obtained in the low Reynolds number range and is free from wall and end effects. This analysis also assumes the value of the power-law index to remain constant over the range of shear rate of interest. However, this difficulty can be circumvented by using the local value of the slope of log $\langle \tau \rangle_N$ versus log $\langle \dot{\gamma} \rangle_N$ , plots, akin to the approach of Metzner and Reed (1955) for the capillary viscometer data analysis. Similarly, no experimental data is available in the literature for shear-thickening fluids ($n$ > 1) to substantiate the validity of the strategy outlined in this work.

Before leaving this section, it is worthwhile to explore the effect of the Reynolds number on the strategy presented here. At the outset it needs to be recognized here that Equation 1 and modifications thereof implicitly assume the Reynolds number to be small (< 1). Conversely, outside the so-called creeping flow region, the ratio $F_V/F_D$, $f_1(n)$ and $f_2(n)$ are expected to show additional dependence on the Reynolds number. Notwithstanding this complexity, limited additional simulations have been performed up to $Re_{PL}$ = 10 to explore this issue. Indeed, the relative errors in the values of $f_1(n)$ and $f_2(n)$ with respect to the corresponding values for $Re_{PL}$ = 0 rose with the increasing Reynolds number and/or the error itself was much higher in shear-thickening ($n$ > 1) fluids than that in shear-thinning fluids. For instance, the error defined as $\frac{f_1(n) - f_1(n)\big|_{Re_{PL}=0}}{f_1(n)\big|_{Re_{PL}=0}}$ ranged from 12% at $n$ = 0.2 to 1262 % at $n$ = 2 for $Re_{PL}$ = 1. The corresponding values were found to be 41% and 2473% respectively at $Re_{PL}$ = 10. This clearly indicates the additional role of the Reynolds number in determining the values of correction factors. Thus, this method is best studied in the creeping flow regime only.

# Chapter 7

# Conclusions and suggestions for future work

This work investigates the flow past axisymmetric particle shapes (i.e., spherical and non-spherical) in steady laminar flow in forced- and free-convection regimes for non-Newtonian fluids, including Newtonian fluids as a limiting case. The main focus of the present work is to understand the momentum and thermal transfer characteristics from axisymmetric shapes over the range of corresponding governing parameters in order to delineate the effect of shape in an unconfined flow. Limited efforts have been made to explore the preliminary understanding of the confinement flow past axisymmetric particles and how it modulates the drag and Nusselt number. Finally, the applicability of the falling ball method (FBM) is studied to predict the zero-shear viscosity and shear-dependent viscosity in the low shear rate limit of non-Newtonian (power-law shear-thinning fluids) fluids using the numerical solution of the momentum equations for the creeping flow of fluids around a sphere.

In particular, extensive results have been obtained for considering the following specific problems for axisymmetric particle shapes (i.e., spherical and non-spherical):

A. Creeping flow
B. Forced convection
    - Newtonian fluids
    - Effect of confined flow in Newtonian fluids
    - Bingham plastic fluids
C. Free convection
    - Sphere and a pair of spheres in low Grashof number power-law fluids
    - Spherical segments in Bingham plastic fluids
D. Falling ball method

The key findings of the present work are summarized in the following section, followed by suggestions for future work.

## 7.1 Conclusions

The present work significantly contributes to understanding the velocity and temperature fields around axisymmetric shapes in Newtonian and non-Newtonian fluids. The main findings can be summarized below:

**A. Creeping flow**

*Chapter 3* represents the sedimentation of the spherical segments and is numerically studied for a wide range of Bingham values in creeping flow. The effect of the yield stress fluid on the different shapes ($30^{o} \leq \alpha \leq 180^{o}$) is studied on the formation of the yielded/unyielded zone around the segment, which shows the front static zone exists for all the *Bn* number, but the rear static zone only appears at high *Bn* values. However, the rear static zones also get smaller and smaller with the increase in $\alpha$ values. The effect of $\alpha$ is also studied for the yield stress values of Bingham plastic fluids for particles which shows that with the increase in $\alpha$, a greater yield stress is required to suspend the particle in the fluid. The correction factor for the fluid and the shape of the particle is also plotted over the range of $\alpha$ and *Bn*. The drag correction factor for the different shapes of spherical segments varies from 0.4 to 1 at low yield stress fluid. However, at high yield stress fluid it even arises from more than 1 for some segments. Finally, the Stoke drag coefficient is correlated in terms of both *Bn* and $\alpha$ with reasonable accuracy.

**B. Forced convection**

The first section of *Chapter 4* deals with the effect of axisymmetric shapes on the forced convection in unconfined Newtonian fluid from an isothermal spherical shape over the range of conditions: $1 \leq Re \leq 150$, $30^{\circ} \leq \alpha \leq 150°$, and $Pr = 0.72$ (air). The effect of shapes of the spherical segments varying in the range of $30^{\circ}$ ($\psi = 0.424$) $\leq \alpha \leq 150°$ ($\psi = 0.996$) on momentum and heat transfer characteristics have also been compared with the similarity in shapes of particles, i.e., cone ($0.324 \leq \psi \leq 0.658$) and short cylinder ($0.541 \leq \psi \leq 0.872$) in this work. The results of streamline profiles for spherical segments are discussed by comparing the critical Reynolds number (from where the onset of flow separation occurs) for each particle shape. The results show that the shape or lateral surfaces of the particles strongly influence the size of the wake and the location of the separation point from the particle surface. The critical Reynolds number for these axisymmetric particles follows the order of short cylinder > cone > spherical segment. The non-dimensional drag force is correlated as a function of sphericity, Reynolds number and diameter to height ratio of the particle. In the case of spherical segments, it is observed that for $Re > 50$, the drag values are maximum for $\alpha = 90°$. With the further increase in $\alpha$, even though they have the same projected area the drag values appear to be less in the case of $\alpha = 120°$ and $150°$ than $\alpha = 90°$. Furthermore, the shape descriptor or sphericity (particles with identical base area and height) of the particle shows significant effect particularly at low Reynolds number in the order of cone < spherical segment < short cylinder. However, at high inertial forces, drag experienced by the different particles almost becomes independent of the Reynolds number. The drag curves are plotted for the range of the sphericity ($0.324 \leq \psi \leq 1$) which suggests that the drag values of short cylinders are significantly deviating from the other two shapes (cone and spherical segment) particularly for $\psi < 0.8$. The correlations proposed for $C_D$ and *Nu* as functions of $\psi$, ($d_c/h_c$), and *Re* enable the estimation of intermediate parameters in new design calculations. Also, the reliability and precision of the correlations to predict the results for $C_D$ and *Nu* have been confirmed by comparing the predicted results with the limited experimental results found to be within the reported experimental uncertainties.

The second section of *Chapter 4* deals with the study of the effect of confinement in a Newtonian media over the range of the Reynolds number ($1 \leq Re \leq 100$) for three spherical segments ($\alpha = 30^{\circ}, 60^{\circ}, 90^{\circ}$) in two different confinement ratios, $\lambda = 0.5, 0.2$. The effect of confinement on drag, heat transfer coefficient, and flow kinematics are studied compared to unconfined flow. The detailed structure of the flow and heat transfer characteristics have been analyzed in terms of streamline, isotherms, velocity profiles, drag and Nusselt number for the axisymmetric particles with $\alpha = 30^{\circ}, 60^{\circ}, 90^{\circ}$. As expected, the increase in confinement stabilizes the flow past the particle by delaying the wake formation and increases the heat transfer rates while thinning the thermal boundaries layer in the vicinity of the particle. The global parameters like drag coefficients and Nusselt number are also compared with the unconfined flow results. The results illustrate that the increase in confinement leads to an increase in the drag experienced by the spherical segment and eventually attains the constant value faster than the unconfined flow with the increase in Reynolds number. The increase in shape factor follows a similar trend of increasing drag as in unconfined flow. However, at $Re = 1$, the increase in confinement from 0 to 0.5 leads to an increase the drag coefficient values ~ seven times for a fixed value of $\alpha$. On the other hand, increase in $\alpha$ shows a decreasing trend for drag values at high values of Reynolds number similar to the unconfined flow. However, for unconfined flow this trend follows the decrease in drag once $\alpha$ values approached 120°. Here, due to the confinement these decreasing values of drag is observed as $\alpha$ values increase from 60° to 90° for $\lambda = 0.5$. Broadly, the heat transfer rates increase with the increase in Reynolds number and decrease with the increase in shape factor. Also, the increase in confinement shows a positive dependency on the Nusselt number. However, at $Re = 1$, the heat transfer rates are lower for the $\lambda = 0.5$ than unconfined flow, irrespective of the shape. This is due to the fact that at the lowest values of the Reynold number the thick thermal boundary layer around the spherical segments gets intervened with the boundaries of the continent. As the thermal boundary layer becomes thinner with the increase in Reynolds numbers, the flip occurs at specific values for each spherical segment. For $\alpha = 30^{\circ}$, it is observed around $Re \sim 5$. The study suggests that from all three shapes, spherical segment ($\alpha = 30^{\circ}$), circular disc, and sphere, spherical cap experiences the highest drag at $Re = 100$ and the heat transfer rates are almost three times in the case of a spherical segment than the sphere at $Re = 1$ for a fixed confinement ratio ($\lambda = 0.5$). The numerical values of the drag coefficient and average Nusselt number have been correlated in terms of pertinent dimensionless parameters with acceptable levels of accuracy over the range of conditions considered in the present study.

The third section of *Chapter 4* investigated the effect of infinite Bingham plastic fluid on the momentum and heat transfer characteristics from the heated spherical segments ($30^{\circ} \leq \alpha \leq 150°$) over the range of Reynolds number ($0.1 \leq Re_B \leq 150$), Bingham number ($0 \leq Bn \leq 100$) and Prandtl number ($0.1 \leq Pr_B \leq 100$). In general, the increase in Reynolds number tends to eliminate the unyielded zones due to the increased fluid inertia, which is further suppressed by the increasing Bingham number due to the increasing yield-stress effects. Drag coefficients show the positive dependency on the Bingham number. The reverse trend of the decreasing drag values after $\alpha \geq 90°$ at high Reynolds number is more prominently

observed for pressure drag coefficient ($C_{DP}$) in Bingham plastic fluid. The drag experienced by the spherical segments is also compared to the spherical particle which shows that at low Reynolds number, $C_{D\alpha}/C_D$ ratio is constant, which is smallest for $\alpha = 30°$ and close to 1 for the $\alpha = 150°$. With the increase Finally, for ease of applicability, correlations are proposed for the drag coefficient as a function of $Re_B$, $Bn$, $\psi$ and $d_c/h_c$ which also include the case of spherical particles. The Bingham number influences the overall heat transfer in two somewhat opposing ways. Firstly, the yielded zones diminish in size with the increasing Bingham number and conduction dominates in the increasingly unyielded regions adjacent to the surface of the heated spherical segments. On the other hand, the temperature gradient sharpens in the thin yielded fluid-like regions. The former tends to impede heat transfer while the latter tends to promote it. Due to which complex behavior is observed. At high Peclet numbers, the sudden drop in the Nusselt number is observed with respect to the increasing Bingham number for $\alpha = 30°$ to 90°. For $Pe_B = 15 \times 10^3$, the drop in the Nusselt number is observed at $Bn \sim 50$ and $Bn \sim 5$ for $\alpha = 30°$ and 90° respectively. The present numerical results have been correlated for average Nusselt number for spherical segments at spanning range of $Re_B$, $Pr_B$, $Bn$ and $\psi$. The correlations presented herein work have split up into two ranges of Peclet number for better accuracy and predictability in the in between range of parameters.

**C. Free convection**

The first section of the *Chapter 5* laminar free convection in power-law fluids over the range of vanishingly small Grashof number ($10^{-4} \leq Gr_{PL} \leq 10$) has been investigated numerically for an isolated sphere and twin spheres for varying centre-to-centre distance (including limiting case of touching spheres). The results of nondimensional total drag ($C_D$), local Nusselt number ($Nu_l$), and average Nusselt numbers ($Nu$) have been examined in detail for both cases to understand the momentum and heat transfer characteristics embracing broad ranges of Prandtl number ($0.72 \leq Pr_{PL} \leq 1000$) and power-law fluid behaviour $0.1 \leq n \leq 2$ for a single sphere and $0.1 \leq n \leq 1.5$ for a pair of spheres with the varying gap ratio ($1 \leq l/d \leq 6$). The effect of power-law index on the drag coefficient for a single sphere flips over somewhere in the range $2 < Gr_{PL} < 15$ when the drag coefficient increases in shear-thinning or pseudoplastic fluids ($n < 1$) as compared to shear-thickening fluids ($n > 1$). The drag correction factor $Y(n)$ results confirm the increase in the Prandtl number postponing the flip over to higher Grashof numbers. The shear-thinning fluids $n < 1$ exhibit the maximum value of the local Nusselt number on the surface of the sphere away from the front stagnation point in contrast to the Newtonian and shear-thickening fluids ($n \geq 1$) for which it occurs at the front stagnation point over the range of $Pr_{PL}$ and $Gr_{PL}$ studied here. Also, the drag coefficient and average Nusselt number for the vertically aligned twin spheres are influenced by the governing parameters ($Gr_{PL}$, $Pr_{PL}$, $n$) and $l/d$ in a complex manner, though qualitatively these are similar to the case of an isolated sphere. The gap ratio plays an important role in determining the severity of interference between the velocity and temperature boundary layers and hence the drag and heat transfer coefficients for the twin spheres. Finally, simple correlations have been proposed for the total drag and average Nusselt number over the range of $Gr_{PL}$ ($10^{-4} \leq Gr_{PL} \leq 10$), $Pr_{PL}$ ($7 \leq Pr_{PL} \leq 1000$), and $n$ ($0.1 \leq n \leq 2$ for isolated sphere and $0.1 \leq n \leq 1.5$ for twin spheres). In the limit of

Newtonian fluids, the present results lend support to the approximate analyses relevant to the low Rayleigh number region whereas the high Grashof number results for a single sphere are consistent with the boundary layer analyses available in the literature. The present results also highlight the requirement of rather large computational domains at low Rayleigh numbers for the velocity field to decay naturally from an isolated sphere. Finally, not only very large gaps between the two spheres are needed to approach the single sphere limit but this will also require countering the effect of mixed flow and preheating of the fluid impinging on the downstream sphere.

The second section of *Chapter 5* includes the study of heated spherical segments in Bingham plastic fluid under free convection regime over the wide range of parameters, $1 \leq Gr_B \leq 10^4$, $0.72 \leq Pr_B \leq 100$, $0 \leq Bn \leq 10^4$ and $30° \leq \alpha \leq 150°$. A detailed examination of the results on the yielded/unyielded zones, streamlines, isotherm contours reveals that a variety of yield surfaces can be encountered depending on the values of the Grashof number ($Gr_B$), Bingham number ($Bn$) and shape factor ($\alpha$). The increase in the Grashof number and/or Prandtl number promotes the heat transfer due to advection. On the other hand, the increase in Bingham number suppresses the fluid like behavior; then the heat transfer is solely governed by conduction. The sharp corner in the spherical segments also induces some convective force due to high shearing and sudden change in the flow and isothermal contours. Hence, the increase in shape factor makes the particle more and more streamlined as a result heat transfer rates have been affected adversely. Finally, the average Nusselt number is correlated as a $Gr_B$, $Pr_B$ and $Bn$ for each case of spherical segment.

**D. Falling ball method**

*Chapter 6* represents the results of a numerical scheme which is used to develop the stress-strain curves using the falling ball method. In this work, numerical results for the creeping flow of power-law fluids past a sphere have been used to extract the values of the zero-shear viscosity and shear-dependent viscosity in the low-shear rate limit. In essence, one needs to apply corrections to both the surface averaged shear stress and shear rate for a sphere falling in Newtonian fluids. For power-law fluids, both these correction factors are functions of the power-law index only in the creeping flow regime. Based on the present numerical results, simple expressions have been developed for these correction factors. The power-law index is given by the slope of the double log plot of the nominal average shear stress and shear rate on the surface of the sphere. The resulting maximum values of these correction factors are of the order of $f_2(n) \approx 3.5$ and $f_1(n) \approx 1.25$, that is, the surface average shear rate is comparable to that in Newtonian fluids. The present work is concluded by presenting extensive comparisons with experimental results for Newtonian fluids and shear thinning polymer solutions in the low-shear region including the zero-shear viscosity and the shear thinning region. Good correspondence between the theoretical and experimental results reported here inspires confidence in the use of this simple method to measure the viscosity of polymeric systems with acceptable levels of accuracy. Limited results are also included here at finite Reynolds number ($Re \leq 10$). These results help delineate the maximum values of the Reynolds number of $Re_{PL} \leq 1$ for shear-thinning fluids ($n \leq 1$) and $Re_{PL} \leq 10^{-5}$ for shear-thickening fluids ($n > 1$).

Beyond these limiting values, the two correction factors themselves become functions of the Reynolds number nor is it possible to evaluate the value of the power-law index as the slope of log $\langle\tau\rangle_N$ - log $\langle\gamma\rangle_N$ data. Thus, on all accounts, this method is only applicable when the inertial effect is negligible.

## 7.2 Suggestion for future work

The present work provides a basic understanding of the physical phenomena involved in the study of Newtonian as well as non-Newtonian fluid for different axisymmetric shapes, i.e., spherical segments. This understanding can open new research directions to further improve our comprehension of shape in complex phenomena.

- One possibility is to examine the effect of the orientation of an axisymmetric shape on momentum and heat transfer characteristics in Newtonian fluids under 3-D flow conditions.
- The vortex shedding phenomena for spherical segments and the critical Reynolds number for onset of unsteady flow can be further studied by exploring the time-dependent behavior of Newtonian and non-Newtonian fluids.
- The study can be extended to other complex axisymmetric shapes, such as convex or concave spherical segments in free-, forced- and mixed-convection regimes in Newtonian fluids under 3-D flow conditions.
- The role of aiding-, opposing-, and cross-buoyancy on flow and thermal behavior of the fluids can be delineated by performing mixed convection for such shapes.
- The effect of the gap between particles on heat transfer rates can be understood by extending single particle analysis to an array in a confined space for both forced and free convection.
- It may be beneficial to consider the time-dependence of physical properties in Bingham plastic fluids to extend the understanding of the behavior of yield stress fluids.

# References


Acrivos, A. A theoretical analysis of laminar natural convection heat transfer to non- Newtonian fluids. AIChE J. **1960**, 6, 584–590.

Agwu, O. E.; Akpabio, J. U.; Alabi, S. B.; Dosunmu, A. Settling velocity of drill cuttings in drilling fluids: A review of experimental, numerical simulations and artificial intelligence studies. Powder Technol. **2018**, 339, 728.

Ahonguio, F.; Jossic, L.; Magnin, A. Motion and stability of cones in a yield stress fluid. AIChE Journal, **2015**, 61(2), 709-717.

Amato, W. S.; Tien, C. Free convection heat transfer from isothermal spheres in water. Int. J. Heat Mass Transf. **1972**, 15, 327–339.

Amato, W. S.; Tien, C. Free convection heat transfer from isothermal spheres in polymer solutions. Int. J. Heat Mass Transf. **1976**, 19, 1257–1266.

Ansley, R.W.; Smith, T. N. Motion of spherical particles in a Bingham plastic. AIChE Journal, **1967**, 13(6), 1193-1196.

Atapattu, D. D.; Chhabra, R. P.; Uhlherr, P. H. T. Creeping sphere motion in Herschel–Bulkley fluids: flow field and drag. J. Non-Newt. Fluid Mech. **1995**, 59, 245.

Bagheri, G.; Bonadonna, C. On the drag of freely falling non-spherical particles. Powder Technol. **2016**, 301, 526–544.

Balmforth, N. J.; Frigaard, I. A.; Ovarlez, G. Yielding to stress: Developments in viscoplastic fluid mechanics. Ann. Rev. Fluid Mech. **2014**, 46, 121-146.

Beaulne, M.; Mitsoulis, E. Creeping motion of a sphere in tubes filled with Herschel–Bulkley fluids. J. Non-Newt. Fluid Mech. **1997**, 72, 55.

Bercovier, M.; Engleman, M. A finite-element method for incompressible non-Newtonian flows. J. Comput. Phys. **1980**, 36, 313-326.

Beris, A. N.; Tsamopoulos, J. A.; Armstrong, R. C.; Brown, R. A. Creeping motion of a sphere through a Bingham plastic. J. Fluid Mech. **1985**, 158, 219-244.

Bharti, R. P.; Chhabra, R. P.; Eswaran, V. Steady forced convection heat transfer from a heated circular cylinder to power-law fluids. Int. J. Heat Mass Transf. **2007**, 50, 977-990.

Bharti, R. P.; Sivakumar, P.; Chhabra, R. P. Forced convection heat transfer from an elliptical cylinder to power-law fluids. Int. J. Heat Mass Transf. **2008**, 51, 1838-1853.

Bharti, R. P.; Chhabra, R. P.; Eswaran, V. Steady flow of power law fluids across a circular cylinder. Can. J. Chem. Eng. **2016**, 84(4), 406-421.

Bird, R. B.; Armstrong, R. C.; Hassager, O. *Dynamics of Polymeric Liquids*, Vol. 1, Fluid Mechanics, Wiley, New York, 1987.

Bird, R. B.; Stewart, W. E.; Lightfoot, E. N. *Transport Phenomena*, 2nd ed., John Wiley & Sons, New York, 2002.

Blackery, J.; Mitsoulis, E. Creeping motion of a sphere in tubes filled with a Bingham plastic material. J. Non-Newt. Fluid Mech., **1997**, 70, 59.

Boardman, G.; Whitmore, R. L. The static measurement of yield stress, Lab. Prac., **1961**, 10, 782.

Bohlin, T. On the drag on a rigid sphere moving in a viscous liquid in a cylindrical tube. Trans. Roy. Inst. Tech. Stockholm **1960**, 155.

Bose, A; Nirmalkar, N.; Chhabra, R. P. Forced convection from a heated equilateral triangular cylinder in Bingham plastic fluids. Num. Heat Transf. A, **2014**, 66, 107-129.

Brizard, M.; Megharfi, M.; Mahe, E.; Verdier, C. Design of a high precision falling-ball viscometer. Rev. Sci. Instrum. **2005**,76, 025109.

Brizard, M.; Megharfi, M.; Verdier, C. Absolute falling-ball viscometer: evaluation of measurement uncertainty. Metrologia. **2005**, 42(4), 298.

Brookes, G. F.; Whitmore, R. L. The static drag on bodies in Bingham plastics. Rheol. Acta, **1968**, 7, 188.

Brummer, R. *Rheology Essentials of Cosmetics and Food Emulsions,* Springer, New York, 2006.

Burgos, G. R.; Alexandrou, A. N.; Entov, V. On the determination of yield surfaces in Herschel–Bulkley Fluids. J. Rheol. **1999**, 43, 463-483.

Campo, A. Correlation equation for laminar and turbulent natural convection from spheres. Warme- und Stoffübertragung **1980**, 13(1), 93–96.

Cartwright, J.H. Stokes' law, viscometry, and the Stokes falling sphere clock. Philos. Trans. Royal Soc. A. **2020**, 378(2179), 20200214.

Chamberlain, M. J.; Hollands, K. G. T.; Raithby, D. Experiments and theory on natural convection heat transfer from bodies of complex shape. J. Heat Mass Transf. **1985**, 107(3), 624–629.

Chhabra, R.P. PhD. Dissertation, Monash University, Melbourne, 1980.

Chhabra, R. P.; Uhlherr, P. H. T. Estimation of zero shear viscosity of polymer solutions from falling sphere data. Rheol. Acta **1980**, 18(5), 593.

Chhabra, R. P. Wall effects on free-settling velocity of non-spherical particles in viscous media in cylindrical tubes. Powder Technol. **1995**, 85, 83–90.

Chhabra, R. P.; Agarwal, L.; Sinha, N. K. Drag on non-spherical particles: an evaluation of available methods. Powder Technol. **1999**, 101, 288–295.

Chhabra, R. P.; Richardson, J. P. *Non-Newtonian Flow and Applied Rheology: Engineering Applications*, 2nd ed., Butterworth-Heinemann, Oxford, 2008.

Chhabra, R. P.; Patel, S. A. *Bubbles, Drops and Particles in Non-Newtonian Fluids*, 3rd ed., CRC Press, Florida, 2023.

Cho, Y. I.; Hartnett, J. P. Drag coefficients of a slowly moving sphere in non-Newtonian fluids. J. Non-Newton. Fluid Mech. **1983**, 12(2), 243.

Cho, Y. I.; Hartnett, J. P.; Lee, W. Y. Non-Newtonian viscosity measurements in the intermediate shear rate range with the falling-ball viscometer. J. Non-Newton. Fluid Mech. **1984**, 15(1), 61.

Churchill, S. W.; Churchill, R. U. A comprehensive correlating equation for heat and component transfer by free convection. AIChE J. **1975**, 21, 604–606.

Churchill, S.W. Comprehensive, theoretically based, correlating equations for free convection from isothermal spheres. Chem. Eng. Comm. **1983**, 24, 339–352.

Cieśliński, J.; Pudlik, W. Laminar free-convection from spherical segments. Int. J. Heat Mass Transf. **1988**, 9(4), 405-409.

Clift, R.; Gauvin, W. H. Motion of entrained particles in gas streams. Can. J. Chem. Eng. **1971**, 49, 439–448.

Clift, R.; Grace, J. R.; Weber, M. E. *Bubbles, Drops, and Particles*, ed. Academic Press, New York, 1978.

Comiti, J.; Sabiri, N. E.; Montillet A. Experimental characterization of flow regimes in various porous media—III: limit of Darcy's or creeping flow regime for Newtonian and purely viscous non-Newtonian fluids. Chem. Eng. Sci. **2000**, 55 (15), 3057–3061.

Coulson, J. M.; Richardson, J. F. *Chemical Engineering*, 5th ed.; vol. II, Butterworth- Heinemann, Oxford, 1990.

D'alessio, S. J. D; Dennis, S. C. R. Steady laminar forced convection from an elliptic cylinder. J. Eng. Math. **1995**, 29, 181–193.

Deglo de Besses, B.; Magnin, A.; Jay, P. Viscoplastic flow around a cylinder in an infinite medium. J. Non-Newt. Fluid Mech. **2003**, 115, 27-49.

Dellino, P.; Mele, D.; Bonasia, R.; Braia, G.; La Volpe, L.; Sulpizio, R. The analysis of the influence of pumice shape on its terminal velocity. Geophys. Res. Lett. **2005**, 32(21), 1–4.

Dennis, S. C. R.; Walker, J. D. A. Calculation of the steady flow past a sphere at low and moderate Reynolds numbers. J. Fluid Mech. **1971**, 48 (4), 771–789.

Dennis, S. C. R.; Walker, J. D. A.; Hudson, J. D. Heat transfer from a sphere at low Reynolds numbers. J. Fluid Mech. **1973**, 60(2), 273–283.

Dhole, S. D.; Chhabra, R. P.; Eswaran, V. Flow of power-law fluids past a sphere at intermediate Reynolds numbers. Ind. Eng. Chem. Res. **2006**, 45(13), 4773–4781.

Dioguardi, F.; Mele, D. A new shape dependent drag correlation formula for non-spherical rough particles: Experiments and results. Powder Technol. **2015**, 277, 222–230.

Dudek, D. R.; Fletcher, T. H.; Longwell, J. P.; Sarofim, A. F. Natural convection induced drag forces on spheres at low Grashof numbers: comparison of theory with experiment. Int. J. Heat Mass Transf. **1988**, 31(4), 863–873.

Elahi, S. H.; Adelnia, H.; Shahverdi, H. R. A simple accurate method for measuring viscosity of liquid metals at high temperatures. J. Rheol. **2012**, 56(4), 941.

Elenbass, W. The dissipation of heat by free convection of spheres and horizontal cylinders. Physica **1942**, 9(3), 285–296.

Faxen, H., Die bewegung einer starren kugel langs der achse eines mit zaher flussigkeit gefullten rohres, Ask. Mat. Arstron. Fys., **1923**, 17, 1.

Fendell, F. E. Laminar natural convection about an isothermally heated sphere at small Grashof number. J. Fluid Mech. **1968**, 34(1), 163–176.

Feng, Z.-G.; Michaelides, E. E. A numerical study on the transient heat transfer from a sphere at high Reynolds and Peclet numbers. Int. J. Heat Mass Transf. **2000**, 43, 219–229.

Francalanci, S.; Paris, E.; Solari, L. On the prediction of settling velocity for plastic particles of different shapes. Environ. Pollut. **2021**, 290, 118068.

Ganser, G. H. A rational approach to drag prediction of spherical and nonspherical particles, Powder Technol. **1993**, 77(2), 143–152.

Geoola, F.; Cornish, A. R. H. Numerical solution of steady-state free convective heat transfer from a solid sphere. Int. J. Heat Mass Transf. **1981**, 24(8), 1369–1379.

Geoola, F.; Cornish, A. R. H. Numerical simulation of free convective heat transfer from a sphere. Int. J. Heat Mass Transf. **1982**, 25, 1677–1687.

Glowinski, R.; Wachs, A. On the numerical simulation of viscoplastic fluid flow. in: P.G. Ciarlet (Eds.), *Handbook of Numerical Analysis*, Elsevier, North-Holland, 483-717, 2011.

Goharzadeh, A.; Khezzar, L.; Molki, A. PIV measurements of laminar flow around a hemisphere. WIT Trans. Eng. Sci. **2012**, 74, 29–36.

Goossens, W.R. Review of the empirical correlations for the drag coefficient of rigid spheres. Powder Technol. **2019**, 352, 350–359.

Gupta, A. K.; Chhabra, R. P. Spheroids in viscoplastic fluids: Drag and heat transfer. Ind. Eng. Chem. Res. **2014**, 53(49), 18943-18965.

Gupta, A. K.; Chhabra, R. P. Combined effects of fluid shear-thinning and yield stress on heat transfer from an isothermal spheroid. Int. J. Heat Mass Transf. **2016**, *93*, 803-826.

Gupta, A. K.; Gupta, S.; Chhabra, R. P. Natural convection in Bingham plastic fluids from an isothermal spheroid: Effects of fluid yield stress, viscous dissipation and temperature-dependent viscosity. Korea-Aust. Rheol. J., **2017**, 29, 163-184.

Gupta, A. K.; Mishra, P.; Chhabra, R. P. Momentum and heat transfer characteristics of a thin circular disk in Bingham plastic fluids. Numer. Heat Transf.A: Appl. **2017**, 72(11), 844-868.

Gupta, R.K. *Polymer and Composite Rheology*, CRC Press, Boca Raton, Florida, 2000.

Gupta, S.V. *Viscometry for liquids: Calibration of Viscometers*, Springer International Publishing, Germany, 2014.

Hadad, Y.; Jafarpur, K. Laminar forced convection heat transfer from isothermal bodies with unity aspect ratio in coaxial air flow. Heat Transf. Eng. **2012**, 33(3), 245–254.

Haider, A.; Levenspiel, O. Drag coefficient and terminal velocity of spherical and nonspherical particles. Powder Technol. **1989**, 58, 63–70.

Han, C. D. *Rheology and Processing of Polymeric Materials*, Vol. 1 and 2, Oxford University Press, New York, 2007.

Hassani, A.V.; Hollands, K. G. T. On natural convection heat transfer from three dimensional bodies of arbitrary shape. J. Heat Transf. **1989**, 111(2), 363–371.

Hieber, C. A.; Gebhart; B. Mixed convection from a sphere at small Reynolds and Grashof numbers. J. Fluid Mech. **1969**, 38(1), 137–159.

Hill, K. B.; Shook, C. A. Pipeline transport of coarse particles by water and by fluids with yield stresses. Particul. Sci. Technol. **1998**, 16(2), 163-183.

Hirota, S.; Takada, M. Analysis of Non-Newtonian flow by falling-sphere method. Bull. Chem. Soc. Jpn. **1959**, 32(11), 1191.

Hochmuth, R. M.; Sutera, S. P. Spherical caps in low Reynolds-number tube flow. Chem. Eng. Sci. **1970**, 25(4), 593–604.

Hossain, A.; Gebhart, B. Natural convection about a sphere at low Grashof number. Heat transfer IV, Proc. Int. Heat Transf. Conf. Paris, **1970**, 1–2.

Hossain, M. A. Laminar Free convection about an isothermal sphere at extremely small Grashof numbers. Ph.D. Thesis, Cornell University, Ithaca, New York, 1966.

Jafarpur, K.; Yovanovich, M. M. Laminar free convective heat transfer from isothermal spheres: a new analytical method. Int. J. Heat Mass Transf. **1992**, 35(9), 2195–2201.

Jaluria, Y.; Gebhart, B. On the buoyancy-induced flow arising from a heated hemisphere. Int. J. Heat Mass Transf. **1975**, 18(3), 415-431.

Jia, H.; Gogos, G. Laminar natural convection heat transfer from isothermal spheres, Int. J. Heat Mass Transf. **1996**, 39(8), 1603–1615.

Jia, H.; Gogos, G. Transient laminar natural convection heat transfer from isothermal sphere, Numer. Heat Tran. A: Appl. **1996**, 29, 83–101.

Kalman, H; Matana, E. Terminal velocity and drag coefficient for spherical particles. Powder Technol. **2022**, 396, 181–190.

Kanchanalakshana, D.; Ghajar, A.J. An improved falling sphere viscometer for intermediate concentrations of viscoelastic fluids. Int. Commun. Heat Mass Transf. **1986**, 13(2), 219.

Kaskas, A. Berechnung dec stationaren und instationaren Bewegung von Kugelm in rehunden und stromenden Medien. Diplomarbeit dem Lehrstuhl fur Thermodynamik und Verfahrenstechnik der T. U. Berlin, 1964.

Khan, A. R.; Richardson, J. F. The resistance to motion of a solid sphere in a fluid. Chem. Eng. Commun. **1987**, 62, 135–150.

Kim, D.; Choi, H. Laminar flow past a hemisphere. Phys. Fluids **2003**, 15(8), 2457–2460.

Kishore, N.; Gu, S. Momentum and heat transfer phenomena of spheroid particles at moderate Reynolds and Prandtl numbers. Int. J. Heat Mass Transf. **2011**, 54, 2595–2601.

Kono, Y.; *Magmas under pressure: advances in high-pressure experiments on structure and properties of melts*, Viscosity Measurement, Magmas Under Pressure, Elsevier, Amsterdam 2018, p. 261.

Kreith, F. *The CRC Handbook of Thermal Engineering*, CRC Press, Boca-Raton, Florida, 2000.

Krishnan, S.; Kaman, A. Effect of blockage ratio on drag and heat transfer from a centrally located sphere in pipe flow. Eng. App. Comp. Fluid Mech. **2010**, 4(3), 396-414.

Krumbein, W. C. Settling velocity and flume behaviour of non-spherical particles. Eos. Trans. Am. Geophy. Union **1942**, 23, 621-623.

Lewandowski, W. M.; Kubski, P.; Khubeiz, J. M.; Bieszk, H.; Wilczewski, T.; SZYMAŃSKI, S. Theoretical and experimental study of natural convection heat transfer from isothermal hemisphere. Int. J. Heat Mass Transf. **1996**, 40(1), 101-109.

Liew, K. S.; Adelman, M. Laminar natural heat transfer from an isothermal sphere to non-Newtonian fluids. Can. J. Chem. Eng. **1975**, 53, 494–499.

Liu, J.; Zhao, C. J.; Liu, H.; Lu, W. Q. Numerical study of laminar natural convection heat transfer from a hemisphere with adiabatic plane and isothermal hemispherical surface. Int. J. Therm. Sci. **2018**, 131, 132-143.

Maheshwari, A.; Chhabra, R. P.; Biswas, G. Effect of blockage on drag and heat transfer from a single sphere and in-line array of three spheres. Powder Technol. **2006**, 168(2),74–83.

Mahony, J. J. Heat transfer at small Grashof numbers. Proc. Royal Soc. London. Series A. Math. and Phy. Sci. **1957**, 238(1214), 412–423.

Mark, J.; Ngai, K.; Graessley, W.; Mandelkern, L.; Samulski, E.; Koenig, J.; Wignall, G. *Physical Properties of Polymers*, 3rd ed., Cambridge University Press, New York, 2004.

Martynenko, O. G.; Khramtsov, P. P. *Free-Convective Heat Transfer*, Springer, New York, 2005.

Masliyah, J. H.; Epstein, N. Numerical study of steady flow past spheroids. J. Fluid Mech. **1970**, 44(3), 493–512.

Mauret, E.; Renaud M. Transport phenomena in multi-particle systems—II. Proposed new model based on flow around submerged objects for sphere and fiber beds-transition between the capillary and particulate representations. Chem. Eng. Sci. **1997**, 52 (11), 1819–1834.

Metzner, A. B.; Reed, J. C. Flow of non-Newtonian fluids—correlation of the laminar, transition, and turbulent-flow regions. AIChE J. **1955**, 1, 434.

Michaelides, E. E. Particles, *Bubbles and Drops: Their Motion, Heat and Mass Transfer*, World Scientific Singapore, 2006.

Michaelides, E. E.; Feng, Z. Drag coefficients of non-spherical and irregularly shaped particles. J. Fluids Eng. **2023**, 145(6), 060801.

Milliken, W. J.; Gottlieb, M.; Graham, A. L.; Mondy, L. A.; Powell, R. L. The viscosity-volume fraction relation for suspensions of rod-like particles by falling-ball rheometry. J. Fluid Mech. **1989**, 202, 217.

Milliken, W. J.; Gottlieb, M.; Graham, A. L.; Mondy, L. A.; Powell, R. L. Effect of the diameter of falling balls on the apparent viscosity of suspensions of spheres and rods, Physico-Chem. Hydrodynamics **1989**, 11, 341.

Mishra, P.; Tiwari, A. K.; Chhabra, R. P. Effect of orientation on the drag of a cone settling in a Bingham plastic fluid. Particuology **2019**, 43, 157–170.

Mitsoulis, E. On creeping drag flow of a viscoplastic fluid past a circular cylinder: wall effects. Chemical Engineering Science, **2004**, 59, 789-800.

Mitsoulis, E.; Zisis, T. Flow of Bingham plastics in a lid-driven square cavity. J. Non-Newt. Fluid Mech. **2001**, 101, 173-180.

Mogarbi, E.; Ziskind, G.; Katoshevski, D.; Bar-Ziv, E. Experimental study of the forces associated with mixed convection from a heated sphere at small Reynolds and Grashoff numbers. Part II: assisting and opposing flows. Int. J. Heat Mass Transf. **2002**, 45, 2423–2430.

Mohammad, H.; Munshi, B., Experimental estimation of the settling velocity and drag coefficient of the hollow cylindrical particles settling in non-Newtonian fluids in an annular channel. Can. J. Chem. Engg. **2023**, 101, 6632-6640

Mondy, L. A.; Morrison, T. G.; Graham, A. L.; Powell, R. L. Measurements of the viscosities of suspensions of oriented rods using falling ball rheometry. Int. J. Multiphase Flow **1990**, 16, 651.

Morrison, F. A. Data correlation for drag coefficient for sphere, Department of Chemical Engineering, Michigan Technological University, Houghton, MI, 2013.

Mossaz, S.; Jay, P.; Magnin, A. Criteria for the appearance of recirculating and non stationary regimes behind a cylinder in a viscoplastic fluid. J. Non-Newt. Fluid Mech. **2010**, 165, 1525-1535.

Mossaz, S.; Jay, P.; Magnin, A. Non-recirculating and recirculating inertial flows of a viscoplastic fluid around a cylinder. J. Non-Newt. Fluid Mech. **2012**, 177, 64 75.

Musong, S. G.; Feng, Z. G.; Michaelides, E. E.; Mao, S. Application of a three- dimensional immersed boundary method for free convection from single spheres and aggregates. J. Fluids Eng. **2016**, 138(4), 041304.

Nalluri, S. V.; Patel, S. A.; Chhabra, R. P. Mixed convection from a hemisphere in Bingham plastic fluids. Int. J. Heat Mass Transf. **2015**, 84, 304-318.

Nirmalkar, N.; Chhabra, R.P.; Poole, R.J. On creeping flow of a Bingham plastic fluid past a square cylinder. J. Non-Newt. Fluid Mech. **2012**, 171-172, 17-30.

Nirmalkar, N.; Chhabra, R. P.; Poole, R. J. Numerical predictions of momentum and heat transfer characteristics from a heated sphere in yield-stress fluids. Ind. Eng. Chem. Res. **2013a**, 52, 6848-6861.

Nirmalkar, N.; Chhabra, R. P.; Poole, R. J. Effect of shear-thinning behaviour on heat transfer from a heated sphere in yield-stress fluids. Industrial and Engineering Chemistry Research, **2013b**, 52, 13490-13504.

Nirmalkar, N.; Chhabra, R.P.; Poole, R.J. Laminar forced convection heat transfer from a heated square cylinder in a Bingham plastic fluid. Int. J. Heat Mass Transf. **2013c**, 56, 625-639.

Nirmalkar, N.; Chhabra, R. P. Momentum and heat transfer from a heated circular cylinder in Bingham plastic fluids. Int. J. Heat Mass Transf. **2014**, 70, 564-577.

Nirmalkar, N.; Gupta, A. K.; Chhabra, R.P. Natural convection from a heated sphere in Bingham plastic fluids. Ind. Eng. Chem. Res. **2014**, 53(45), 17818-17832.

Nitin, S.; Chhabra, R. P. Wall effects in two-dimensional axisymmetric flow over a circular disk oriented normal to flow in a cylindrical tube. Can. J. Chem. Eng. **2005**, 83(3), 450–457.

Nitin, S.; Chhabra, R. P. Sedimentation of a circular disk in power law fluids. J. of colloid and interface Sci. **2006**, 295(2), 520-527.

O'Donovan, E. J.; Tanner, R. I. Numerical study of the Bingham squeeze film problem. J. Non-Newt. Fluid Mech. **1984**, 15, 75-83.

Okesanya, T.; Abdukarimov, A.; Kuru, E. Generalized models for predicting the drag coefficient and settling velocity of rigid spheres in viscoelastic and visco inelastic power-law fluids. J. Pet. Sci. Engg. **2020**, 191, 107077.

Pang, B.; Wang, S.; Chen, W.; Hassan, M.; Lu, H. Effect of flow behaviour index and consistency coefficient on hydrodynamics of power-law fluids and particles in fluidized beds. Powder Technol. **2020**, 366, 249-260.

Papanastasiou, T. C. Flow of materials with yield. J. Rheol. **1987**, 31, 385-404.

Patel, O. P.; Patel, S. A.; Raja, A. J.; Chhabra, R. P. Forced convection heat transfer from a hemisphere in Bingham plastic fluids: Effect of orientation and thermal boundary condition, J. Energy Heat Mass Transf. **2015**, 37, 2-56.

Patel, S. A.; Chhabra, R. P. Steady flow of Bingham plastic fluids past an elliptical cylinder. J. Non-Newt. Fluid Mech. **2013**, 202, 32–53.

Patel, S. A.; Chhabra, R. P. Heat transfer in Bingham plastic fluids from a heated elliptical cylinder. Int. J. Heat Mass Transf. **2014**, 73, 671– 692.

Patel, S. A., & Chhabra, R. P. Laminar free convection in Bingham plastic fluids from an isothermal elliptic cylinder. J. Thermophys. Heat Transf. **2016**, *30*(1), 152-167.

Patel, S.A.; Chhabra, R. P.; Raithby, G. D.; Hollands, K. G. T., Natural convection, in: R. P. Chhabra (Ed.), *CRC Handbook of Thermal Engineering*, 2nd ed., Taylor and Francis, Boca Raton, FL, 2017.

Pazwash, H.; Robertson, J. M. Fluid-dynamic consideration of bottom materials. J. Hydraulics Div. **1971**, 97(9), 1317-1329.

Pazwash, H.; Robertson, J. M. Forces on bodies in Bingham fluids. J. Hydraulic Res. **1975**, 13(1), 35-55.

Peev, G.; Nikolova, A.; Todorova, D. Mass transfer from solid particles to power law non-Newtonian fluid in granular bed at low Reynolds numbers. Chem. Eng. J. **2002**, 88 (1–3), 119–125.

Pettyjohn, E. S.; Christiansen, E. B. Effect of particle shape on free-settling rates of isometric particles. Chem. Engg. Prog. **1948**, 44, 157–172.

Polyanin, A. D.; Kutepov, A. M.; Kazenin, D. A.; Vyazmin, A.V. *Hydrodynamics, Mass and Heat Transfer in Chemical Engineering*, Tylor & Francis, London, 2001.

Poole, R. J.; Chhabra, R. P. Development length requirements for fully developed laminar pipe flow of yield stress fluids. J. Fluids Eng. **2010**, 132, 0345011-0345014.

Powell, R. L.; Morrison, T. G.; Milliken, W. J. Apparent viscosity of suspensions of rods using falling ball rheometry. Phys. Fluids. 2001, 13(3), 588-593.

Prakash, O; Patel, S. A.; Gupta, A. K.; Chhabra, R. P. Coarse particles in homogeneous non-Newtonian slurries: Combined effects of shear-thinning viscosity and fluid yield stress on drag and heat transfer from hemispherical particles. Trans. Indian Inst. Met. **2017**, 70, 341–358.

Prhashanna, A.; Chhabra, R. P. Free convection in power-law fluids from a heated sphere. Chem. Eng. Sci. **2010**, 65, 6190–6205.

Prhashanna, A.; Chhabra, R. P. Laminar natural convection from a horizontal cylinder in power-law fluids. Ind. Eng. Chem. Res. **2011**, 50(4), 2424–2440.

Putz, A.; Frigaard, I. A. Creeping flow around particles in a Bingham fluid. J. Non-Newt. Fluid Mech. **2010**, 165, 263-280.

Rae, D. Yield stress exerted on a body immersed in a Bingham fluid, Nature **1962**, 194, 272.

Raithby, G. D.; Hollands, K. G. T. Laminar and turbulent free convection from elliptic cylinders, with a vertical plate and horizontal circular cylinder as special cases. J. Heat Transf. **1976**, 98, 72–80.

Ranz, W. E.; Marshall, W. R. Evaporation from drops part I. Chem. Eng. Prog. **1952**, 48, 141–146.

Rodriguez, I.; Campo, A. Numerical investigation of forced convection heat transfer from a sphere at low Prandtl numbers. Int. J. Therm. Sci. **2023**, 184, 107970.

Roquet, N.; Saramito, P. An adaptive finite element method for Bingham fluid flows around a cylinder. Comp. Meth. App. Mech. Eng. **2003**, 192, 3317-3341.

Sagar, T. V.; Patel, S. A.; Gupta, A. K.; Chhabra, R. P. Effects of severe blockage on heat transfer from a sphere in power-law fluids. Int. Comm. Heat and Mass Transf. **2017**, 84, 27–34.

Sairamu, M.; Nirmalkar, N.; Chhabra, R. P. Natural convection from a circular cylinder in confined Bingham plastic fluids. Int. J. Heat Mass Transf. **2013**, 60, 567-581.

Saitoh, T.; Sajiki, T.; Maruhara, K. Benchmark solutions to natural convection heat transfer problem around a horizontal circular cylinder. Int. J. Heat Mass Transf. **1993**, 36(5), 1251–1259.

Sasmal, C.; Shyam, R.; Chhabra, R. P. Laminar flow of power-law fluids past a hemisphere: Momentum and forced convection heat transfer characteristics. Int. J. Heat Mass Transf. **2013**, 63, 51-64.

Sasmal, C.; Chhabra, R. P. Laminar free convection in power-law fluids from a heated hemisphere. J. Thermophys. Heat Transf. **2014**, 28(4), 750-763.

Shahcheraghi, N.; Dwyer, H. A. Fluid flow and heat transfer over a three-dimensional spherical object in a pipe. 1998, 985-990.

Sharma, M. K.; Chhabra, R. P. An experimental study of free fall of cones in Newtonian and non-Newtonian media: drag coefficient and wall effects. Chem. Eng. Process. Process Intensif. **1991**, 30(2), 61–67.

Shaw, M. T. On finding the zero-shear-rate viscosity of polymer melts. Polym. Eng. Sci. **2021**, 61(4), 1166.

Shenoy, A. R.; Kleinstreuer, C. Flow over a thin circular disk at low to moderate Reynolds numbers, J. Fluid Mech. **2008**, 605, 253–262.

Singh, S. N.; Hasan, M. M. Free convection about a sphere at small Grashof number. Int. J. Heat Mass Transf. **1983**, 26, 781–783.

Sivakumar, P.; Bharti, R. P.; Chhabra, R. P. Steady flow of power-law fluids across an unconfined elliptical cylinder. Chem. Eng. Sci. **2007**, 62, 1682-1702.

Slattery, J. C. Approximations to the drag force on a sphere moving slowly through either an Ostwald-De Waele or a Sisko fluid. AIChE J. **1962**, 8, 663.

Song, D.; Gupta, R.K.; Chhabra, R.P. Wall effects on a sphere falling in quiescent power law fluids in cylindrical tubes. Ind. Eng. Chem. Res. **2009**, 48, 5845–5856.

Song, D.; Gupta, R. K.; Chhabra, R. P. Drag on a sphere in Poiseuille flow of shear-thinning power-law fluids. Ind. Eng. Chem. Res. **2011**, 50, 13105–13115

Song, D.; Gupta, R.K.; Chhabra, R.P. Heat transfer to a sphere in tube flow of power-law liquids. Int. J. Heat Mass Transf. **2012**, 55, 2110–2121.

Stewart Jr, W. E.; & Johnson, J. C. Experimental natural convection heat transfer from isothermal spherical zones. ASME Journal of Heat Transfer, **1985**, 107, 463-465.

Stewart, W.E. Asymptotic calculation of free convection in laminar three- dimensional systems. Int. J. Heat Mass Transf. **1971**, 14, 1013–1031.

Sun, X.; Zhang, K.; Chen, Y.; Li, W.; Qu, J. Study on the settling velocity of drilling cuttings in the power law fluid. Powder Technol. **2020**, 362, 278.

Suri, P.; Patel, S. A. Particle shape matters: Flow and heat transfer characteristics of nonspherical particles. Powder Technol. **2024**, 431, 119102.

Sutterby, L. Falling sphere viscometer. J. Phys. E: Sci. Instr. **1973**, 6(10), 1001.

Tanner, R.I. End effects in falling-ball viscometry. J. Fluid Mech. **1963**, 17(2), 161.

Thompson, T. L.; Clark, N. N. A holistic approach to particle drag prediction. Powder Technol. **1991**, 67, 57–66.

Thorpe, A. D.; Mason, B. J. The evaporation of ice spheres and ice crystals. Br. J. Appl. Phys. **1966**, 17(4), 541.

Thumati, V. T. Spheres in non-Newtonian fluids: wall effects, drag and heat transfer, M.Tech. Thesis Department of Chemical Engineering, IIT Kanpur, India, 2016.

Tiwari, A. K.; Chhabra, R. P. Momentum and heat transfer from a semi-circular cylinder in Bingham plastic fluids. Applied Mathematical Modelling, **2015**, 39(22), 7045-7064.

Tokpavi, D. L.; Magnin, A.; Jay, P. Very slow flow of Bingham viscoplastic fluid around a circular cylinder. J. Non-Newt. Fluid Mech. **2008**, 154, 65-76.

Tripathi, A.; Chhabra, R.P.; Sundararajan, T. Power law fluid flow over spheroidal particles. Ind. Eng. Chem. Res. **1994**, 33(2), 403-410.

Tsubouchi, T.; Sato, S.; Nagakura, K. Heat transfer from fine wires and particles by natural convection. Trans. Jpn. Soc. of Mech. Eng. C. **1959**, 25(156), 798–809.

Uhlherr, P. H. T.; Le, T. N.; Tiu, C. Characterisation of inelastic power law fluids using falling sphere data. Can. J. Chem. Eng. **1976**, 54(5), 497.

Uhlherr, P. H. T.; Chhabra, R. P. Wall effect for the fall of spheres in cylindrical tubes at high Reynolds number. Can. J. Chem. Eng. **1995**, 73, 918–923.

Unnikrishnan, A.; Chhabra, R. P. An experimental study of motion of cylinders in Newtonian fluids: wall effects and drag coefficient. Can. J. Chem. Eng. **1991**, 69, 729–735

Vakil, A.; Green, S. I. Drag and lift coefficients of inclined finite circular cylinders at moderate Reynolds numbers. Comput. Fluids **2009**, 3, 1771–1781.

Valentik, L.; Whitmore, R. L. The terminal velocity of spheres in Bingham plastics. Br. J. Appl. Phys., **1965**, 16, 1197.

Volarovich, M. P.; Gutkin, A. M. Theory of flow of a viscoplastic medium. Colloid J. USSR, **1953**, 15, 153.

Wadell, H. The coefficient of resistance as a function of Reynolds number for solids of various shapes. J. Franklin Inst. **1934**, 217, 459–490.

Wang, J.; Qi, H.; You, C. Experimental study of sedimentation characteristics of spheroidal particles. Particuology. **2009**, 7, 264–268.

Wasserman, M. L.; Slattery, J.C. Upper and lower bounds on the drag coefficient of a sphere in a power-model fluid. AIChE J. **1964**, 10, 383.

Wham, R. M.; Basaran, O. A.; Byers, C. H. Wall effects on flow past solid spheres at finite Reynolds number. Ind. Eng. Chem. Res. **1996**, 35, 864–874.

Whitaker, S. Forced convection heat transfer calculations for flow in pipes, past flat plates, single cylinder, single sphere and for flow in packed beds and tube bundles. AICHE J. **1972**, 18, 361–371.

Xie H. Y.; Zhang, D. W. Stokes shape factor and its application in the measurement of sphericity of non-spherical particles. Powder Technol. **2001**, 114, 102–105.

Yang, S.; Raghavan, V.; Gogos, G. Numerical study of transient laminar natural convection over an isothermal sphere. Int. J. Heat Fluid Flow **2007**, 28(4), 821–837.

Yow, H. N.; Pitt, M. J.; Salman, A. D. Drag correlations for particles of regular shape. Advanced Powder Technology, **2005**, 16(4), 363-372.

Yuge, T. Experiments on heat transfer from spheres including combined natural and forced convection. J. Heat Transf. **1960**, 82, 214–220.

Zhang, J.; Zhen, Q.; Liu, J.; Lu, W. Q. Effect of spacing on laminar natural convection flow and heat transfer from two spheres in vertical arrangement. Int. J. Heat Mass Transf. **2019**, 134, 852–865.

Zisis, T. H.; Mitsoulis, E. Viscoplastic flow around a cylinder kept between parallel plates. J. Non-Newt. Fluid Mech. **2002**, 105, 1-20.

Ziskind, G.; Zhao, B.; Katoshevski, D.; Bar-Ziv, E. Experimental study of the forces associated with mixed convection from a heated sphere at small Reynolds and Grashoff numbers. Part I: cross flows. Int. J. Heat Mass Transf. **2001**, 44, 4381–4389.

# APPENDIX-A

## A1. Sample calculations for the non-dimensional number with examples in practical applications.

### A.1.1 Calculations for Grashof (*Gr*) and Prandtl (*Pr*) numbers

Two different polymer systems were considered (Amato and Tien, 1976). CMC-7H (0.5% and 1.0%) and Polyox WSR (0.25% and 0.5%). Density-temperature correlation along with their coefficients for the mentioned polymer solution is given in the following table which is valid over the temperature range of $293.15 \leq T \leq 333.15$:

**Table A1 Density-temperature polynomial coefficients**

$$\rho = 1000\left(a + b\left(T - 273.15\right) + c\left(T - 273.15\right)^2\right)$$

$T$ (K), $\rho$ (kg/m$^3$)

| Solution | *a* | *b* | *c* |
|---|---|---|---|
| 0.5% CMC-7H | 1.0045 | $-1.7396 \times 10^{-4}$ | $-2.3897 \times 10^{-6}$ |
| 1.0% CMC-7H | 1.005 | $-5.8154 \times 10^{-5}$ | $-3.7971 \times 10^{-6}$ |
| 0.25% Polyox WSR-FRA | 0.9939 | $-9.6665 \times 10^{-5}$ | $-3.3115 \times 10^{-6}$ |
| 0.5% Polyox WSR-FRA | 0.99997 | $-1.5559 \times 10^{-4}$ | $-2.7478 \times 10^{-6}$ |

where $T$ (K) and $\rho$ (kg/m$^3$) is the temperature and density of the fluid.

Coefficient of thermal expansion can be calculated from the density formula through the use of the equation: $\beta = \frac{1}{\rho}\left(\frac{\partial \rho}{\partial T}\right)_p$

Similarly, the thermal conductivity and temperature polynomial coefficient for the polymer system is given by the following table for the temperature range $298.15 \leq T \leq 323.15$ K:

**Table A2 Thermal conductivity temperature polynomial coefficients**

$$k = 4.1868 \times 10^2\left[a + b\left(T - 273.15\right)\right]$$

$k$ (J/m s K), $T$(K)

| Solution | *a* | *b* |
|---|---|---|
| 0.5% CMC-7H | $1.251 \times 10^{-3}$ | $6.626 \times 10^{-6}$ |
| 1.0% CMC-7H | $1.194 \times 10^{-3}$ | $9.906 \times 10^{-6}$ |
| 0.25% Polyox WSR-FRA | $1.121 \times 10^{-3}$ | $9.323 \times 10^{-6}$ |
| 0.5% Polyox WSR-FRA | $1.121 \times 10^{-3}$ | $9.323 \times 10^{-6}$ |

The rheological data is valid for temperature range $298.15 \leq T \leq 308.15$ K:

**Table A3 Rheological data for polymer systems**

| Solution | *A* | *B* | *n* |
|---|---|---|---|
| $m = Aexp(B/T)$ | | | |
| $m$ (N s$^n$/m$^2$), $T$(K) | | | |
| 0.5% CMC-7H | $1.251 \times 10^{-3}$ | $6.626 \times 10^{-6}$ | 0.948 |
| 1.0% CMC-7H | $1.194 \times 10^{-3}$ | $9.906 \times 10^{-6}$ | 0.818 |
| $m = A + B(T - 273.15)$ | | | |
| 0.25% Polyox WSR-FRA | $1.121 \times 10^{-3}$ | $9.323 \times 10^{-6}$ | 0.592 |
| 0.5% Polyox WSR-FRA | $1.121 \times 10^{-3}$ | $9.323 \times 10^{-6}$ | 0.905 |

**Table A4 Average properties of polymer solutions**

| Solution | $\rho_{avg}$ | $k_{avg}$ | $\beta$ | *m* |
|---|---|---|---|---|
| 0.5% CMC-7H | 992.76 | 0.6278 | $1.0073 \times 10^{-3}$ | 0.314 |
| 1.0% CMC-7H | 995.08 | 0.6554 | $1.0050 \times 10^{-3}$ | 0.328 |
| 0.25% Polyox WSR-FRA | 983.41 | 0.6157 | $1.0169 \times 10^{-3}$ | 0.308 |
| 0.5% Polyox WSR-FRA | 988.25 | 0.6157 | $1.0119 \times 10^{-3}$ | 0.308 |

The Grashof and Prandtl number calculated based on these fluid properties for four different spherical particle at $\Delta T = 5$ and heat capacity $C = 4.19 \times 10^3$ J/kg K.

**Table A5 Grashof and Prandtl numbers for a sphere in power-law fluids (PL) in natural convection regime**

| Solution | Diameter of spheres (m) | | | | | | | |
|---|---|---|---|---|---|---|---|---|
| | 0.0254 | | 0.0508 | | 0.0762 | | 0.1016 | |
| | *Gr* | *Pr* | *Gr* | *Pr* | *Gr* | *Pr* | *Gr* | *Pr* |
| 0.5% CMC-7H | 16.49 | 0.190 | 127.3 | 0.370 | 420.5 | 0.546 | 982.0 | 0.720 |
| 1.0% CMC-7H | 0.304 | 7.650 | 2.144 | 13.79 | 6.720 | 19.46 | 15.12 | 24.85 |
| 0.25% Polyox WSR-FRA | 7.021 | 6.259 | 42.33 | 9.589 | 121.1 | 12.31 | 255.2 | 14.69 |
| 0.5% Polyox WSR-FRA | 0.022 | 12.53 | 0.164 | 23.80 | 0.533 | 34.63 | 1.229 | 45.19 |

### A.1.2 Calculations for Reynolds (*Re*) and Bingham (*Bn*) numbers

The properties of the fluids are mentioned in the following table (Khahledi *et al.*, 2020):

| Fluid | Fluid type | Conc. % | $\rho$ (kg/m$^3$) | $m$ (Pa s$^n$) | $n$ | $\tau$ (Pa) | $\mu$ (Pa s) |
|---|---|---|---|---|---|---|---|
| **Kaolin v/v** | HB | 20.3 | 1336 | 3.98 | 0.36 | 39.4 | – |
| | HB | 13.1 | 1217 | 0.067 | 0.72 | 8.9 | – |
| **CMC w/w** | PL | 7.55 | 1043 | 2.39 | 0.64 | – | – |
| | PL | 6.58 | 1037 | 0.882 | 0.7 | – | – |
| | PL | 5.21 | 1029 | 0.209 | 0.79 | – | – |
| | PL | 2.81 | 1016 | 0.017 | 0.97 | – | – |
| | N | 2.4 | 1014 | 0.006 | 1 | – | – |
| **Bentonite w/w** | BP | 7.3 | 1046 | 0.021 | 1 | 30.5 | – |
| | BP | 6.99 | 1044 | 0.014 | 1 | 15.7 | – |
| | BP | 3.77 | 1023 | 0.006 | 1 | 1.13 | – |
| **Glycerine** | N | 100 | 1258 | – | – | – | 0.973 |
| | N | 96 | 1248 | – | – | – | 0.304 |
| | N | 93 | 1242 | – | – | – | 0.129 |
| | N | 65 | 1179 | – | – | – | 0.019 |

N: Newtonian fluid, PL: power-law fluid, BP: Bingham plastic fluid, HB: Herschel-Bulkley fluid

For the fluid velocity $U$ = 0.05 m/s. The Reynolds and Bingham number is calculated in the subsequent table for the three different sized spherical particles.

| Fluid | Fluid type | Diameter (m) | | | | | |
|---|---|---|---|---|---|---|---|
| | | 0.1016 | | 0.0508 | | 0.1016 | |
| | | ***Re*** | ***Bn*** | ***Re*** | ***Bn*** | ***Re*** | ***Bn*** |
| **Kaolin v/v** | HB | 0.052 | 7.758 | 0.070 | 9.956 | 0.094 | 12.78 |
| | HB | 0.199 | 81.57 | 0.335 | 134.4 | 0.558 | 221.3 |
| **Carboxymethyl cellulose (CMC) w/w** | PL | 0.707 | – | 1.102 | – | 1.718 | – |
| | PL | 1.830 | – | 2.972 | – | 4.828 | – |
| | PL | 7.208 | – | 12.46 | – | 21.55 | – |
| | PL | 77.46 | – | 151.7 | – | 297.2 | – |
| | N | 214.6 | – | 429.3 | – | 858.5 | – |
| **Bentonite w/w** | BP | 0.043 | 737.8 | 0.087 | 1475.6 | 0.174 | 2951.2 |
| | BP | 0.083 | 569.7 | 0.168 | 1139.4 | 0.337 | 2278.7 |
| | BP | 1.061 | 95.67 | 2.207 | 191.3 | 4.505 | 382.69 |
| **Glycerine** | N | 1.642 | – | 3.284 | – | 6.568 | – |
| | N | 5.214 | – | 10.43 | – | 20.85 | – |
| | N | 12.23 | – | 24.45 | – | 48.91 | – |
| | N | 78.81 | – | 157.6 | – | 315.2 | – |

N: Newtonian fluid, PL: power-law fluid, BP: Bingham plastic fluid, HB: Herschel-Bulkley fluid

## A2. Velocity and temperature profiles for spherical segments in Bingham plastic fluids in steady free convection regime

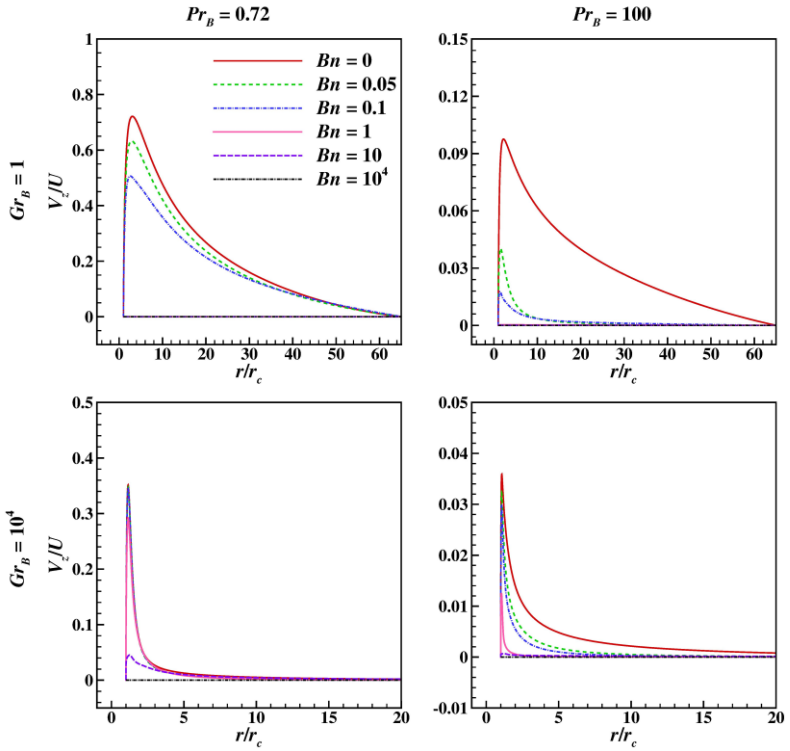


**Fig A1.** Velocity profile in the *r*- direction at the base of the spherical segment ($z = 0$) for $\alpha = 90^o$.

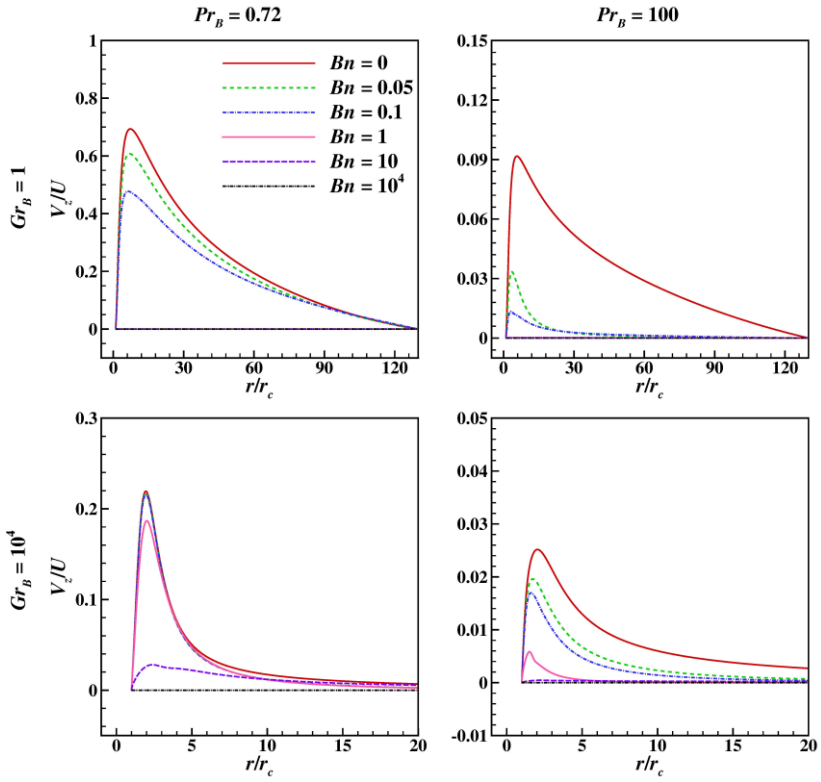


**Fig A2.** Velocity profile in the *r*- direction at the base of the spherical segment ($z = 0$) for $\alpha = 150^o$.

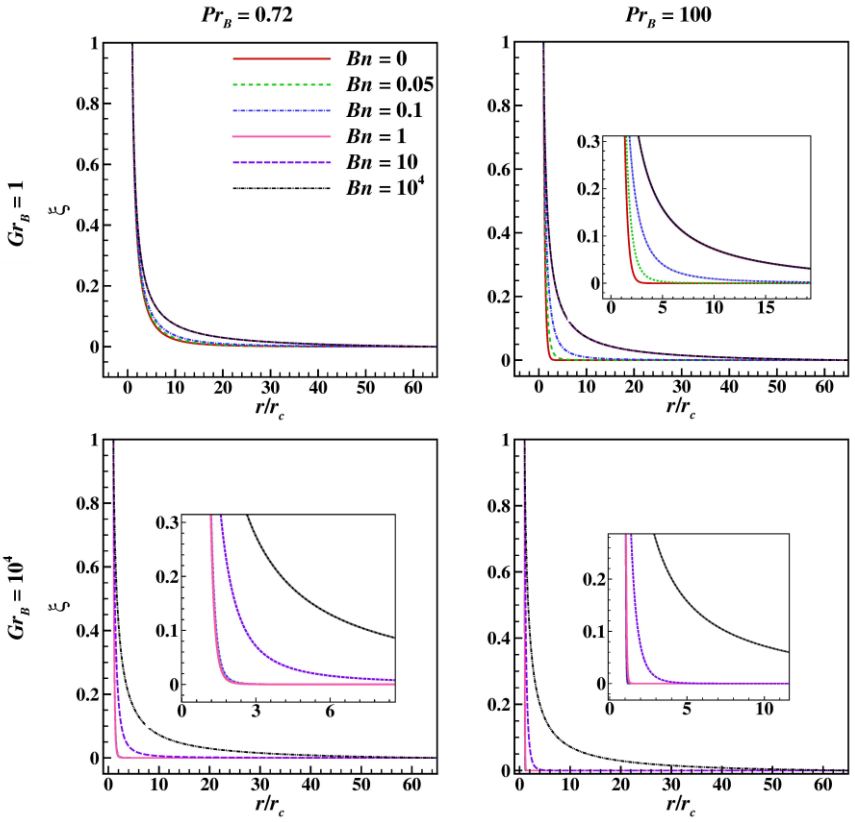


**FigA3.** Temperature profile in the *r*- direction at the base of the spherical segment ($z = 0$) for $\alpha = 90^o$.

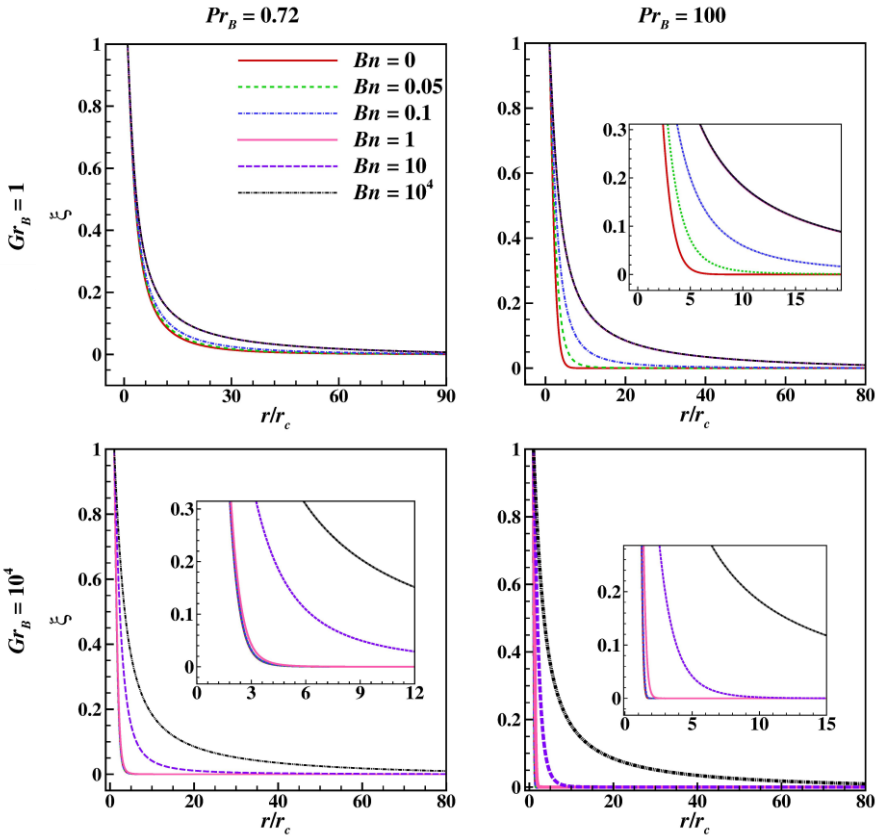


**Fig A4.** Temperature profile in the *r*- direction at the base of the spherical segment ($z = 0$) for $\alpha = 150^o$.

## A3. Numerical scheme to develop shear stress-shear rate in case of power-law fluid using FBM method

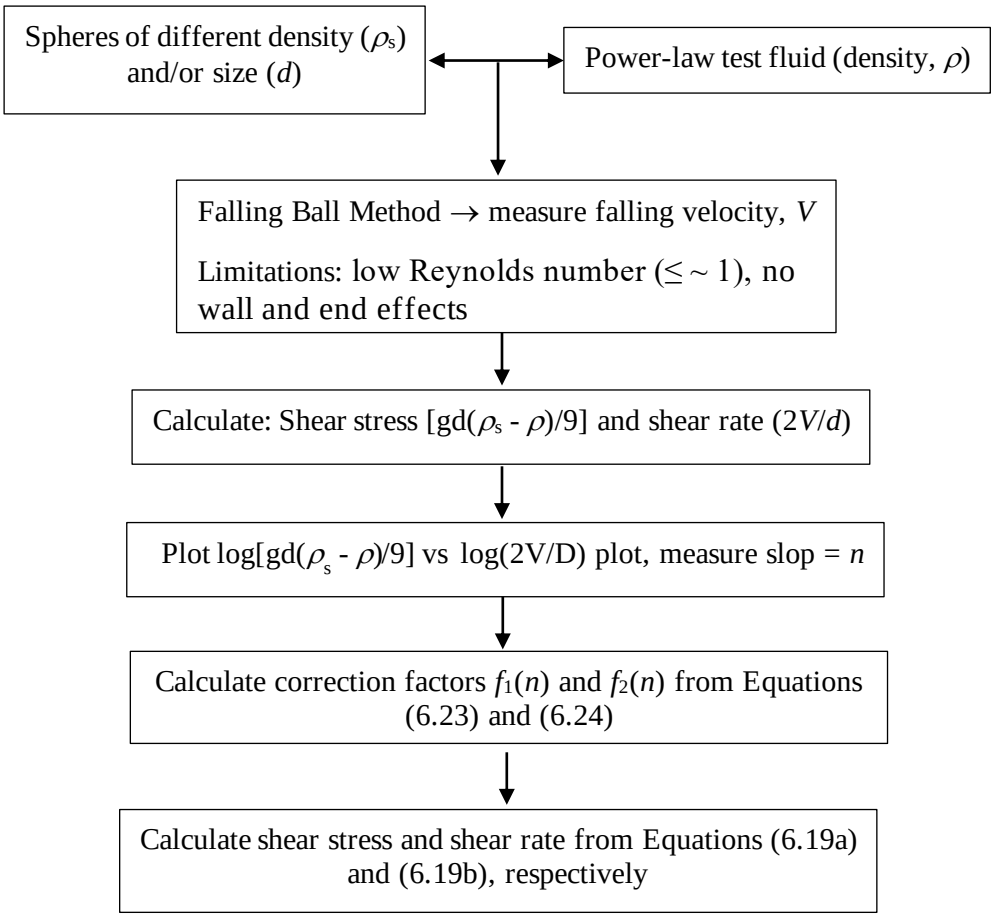


**Fig. A5** Flow chart for developing flow curve for power-law fluids using FBM.